



**Fraunhofer**

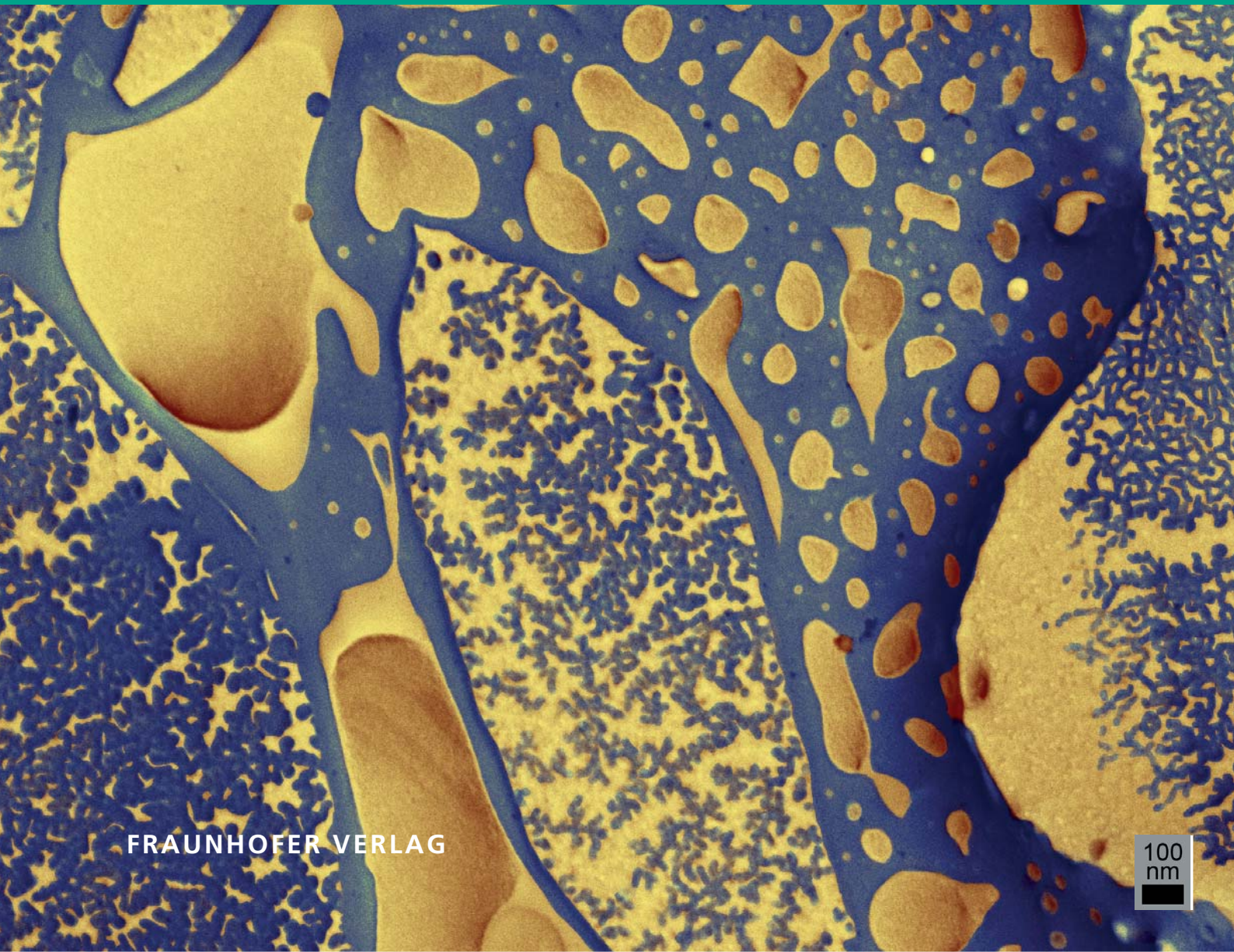
ISE

FRAUNHOFER INSTITUTE FOR SOLAR ENERGY SYSTEMS ISE

SOLAR ENERGY AND SYSTEMS RESEARCH

Christian Geisler

**CHARACTERIZATION OF LASER DOPED SILICON AND  
OVERCOMING ADHESION CHALLENGES OF SOLAR  
CELLS WITH NICKEL-COPPER PLATED CONTACTS**



FRAUNHOFER VERLAG

100  
nm

Fraunhofer Institute for Solar Energy Systems ISE

SOLARE ENERGIE- UND SYSTEMFORSCHUNG /  
SOLAR ENERGY AND SYSTEMS RESEARCH

Characterization of Laser Doped Silicon and  
Overcoming Adhesion Challenges of Solar  
Cells with Nickel-Copper Plated Contacts

Christian Geisler

FRAUNHOFER VERLAG

**Contact:**

Fraunhofer Institute for Solar Energy Systems ISE  
Heidenhofstrasse 2  
79110 Freiburg  
Phone +49 761/4588-5150  
Fax +49 761/4588-9342  
E-Mail [info@ise.fraunhofer.de](mailto:info@ise.fraunhofer.de)  
URL [www.ise.fraunhofer.de](http://www.ise.fraunhofer.de)

**Bibliographic information published by Die Deutsche Bibliothek**

Die Deutsche Bibliothek lists this publication in the Deutsche Nationalbibliografie;  
detailed bibliographic data is available in the Internet at [<http://dnb.d-nb.de>](http://dnb.d-nb.de).

D 25

Zugl.: Freiburg, Univ., Diss., 2015

Book Series: »Solare Energie- und Systemforschung / Solar Energy and Systems Research«

**Printing and Bindery:**

Mediendienstleistungen des  
Fraunhofer-Informationszentrum Raum und Bau IRB, Stuttgart

Printed on acid-free and chlorine-free bleached paper.

All rights reserved; no part of this publication may be translated, reproduced, stored in a retrieval system, or transmitted in any form or by any means, electronic, mechanical, photocopying, recording or otherwise, without the written permission of the publisher.

Many of the designations used by manufacturers and sellers to distinguish their products are claimed as trademarks. The quotation of those designations in whatever way does not imply the conclusion that the use of those designations is legal without the consent of the owner of the trademark.

© by Fraunhofer Verlag, 2015, ISBN 978-3-8396-0916-3

Fraunhofer Information-Centre for Regional Planning and Building Construction IRB  
P.O. Box 80 04 69, D-70504 Stuttgart  
Nobelstrasse 12, D-70569 Stuttgart  
Phone +49 (0) 7 11/9 70-25 00  
Fax +49 (0) 7 11/9 70-25 07  
E-Mail: [verlag@fraunhofer.de](mailto:verlag@fraunhofer.de)  
URL [www.verlag.fraunhofer.de](http://www.verlag.fraunhofer.de)

**Characterization of  
Laser Doped Silicon and  
Overcoming Adhesion Challenges of  
Solar Cells with  
Nickel-Copper Plated Contacts**

Dissertation  
zur Erlangung des Doktorgrades der  
Technischen Fakultät der  
Albert-Ludwigs-Universität  
Freiburg im Breisgau

vorgelegt von

Christian Geisler

Angefertigt am  
Fraunhofer Institut für Solare Energiesysteme

2015

Mündliche Prüfung am: 17. Juli 2015  
Dekan: Prof. Dr. Georg Lausen  
Referent: Prof. Dr. Eike R. Weber  
Korreferent: Prof. Dr.-Ing. Jürgen Wilde

*Und jedem Anfang wohnt ein Zauber inne*

Hermann Hesse

Schlagwörter: Silizium, Solarzelle, Ni-Cu Metallabscheidung, Selektiver-Emitter, Metallkontakthaftung, Laserdotierung, Emitterrekombination, Laser-induzierte Defekte, SiN<sub>x</sub> Ablation

Keywords: Silicon, Solar cell, Ni-Cu plating, Selective emitter, Metal contact adhesion, Laser doping, emitter recombination, Laser induced defects, SiN<sub>x</sub> ablation

# Zusammenfassung

Die Verbindung von Laser-Bearbeitung und galvanischer Metallabscheidung ist eine vielversprechende Option um durch das Ersetzen des relativ teuren Silber-Siebdrucks durch kostengünstiges Kupfer den Preis der Vorderseitenmetallisierung einer kristallinen Silizium-Solarzelle zu senken. Obwohl die industrielle Fertigung von effizienten, Laser-dotierten Solarzellen mit Nickel-Kupfer Kontakten bereits in mehreren Pilotprojekten demonstriert worden ist, bleibt dennoch ein Zweifel bezüglich der Qualität der Haftverbindung zwischen Silizium und Metallkontakt. Leider gibt es zu diesem Punkt bisher nur wenige veröffentlichte Untersuchungen.

In dieser Arbeit wird ein Laserdotierprozess in einem Laboraufbau implementiert um die grundlegenden physikalischen und chemischen Vorgänge zu untersuchen, welche sich bei dem aufschmelzen von Silizium mit einem grünen Dauerstrichlaser abspielen. Dabei wird ein besonderes Augenmerk auf zuvor veröffentlichte Probleme mit inhomogener Metallabscheidung und geringer Haftung, sowie deren Ursachen, gelegt. Es wird ein Modell der Siliziumnitrid Ablation aus Rasterelektronenmikroskopaufnahmen (SEM) und quasi-statischen Photoleitfähigkeitsmessungen (QSSPC) abgeleitet. Dazu wird eine Methode entwickelt, welche eine genaue Bestimmung von Rekombinationseigenschaften aus QSSPC Messungen erlaubt. Eine Oberflächenuntersuchung mit der Röntgenphotoelektronenspektroskopie ermöglicht den Nachweis einer parasitären Oberflächenschicht aus Silizium-Oxynitrid ( $\text{SiO}_x\text{N}_y$ ). Diese dichte  $\text{SiO}_x\text{N}_y$ -Schicht ist eine Diffusionsbarriere und verhindert die Bildung von Silizium-Silizid, welches für die Ausprägung eines ohmschen Kontaktes mit ausreichender Haftung benötigt wird. Nach der Entfernung dieser  $\text{SiO}_x\text{N}_y$ -Schicht zeigen Testzellen zwar eine deutliche Verbesserung der Kontakthaftung, die elektrischen Eigenschaften weisen jedoch auf ausgeprägte lokalisierte Kurzschlüsse hin. Diese Kurzschlüsse werden mittels Sperrspannungs-Elektrolumineszenz-Mikroskopie (ReBEL) und SEM Bildgebung untersucht. Aus den Beobachtungen wird zuerst ein Kurzschlussmechanismus abgeleitet und dieser dann experimentell belegt. Durch die gewonnenen Erkenntnisse wird es ermöglicht alternative Prozessführungen zu entwickeln. Diese alternativen Prozessführungen erlauben die Herstellung von elektrisch und mechanisch stabilen Testzellen mit Nickel-Kupfer Kontakten. Abschließend werden diese Alternativen anhand ihrer industriellen Umsetzbarkeit und des erreichbaren Effizienzpotentials anhand von Computersimulationen bewertet. Unter optimierten Bedingungen führen diese Berechnungen zu effizienten und industriell umsetzbaren Solarzellen mit einem Wirkungsgrad von 21.5 %.



# Abstract

The combination of localized laser patterning and metal plating allows to replace conventional silver screen printing with nickel-copper plating to form inexpensive front contacts for crystalline silicon solar cells. Although efficient laser doped solar cells with plated contacts have been demonstrated on an industrial scale, little data on the quality of the metal contact adhesion is published.

In this work, a laser patterning process is implemented into a research tool in order to study the fundamental physical and chemical mechanisms that govern continuous wave laser doping. A focus is put on effects that could cause previously reported inhomogeneous metal deposition and low metal contact adhesion. A descriptive model of the silicon nitride ablation mechanism is derived from scanning electron microscopy (SEM) and a precise recombination analysis using a quasi-steady-state photoconductance (QSSPC) measurement. Surface sensitive x-ray photoelectron spectroscopy is conducted to prove the existence of a parasitic surface layer, identified as silicon oxynitride  $\text{SiO}_x\text{N}_y$ . The dense  $\text{SiO}_x\text{N}_y$  layer is an effective diffusion barrier, hindering the formation of a nickel silicide interlayer, which is needed to form ohmic contacts with sufficient adhesion. After removal of the  $\text{SiO}_x\text{N}_y$  layer, test cells show severe degradation caused by metal-induced shunting. These shunts are imaged using reverse biased electroluminescence microcharacterization (ReBEL) and SEM imaging. From the observations a shunting mechanism is first proposed, and then experimentally verified. Alternative laser process sequences are devised and proven to produce stable cells with adhering nickel-copper contacts. Conclusively the developed process sequences are assessed based on their industrial feasibility as well as on their efficiency potential, using computer simulations. Under optimized conditions these simulations predict an efficiency potential of 21.5 % for industrial feasible silicon solar cells with nickel-copper plated contacts.



# Acknowledgments

In the first place, I would like to thank Professor Weber, Professor Schwarz and Doctor Glunz for the opportunity to conduct this thesis at the Fraunhofer Institute of Solar Energy Systems and the Faculty of Engineering at the University of Freiburg. I am especially grateful for the friendly and helpful atmosphere I experienced at the Fraunhofer Institute.

I would like to thank the many hands and brains that helped conducting the experiments featured in this thesis. Annika Raugewitz, Rainer Neubauer, Rupprecht Ackermann, Heike Brinckheger, Antonio Leimenstoll, Felix Schätzle, Marc Retzlaff and Aleksander Filipović helped with skillfull precursor production. Gisela Cimiotti, Limeng Ni, Tobias Ensslen, Mathias Kamp, Achim Kraft, and Andrew Mondon were the alchemists producing solid metal from colored water. Careful scanning electron microscopy imaging is attributed to Christoph Fleischmann and Jutta Zielonka. Shunts were located by the treasure hunters Friedemann Heinz and Andreas Büchler.

The cw-laser processing was conducted with strong support from Wilhelm Hördt, Matthias Mesec and Florian Gorenflot.

I would like to thank Martin Lieder, Jonas Bartsch, Martin Heinrich, Johannes Giesecke, and Juliana Miyazaki for their proofreading skills and mental support.

Finally, I owe special thanks to Sven Kluska, Sybille Hopman, and Markus Glatthaar whose support and guidance is the basis of this work.



# Contents

<b>1</b>	<b>Introduction</b>	<b>1</b>
1.1	Scientific Background . . . . .	2
1.2	Scope of This Thesis . . . . .	3
1.3	Outline . . . . .	4
<b>2</b>	<b>Physics of Silicon Solar Cells</b>	<b>7</b>
2.1	Semiconductors . . . . .	7
2.2	Generation of Charge Carriers . . . . .	8
2.3	Recombination . . . . .	10
2.3.1	Radiative Recombination . . . . .	10
2.3.2	Auger Recombination . . . . .	10
2.3.3	Recombination via Impurities . . . . .	11
2.3.4	Surface Recombination . . . . .	12
2.4	p-n junction . . . . .	13
2.4.1	Transport . . . . .	13
2.4.2	Current-Voltage Curve . . . . .	14
2.4.3	Emitter Saturation Current Density . . . . .	16
2.5	Selective Emitter . . . . .	18
2.5.1	Emitter Transparency . . . . .	19
2.5.2	Contact Properties . . . . .	20
2.5.3	Ideal Selective Emitter Properties . . . . .	22
<b>3</b>	<b>Laser Processing for Solar Cells</b>	<b>23</b>
3.1	Industrial Solar Cell Production . . . . .	23
3.1.1	Industrially Feasible High-Efficiency Technologies . . . . .	24
3.2	Laser Processing Technologies . . . . .	24
3.2.1	Laser Ablation . . . . .	25
3.2.2	Metal Plated Contacts on Laser Contact Opening . . . . .	26
3.2.3	Laser Doping . . . . .	26
3.3	Fundamentals of Laser Doping . . . . .	27
3.3.1	Laser Heating . . . . .	28
3.3.2	Laser Melting . . . . .	29
3.3.3	Dynamics of Molten Pool . . . . .	30
3.3.4	Solidification . . . . .	32
3.4	Fundamentals of Contact Formation . . . . .	34
3.4.1	Metal Plating . . . . .	34
3.4.2	Nickel Silicide Formation . . . . .	36

3.5	Challenges for Laser Doped Selective Emitters with Ni-Cu Contacts	37
<b>4</b>	<b>Characterization Techniques</b>	<b>39</b>
4.1	Electron Analysis Methods	39
4.1.1	Interaction Processes	39
4.1.2	SEM Imaging Capabilities	40
4.1.3	Energy-Dispersive X-ray Spectroscopy (EDX)	45
4.1.4	Electron-Beam-Induced Current (EBIC)	45
4.1.5	Transmission Electron Microscopy (TEM)	46
4.2	X-ray Photoelectron Spectroscopy (XPS)	46
4.3	Confocal Microscopy (LEXT)	48
4.3.1	Film Thickness Analysis	48
4.4	Quasi-steady-state photoconductance (QSSPC)	49
4.4.1	Charge Carrier Lifetime	50
4.4.2	QSSPC Measurement	51
4.4.3	Effective Lifetime under Transient Excitation	52
4.4.4	Effective Lifetime under Steady-State Excitation	55
4.5	Other Characterization Techniques	56
4.5.1	Four-Point Probe	56
4.5.2	Electrochemical C-V Profiling (ECV)	57
4.5.3	Quasi-Steady-State $V_{oc}$ Method (Suns- $V_{oc}$ )	57
4.5.4	Reverse Biased Electroluminescence (ReBEL)	57
4.5.5	Adhesion Tester	58
<b>5</b>	<b>Experimental Setup</b>	<b>59</b>
5.1	Laser Process	59
5.1.1	Dopant Source Application	59
5.1.2	Laser Induced Dopant Incorporation	60
5.1.3	Cleaning	61
5.2	Plating Process	61
5.2.1	Light-Induced Plating (LIP)	62
5.2.2	Nickel Silicide Formation	63
<b>6</b>	<b>Evaluation of Suitable Laser Doping Parameters</b>	<b>65</b>
6.1	Requirements for Laser Doped Structures	65
6.2	Laser Ablation	66
6.2.1	Beam Optics	66
6.2.2	Optical Appearance of Laser Lines	67
6.2.3	Nickel Plating on Laser Lines	71
6.2.4	Surface Characterization	73
6.3	n-Type Laser Doping	75
6.3.1	Spin-On Dopant Type and Thickness	75
6.3.2	Depth and Width of Laser Doping	79
6.3.3	Recrystallization Defects	82
6.4	Suitable Laser Doping Parameters	87

<b>7</b>	<b>Cavity Defects in Laser Doped Silicon</b>	<b>89</b>
7.1	Development of a Precise Method for $j_{0e}$ Determination . . . . .	89
7.1.1	Asymmetric Lifetime Samples . . . . .	90
7.1.2	CESS-Method . . . . .	92
7.1.3	Uniform Charge Carrier Approximation . . . . .	95
7.1.4	Transient Excitation Approximation . . . . .	98
7.2	Experimental . . . . .	99
7.2.1	Sample Preparation . . . . .	99
7.2.2	Emitter Saturation Current Densities . . . . .	100
7.2.3	Delineation Etch and Microscopy Study . . . . .	100
7.3	Results and Discussion . . . . .	100
7.3.1	Methodology of $j_{0e}$ Determination . . . . .	100
7.3.2	Emitter Recombination Analysis . . . . .	101
7.3.3	Delineation Etch and Microscopy Study . . . . .	103
7.4	Development of a Model of $\text{SiN}_x$ Ablation and Cavity Formation	105
7.4.1	General Case for Indirect Ablation . . . . .	106
7.4.2	cw-Laser Ablation . . . . .	106
7.4.3	Reduction of Cavity Formation . . . . .	107
7.5	Conclusion . . . . .	107
<b>8</b>	<b>Analysis of Detrimental Surface Layer on Laser Doped Silicon</b>	<b>109</b>
8.1	Experimental . . . . .	109
8.2	Results and Discussion . . . . .	110
8.2.1	Nickel Plating and Silicidation . . . . .	110
8.2.2	XPS Surface Characterization . . . . .	111
8.2.3	Silicon Oxynitride ( $\text{SiO}_x\text{N}_y$ ) Formation . . . . .	113
8.2.4	ns-Pulsed Laser Ablation . . . . .	115
8.3	Laser Induced $\text{SiO}_x\text{N}_y$ Formation . . . . .	117
8.3.1	Formation and Structure of $\text{SiO}_x\text{N}_y$ . . . . .	117
8.3.2	Microstructuring using Silicon Oxynitride . . . . .	118
8.4	Implications for Solar Cell Laser Processing . . . . .	121
8.4.1	Consequences of $\text{SiO}_x\text{N}_y$ Formation . . . . .	122
8.4.2	Overcoming $\text{SiO}_x\text{N}_y$ Connected Challenges . . . . .	122
8.5	Conclusion . . . . .	123
<b>9</b>	<b>Overcoming Mechanical Challenges for Ni-Cu Plated Contacts</b>	<b>125</b>
9.1	Experimental . . . . .	126
9.1.1	Basic Sample Design . . . . .	126
9.1.2	Front Contact Formation . . . . .	126
9.1.3	Electrical and Mechanical Characterization . . . . .	129
9.2	Results and Discussion . . . . .	129
9.2.1	Front Contact Formation . . . . .	129
9.2.2	Microscopic Localization of Ni Induced Shunts . . . . .	133
9.2.3	Adhesion of Ni-Cu Contacts . . . . .	135
9.3	Overcoming Failure Mechanisms . . . . .	137

## Contents

9.3.1	Alternative Processing Sequences . . . . .	137
9.3.2	SiO <sub>x</sub> N <sub>y</sub> Removal . . . . .	139
9.3.3	Prevention of Ni <sub>x</sub> Si <sub>y</sub> Shunting . . . . .	141
9.3.4	Contact Adhesion . . . . .	143
9.4	Simulation of Solar Cell Efficiency Potential . . . . .	145
9.4.1	Setup . . . . .	145
9.4.2	Results and Discussion . . . . .	147
9.5	Conclusion . . . . .	150
<b>10</b>	<b>Summary and Outlook</b>	<b>153</b>
10.1	Outlook . . . . .	155
	<b>References</b>	<b>157</b>
	<b>List of Publications</b>	<b>175</b>

# Nomenclature

4PP	Four-point-probe
BHF	Buffered oxide etch (HF 7%)
BSE	Backscattered electrons
BSF	Back surface field
CASINO	monte carlo simulation of electron trajectory in solids
CESS	solving the continuity equation under steady-state excitation
CZ	Czochralski (crystal growth process)
cw	Continuous wave
DI	Deionized
EBIC	Electron beam induced current
ECV	Electrochemical C-V profiling
EDX	Energy dispersive x-ray analysis
HF	Hydrofluoric acid
HLI	High level injection
IR	Infra red
ISE	Institute for solar energy systems
LBSF	Local back surface field
LCO	Laser contact opening
LCP	Laser chemical processing
LD	Laser doped
LDSE	Laser doped selective emitter
LEXT	Olympus LEXT microscope
LFC	Laser fired contacts
LIP	Light-induced plating
LLI	Low level injection
MC	Multicrystalline (silicon material class)
PECVD	Plasma enhanced chemical vapor deposition
PERC	Passivated emitter rear contact
PERL	Passivated emitter rear locally diffused
QSSPC	Quasi-steady-state photoconductance
RMS	Root mean squared
RPM	Rounds per minute
ReBEL	Reverse biased electroluminescence
SE	Secondary electrons
SEM	Scanning electron microscope

SOD	Spin-on dopant
SRH	Shockley-Read-Hall (recombination statistics)
STEM	Scanning transmission electron microscopy
TEM	Transmission electron microscope
TEM <sub>00</sub>	Fundamental transverse mode
UNSW	University of New South Wales
UV	Ultra violet
XPS	X-ray photoelectron spectroscopy
SiN <sub>x</sub>	Silicon nitride
SiO <sub>x</sub> N <sub>y</sub>	Silicon oxynitride

$\hbar$	Reduced Planck constant	$1.055 \cdot 10^{-34} \text{ J s}$
$k_B$	Boltzmann constant	$1.381 \cdot 10^{-23} \text{ J K}^{-1}$
$q$	Elementary charge	$1.602 \cdot 10^{-19} \text{ A s}$

$\alpha_T$	Transport factor	1
$\alpha_\lambda$	Absorption coefficient	$\text{cm}^{-1}$
$\Delta\sigma$	Change in wafer conductance	$\Omega^{-1}$
$\Delta n$	Excess electron density	$\text{cm}^{-3}$
$\Delta n_{\text{av}}$	Average excess carrier density	$\text{cm}^{-3}$
$\Delta p$	Excess hole density	$\text{cm}^{-3}$
$\Delta_{\text{edge}}$	Edge parameter	$\mu\text{m}$
$\Delta_{pFF}$	Shunting induced $pFF$ degradation	%
$\eta$	Efficiency	%
$\kappa$	Thermal conductivity	$\text{W m}^{-1} \text{ K}^{-1}$
$\lambda$	Wavelength	nm
$\mu$	Mobility	$\text{cm}^2 \text{ V}^{-1} \text{ s}^{-1}$
$\omega$	Frequency	$\text{s}^{-1}$
$\rho_B$	Bulk resistivity	$\Omega \text{ cm}$
$\sigma$	Capture cross section	$\text{cm}^2$
$\tau$	Recombination lifetime	s
$\tau_B$	Bulk carrier lifetime	s
$\varepsilon$	Linear energy density	$\text{W s m}^{-1}$
$c_p$	Specific heat at constant pressure	$\text{J K}^{-1}$
$D$	Diffusion coefficient	$\text{cm}^2 \text{ s}^{-1}$
$d_0$	Laser beam waist diameter	$\mu\text{m}$
$E$	Energy	eV, J
$E_G$	Bandgap energy	eV
$E_{\text{pulse}}$	Pulse Energy	J
$E_F$	Fermi energy	eV

$G, g$	Generation rate	$\text{cm}^{-3} \text{ s}^{-1}$
$I$	Current	A
$j$	Current density	$\text{A cm}^{-2}$
$j_0$	Saturation current density	$\text{fA cm}^{-2}$
$j_\lambda$	Photon flux	$\text{cm}^{-2} \text{ s}^{-1}$
$j_{mp}$	Current density of maximum power	$\text{A cm}^{-2}$
$j_{sc}$	Current density at short circuit	$\text{A cm}^{-2}$
$L$	Diffusion length	cm
$n$	Electron concentration	$\text{cm}^{-3}$
$N_a$	Acceptor concentration	$\text{cm}^{-3}$
$N_d$	Donor concentration	$\text{cm}^{-3}$
$n_i$	Intrinsic carrier concentration	$\text{cm}^{-3}$
$P$	Laser power	W
$p$	Hole concentration	$\text{cm}^{-3}$
$R$	Recombination rate	$\text{cm}^{-3} \text{ s}^{-1}$
$R_{sh}$	Sheet resistance	$\Omega$
$S$	Surface recombination velocity	$\text{cm s}^{-1}$
$T$	Temperature	K
$t$	Time	s
$V$	Voltage	V
$v$	Scanning velocity	$\text{m s}^{-1}$
$V_{mp}$	Voltage of maximum power	V
$V_{oc}$	Voltage at open circuit	V
$W$	Wafer thickness	cm
$w_d$	Width of doping at surface level	$\mu\text{m}$
$w_o$	Width of contact opening	$\mu\text{m}$
$Z$	Atomic number	1
$z_R$	Rayleigh length	m
$j_{0e}$	Emitter saturation current density	$\text{fA cm}^{-2}$
$\tau_{\text{eff}}$	Effective carrier lifetime	s
$FF$	Fill factor	%
$pFF$	Pseudo fill factor	%



# 1 Introduction

To achieve a competitive advantage, it is imperative for a company which is producing a commodity good to have lower production costs than its rivals. Industrially produced photovoltaic modules are considered to be such commodities, with only little brand differentiation. The cost of a photovoltaic module is typically expressed on terms of cost per peak power produced by the module. Thus a competitive advantage can be achieved by low production costs or high conversion efficiency.

With of market share of 7% Suntech Power was the largest producer of photovoltaic modules in 2010 [1]. Besides the expansion of its production capacity, Suntech Power's strategy relied on implementing novel process technologies into industrial mass production in order to drive down costs and increase solar cell efficiency. Its Pluto solar cell technology relied on an innovative patterning technique for the silicon nitride coating and a low cost replacement for the silver contacts by a self aligned metallization technique [2]. In close cooperation with Suntech Power, researchers at the University of New South Wales have developed a method to simultaneously ablate the silicon nitride coating and introduce dopants into the underlying silicon by means of laser processing. A solar cell patterned in this way, can then be contacted by self aligned electrochemical metal deposition of a stack of nickel and copper [3]. Localized doping and fine metallization structures allow a significant increase of device efficiency while at the same time the precious silver is replaced with inexpensive copper, yielding substantial cost reduction potential [4]. However, Suntech Power was not able to turn the innovative Pluto cell into a commercial success and declared bankruptcy shortly after defaulting on a half a billion dollar bond payment in early 2013 [5]. Although the photovoltaic industry is skeptical after Suntech Power's prominent failure, the combination of laser patterning and a metal plating process, replacing conventional silver screen printing, remains to be a promising option to lower the cost per peak power ratio.

To the disfavor of the industry, Suntech Power has not published a description of the technological challenges that may have prevented the commercialization of the Pluto cell. This open question is the starting point of the work presented here.

### 1.1 Scientific Background

The passivated emitter and rear locally diffused (PERL) solar cell, which was developed and optimized at the University of New South Wales (UNSW), took solar cell efficiencies beyond 23 % in the 1990's [6–9], and still holds the world record for a single silicon crystal solar cell with a champion efficiency of 25 % under 1-sun illumination [10]. The superb performance of this laboratory-scale device relies on advanced micro-electronic processing. A high quality oxide on the front and back surface, and a locally diffused highly doped region below the rear metal contacts minimizes the charge carrier recombination at the surfaces and results in a high open-circuit voltage. A high short-circuit current voltage is achieved through a double layer antireflection coating in combination with an inverted pyramid texture, which is defined by photolithography. By using a selective emitter, which is the combination of a lowly doped blanket emitter and a highly doped emitter localized below the front metal contacts, the cell performance is further improved. The effect of the selective emitter relies on shielding the minority carriers from the highly recombinative metal surface, and will be detailed in Sec. 2.5. The selective emitter as well as the evaporated titanium-palladium-silver front side metallization is defined by photolithography.

Within the cooperation of Suntech Power and the UNSW the costs and benefits of the individual processes needed for the production of the PERL cell were assessed and processing steps were removed, modified, or replaced to produce a marketable product. To give an example, the double layer structure of a thermal oxide and an antireflection coating can be replaced by a single layer of silicon nitride and the inverted pyramid texture can be replaced by wet anisotropic etching, creating random pyramids. By balancing the tradeoffs and interactions between materials and processes, the Pluto technology achieves a 10-15 % performance advantage at costs per unit area similar to the costs of conventional screen printed solar cells [2].

The benefits of a selective emitter and fine metallization lines can be achieved without costly photolithography by using a laser based process, coined laser doped selective emitter (LDSE) [11–30]. In this process, which was also developed at the UNSW, a focused laser beam is used to locally melt the surface of the silicon wafer, which is coated with a dopant source. The antireflection coating atop the molten silicon is decomposed and dopants are incorporated, thereby forming a region of exposed and heavily doped silicon. By means of metal plating a self-aligned metal contact can be formed on this exposed silicon. Replacing silver screen printing by plating of the nickel-copper front contact yields a substantial cost reduction potential [4, 31, 32]. The fundamental physical and chemical mechanisms that govern the laser doping and the metal plating process will be explained in detail in chapter 3.

Great effort has been invested into optimizing the dopant and laser sources [11–13], reducing the laser induced damage [14–17], and scaling up the technology for mass production [18–20]. Although efficiencies exceeding 19 % were demonstrated using standard production equipment, inhomogeneous metal plating [21, 22, 33] and low adhesion of the metal contact [17, 33, 34] have been reported.

An inhomogeneous nickel layer and low contact adhesion are particularly detrimental for the long term stability of a photovoltaic module. A dense and closed nickel layer between silicon and copper is imperative to hinder the diffusion of copper into the silicon, where it creates highly active recombination centers [35], thereby lowering the efficiency of the solar cell. Poor adhesion can cause problems during automated module manufacturing, leads to detachment of contact fingers and reduces long-term module performance.

On the one hand, the uniformity of the plated nickel layer can be improved by adjusting the plating process [33] and propositions have been made to enhance the contact adhesion by mechanical interlocking of the metal layer at keying features [17, 36]. On the other hand, quantified data are rare and a detailed analysis explaining the cause of these issues has not been published.

## 1.2 Scope of This Thesis

Laser doping is considered to be a promising industrially feasible technology to produce a selective emitter. The combination of this laser doping and the removal of the antireflection coating into a single processing step is most advantageous from an economical point of view. Efficient laser doped solar cells with nickel-copper plated contacts have been demonstrated on an industrial scale using the LDSE process. All these statements qualify the LDSE technology in combination with the nickel-copper plating for a successful commercialization. However, even four years after the integration of the technology into mass production, solar cells produced with the LDSE process are not commercially available.

The primal objective of this work is to implement the LDSE process into a flexible research tool in order to study the fundamental physical and chemical mechanisms that govern the laser doping process. The goal of this conduct is to identify the technological challenges that hinder the commercial success of innovative laser doped cells with nickel-copper plated contacts. A focus is put on effects that could produce the previously reported inhomogeneous metal deposition and low metal contact adhesion. Options to overcome these challenges need to be developed and experimentally verified. An assessment of the complexity and efficiency potential of these options will then allow a reevaluation of the industrial feasibility of laser doping in conjunction with nickel-copper plating.

### 1.3 Outline

This thesis is structured according to the following outline:

#### **Physics of Silicon Solar Cells**

Chapter 2 presents the fundamental working principle of a crystalline silicon solar cell. A focus is put on the concept of a selective emitter, which allows to tailor the front side of the cell in a way that is favorable for device efficiency and nickel-copper plated contacts.

#### **Laser Processing for Solar Cells**

Chapter 3 outlines industrial state-of-the-art processes to produce efficient silicon solar cells. In particular laser ablation, metal plating on contact openings, and laser doping is discussed. This is followed by a description of the fundamental physical and chemical mechanisms that govern these processes. The chapter is concluded with an assessment of the challenges that laser doping processes for nickel-copper plated silicon solar cells are facing.

#### **Characterization Techniques**

Chapter 4 reviews the characterization methods that form the basis for the analysis of laser processed silicon and the properties of the nickel-copper plated contacts. A focus is put on the scanning electron microscopy and on the contactless photoconductivity decay method. The former method allows imaging and elemental analysis of laser processed silicon, whereas the latter method is used to determine its recombination properties.

#### **Experimental Setup**

Chapter 5 describes for one thing the experimental setup for the laser process which was implemented within this thesis, and for another thing the experimental realization of the contact formation by light-induced nickel plating and thermal nickel silicide formation. These processes form the basis of the experiments conducted in the following chapters.

#### **Evaluation of Suitable Laser Doping Parameters**

Chapter 6 starts with a brief discussion of the general requirements on an industrially feasible laser doping process. In the main part of the chapter, the parameter space of the laser process is studied with a row of dedicated experiments, which are designed to find suitable parameters for dielectric ablation, silicon doping, and epitaxial recrystallization. By this measure a parameter set is picked that serves as a baseline process which is studied in detail in the following chapters.

### **Cavity Defects in Laser Doped Silicon**

Chapter 7 is dedicated to a thorough analysis of the recombination properties of the laser doped silicon. The basis of this analysis is the development of a precise method for the determination of the emitter saturation current density from photoconductivity decay measurements. This refined method is then used to determine the quality of laser doped emitters and specifically reveal the decline of quality if the laser doping process is performed on silicon nitride coated wafers. In that case, scanning electron microscopy reveals macroscopic defects in the recrystallized silicon. From these observations a descriptive model for the silicon nitride ablation and defect formation during laser processing is derived.

### **Analysis of Detrimental Surface Layer on Laser Doped Silicon**

Chapter 8 studies the composition of the silicon surface after laser ablation by means of x-ray photoelectron spectroscopy. This measurement is correlated to nickel deposition, nickel silicide formation, and high resolution electron imaging to prove the formation of a parasitic silicon oxynitride surface layer, which hinders nickel deposition and prevents nickel silicide formation. From these results, implications for solar cell laser processing are drawn, which are used to produce test cells in the next chapter.

### **Overcoming Mechanical Challenges for Ni-Cu Plated Contacts**

Chapter 9 concludes this thesis with a detailed investigation of the adhesion of nickel-copper plated contacts on laser doped silicon. In the first part of this chapter, it is experimentally verified that laser doped devices need to fulfill two necessary requirements with regard to the extend of the laser doped region and the condition of the silicon surface, in order to produce excellent contact adhesion. Based on this insight, three process sequences are developed, all of which result in electrically stable cells with excellent contact adhesion. This is proven by conducting electrical and mechanical characterization on solar cell test samples. With the knowledge of the recombination parameters of the laser doped silicon and the design constraints for the production of stable solar cells, numerical device simulations are performed. This allows to conclusively assess the developed process sequences based on their industrial feasibility as well as on their efficiency potential.



## 2 Physics of Silicon Solar Cells

Solar cells allow the conversion of light into electrical energy. The vast majority of solar cells are based on the crystalline silicon. If visible light is absorbed in silicon free moving electrons and holes are created. Due to the ability of a p-n junction within the silicon material to separate electrons and holes, a charge current can be driven through an external circuit.

This chapter will present the basic physical principles the operation of a crystalline silicon solar cell is based on. In addition to this, the concept of a selective emitter will be motivated by solving the carrier transport equation for a well passivated and a metallized surface. The benefit of a selective emitter in terms of surface recombination, silicon metal contact, as well as its transparency will be discussed.

### 2.1 Semiconductors

A semiconductor is a solid state crystal characterized by a small range of forbidden energy levels adjacent to the energy levels occupied by the valence electrons. This so-called bandgap separates the valence band from the conduction band. For the semiconductor silicon the width of the bandgap is 1.1 eV. An insulator like silicon oxide has a much wider bandgap of 9 eV. Because of the bandgap semiconductors are isolating at temperatures close to 0 K. But in contrast to insulator, the conductivity increases with temperature  $T$  as more electrons occupy states in the conduction band and can move freely in the semiconductor crystal. The probability  $p(E)$  at which a certain energy level  $E$  is occupied by an electron is described by the Fermi-Dirac distribution

$$p(E) = \frac{1}{1 + \exp\left(\frac{E - E_F}{k_B T}\right)}, \quad (2.1)$$

with Boltzmanns constant  $k_B$  and Fermi level  $E_F$ . The Fermi level is defined as the energy level at which  $p(E)$  equals 50% and characterizes the sudden drop in the occupation density. For pure (intrinsic) silicon  $E_F$  is approximately mid-bandgap.

The conductivity of a semiconductor can also be increased by doping. In a doped (extrinsic) semiconductor tiny fractions (1 in  $10^{11}$ ) of the semiconductor atoms are replaced by atoms that have a different number of valence atoms. The dopant is bound covalently to the crystal lattice which presents a tetravalent bond leaving an excess electron in the case of a pentavalent dopant and a vacancy (hole) in the case of a trivalent dopant. The former is a donor forming

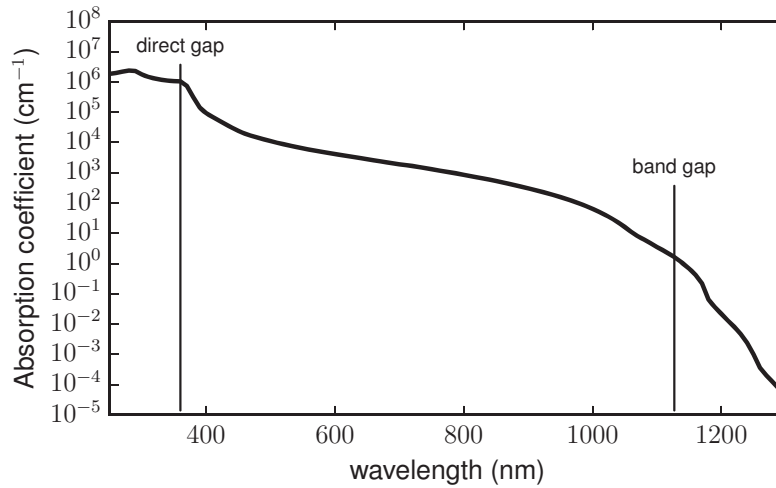


Figure 2.1: Absorption coefficient as a function of the wavelength for crystalline silicon. (data from [37])

n-type material, and the latter is an acceptor leading to a p-type semiconductor. Donor doping raises  $E_F$  close to the conduction band and acceptor doping lowers  $E_F$  close to the valence band. Doping and the consequential shift of  $E_F$  results in a high concentration of free electrons or holes. These are called the majority carriers. Dopants typically used in solar cell applications are Phosphorus and Boron.

## 2.2 Generation of Charge Carriers

Each electron that is lifted from the valence band to the conduction band leaves a vacancy called hole in the valence band. These (quasi-) particles are called excess charge carriers and their densities are denoted as  $\Delta n$  and  $\Delta p$  for electrons and holes accordingly. The energy needed to create an electron-hole pair can be provided by processes that supply at least the minimum energy to overcome the bandgap  $E_G$ . For solar cells the absorption of photons is the most important process. For silicon the lowest photon energy that can create an electron-hole pair is in the infrared at a wavelength  $\lambda$  of about 1100 nm.

The probability of a photon to be absorbed in a material is proportional to its absorption coefficient  $\alpha_\lambda$ , which is shown as a function of the wavelength of the photon in Fig. 2.1. Photons with an energy well above the band-gap energy cause interband transitions which results in strong absorption. The sudden decrease of the absorption coefficient at 360 nm ( $\hbar\omega = 3.4$  eV), still well above the wavelength corresponding to the band-gap energy of 1100 nm ( $\hbar\omega = 1.1$  eV), is explained by the fact that there are two different kinds of interband transitions in materials like silicon. Direct interband transitions, are transitions from the valence band to the conduction band without a change in crystal momentum, the corresponding direct energy gap is for silicon is 3.4 eV. Indirect interband transitions involve valence and conduction band

states with a difference in crystal momentum. The momentum change needs to be balanced by an additional phonon, since a photon itself only carries a negligible momentum. The probability of an indirect transition is reduced due to the involvement of a third particle which results in the gradual decrease in the absorption coefficient. The small peak shown in Fig. 2.1 in the near-infrared at  $10^4$  nm is caused by low energy photons coupling to lattice vibrations.

Assuming that any photon with an energy above 1.1 eV is absorbed within the silicon via excess charge carrier generation only, this generation  $g_\lambda(z)$  in the material at a distance  $z$  from the surface can be described by the Beer-Lambert law. For a monochromatic illumination with wavelength  $\lambda$  and the photon flux  $j_\lambda$  impinging on the surface the generation can thus be expressed as:

$$g_\lambda(z) = j_\lambda \exp(-\alpha_\lambda z). \quad (2.2)$$

In thermal equilibrium (here: in the dark) the rate of generation for electron-hole pairs  $G$  does not depend on the concentration of electrons in the conduction band  $n$  or of holes in the valence band  $p$ . However, the recombination rate of charge carriers  $R$  is proportional to the electron or hole concentration in thermal equilibrium  $n_0$  and to  $p_0$  with the constant recombination probability  $r$ . In thermal equilibrium  $G = R$ , therefore  $G = R = rn_0p_0$ . As a consequence the quotient  $G/r$  is independent  $n_0$  and  $p_0$  and can be expressed by the intrinsic charge carrier density  $n_i$ :

$$n_0 p_0 = n_i^2 = G/r. \quad (2.3)$$

Since  $r$  is a constant  $n_i$  solely depends on  $G$  and thus on the temperature. This relation holds for intrinsic and extrinsic semiconductors in thermal equilibrium. The intrinsic carrier concentration of silicon at room temperature is about  $10^{10}$ . An accurate measurement of  $n_i$  for silicon as a function of temperature was conducted by Misiakos and Tsamakis [38].

In a p-type doped (n-type doped) semiconductor  $n_i$  is negligible compared to the concentration of acceptors  $N_a$  (donors  $N_d$ ). Therefore,  $p_0 = N_a$  ( $n_0 = N_d$ ) and thus:

$$\begin{aligned} n_0 &= n_i^2/N_a && \text{(n-type),} \\ p_0 &= n_i^2/N_d && \text{(p-type).} \end{aligned} \quad (2.4)$$

In an illuminated semiconductor both  $n$  and  $p$  are increased from their equilibrium value by  $\Delta n$  and  $\Delta p$ :

$$n = n_0 + \Delta n, \quad p = p_0 + \Delta p. \quad (2.5)$$

Since electrons and holes are generated in pairs  $\Delta n = \Delta p$ .

## 2.3 Recombination

When the illumination or any other process creating excess charge carriers in a semiconductor, is turned off, the system must return to a state of thermal equilibrium and the excess carriers must disappear. Electron hole pairs diffuse through the semiconductor until they meet up and recombine. The rate of recombination  $R$  and the recombination lifetime  $\tau$ , which is the average time for an electron hole pair to recombine after its generation, are related by

$$\tau = \frac{\Delta n}{R}. \quad (2.6)$$

Crystal defects within the bulk or surfaces create energy states within the bandgap and promote recombination. Auger recombination, a process involving three particles, becomes important in the case of high concentrations of one or both charge carriers. In addition to this, each generation process mentioned in the previous section has its inverse radiative recombination process.

### 2.3.1 Radiative Recombination

Radiative recombination is the inverse process to the absorption of light. This recombination is a transition of an electron from the conduction band into the valence band which releases a photon. Most of the released photons have an energy similar to the energy of the bandgap. In indirect semiconductors like silicon this recombination also needs the participation of a phonon to balance the impulse. For this reason the radiative recombination rate in silicon solar cells is negligible compared to non-radiative recombination processes, which will be discussed below. Radiative recombination in thermal equilibrium and out of thermal equilibrium is discussed in detail by Roosbroeck and Shockley [39] and Schlangenotto et al. [40].

### 2.3.2 Auger Recombination

In the case of Auger recombination the energy released from the recombination of an electron hole pair is taken up by another particle. In addition to the recombining electron hole pair a third particle partakes in the reaction. The energy is transferred to an electron or hole as kinetic energy that is subsequently lost to the lattice through collisions with phonons. This rate at which this process occurs is high when there is a high density of carriers in one or both of the bands. This is the case for highly doped silicon or under conditions of high carrier injection.

Traditionally, the Auger recombination rate is given by an expression of the form [41]:

$$R_A = (C_p p + C_n n) (np - n_i^2). \quad (2.7)$$

The first term will be the dominant contribution for p-type doped material, whereas the second term will dominate for n-type material. In the low level

injection (LLI) limit, i.e.,  $\Delta n \ll N_d$  ( $\Delta p \ll N_a$ ), the Auger lifetime (cf. Eq. 2.6 independent of the excess carrier density:

$$\tau_{A,n} = \frac{1}{C_n N_d^2}, \quad \tau_{A,p} = \frac{1}{C_p N_a^2} \quad (\text{LLI}). \quad (2.8)$$

In the limit of high level injection (HLI), i.e.,  $\Delta n \gg N_d$  ( $\Delta p \gg N_a$ ), both terms will contribute and Eq. 2.7 becomes independent of the doping level:

$$\tau_A = \frac{1}{(C_n + C_p) \Delta n^2} = \frac{1}{C_a \Delta n^2} \quad (\text{HLI}), \quad (2.9)$$

with the so-called ambipolar Auger coefficient  $C_a$  [42]. The emitter, a usually highly doped region of a solar cell, is under 1-sun illumination conditions in low level injection. The Auger recombination within the emitter can thus be described by Eq. 2.8 and is independent of the injection level.

At high injection levels this traditional theory of Auger recombination was experimentally verified. However, at intermediate carrier concentrations higher Auger coefficients were found. This difference was explained by an attractive interaction between the carriers of opposite charge and repulsive interaction between charge carriers of the same type. Equation 2.7 can be modified to reflect these effects by multiplying the Auger coefficients with the so-called Coulomb enhancement factors  $g_{eeh}$  and  $g_{ehh}$ . A detailed discussion as well as the most recent parametrization of these factors was done by Richter et al. [43].

### 2.3.3 Recombination via Impurities

In most cases the dominant recombination mechanism in silicon devices is the recombination via impurities, crystal defects, or defect levels at semiconductor surfaces. These can create electron states with energies deep within the forbidden zone. Shockley and Read [44], and Hall [45] have developed a theory describing the recombination via such defects.

For a defect level four fundamental processes are possible: a) an electron from the conduction band can be captured in a vacant defect level or b) an electron at defect level can be emitted into the conduction band. Accordingly, c) a hole can be captured in a vacant defect level or d) a hole can be emitted from the defect level into the valence band. From the probability of these processes the so-called Shockley-Read-Hall recombination (SRH recombination) rate can be derived:

$$R_{SRH} = \frac{v_{th} N_t (np - n_i^2)}{(1/\sigma_p)(n + n_1) + (1/\sigma_n)(p + p_1)}, \quad (2.10)$$

where  $v_{th}$  is the thermal carrier velocity,  $N_t$  is the concentration of defects, and  $\sigma_p$  and  $\sigma_n$  are the capture cross sections of the hole and electrons. The densities  $n_1$  and  $p_1$  can be approximated by the Boltzmann distribution by

$$n_1 = N_c \exp\left(-\frac{E_c - E_t}{k_B T}\right) \quad \text{and} \quad p_1 = N_v \exp\left(-\frac{E_t - E_v}{k_B T}\right), \quad (2.11)$$

with the energy level of the defect  $E_t$ , the effective densities of states in the conduction and valance bands  $N_c$  and  $N_v$ , and the energies of the conduction and the valance bands  $E_c$  and  $E_v$ , if the energy difference  $E_c - E_t$  and  $E_t - E_v$  are small compared to the width of the “Fermi-transition zone” ( $2k_B T$ ). The thermal carrier velocity is at 300 K about  $10^7$  cm/s. With the capture time constants

$$\tau_{n0} := \frac{1}{N_t \sigma_n v_{th}} \quad \text{and} \quad \tau_{p0} := \frac{1}{N_t \sigma_p v_{th}}, \quad (2.12)$$

the Shockley-Read-Hall lifetime is

$$\tau_{SRH} = \tau_{n0} \frac{p_0 + p_1 + \Delta n}{n_0 + p_0 + \Delta n} + \tau_{p0} \frac{n_0 + n_1 + \Delta n}{n_0 + p_0 + \Delta n}. \quad (2.13)$$

The SRH recombination depends on the injection level, on the doping level, as well as on the specific defect properties. Defect levels in the middle of the forbidden zone are, independent of the dopant level, effective recombination sites. The SRH recombination rate of defects with a energy closer to the band edges increases with the doping level. A detailed discussion of the SRH recombination mechanism, as well as properties of trace contaminations relevant for silicon device processing have been compiled by Schroder [46].

### 2.3.4 Surface Recombination

On the surface of the bulk semiconductor, the chemical bonds to neighboring atoms are broken. This leads to surface states that are different from the band structure in the bulk. The surface states are derived from the bulk valence and conduction band but the corresponding donator-like and acceptor-like surface states can form a single broad band. This band offers energy states in the forbidden zone, which are effective mediators for non-radiative recombination. Surface recombination can be described using the SRH recombination statistics as discussed above. In contrast to the defect levels in the volume, the continuous band of defect levels at the surface is accounted for by integrating Eq. 2.10 over the forbidden energies:

$$R_s = \int_{E_v}^{E_c} \frac{v_{th} D_{it}(E) (n_s p_s - n_i^2)}{(1/\sigma_p(E)) (n + n_1) + (1/\sigma_n(E)) (p + p_1)} dE \quad (2.14)$$

with the density of surface states  $D_{it}(E)$ .

Analogous to the lifetime  $\tau$  defined for the recombination processes in the volume of the material, a recombination velocity  $S$  can be defined from the surface recombination rate  $R_s$ :

$$S = \frac{R_s}{\Delta n} \quad (2.15)$$

## 2.4 p-n junction

In order to convert light into electrical energy in a solar cell electrons and holes not only have to be created, but need be separated and driven out of the absorbing bulk to their respective terminal. In a silicon solar cell the separation of charge carriers can be realized by a p-n junction within the absorber. The p-n junction is the region of direct contact of a p-type and an n-type doped material. In industrial solar cells a p-n junction is typically created by thermally diffusing phosphorus (n-type) dopants into the surface of a boron (p-type) doped bulk. The highly doped surface layer is the so-called emitter and the lowly doped bulk is the so-called basis of the silicon device.

### 2.4.1 Transport

The driving forces that govern the charge carriers are the electric field and the diffusion. The electric field acts on the charge, and the diffusion acts on the concentration. Contact of n-type and p-type silicon in the p-n junction leads to a diffusion current of electrons from the donors to the acceptors and of holes vice versa. In thermal equilibrium this current is compensated by a drift current caused by the electric field of the immobile dopant ions. The strength of the opposing field can be characterized by the so-called diffusion voltage. The region swept free of charge carriers is called the depletion zone or space charge region.

The selectivity of the p-n junction can be put down to two essential features: The electric field of the space charge region, and the large difference between majority and minority carrier conductivities. Due to the strong electric field of the space charge region carriers can be transported against a chemical gradient. For minority carriers a transfer across the p-n junction is favorable. The minority carriers reach the p-n junction by diffusion, but are transported across the p-n junction by a drift in the built in field. After passing the p-n junction this carrier now becomes a majority carrier. For the majority carrier it is not possible to overcome the electric field of the space charge region. In an illuminated p-n junction excess charge carriers and the selectivity of the p-n junction cause a high chemical potential of excess majority carriers at the respective terminals. By connecting an external load to the electrodes of the solar cell this chemical potential can be converted to electric energy.

The kinetics of steady-state transport of minority carriers to the p-n junction is governed by their random motion which is described by the continuity equation for excess charge carriers:

$$D \frac{d^2 \Delta n(z)}{dz^2} = G - R \quad (2.16)$$

with the diffusion coefficient  $D$ .

### 2.4.2 Current-Voltage Curve

In thermal equilibrium drift and diffusion current cancel each other. If an external voltage is applied, this equilibrium will be disturbed. The diffusion current of minority carriers across the p-n junction is independent of the diffusion voltage  $V_D$  or external voltage  $V$ . This current is called generation current because the carriers are constantly created by thermal excitation. This generation current can be expressed in terms of a current per surface area as the current density  $j^{\text{gen}}$ . However, majority carriers need to overcome the electric field of the space charge region to diffuse across the p-n junction. The fraction of majority carriers that is able to cross the p-n junction is given by the Boltzmann factor  $\exp(-q(V_D - V)/k_B T)$  and thus depends strongly on the external voltage. This current density is called recombination current density  $j^{\text{rec}}$ .

Following the procedure outlined by Ibach and Lüth [47], the current-voltage characteristic of a p-n junction can be derived from the following relations: (1) The electron recombination current density at  $V = 0$  cancels the electron generation current density at any external voltage

$$j_n^{\text{rec}}(V = 0) = j_n^{\text{gen}}(V \neq 0), \quad (2.17)$$

and (2) the recombination current density is proportional to the Boltzmann factor

$$j_n^{\text{rec}} \propto \exp\left(-\frac{q(V_D - V)}{k_B T}\right). \quad (2.18)$$

This leads to the recombination current density

$$j_n^{\text{rec}} = j_n^{\text{gen}} \exp\left(\frac{qV}{k_B T}\right). \quad (2.19)$$

and the total current density

$$j_n = j_n^{\text{rec}} - j_n^{\text{gen}} = j_n^{\text{gen}} \left( \exp\left(\frac{qV}{k_B T}\right) - 1 \right). \quad (2.20)$$

The current density of holes across the p-n junction  $j_p$  can be calculated accordingly. Now the current-voltage characteristic of a p-n junction can be derived:

$$j(V) = j_0 \left( \exp\left(\frac{qV}{k_B T}\right) - 1 \right), \quad (2.21)$$

with the so-called saturation current density  $j_0 = j_n^{\text{gen}} + j_p^{\text{gen}}$ . This is the so-called Shockley solar cell equation or one diode model. Figure 2.2 shows the resultant  $j(V)$  curve, which is rectifying the current. If a positive voltage  $V$  is applied the potential barrier of the p-n junction is lowered. As a consequence the electrical resistance is reduced and the current increases exponentially. This polarity is called the forward bias. If a reverse bias voltage is applied the

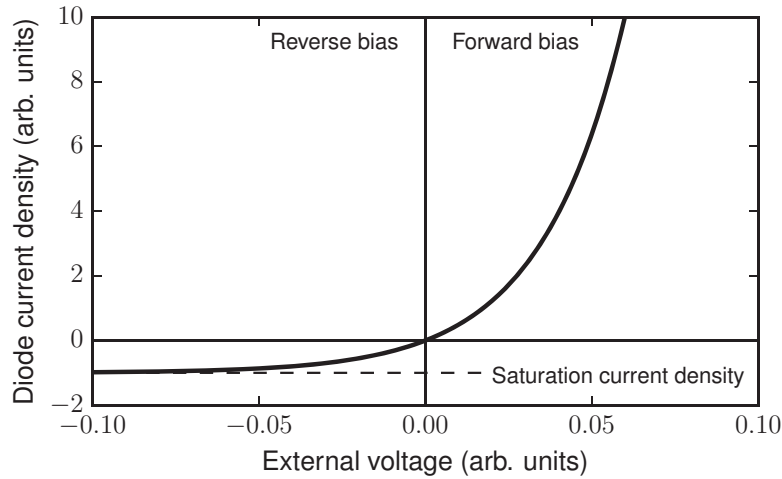


Figure 2.2: Current density-voltage (J-V) curve of a p-n junction. If the junction is operated in forward bias the current density increases rapidly, whereas a diode in reverse bias only permits the flow of the small saturation current density. This saturation current density is determined by the sum of the generation current of electrons and holes.

depletion zone widens. This increases the electric field, thus allowing minimal electric current to cross the p-n junction. This minimal current defines the saturation current density  $j_0$ , which is an important parameter for the conversion efficiency of a solar cell. The saturation current density is connected to the open-circuit voltage of a solar cell through the  $j(V)$  curve of an illuminated p-n junction:

$$j(V) = j_0 \left( \exp \left( \frac{qV}{k_B T} \right) - 1 \right) - j_\gamma, \quad (2.22)$$

where  $j_\gamma$  is the photo current density produced by the impinging photons.

In Fig. 2.3 the  $j(V)$  curve of a solar cell is shown at a photo current density of  $j_\gamma = 37 \text{ mA/cm}^2$ . In contrast to the  $j(V)$  curve of a diode the current axis of the  $j(V)$  curve of a solar cell is inverted because it is generating power. The circles in Fig. 2.3 mark the voltage of maximum power  $V_{mp}$  and the current density of maximum power  $j_{mp}$  at which a solar cell is operated to maximize the energy yield. The square marks the maximum power point (*MPP*). The fill factor of a solar cell (*FF*) is a parameter which, in conjunction with the open-circuit voltage  $V_{oc}$  and the short-circuit current density  $j_{sc}$ , determines the maximum power which can be generated by a solar cell. It is defined by

$$FF = \frac{j_{mp} V_{mp}}{j_{sc} V_{oc}}. \quad (2.23)$$

The open-circuit voltage  $V_{oc}$  is derived by setting  $j(V) = 0$  and solving for  $V$ :

$$V_{oc} = \frac{k_B T}{q} \log \left( \frac{j_\gamma}{j_0} \right). \quad (2.24)$$

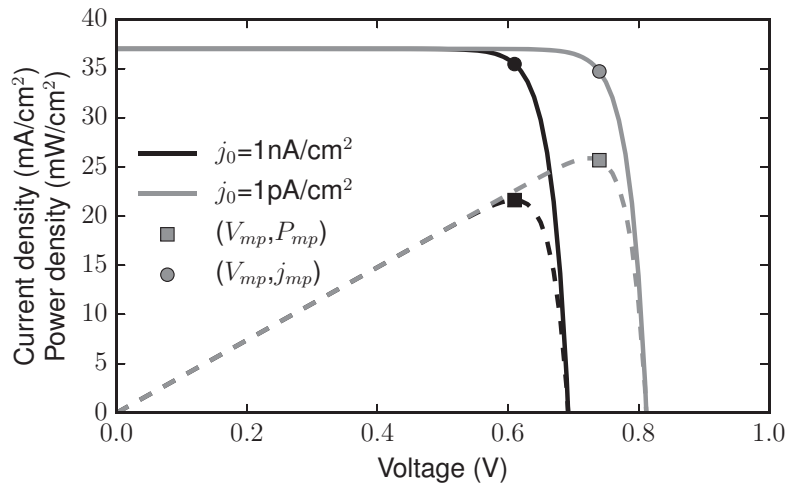


Figure 2.3: Current density-voltage (J-V) curve of a solar cell under illumination (solid line) and power output density of the cell (dashed line). The red line represents a cell with an emitter saturation current of  $1 \text{ nA/cm}^2$  and the green line a cell with a smaller saturation current of  $1 \text{ pA/cm}^2$ . The squares mark the voltages of maximum power output and the circles mark the corresponding current density.

In order to achieve high conversion efficiencies the open-circuit voltage of a solar cell should be as high as possible. Besides increasing the photo current by efficient light absorption, the main handle to increase efficiency is to reduce the saturation current density. The total saturation current density can be divided up into contributions from the base, which is the bulk material of the solar cell and typically lowly p-type doped silicon, and the emitter, which is a thin region of highly n-type doped silicon. The contributions from the base and from the emitter will be denoted  $j_{0e}$  and  $j_{0b}$ .

### 2.4.3 Emitter Saturation Current Density

In advanced solar cell concepts it is one of the primal challenges to achieve a low emitter saturation current density  $j_{0e}$ . In the following the  $j_{0e}$  will be calculated for a simplified emitter with constant dopant concentration  $N_d$ .

The holes injected into the emitter are diffusing according to the continuity equation Eq. 2.16. In the dark, the generation rate  $G = 0$ . The recombination rate  $R$  is expressed by using the charge carrier lifetime  $\tau$  and the diffusion length  $L$  of a charge carrier. For holes this is

$$\tau_p = \Delta p / R \quad (2.25)$$

and

$$L_p = \sqrt{D_p \tau_p}. \quad (2.26)$$

The resulting differential equation for holes in the emitter region is:

$$\frac{d^2 \Delta p}{dz^2} = \frac{\Delta p}{L_p^2}. \quad (2.27)$$

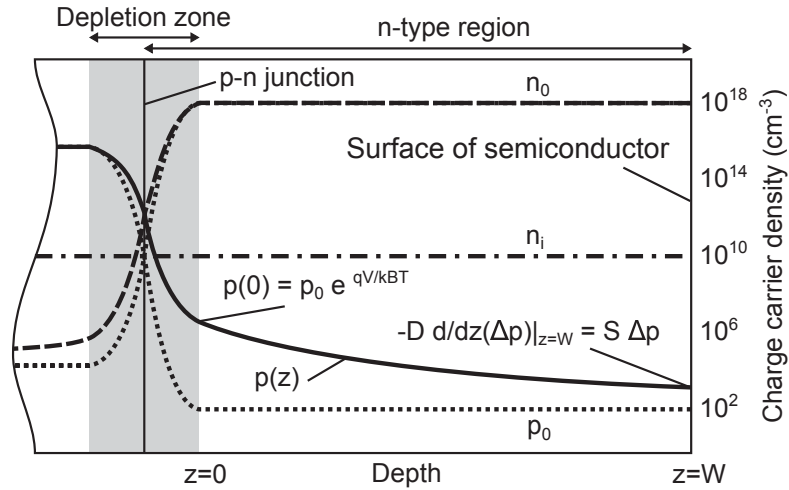


Figure 2.4: Schematic doping concentration (dotted line), electron concentration (dashed line), hole concentration (solid line), and intrinsic carrier concentration (dot-dashed line) within a p-n junction device. At the right side of the figure the semiconductor crystal ends. The wavy line at the left indicates that the structure can be thought of infinitely extended into that direction.

A general solution is

$$\Delta p = A \exp(z/L_p) + B \exp(-z/L_p). \quad (2.28)$$

The constants  $A$  and  $B$  can be extracted using the two boundary conditions at the surfaces of the emitter. The emitter region may be limited at  $z = 0$  by the emitter side of the space charge region and at  $z = W$  by the surface of the semiconductor as illustrated in Fig. 2.4.

The concentration of holes  $p(z)$  at  $z = 0$  can be expressed using Eq. 2.19

$$p(0) = p_0 e^{\left(\frac{qV}{k_B T}\right)} \quad (2.29)$$

using Eq. 2.5 and 2.5 the excess hole density at  $z = 0$  is

$$\Delta p(0) = \frac{n_i^2}{N_d} \left( e^{\left(\frac{qV}{k_B T}\right)} - 1 \right). \quad (2.30)$$

At the surface of the semiconductor the surface recombination governs the concentration of excess holes according to Eq. 2.15:

$$S \Delta p(W) = -D_p \frac{d \Delta p}{dz} \Big|_{z=W} \quad (2.31)$$

By inserting Eq. 2.28 into the boundary conditions Eq. 2.30 and 2.31 the coefficients  $A$  and  $B$  can be determined. The resulting excess hole concentration is

$$\Delta p(z) = \left( \frac{n_i^2}{N_d} \right) \frac{\left( \frac{D_p}{L_p S} \right) \cosh\left(\frac{z-W}{L_p}\right) - \sinh\left(\frac{z-W}{L_p}\right)}{\left( \frac{D_p}{L_p S} \right) \cosh\left(\frac{W}{L_p}\right) + \sinh\left(\frac{W}{L_p}\right)} \left( e^{\left(\frac{qV}{k_B T}\right)} - 1 \right). \quad (2.32)$$

The gradient of  $\Delta p$  evaluated at the edge of the space charge region  $z = 0$  determines the total diffusion current density of holes into the emitter  $j_p$  which can also be expressed using the one diode equation Eq. 2.21 in terms of the emitter saturation current density  $j_{0e}$ .

$$j_p = qD_p \left. \frac{d}{dx} \Delta p(x) \right|_{x=0} \quad (2.33)$$

$$= j_{0e} \left( e^{\left( \frac{qV}{k_B T} \right)} - 1 \right) \quad (2.34)$$

Solving for  $j_{0e}$  yields:

$$j_{0e} = \left( \frac{qn_i^2 D_p}{N_d L_p} \right) \frac{\left( \frac{D_p}{L_p S} \right) \sinh \left( \frac{W}{L_p} \right) + \cosh \left( \frac{W}{L_p} \right)}{\left( \frac{D_p}{L_p S} \right) \cosh \left( \frac{W}{L_p} \right) + \sinh \left( \frac{W}{L_p} \right)}. \quad (2.35)$$

The calculation presented above is valid for an emitter with a constant doping concentration, a so-called box profile. However, emitters for solar cells are usually produced in a high temperature process by diffusing dopants from a dopant rich glass layer into the crystalline material. The dopant profile of most emitters can thus be better described by a Gaussian distribution. For a precise calculation of the emitter saturation current density, the dependency of the diffusion coefficient  $D_p$  and diffusion length  $L_p$  on the dopant concentration, as well as the presence of a drift-field, a dead layer, and bandgap-narrowing needs to be taken into consideration. These effects are discussed in detail in the textbook by Green [41]. Precise calculations of emitter properties from a dopant profile and surface recombination velocity can be performed e.g., by the computer program EDNA [48]. However, the doping profile created by laser doping, which is in the focus of this thesis, shows resemblance to a box profile. Moreover, the calculation presented here motivates the idea behind the concept of a selective emitter presented in the next section, and allows to study the influence of different solar cell parameters.

## 2.5 Selective Emitter

In order to optimize the dopant profile of a furnace diffused emitter, the effect of the dopant concentration and p-n junction depth on the device parameters needs to be considered. Increasing dopant concentration lowers the contact resistance and thus, the  $FF$ . On the other hand a high dopant concentration results in a reduced blue response. A lowly doped emitter can be well passivated, exhibits reduced Auger recombination, and improves the blue response, which raises the short-circuit current density  $j_{sc}$ .

By introducing different emitter profiles in contacted and non-contacted areas the dopant profiles can be optimized separately. The concept of decoupling the emitter properties below the contacted area from the emitter properties of the non-contacted area is called a selective emitter. Figure 2.5 presents a schematic

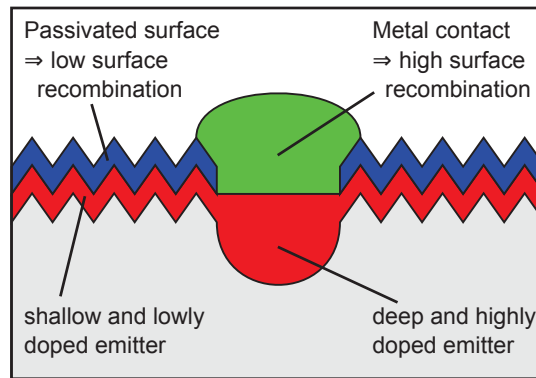


Figure 2.5: Scheme of a silicon solar cell with a selective emitter. The selective emitter is shallow and lowly doped below the passivated surfaces and deep with a high dopant concentration below the metal contacts.

of a selective emitter. For the contacted area a high surface dopant concentration and a high depth are beneficial. A low surface dopant concentration for the passivated, non-contacted, area results in less Auger recombination and better surface passivation. In this section the benefits of a selective emitter with respect to the reduction of  $j_{0e}$ , the blue response, and the contact properties will be discussed.

### 2.5.1 Emitter Transparency

Figure 2.6 shows the influence of the depth of the emitter region  $W$  on the emitter saturation current density as a function of the surface recombination velocity. The  $j_{0e}$  values have been calculated using Eq. 2.35. The surface recombination velocity of silicon covered with a thin dielectric layer of  $\text{SiN}_x$  or  $\text{SiO}_2$  can be as low as  $10 \text{ cm/s}$  [41]. These passivation layers reduce the density of surface states in the forbidden zone and thereby effectively reduce the surface recombination rate. According to Fig. 2.6 a very small  $j_{0e}$  can be achieved if a shallow emitter with a depth of  $100 \text{ nm}$  and a well passivated surface is used. At low  $S$  the saturation current of the shallow emitter is limited by bulk recombination effects, predominantly by Auger recombination.

On the other hand  $S$  can be as high as  $10^6 \text{ cm/s}$  for a silicon surface in direct contact with a metallization layer which creates many surface states in the forbidden zone [41]. The emitter saturation current density increases rapidly if the emitter below a metallized contact is only a few hundred nanometers deep<sup>1</sup>. Here the saturation current is dominated by the highly recombinative surface in close proximity to the p-n junction. According to Eq. 2.35, such a highly recombinative surface may be shielded by an emitter with a large p-n junction depth  $W$  of more than a micrometer, or by increasing the dopant level  $N_d$ . In the case of deep emitters with  $W > L_p$ , the recombination of minority carriers that are injected into the emitter is dominated by Auger recombination because

<sup>1</sup>assuming the same dopant concentration ( $N_d = 10^{19}$ ).

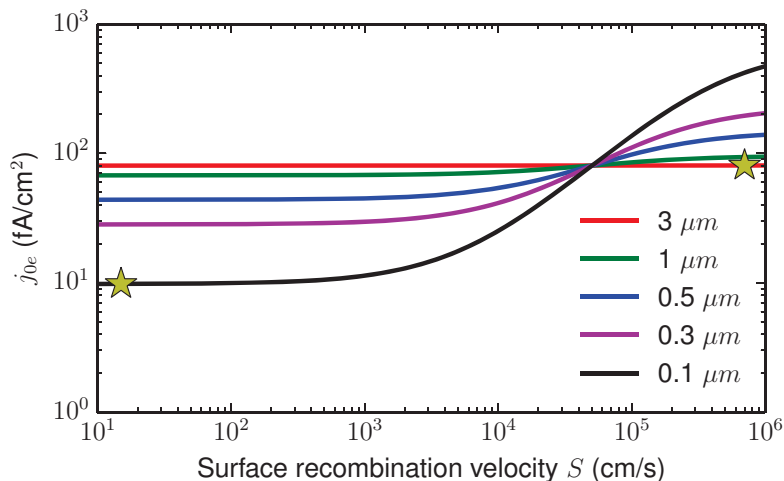


Figure 2.6: Emitter saturation current  $j_{0e}$  as a function of the surface recombination velocity  $S$  with the depth of the emitter  $W$  as a parameter.  $j_{0e}$  has been calculated for a box emitter profile with a constant dopant concentration of  $N_d = 10^{19}$ . At low  $S$  (passivated surface)  $j_{0e}$  is dominated by Auger recombination and thus increases with  $W$ . If  $S$  is high (metallized surface) the recombination is still dominated by Auger processes for the  $3 \mu\text{m}$  deep emitter but in the case of the shallow emitter  $j_{0e}$  is limited by the highly recombinative surface. A selective emitter is designed to be deep below the metallization grid and shallow in the well passivated area, as outlined in Fig. 2.5 and indicated by the stars.

the highly recombinative surface is more than a diffusion length ( $L_p$ ) away. Such an emitter is called "opaque", in contrast to a "transparent" shallow and lowly doped emitter. The transparency of a layer can be characterized by a transport factor  $\alpha_T$  [49]. It is defined as the minority carrier current density reaching the (highly recombinative) surface divided by the current injected into the layer:

$$\alpha_T = \frac{j(W)}{j(0)} \quad (2.36)$$

with the positions  $z = W$  and  $z = 0$  being the surface and the junction, respectively.

In a selective emitter design, the emitter below the contacted area should be opaque, whereas the well passivated emitter may as well be transparent. A transparent shallow and lowly doped emitter exhibits reduced Auger recombination and lower surface recombination velocity if passivated.

### 2.5.2 Contact Properties

An ohmic contact with a low contact resistance between the emitter and the metal contact is imperative to achieve a high cell fill factor. If a metal is brought into contact with a semiconductor surface a Schottky contact is formed. This contact is characterized by a barrier, hindering electronic transport, whose height depends on the work function difference between metal and silicon.

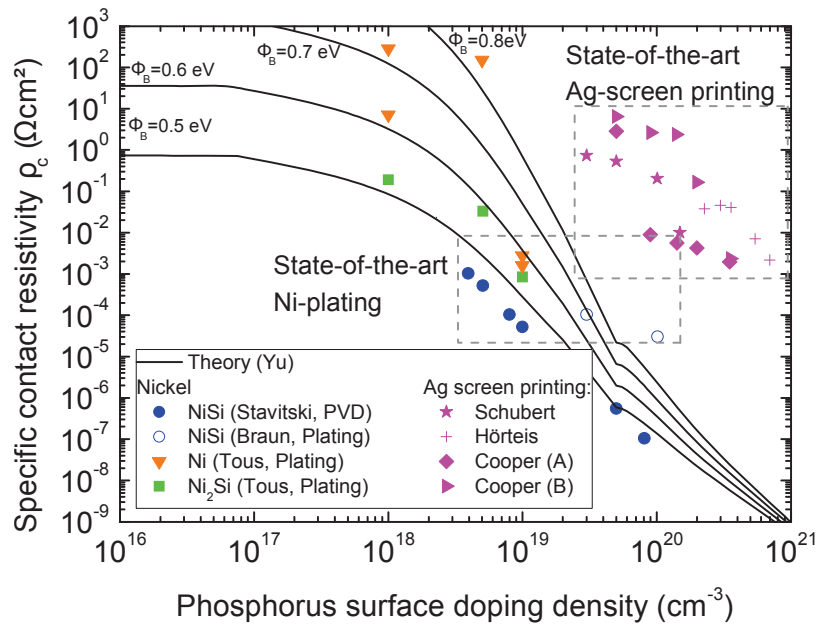


Figure 2.7: Measured and modeled contact resistivities of plated Ni and screen printed Ag contacts on n-type doped surfaces with varying surface doping densities. The presented data are measurements of  $\rho_c$  of Ni, different Ni silicide phases and screen printed Ag contacts from Stavitski [51], Braun [52], Tous [53], Schubert [54], Hörteis [55], and Cooper [56]. The calculated contact resistivities are based on the model of Yu [57]. (from [58])

Electrons can overcome this barrier by tunneling, by thermionic emission or a combination of both mechanisms (thermionic field emission) [50]. The tunneling transport is an efficient transport mechanism allowing low contact resistivities, if the surface dopant concentration is sufficiently high. The transport by thermionic emission generally increases with a decrease of the metals work function. Kluska compiled measured and modeled contact resistivities for screen printed silver and plated nickel contacts as a function of the surface dopant density, shown in Fig. 2.7. Considering the contact geometry, such as the contact width and the finger pitch, he derived limits on the maximum contact resistivities for silver printed and nickel plated contact schemes.

Narrow finger widths, which are achievable with laser contact opening and nickel plating, demand low contact resistances in order to not limit the cell efficiency by fill factor losses. The required low contact resistivities can be achieved by surface doping densities above about  $10^{19} \text{ cm}^{-3}$  and the formation of a nickel silicide. Silicides are typically formed by an annealing step at elevated temperatures, during which nickel diffuses into the silicon. Great care needs to be taken to prevent the penetration of the space charge region by the silicide and the resultant severe degradation of cell performance. In this regard, a deep emitter opens a wider process window for the nickel silicidation process. Laser contact opening, nickel plating, and nickel silicide formation will be discussed in detail in the next chapter.

From these findings two requirements on the emitter below the contact area

can be deduced. For a nickel contacted surface, the dopant concentrations should exceed  $10^{19} \text{ cm}^{-3}$  and the depth of the emitter should be sufficient to prevent nickel silicide growth induced shunting of the p-n junction.

### 2.5.3 Ideal Selective Emitter Properties

From a performance point of view, disregarding the industrial implementation, the ideal selective emitter can be constructed.

The non-contacted emitter should be lowly doped which allows a low surface recombination by effective passivation using e.g.,  $\text{SiN}_x$  [59] or  $\text{SiO}_2$  [60], as well as low Auger recombination. The emitter saturation current density of a well passivated emitter, e.g., with a surface doping concentration of  $5 \cdot 10^{18} \text{ cm}^{-3}$  and a sheet resistance of  $120 \Omega$ , can be as low as  $18 \text{ fA/cm}^2$ , as will be shown in chapter 7. Such an emitter with a low surface recombination of about  $100 \text{ cm/s}$  has near perfect blue response, since minority carriers generated in the emitter region are likely to reach the p-n junction and contribute to the photo current. At the same time the sheet resistance is sufficiently low not to limit the fill factor at a reasonable finger pitch.

The contacted emitter should be highly doped and deep. This increases its opacity, shielding the minority carriers injected into the emitter from the highly recombinative surface. To give an example, a three micrometer deep emitter with a gaussian depth profile, a peak doping concentration of  $1 \cdot 10^{20} \text{ cm}^{-3}$ , and a sheet resistance of about  $10 \Omega$ , results in a transport factor  $\alpha_T$  of about 33 % if the surface recombination velocity at the metal contact is  $10^6 \text{ cm/s}$ . This effective shielding of the metal contact causes a low emitter saturation current density of  $150 \text{ fA/cm}^2$ . The poor blue response of the highly doped emitter is not a disadvantage, since it is shadowed by the metal contact anyway.

With a metallized fraction of about 5%<sup>2</sup> in a nickel-copper plating scheme, the combined emitter saturation current density of this exemplary selective emitter is about  $25 \text{ fA/cm}^2$ . At the same time the contact resistance is with  $5 \cdot 10^{-2} \Omega \text{ cm}^3$  low and the space charge region is sufficiently far away from the nickel covered surface to prevent penetration during nickel silicide formation.

This is the ideal of the selective emitter concept whose implementation into an industrial production has been pursued since the 1990's [41]. In this thesis a method to create highly doped and deep emitters using laser processing will be thoroughly analyzed with regard to its suitability for the industrial production of efficient silicon solar cells with selective emitters and nickel-copper plated contacts.

---

<sup>2</sup>assuming 1 mm finger pitch,  $20 \mu\text{m}$  contact width, and three busbars with a width of 1.5 mm on a  $156 \times 156 \text{ mm}^2$  wafer

<sup>3</sup>assuming a contact resistivity  $\rho_c = 10^{-4} \Omega \text{ cm}^{-2}$  (cf. Fig. 2.7))

## 3 Laser Processing for Solar Cells

After outlining the industrial standard process for producing silicon solar cells, advanced methods to increase the solar cell efficiency are presented briefly at the beginning of this chapter. Many of these advanced methods can be industrially implemented with laser based processes. The development of laser ablation, metal plating on contact opening, and laser doping, as well as the state-of-the-art of these processes is presented in Sec. 3.2. This is followed by a description of the fundamental physical and chemical processes that govern laser doping and the contact formation via metal plating in Sec. 3.3 and 3.4. This chapter is concluded with an assessment of the challenges that laser processes for selective doping for nickel–copper plated silicon solar cells are facing.

### 3.1 Industrial Solar Cell Production

The standard industrial process to manufacture crystalline solar cells can be divided into distinct steps. These steps are outlined here for a typical so-called aluminum back surface field (Al-BSF) solar cell produced from a monocrystalline p-type doped silicon wafer:

1. A 150 – 250  $\mu\text{m}$  thick Czochralski-grown (CZ) silicon wafer is textured using an alkaline etching process. This creates a random pyramid structure on the surface of the wafer that improves the coupling of sunlight into the wafer and thus increases the short-circuit current of the finished cell.
2. A  $\text{POCl}_3$  diffusion in an open-tube furnace creates a n-type doped emitter on both sides of the wafer.
3. The phosphorus-rich glass layer created during the emitter diffusion is removed using wet chemical etching.
4. The junction at the edge of the wafer is removed to eliminate the conducting path between the front and rear metal contacts.
5. A hydrogen-rich  $\text{SiN}_x$  layer is deposited on the front side, e.g. by plasma-enhanced chemical vapor deposition (PECVD).
6. The back contact is screen printed on the rear of the wafer using an aluminum paste. For this solar cell design the back contact is printed full-screen.
7. The front contact grid of fingers and busbars is screen printed using silver paste.

8. A co-firing step in a belt furnace forms an Al-BSF by alloying aluminum into the silicon, fires the front contact paste through the  $\text{SiN}_x$  layer to contact to the emitter and releases atomic hydrogen from the  $\text{SiN}_x$  layer into the silicon bulk to increase its passivating effect. The emitter on the rear is overcompensated by the Al-BSF which forms a p+ region. A so-called high-low junction is formed which reduces the recombination current of the base by shielding the charge carriers from the recombinative rear surface [61]<sup>1</sup>.

#### 3.1.1 Industrially Feasible High-Efficiency Technologies

The Al-BSF design is the dominant cell design in industrial production and allows conversion efficiencies of up to 19.9% [62]. Nevertheless, full-screen printing of the rear side, the width of screen printed contact fingers, and a homogeneous emitter limits the maximum cell efficiency. For this reason alternative cell concepts, which allow to overcome these limitations have been developed by industrial and academic research groups. In order to introduce these so-called high-efficiency designs on an industrial scale with a limited risk of commercial failure and without the costly exchange of most of the equipment in a cell manufacturing plant, a new cell design has to meet the following criteria [59]:

- Possibility of integration into existing production lines
- Small number of extra steps
- No loss in production yield by e.g. cell breakage
- Increase of efficiency on module level

The most prominent approaches to fulfill these criteria are: a) alternatives to the fully covered Al-BSF, b) a change from a homogeneous emitter to a selective emitter, and c) the introduction of plated narrow front contact fingers. Many of these high-efficiency designs can be approached with processing tools based on laser technology.

## 3.2 Laser Processing Technologies

Laser based processes are used in the production of advanced high-efficiency designs such as laser fired contacts [63], laser doped selective emitters [59] and laser contact opening [31] for plated metal contacts. The wide spread use of lasers in solar cell research can be put down to the following points [64]:

- A laser tool can often be used for multiple advanced concepts, which makes it a versatile research tool and drives the development of various laser based processes.

---

<sup>1</sup>This mechanism is similar to the charge-shielding mechanism described in Sec. 2.5.

- Laser processing is contactless and suitable to use with thin silicon wafers.
- Laser processing usually uses little to none consumables and is relatively easy to scale up, which makes it a viable technology for mass production.

The discussion in the following sections will focus on two industrially feasible high-efficiency concepts. The next section will focus on laser induced ablation of the passivating layer, which allows the use of metal plated front contacts. The line width achieved with plated contact fingers is very small which can reduce shading effects and increase the short-circuit current. Additionally, the silver paste used for the standard screen printing of the front contact grid can be replaced by a nickel-copper stack which allows a significant cost reduction, since copper is about a factor 100 times cheaper than silver.

Section 3.3 will discuss selective laser doping, which allows to create regions of deep and highly doped silicon below the metallized contacts, while the emitter below the well passivated region is lowly doped and shallow. This selective emitters brings benefits in terms of a reduced emitter saturation current, an increased blue response, a reduced contact resistance between silicon and metal, and increases the devices resistance to metal-induced shunting. The latter aspect will be discussed in detail in chapter 9.

### 3.2.1 Laser Ablation

The intense irradiation of a laser can be used for the ablation of the passivating dielectric layer of solar cells. This dielectric is usually a 75 – 80 nm thin  $\text{SiN}_x$  layer, a 100 – 110 nm thin  $\text{SiO}_2$  layer, or a double layer with a  $\text{SiO}_2$  layer of 6 – 15 nm below a  $\text{SiN}_x$  layer of about 70 nm thickness [61]. The thickness of this layer is chosen so that interference effects in the coating cause the sunlight reflected from the coating top surface to be out of phase with the light reflected from the silicon surface.

Patterning of the dielectric can be performed by focusing a laser beam onto the substrate by means of a galvanometer scanning head and an f-theta lens. The dielectric layer is transparent at wavelengths down to the UV regime. At wavelengths laser processing is typically performed (IR to UV), only a minute fraction of irradiation is absorbed directly within the thin layer. The laser irradiation is mostly absorbed in the underlying silicon. Here single-photon or multi-photon material excitation is transformed into heat. The increase in temperature changes the absorption within the silicon. Depending on the intensity and duration of the irradiation this rise in temperature can result in surface melting or silicon vaporization [65].

Ablation of the dielectric layer can be put down on two effects. Heat transfer from the hot silicon to the dielectric atop and stress induced by a thermal expansion mismatch between silicon and dielectric. In the case of long irradiation duration as it is the case for continuous wave or ns-pulsed lasers the principal ablation mechanism is heat transfer and decomposition of the dielectric layer. In the case of ultra-short pulsed excitation by a ps-pulsed or fs-pulsed laser a

rapid evaporation of the silicon and thermal stress in the dielectric results in a lift off of the thin film [66].

#### 3.2.2 Metal Plated Contacts on Laser Contact Opening

Metal plating is the electrochemical deposition of metal from a solution of metal ions. It is a metallization scheme for solar cells that was first used in the 1950s at Bell laboratories where dipping of the silicon into a hot lithium bath was used to establish a metal contact to silicon [67]. In the 1990s metal plated solar cells were manufactured on an industrial scale by BP Solar [68]. This innovative solar cell was called the Saturn cell.

Their laser grooved, buried grid solar cell design used laser grooving to define the front contact grid and electroless plating for metal deposition [69]. The metal contact was plated in a stack consisting of three metal layers. A thin nickel layer which improves adhesion between metal and silicon, allows ohmic contact and serves as a diffusion barrier. The second layer consists of plated copper a few ten  $\mu\text{m}$  thick providing conductivity. Copper forms defect states mid-bandgap if it diffuses into the silicon which necessitates that the nickel diffusion barrier is fully closed. A thin layer of plated silver provides solderability for the interconnection of the busbars.

However, this high-efficiency solar cell required high-quality silicon substrates and employed multiple additional process steps. Despite initial calculations [70] the increases in manufacturing expense was not compensated by the gain in efficiency [71]. This led BP Solar to shut down production in 2009.

The introduction of new plating technologies allows simpler fabrication of finer front surface contacts. In light-induced plating (LIP) a p-n junction device is immersed into an electrolyte and illuminated. This causes the n-doped side to adopt a negative potential and thus electrolyte ions are reduced to elemental metal at the surface of the silicon. To control the deposition rate the p-type area of the device can be contacted to a voltage source. A higher negative potential will increase the metal deposition rate. Metal plating will be detailed in Sec. 3.4.1. LIP is assumed to be the technology used for the production of the Pluto cell design developed at the University of New South Wales and commercialized by Suntech Power in 2009 [2]. This technology is still under heavy research [4] and further attempts are made to implement laser induced ablation in combination with LIP into industrial production lines to increase efficiency and decrease cost [18, 31, 32].

#### 3.2.3 Laser Doping

Laser induced heating of silicon can be used to incorporate dopants into the material. The absorbed light intensity must be high enough to substantially heat or even melt the sample surface. Dopants from an external source, which can be present as a gas, liquid, or evaporated film, diffuse rapidly within the liquid phase of the molten Si. The diffusion of phosphorous within the liquid

phase of silicon is increased by more than four orders of magnitude [72]. This allows to utilize the focusability of lasers and the high heating and cooling rates of pulsed lasers in particular to create laterally defined highly doped regions. Especially, green ns-pulsed or continuous wave (cw) lasers prove to be suited for this selective doping in solar cell applications.

Laser doping of solar cells is performed to create a selective emitter on the front (cf. 2.5) or local back surface fields on the rear of the cell [73, 74]. In laser chemical processing (LCP) [75] a pulsed laser is guided by a liquid jet onto the surface of the work piece. Here, the liquid serves as the dopant source. With LCP it is possible to create cells with local back surface field structures but technological hurdles such as nozzle or pipe plugging necessitates further optimization of the process chemicals [76]. Selective LCP doping has also been used to produce efficient and reliable selective emitter cells with nickel–copper plated contacts [77].

At the University of New South Wales a laser doping process was developed, in which the dopant source is deposited on the wafer in form of a dry or liquid film. A continuous wave or pulsed laser is guided by a galvanometer scanning head and focused on the work piece by a f-theta lens. Like LCP, this selective doping can be used to create selective emitters or local back surface fields [22, 78]. The so-called laser doped selective emitter (LDSE) cell design is based on simultaneous ablation of the passivating  $\text{SiN}_x$  layer and doping of the underlying silicon [79]. Like LCP, LDSE enables self-aligned light-induced plating of the front metal contact. LDSE is assumed to be the structuring technology of Suntech’s Pluto cell whose mass production started in 2009 and ended in 2013 with the bankruptcy of its solar-panel operations in Wuxi, China [80].

Most of the experiments conducted in this work are based on the LDSE approach. The connection of LDSE and LIP is treated as a promising technology to increase efficiency beyond that of standard screen-printed solar cells while keeping the cost of production low. The major scope of this work is to understand the laser doping process, identify the challenges that prevented the commercial success of the Pluto cell, and to evaluate options to overcome these problems.

In the following section the fundamental processes involved in laser doping with cw-lasers are presented. They serve as a basis for the interpretations of the experimental observations throughout this thesis.

### 3.3 Fundamentals of Laser Doping

Laser doping relies on melting of the silicon at high laser intensities and the incorporation of dopants into the molten material. Before laser irradiation the dopant source is brought into proximity of the sample surface in form of a gas, liquid or thin film. During irradiation, the dopant source is either thermally decomposed at the surface or directly photodissociated by the laser irradiation,

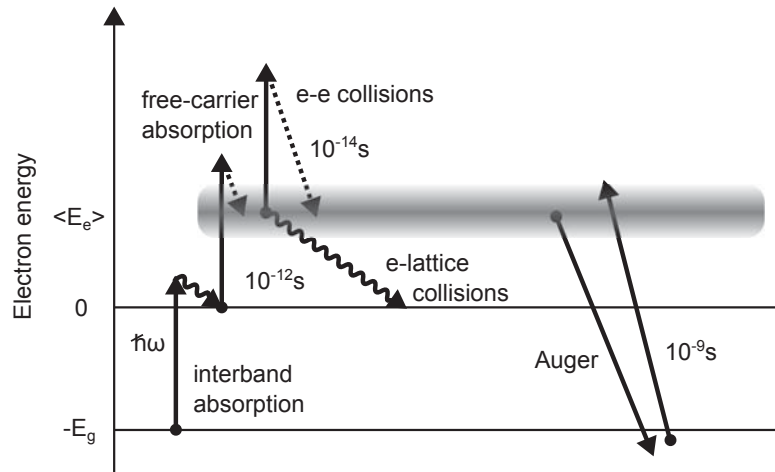


Figure 3.1: Schematic diagram of electron energies in a laser-irradiated semiconductor, showing the free-electron plasma exchanging energy with the beam and the lattice. An analogous diagram holds for holes. (redrawn from [81])

releasing the atomic dopant from its molecular binding [65]. The dopant is effectively incorporated into the silicon material due to enhanced transport in the liquid phase, by both diffusion and convection. The following section will detail on heating, melting, melt convection, and solidification of laser treated silicon.

### 3.3.1 Laser Heating

The primary product of the absorbed photons in silicon is not heat but particle excess energy. If the energy of an impinging photon is larger than the band-gap energy of silicon, the photon may cause the transition of an electron from a state in the valence band to a state in the conduction band. In this interband absorption process (detailed in Sec. 2.2), every absorbed photon creates a charge carrier pair. With the number of free charge carriers, also the free-carrier absorption of photons increases. Free-carrier absorption causes the transition of a charge carrier to a higher energy level within the same band as depicted in Fig. 3.1. Under conditions typical for laser induced silicon remelting, the charge carrier density may reach values at which the energy absorbed by the free charge carriers exceeds that absorbed by the crystal lattice. At high charge carrier densities, collisions among the charge carriers begin to dominate over collisions with the lattice. In that case the excited charge carriers can be regarded as an independent system which absorbs a major fraction of the incident laser light. This plasma of charge carriers gains energy from interband absorption, free-carrier absorption, and from Auger recombination processes [81]. The plasma loses energy by phonon emission. The material is heated by these collisions of excited charge carriers with the crystal lattice.

The degradation of the ordered and localized primary excitation energy into uniform heat involves the randomization of the movement of the excited

charge carriers, the equipartition of the energy among the degrees of freedom of the material, and the flow of heat. Typical time constants connected to randomization by collisions within the plasma as well as equipartition processes such as electron-lattice collisions are shown in Fig. 3.1. For cw or ns-pulsed laser processing these fast processes can be treated as instantaneous. Heat conduction is based on the assumption that the heat flux is proportional to the local temperature gradient. From this, a linear differential equation describing the flow of heat can be derived [65]:

$$\frac{\partial}{\partial z} \left( \kappa \frac{\partial T}{\partial z} \right) = \frac{c_p}{V} \frac{\partial T}{\partial t}, \quad (3.1)$$

with the thermal conductivity  $\kappa$ , the specific heat at constant pressure  $c_p$ , and the molar volume  $V$ . Although Eq. 3.1 neglects the finite mean free path of the heat carriers, this linear heat conduction theory is sufficient for typical laser applications in materials processing [81].

### 3.3.2 Laser Melting

If the temperature of the laser irradiated material rises above its melting temperature, the material changes its optical properties as well as its shape. The reflection and absorption coefficients of molten silicon are significantly higher than those of the solid state. The absorption length ( $1/\alpha$ ) for green light in crystalline silicon is about 500 nm with 36 % of the light being reflected. After melting the absorption length decreases to 8 nm with a reflection of 72 %.

If the laser beam used for melting has a Gaussian intensity distribution the temperature distribution of the surface will also be bell-shaped. Since the surface tension usually depends on the temperature of the melt, the gradient in surface temperature leads to a lateral variation of the surface tension. The temperature coefficient of the surface tension of molten silicon is negative ( $-0.13 \cdot 10^{-3}$  N/mK) [82], which results in the molten film pulling away from the hot center, piling up material at the relatively cool rim. By this so-called Marangoni effect [83], a depression is formed in the center which opposes this flow by capillary pressure. In the case of cw-laser processing or long irradiation pulses the surface takes on an equilibrium shape, balancing these two forces out [84]. In the case of ns-pulse laser processing this steady state is not reached, due to the relatively short time in which the system is in a liquid state, and hole shapes are governed by viscous and inertial forces [81].

In addition to the optical properties also other material properties change upon melting. Important for laser induced silicon doping is the rapid rise of the diffusion coefficient, e.g., of phosphorus, by more than three orders of magnitude with the transition to the liquid phase. Due to increased liquid-state diffusion, short melt times below one microsecond produced by ns-laser pulses are sufficient to create highly doped silicon. In the case of cw-laser processing dopant mixing within the molten pool is enhanced by a fluid flow that is driven by the lateral change of the surface tension.

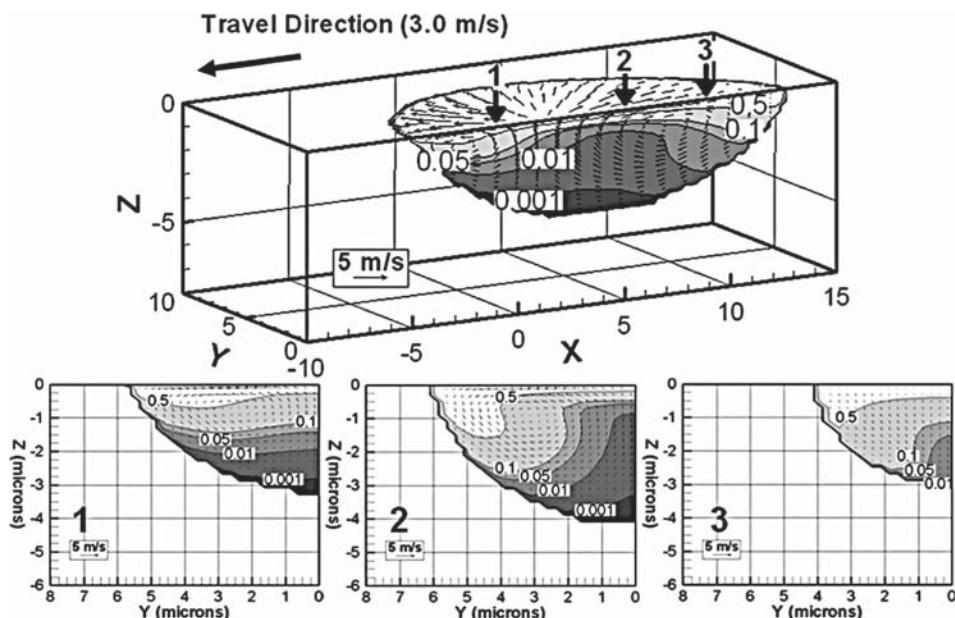


Figure 3.2: Evolution of the dopant distribution during cw-laser processing at a laser power of 15 W and scanning speed of 3.0 m/s. The bottom row represents the single y-z planes whose locations within the molten pool are indicated with numbered arrows. The dopant concentration contours are fractions of the top surface concentration,  $2.7 \cdot 10^{19} \text{ cm}^{-3}$ . (from [90])

### 3.3.3 Dynamics of Molten Pool

In order to predict the impact of laser processing conditions on the performance of solar cells, computer models simulating the fundamental laser-silicon interactions and the resulting molten pool geometry and concentration profiles have been investigated by many researchers. Most of these consider solely conductive heat transport and diffusive dopant motion to determine the resulting dopant profile [85–87]. Researchers at the Pennsylvania State University have developed a three-dimensional, numerical heat transfer and fluid flow simulation for the analysis of welding processes [88]. Blecher et al. [89] have extended this model to devise a model of the selective emitter formation using a cw-laser setup similar to the one used in this work. The advantage of this model over existing simulations of the doping process is the incorporates of the fluid flow, which is of importance in a cw-laser driven process.

Figure 3.2 displays the fluid flow within a molten silicon pool created by a Gaussian shaped cw-laser spot that is scanned across a sample coated with a phosphorus precursor layer. The convective flow is driven by the Marangoni effect. From the fluid flow and liquid phase diffusion, Blecher et al. have calculated the dopant profile after resolidification. They found that phosphorus transport in the molten pool by convective fluid flow dominates liquid phase diffusion. On the other hand, thermal diffusion remains the primary heat transport mechanism due to the small length scale of the molten pool and the relatively high thermal diffusivity of silicon [89]. As shown in Fig. 3.2, due to enhanced mixing, cw-laser processing allows to produce doped silicon with

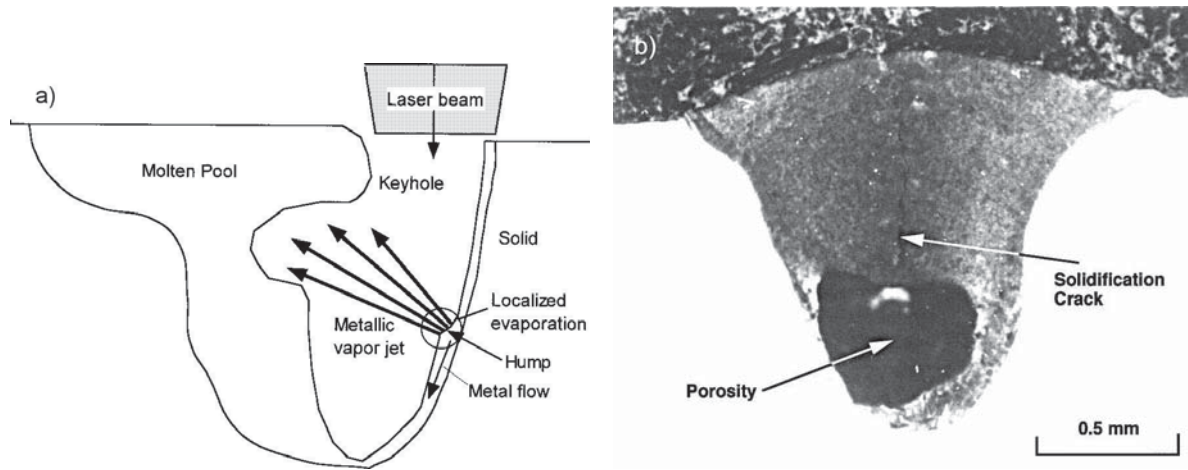


Figure 3.3: Schematic of the localized evaporation of metal in the keyhole front wall and its effect on perturbation of the keyhole rear wall and molten pool during laser welding (a). The direction of laser beam movement in (a) is to the right. Cross-sectional microscopy image of characteristic porosity formation in pulsed laser spot welding with a 10 ms long pulse (b). (both from [91])

doping depths on a micrometer scale at scanning speeds of meters per second.

At high laser intensities the molten pool is not only deformed by the Marangoni effect but also by the vapor pressure of evaporated silicon. Evaporated surface material exerts a pressure on the molten pool and further depresses the molten pool by pushing the melt to side of the pool. At high intensities the focused beam forms a narrow cylindrical vapor cavity in the melt. This so-called keyhole traps the laser light and significantly reduces the reflection. After the termination of the laser irradiation the keyhole opening closes quickly. A characteristic porosity observed in laser welded joints was also observed during cw-laser doping of silicon within this thesis. Matsuna et al. have optically observed the keyhole and studied the dynamics of the molten pool created with a cw-laser on a sheet of an aluminum alloy. The authors used high-speed optical and x-ray transmission methods to reveal the mechanism of cavity formation. They observed that fluctuations of the keyhole opening coincided with a tilting motion of the vaporization induced plasma above the keyhole. They concluded that a deep depression that is forming on the rear wall of the keyhole, which moves from the top to the bottom periodically, is the cause for the characteristic porosity [91]. The proposed mechanism as well as an microscopy image of a keyhole welded joint with an enclosed pore is shown in Fig. 3.3.

The evolution of the molten pool during keyhole laser welding has been widely studied over the last ten years using numerical computer simulations [92–97]. Recently Courtois et al. published accurate simulations of a keyhole laser welding process [98]. Figure 3.4 shows the time evolution of a molten pool created by a 20 ms long 1500 W (upper row) and a 25 ms long 1250 W (lower row) laser pulse. At 1500 W a cavity in the center of the resolidified pool is formed due to instabilities of the keyhole, whereas no cavity is observed at lower power where all gas can escape the collapsing keyhole. The numerical

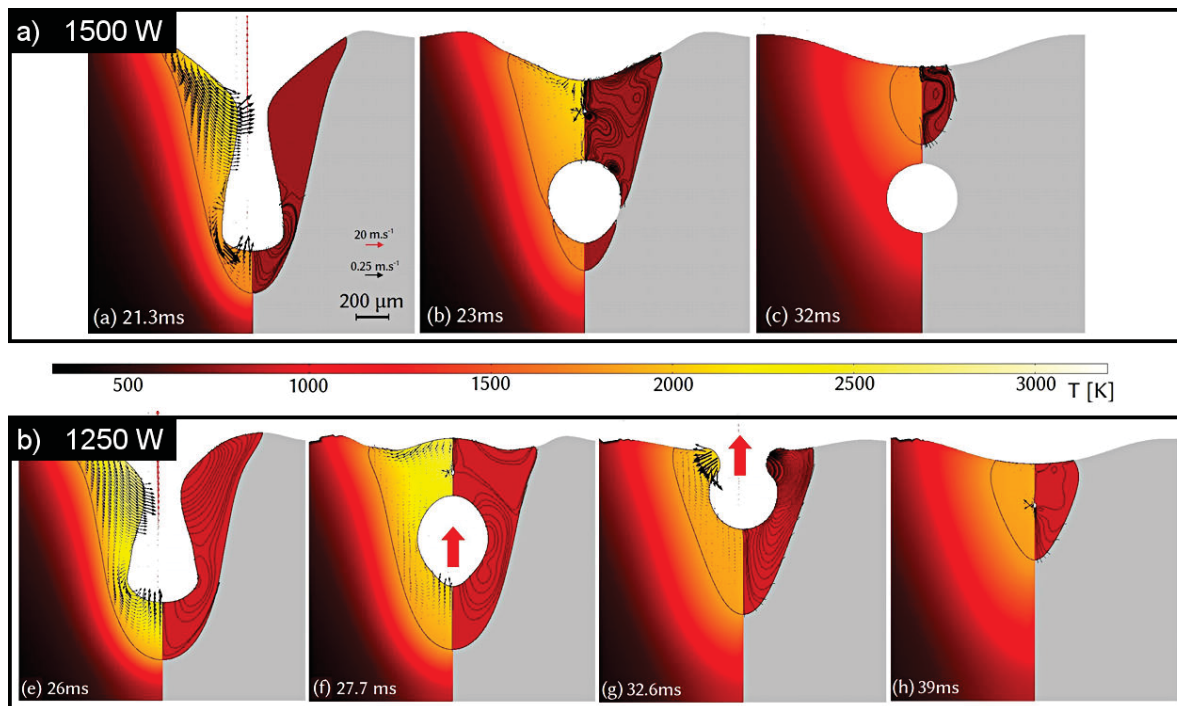


Figure 3.4: Simulated melt pool shapes after irradiation with a 20 ms long laser pulse at a laser power of 1500 W (a) and a 25 ms pulse at 1250 W (b). The individual plots show the velocity fields in the gas and liquid phase on the left side. (adapted from [98], supplementary media available at [stacks.iop.org/JPhysD/46/505305/mmedia](https://stacks.iop.org/JPhysD/46/505305/mmedia))

simulations conducted by the authors revealed that cavity formation increases with laser power.

### 3.3.4 Solidification

The molten silicon recrystallizes if the temperature of the solid-liquid (crystal-melt) interface is kept below the equilibrium melting point. The recrystallization process only progresses if the latent heat released by the phase change is carried away by heat conduction. The velocity of the solid-liquid interface is thus governed by the flow of heat from the recrystallization interface. However, the temperature of the interface is not determined by the heat flow but by the kinetics of recrystallization. In the case of small thermal gradients the recrystallization velocity will be slow and the melt will crystallize, while for a high thermal gradients and fast solid-liquid interface velocities the melt will freeze into a glass. Crystalline growth of silicon is observed up to a velocity of about 20 m/s, but at faster velocities it resolidifies as amorphous silicon [81].

Silicon forms covalent crystals but metallic melts, thus crystallization requires a change in atomic coordination. This, and a 10% change in density required for recrystallization, reduces the kinetic velocity of the liquid-solid interface, in comparison to the crystallization velocity of metals. In addition to this, the growth velocity, at a given undercooling, depends on the silicon crystal orientation. Differences in the accommodation probability causes fastest growth

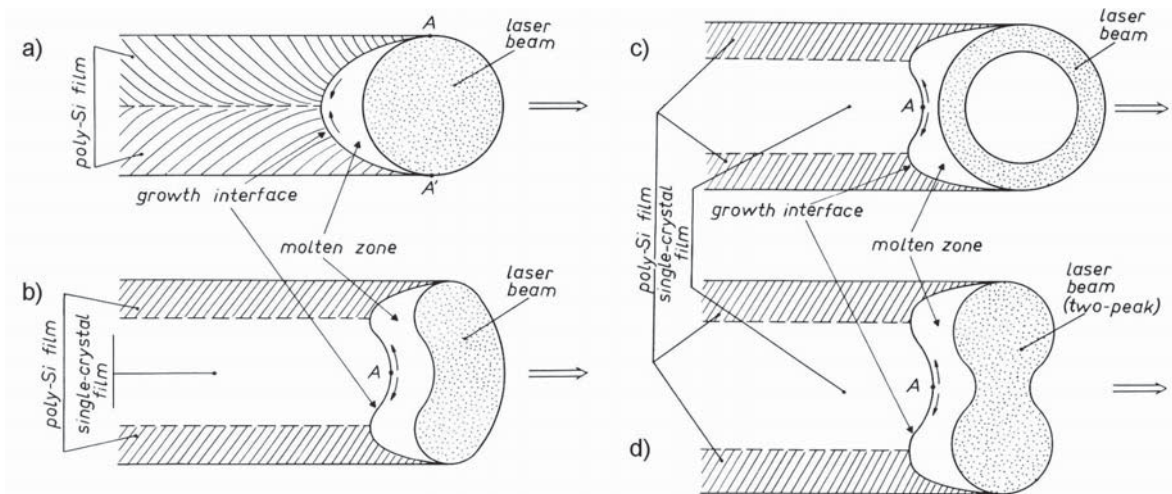


Figure 3.5: Beam recrystallization of films on amorphous substrates depending on the shape of the beam. Single arrows along the growth interface indicate propagation of nucleating crystalline layers; double arrows indicate movement of the beam. Circular beam (a) forms chevron like structure of elongated crystallites. Lens-shaped (b), doughnut-shaped (c), and two-peak (d) laser beams form a single crystalline film in the center and poly crystalline film at the edge of the laser line. (adapted from [102])

in  $\langle 100 \rangle$  and slowest growth in  $\langle 111 \rangle$  direction [99]. Cullis et al. found that defect free silicon can be produced with growth velocities of up to 18 m/s in  $\langle 100 \rangle$  direction and 6 m/s in  $\langle 111 \rangle$  direction. At higher velocities heavily defective silicon is produced. At velocities above 14 m/s solidification in  $\langle 111 \rangle$  direction results in amorphous growth [100].

At high undercooling of the melt, crystal growth may start from a crystal nucleus within the melt pool. These crystal-like clusters form by fluctuations until they reach a critical size. An increase in nucleation is observed in the presence of impurity particles in the melt as well as material boundaries [81]. Nucleation within laser remelting is usually undesirable since it results in a polycrystalline growth.

The shape of the laser beam affects the growth of crystalline thin-film in laser remelting of amorphous substrates. Gat et al. showed that laser remelting using a circular cw-laser spot created long and narrow silicon crystallites that are arranged at an angle to the scanning direction [101]. Such a beam and the corresponding crystallite orientation is shown schematically in Fig. 3.5 a). This particular structure is a result of the crystallite growth perpendicular to the liquid-solid interface at the trailing edge of the circular molten zone. Such a structure is characteristic for crystal growth on an amorphous substrate and a convex liquid-solid interface. By choosing a convex beam shape it is possible to create single-crystalline growth in the center of the laser processed line, as shown in (b). Here, the recrystallized film grows from the center outwards, resulting in wider crystallites. Other shapes such as a doughnut-shaped laser beam [103] or a double peaked laser beam [104] elaborate on this approach.

## 3.4 Fundamentals of Contact Formation

Replacing expensive silver of the standard front side metallization by plated copper yields cost and efficiency benefits, as outlined above. However, due to the high diffusion of copper into silicon at operating temperatures of a solar cell and its detrimental effect on performance, a diffusion barrier layer between silicon and copper needs to be formed. In semiconductor applications typically a thin layer of nickel is used as a diffusion barrier [105, 106]. Following this approach, nickel also served as the diffusion barrier in the design of the Saturn solar cell [68]. Bartsch and colleagues have studied the impact of copper metallization on long-term stability of solar cells with various metallization stacks [106, 107]. They confirmed that nickel diffusion barriers are well suited for application in solar cell modules.

Besides the degradation of solar cell performance by copper diffusion, the adhesion of the metal contact to the silicon material has been identified as a serious challenge [26, 33, 34, 108]. It is presumed that insufficient adhesion of busbars and contact fingers have caused Suntech Power's failure with the commercial launch of the Pluto solar cell [80]. A promising approach to overcome low adhesion is based on the creation of a nickel silicide layer jointing silicon and nickel by chemical bonding [109–111]. Latest results from Mondon et al. demonstrate adhesion of nickel–copper plated contacts exceeding the wafer breakage force by controlled silicide formation [32, 112].

### 3.4.1 Metal Plating

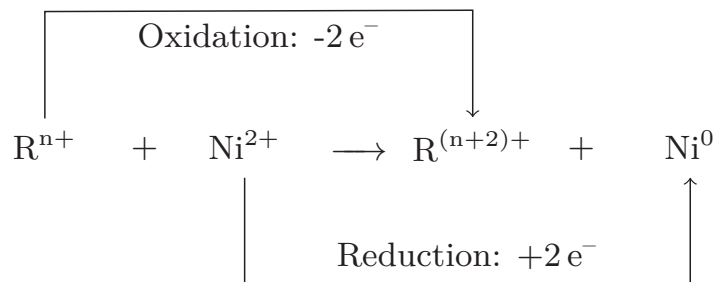
The metal contact stack of a solar cells can be formed by metal deposition from aqueous electrolyte solutions in a process called metal plating. The metal ions in the electrolyte need to be reduced to elemental metal by electrons provided at the surface that is to be covered. Two fundamental processes can be typically used to achieve this: The so-called electroless metal plating is in principle a chemical oxidation reaction that liberates electrons and a metal reduction reaction that consumes electrons [113]. During the other method, the so-called electrochemical metal deposition, an external voltage source typically promotes the solution of metal into ions at an anode and the deposition of these metal ions in the form of elemental metal at a cathode [114].

#### Electroless Plating

The simplest form of electroless plating is a so-called displacement reaction. Here electrons are transferred from less noble atoms to noble cations in the electrolyte solution. This results in the replacement of the less noble elemental metal with the noble metal and the dissolution of the less noble atom into the electrolyte.

In order to continuously deposit metal on a substrate, an alternative oxidation reaction, other than the dissolution of the surface, needs to be employed.

Typically a reducing agent is added to the electrolyte. During electroless plating the metal ions are then reduced by the oxidation of the reducing agent. In the case of electroless nickel deposition the chemical redox reaction is:



Electroless electrolytes are designed in such a way that the elemental metal is only deposited on suitable surfaces. The surface then acts as a catalyst promoting the redox reaction by conducting electrons from the reducing agent to the metal ions [113].

### Electrochemical Plating

If an electrode is immersed into an electrolyte solution a chemical equilibrium between the dissolution of the electrode material into cations and the deposition of cations as elemental metal onto the anode is established. In the case of a nickel electrode this is expressed by:



While in electroless plating the electrolyte contains a reducing agent, in electrochemical plating the electrolyte serves mainly as an ionic conductor. If two metal electrodes are immersed into this electrolyte solution and connected to an external voltage source, the so-called anodic dissolution and the so-called cathodic deposition can be controlled by an the applied voltage. The two electrodes, the electrolyte, and the electric connection form a so-called galvanic cell. During electrochemical plating the external voltage causes an electron current to the cathode, the equilibrium at the anode is pushed toward the dissolution of anode material into the electrolyte. These metal cations are transported by diffusion, convection, and drift in the resulting electric field to the cathode. At the cathode the metal cations are deposited as elemental metal. The transport of the anions in the electrolyte solution is in the opposite direction.

For nickel plating on the contact openings on the front side of a solar cell, the exposed silicon it put on a negative potential with respect to an nickel anode immersed in an electrolyte solution. If the front side of the solar cell is brought into contact with the electrolyte a galvanic cell is formed. At sufficiently high voltages [106] nickel is dissolved from the anode and deposited on the conducting silicon surface.

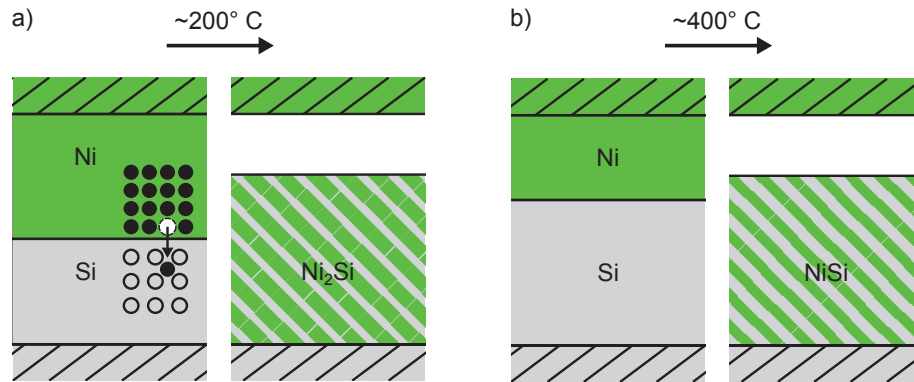
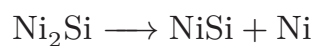


Figure 3.6: Schematic of the nickel diffusion into silicon. Nickel is the dominant diffusing species causing vacancies in the metal (a). Accumulation of vacancies can cause the formation of voids and gaps between the formed Ni<sub>2</sub>Si at about 200° C (a) or NiSi at about 400° C (b) and the bulk nickel.

### 3.4.2 Nickel Silicide Formation

The formation of a nickel silicide layer between silicon and the nickel-copper metallization stack allows to establish an adhering contact with low contact resistance. Nickel silicides can be formed by solidification from a melt, e.g., by rapid remelting of a nickel covered silicon surface using a laser pulse [115]. However, throughout this work silicides are created through solid state diffusion at elevated temperatures in a furnace process.

Six stable phases are found in the nickel–silicon system. The Ni<sub>2</sub>Si and NiSi phases are the preferred silicide phases in semiconductor and photovoltaic engineering due to their excellent resistivities and high phase stability. They can be created through annealing at intermediate temperatures in the range between about 300 and 700° C [116–118]. The formation of Ni<sub>2</sub>Si has been reported as being diffusion controlled. This growth mode is in principle characterized by planar growth fronts, and results in a silicide thickness which is proportional to the square root of time. However, the NiSi phase forms by a process where the NiSi phase grows on the NiSi–Ni<sub>2</sub>Si interface as well as on the NiSi–Si interface [119]. Nickel atoms that are produced at the Ni<sub>2</sub>Si–NiSi interface by the reaction



diffuse in the NiSi layer and react with silicon at the NiSi–Si interface according to the reaction



The growth of the NiSi phase is linear in time which indicates that this growth is not diffusion but reaction limited [117]. Independent of the growth mode, nickel is found to be the dominant diffusing species. This results in a movement of vacancies from the silicon into the nickel as depicted in Fig. 3.6 a). This so-called Kirkendall effect can lead to the development of diffusional porosity in

the nickel layer [120]. With the thickness of the formed silicide layers also the Kirkendall voiding increases. By this mechanism a gap between the silicide and the nickel contact may be formed, which is detrimental for the electrical contact and the mechanical adhesion of the metallization [111]. The resultant gap formed after the creation of Ni<sub>2</sub>Si and NiSi is schematically shown in Fig. 3.6.

The formation of nickel silicide can be prevented by barrier layers that hinder the diffusion of nickel into the silicon. Lee et al. showed that a native silicon oxide layer as thin as 2 nm is enough to retard any reaction between nickel and silicon up to 800° C [121]. The initially bare silicon surface of a solar cell contact opening is significantly oxidized even at room temperature in production environments where oxygen and moisture coexist. To address this, a deglazing dip in diluted HF is typically performed shortly before nickel deposition and the annealing step is optimally performed within minutes after the metal deposition.

### 3.5 Challenges for Laser Doped Selective Emitters with Ni-Cu Contacts

Before its bankruptcy in 2013 Suntech has been promising for years to scale up production of its Pluto solar cells [122]. Because the ultra-thin front cell fingers were not always in their perfect position, which is presumed to be caused by low adhesion of the metal contact, Suntech was not able to deliver its Pluto HiPerforma™ Ade-200 module to the European market [123]. This module is built from monocrystalline solar cells which are based on designs from the University of New South Wales (UNSW). However, the development of the Pluto solar cell is merely the most prominent case of a novel technology, presumably based on laser processing and metal plating, whose commercial success was impeded by technological challenges.

With add-on laser doping processes, which could be integrated into existing production lines, a substantial efficiency gain of up to 0.5 %abs. could be achieved using standard screen printing for front side metallization [124, 125]. This efficiency increase is mostly attributed to improved contact properties between screen printed fingers and selective emitter. However, the development of improved silver pastes that allow to contact even lowly doped emitters superseded the need for this add-on process [62].

The use of copper as a replacement for silver for the front side metallization promises a significant reduction of the production costs. Laser chemical processing (LCP), which was developed at Fraunhofer ISE in cooperation with the RENA company, allows simultaneous ablation of the dielectric layer and selective doping. Using LCP and nickel–copper plating Kluska et al. showed efficiency gains compared to standard screen printing [77]. However, the process suffers from the high complexity and low throughput of the LCP tool as well as an inefficient use of the process consumables.

The laser doped selective emitter (LDSE) process developed at the UNSW represents a simplified approach to achieve doped contact openings for metal

plated contacts. Solar cells with efficiencies as high as 19.3% were produced from CZ silicon wafers using a standard production line with the addition of laser doping and light-induced plating equipment [18]. Low consumption of chemicals, high processing speeds, and simplified guidance of the laser beam are advantages that qualify this process for industrial implementation. Nevertheless, solar cells produced with the LDSE process are not commercially available. This is possibly due to poor adhesion of the plated metal contacts reported by several researchers [26, 33, 34, 108], which can cause problems during automated module manufacturing, leads to detachment of contact fingers and reduces long-term module stability.

In this work it will be shown that mechanical contact adhesion can be improved by proper conditioning of the LDSE treated silicon surface and the formation of a nickel silicide interlayer. However, the increase of adhesion comes at a price: inhomogeneous silicide formation may cause penetration of the p-n junction and result in severe degradation of device performance. Laser processing using a cw-laser allows forming micrometer deep p-n junctions which can be used to prevent silicide induced degradation. By employing additional processing steps mechanically and electrically stable test cells were produced and will be presented in chapter 9. However, the proposed alterations to the processing sequence increase complexity and production costs compared to the original LDSE process <sup>2</sup>.

---

<sup>2</sup>This aspect has been evaluated quantitatively in the course of a master thesis by Geyer [126].

## 4 Characterization Techniques

In this chapter the techniques for the characterization of the samples studied throughout this work will be presented. A focus is put on the scanning electron microscopy (SEM) and on the QSSPC lifetime tester. The SEM proves to be a versatile tool for imaging structural as well as electrical properties of silicon samples. The QSSPC technique is a common method to measure not only the charge carrier lifetime of silicon samples but allows to determine the recombination properties of emitters and surfaces. A detailed evaluation of different analysis techniques in this chapter will be the base of a precise characterization of laser treated silicon in the following chapters.

### 4.1 Electron Analysis Methods

In a scanning electron microscope (SEM) a well focused electron beam is scanned over the sample area in a sealed vacuum chamber. Detectors collect backscattered electrons or secondary particles and allow imaging as well as other spectroscopic measurements. A transmission electron microscope (TEM) allows highest magnifications by detecting electrons that have traversed the sample. Well written textbooks that cover this subject include [46, 127, 128].

#### 4.1.1 Interaction Processes

Electron microscopy requires the illumination of the specimen with an electron beam. The properties of the source of these so called primary electrons is key for the quality of SEM imaging. The lateral resolution of a SEM image depends on the virtual source size. The brightness determines the signal to noise ratio and enables quicker scanning. A large energy spread of the emitted primary electrons causes chromatic aberrations [127]. The scanning electron microscopes used in this thesis have either a simple tungsten filament or a Schottky emitter as the primary electron source. The latter is considered a good compromise between efficiency and operating expense [128].

Like in optical microscopes, lenses and apertures are used to shape and define the beam. Electrons are deflected by magnets and the focal length of these electromagnetic lenses can be tuned by the driving current. For the SEM imaging mode the beam is scanned across the sample surface by an additional deflecting coil.

A SEM works in reflection mode, where the electron beam is focused on the sample surface to a size of about 1 – 10 nm. When the beam impinges on

## 4. Characterization Techniques

the sample the electrons interact with the sample and particles or radiation is released. The five most important processes are [128]:

- **Elastic Backscattering:** An electron that undergoes elastic scattering changes its trajectory, but its kinetic energy and velocity remain essentially constant. This is caused by the large mass difference between the electron and the atomic nuclei. These are the so-called backscattered electrons (BSE).
- **Inelastic Scattering:** An inelastic scattered electrons only slightly changes its trajectory, but interactions with the orbital electrons of the atoms in the specimen causes the transfer of energy from the incident electron to other electrons or the creation of bremsstrahlung.
- **Characteristic x-rays:** Electrons can ionize atoms by removing an electron from a inner shell orbital. An electron from an outer shell orbital immediately fills this vacancy and emits a photon with energy equal to the difference in energy of both shells. The energy of the emitted photons is characteristic for the irradiated element and thus this hard radiation is called characteristic x-rays. By an energy dispersive x-ray analysis (EDX) an element specific surface analysis can be performed.
- **Auger Electrons:** Ionized atoms created by knock-on effects from the incident electron can emit Auger electrons. Similar to the Auger recombination discussed in Sec. 2.3.2 in this process the excess energy is transferred from the electron that fills the vacancy to a second outer shell electron that is released from the atomic bond. The energy of Auger electrons is in the range from 100 eV to 1 keV and highly element specific.
- **Secondary Electrons:** Incident electrons that excite electrons in the sample causes the release of secondary electrons (SE). The excited electrons move towards the surface of the sample undergoing elastic and inelastic collisions until they leaves the surface. The energy distribution of secondary electrons is broad with a maximum below 50 eV.

By using different detectors that are sensitive to electrons of different energy or allow x-ray spectroscopy, a SEM imaging mode is specific to certain material properties such as topography and elemental composition.

### 4.1.2 SEM Imaging Capabilities

The lateral resolution that can be achieved depends on the size of the illuminated spot but also on the detection mode used. Figure 4.1 a) shows a sketch of the processes that occur if a sample is illuminated by an electron beam. Particles and photons released do not necessary originate from the small area of the illuminated surface. Characteristic x-rays may originate from an excited area that is larger than the spot size of the electron beam on the surface. Also

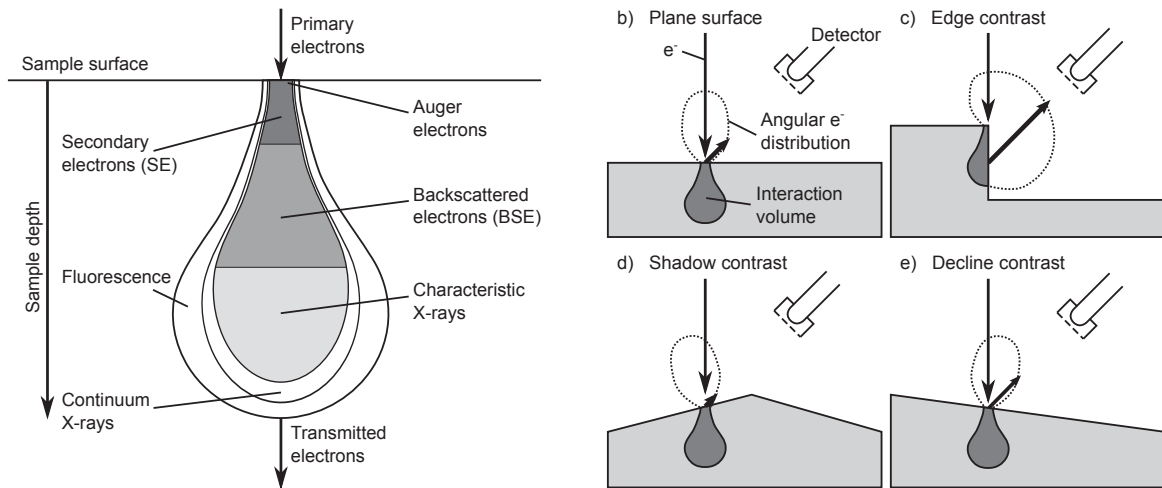


Figure 4.1: Schematic of the interaction processes in scanning electron microscopy after a focused beam of primary electrons hits a sample. The interaction volume extends into the depth and laterally into the sample. Characteristic x-ray radiation is emitted from all shaded areas. The range of the secondary electrons is smaller than the range of the backscattered electrons (a). Topographic features, e.g., plane surfaces (b), edges (c), shaded areas (d), or tilted surfaces (e) result in different intensities in the detector.

backscattered electrons have a large mean free path and escapes the surface in an area larger than the spot size. The best lateral resolution is possible by SEM imaging using secondary electrons because the mean free path is short. In the work presented here a lateral resolution of about 5 nm was achieved by secondary electron imaging using the Hitachi SEM SU-70 with an ZrO/W Schottky emission electron source.

### Topography Imaging

The information of a secondary electron SEM image is the number of electrons that are collected for each illuminated point. The number of detected secondary electrons depends on a the surface topography of the sample. If an edge is present in the focal spot more secondary electrons are emitted. Therefore, an edge appears bright in the image. If the detector is positioned off-axis also a tilted surface alters the number of detected electrons as a function of orientation. Topographic features that result in an intensity contrast are shown schematically in Fig. 4.1.

### Material Contrast

A contrast in material is caused by a difference in backscatter probability which depends on the atomic number  $Z$  of the illuminated material.

Figure 4.2 shows the interaction volume of a 15 keV electron beam in three different materials and thus different atomic numbers: silicon ( $Z = 14$ ), nickel silicide, and pure nickel ( $Z = 28$ ). The data has been simulated using the Monte Carlo simulation program Casino [129]. The interaction volume tends

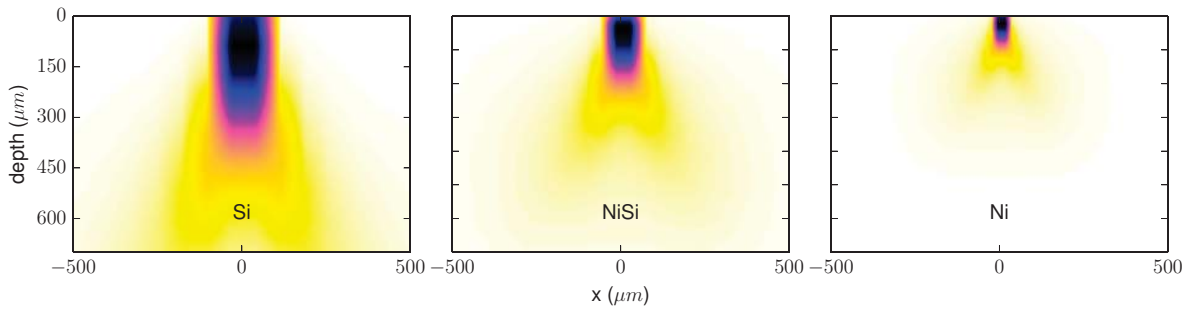


Figure 4.2: Energy deposition of a 15 keV electron beam in silicon (Si), nickel silicide (NiSi) and nickel (Ni) as a function of position (dark color represents high energy deposition). The mean free path of the electrons in Si is larger than the mean free path in Ni due to the higher atomic number of Ni and the resulting stronger interaction with the charged electrons. The reduced mean free path also results in an increase of the backscatter coefficient from 0.14 (Si) to 0.22 (NiSi) to 0.27 (Ni).

to be pear shaped for atomic numbers  $Z < 15$ . For  $15 < Z < 40$  it approaches a sphere, and for  $Z > 40$  it becomes hemispherical [46]. At  $Z = 28$  the interaction volume within nickel is reduced to about 100 nm. The interactions that lead to the creation of BSE and SE is close to the surface and thus the chance of collection in the detector is higher compared to the case where the interaction volume extends deep into the material as it is the case with silicon at  $Z = 14$ . The contrast can be expressed as the fraction of BSE in terms of a backscatter coefficient. The difference in  $Z$  results in a material contrast with nickel represented by high BSE count rates (backscatter coefficient: 0.27) and silicon with relatively low BSE count rates (backscatter coefficient: 0.14). An example of this material contrast is shown in Fig. 4.3 which shows a top view SEM image of the front side of a cw-laser processed monocrystalline solar cell. Figure 4.3 a) shows the line before nickel deposition and b) shows a similar spot after nickel silicide has been created along the laser processed line. The inset c) shows the corresponding EDX spectrum of a spot on the laser line which shows the presence of nickel.

### Imaging of Buried Structures

In chapter 6 and 7 the SEM technique will be used to detect cavities buried within the silicon material. During laser processing, macroscopic defects can form in a depth of up to  $5 \mu\text{m}$  below the surface. These spherical cavities have a diameter of up to  $3 \mu\text{m}$  and are fully enclosed within the silicon. Imaging using BSE from a beam of 30 keV electrons allows to detect these cavities. This is due to a large interaction volume with a depth greater than  $1.5 \mu\text{m}$  and a change in the backscatter coefficient in the presence of a cavity. The change in the backscatter coefficient of a 15 keV and a 30 keV beam caused by a spherical cavity with a diameter of  $1 \mu\text{m}$  at various depths has been simulated using Casino and is displayed in Fig. 4.4. 15 keV electrons are more sensitive to

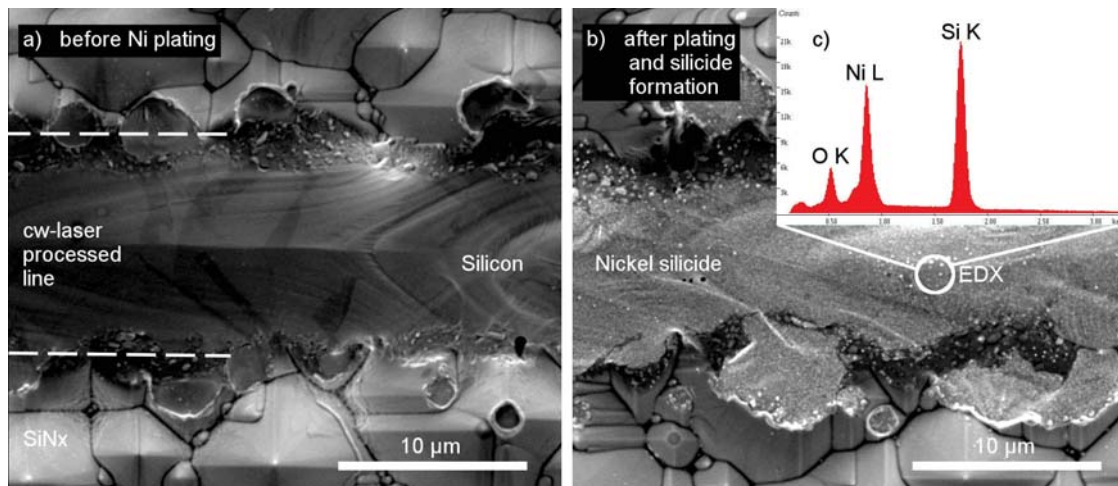


Figure 4.3: SEM images of a laser processed silicon surface before (a) and after (b) nickel silicide formation. The brightness of the nickel silicide is increased due to its higher atomic number. The existence of nickel is also detected by x-ray spectroscopy (EDX) on the spot marked with the circle. The corresponding spectrum is shown in inset (c) with a pronounced NiL peak at 0.85 eV.

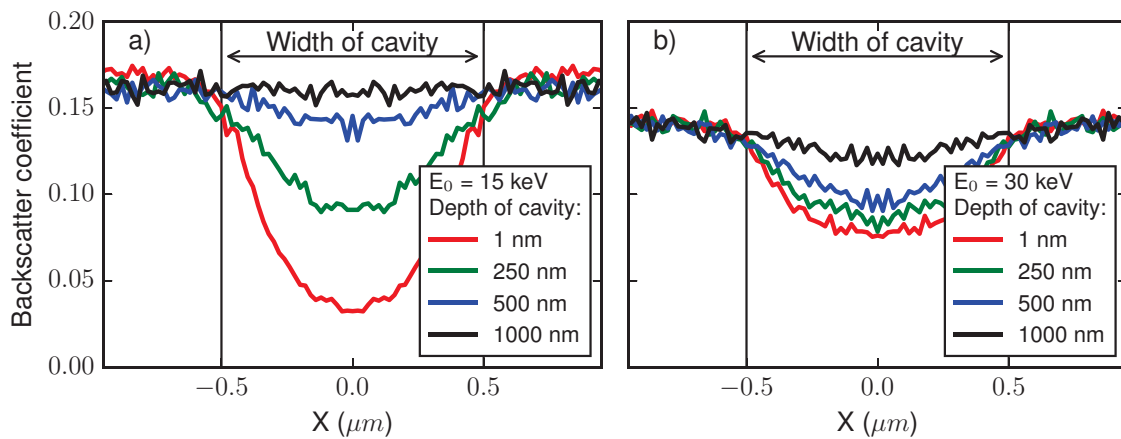


Figure 4.4: Backscatter coefficient as a function of position of the electron beam over a cavity buried in silicon at various depths. Electrons at 15 keV (a) are more sensitive to cavities near the surface, whereas it is possible to detect cavities of greater depth using electrons at 30 keV (b).

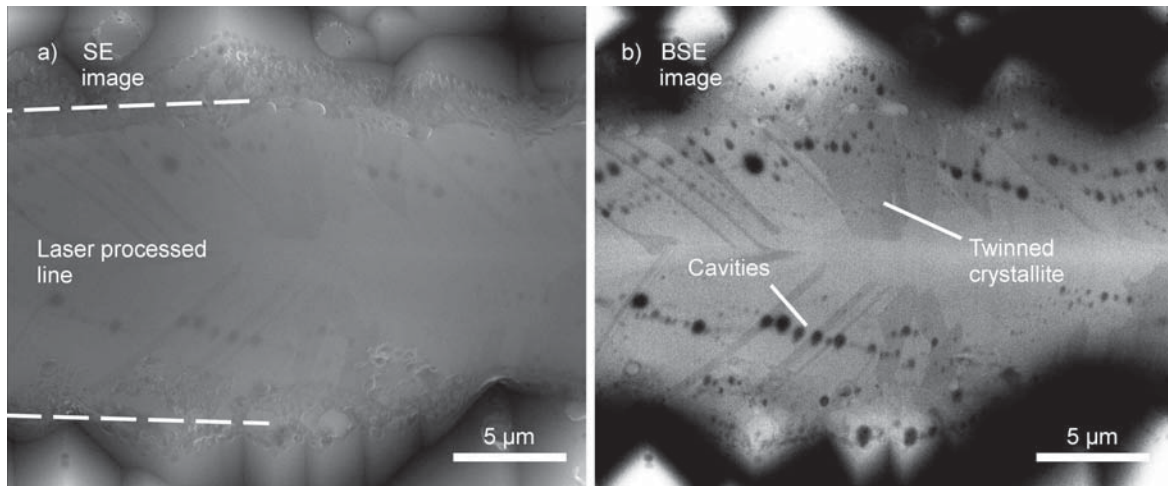


Figure 4.5: SEM images of a laser drawn line on a silicon wafer. The SE image (a) is more sensitive to topographic features, whereas the BSE image (b) allows the detection of buried structures as well as differences in grain orientation by channeling contrast. The acceleration voltage was in both cases 30 kV.

cavities just below the surface, but since the depth of the interaction volume is only a few 100 nm a cavity buried at a depth of  $1\ \mu\text{m}$  cannot be detected. Using 30 keV electrons cavities at micrometer depths can be detected, as shown in Fig. 4.4 b). Figure 4.5 shows an example of the same laser structured area imaged at 30 keV using SE in (a) and using BSE in (b). The cavities buried in the silicon are clearly visible as spots of reduced intensity in the BSE image.

### Electron Channeling Contrast Imaging

Depending on the orientation of a crystalline sample and the position of the detector, electrons which channel down a crystal plane will be collected at a higher count rate in the detector. In this way, BSE provides not only information about material composition, surface topography, but also about the crystal orientation by this so-called channeling contrast.

The channeling mechanism relies on the excitation of two Bloch waves in dependence on the incidence angle of the impinging electrons. At incidence angles larger than the Bragg angle a channeling Bloch wave with the electron density located in the channels between the lattice planes is preferentially excited. This leads to a reduced chance of scattering and a small backscatter coefficient. At incidence angles smaller than the Bragg angle a Bloch wave which causes strong backscattering and heavy attenuation dominates [130].

Channeling contrast allows to detect grain boundaries in laser processed silicon. The amount and order of these boundaries will be used in chapter 6 to study the influence of process parameters on the crystal quality of laser processed silicon. An example of an SEM image with channeling contrast between twinned crystallites is presented in Fig. 4.5 b).

### 4.1.3 Energy-Dispersive X-ray Spectroscopy (EDX)

The characteristic x-rays generated by scanning electron bombardment can be used for material characterization. The x-rays have energies characteristic to the elements from which they originate, which allows elemental identification. For a quantitative analysis the x-ray intensity can be compared with intensities from known samples. The ratio of the sample intensity to the intensity of the standard can be considered a measure of the amount of the element in the sample. However, this interpretation is complicated if samples with an inhomogeneous concentration profile or thin films with unknown thicknesses are analyzed [127].

If the x-ray emission is a result of a transition from the  $L$  to the  $K$  shell the x-rays are known as  $K\alpha$  x-rays.  $K\beta$  x-rays result from  $M$  to  $K$  transitions and  $L\alpha$  x-rays are due to  $M$  to  $L$  transitions. Important EDX x-ray lines within this work are the x-ray lines of nitrogen ( $E(K\alpha) = 0.39$  keV), nickel ( $E(L\alpha) = 0.85$  keV), and silicon ( $E(K\alpha) = 1.74$  keV) which are shown in Fig. 4.3 c).

### 4.1.4 Electron-Beam-Induced Current (EBIC)

The so-called electron-beam-induced current (EBIC) method relies on measuring the current generated by a scanned electron beam in a junction device. Mapping of the EBIC allows to directly image recombination sites, measure transport properties, and to determine junction depths, among other things [131].

A primary electron at 1 to 30 keV impinging a semiconductor generates  $10^3$  to  $10^4$  electron-hole pairs in the so-called generation volume. If the diffusion length of the generated minority charge carriers is long enough, they reach the p-n junction and contribute to a current that can be measured externally. This is the EBIC, which can be recorded synchronous to the scanned electron beam to produce a mapping of the EBIC collected at every scanned point. In a material with homogeneous bulk recombination, the probability that a minority charge carriers reaches the junction decreases as the generation volume moves away from the junction due to bulk and surface recombination effects. In Fig. 4.6 a cross-sectional SEM image (a), as well as the position dependent EBIC of a laser doped selective emitter device is shown (b). The EBIC is represented in (b) by white for a high and black for a low current. If the electron beam is scanned perpendicular to the p-n junction, the position dependent EBIC is highest at the position of the p-n junction because there the separation of charge carriers is most effective. Deviations between the maximum of the EBIC and the position of the p-n junction can arise e.g., for textured samples as discussed in detail by Kluska et al. [77]. For planar structures, such as cw-laser doped lines, these deviations are negligible.

In this work the EBIC technique will be used for p-n junction mapping of laser processed silicon. As can be seen from Fig. 4.6 the combination of SEM imaging and EBIC allows to study the influence of laser processing on the

## 4. Characterization Techniques

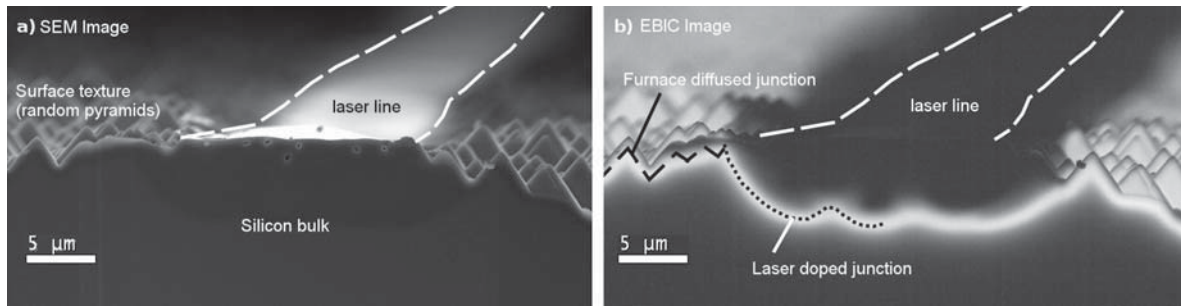


Figure 4.6: SE image of a cross section of a laser drawn line on a silicon wafer (a) and corresponding EBIC image (b). Topographic features like the edge of the laser line are clearly visible in the SE image. The EBIC image allows the mapping of the p-n junction from the maximum of the signal. The shallow junction created by furnace diffusion is indicated by the dashed line and the junction created by laser processing is indicated by the dotted line.

geometry of the laser doped lines. To give an example: A closer inspection of the SEM image a) reveals that the silicon nitride passivation layer is ablated at a width of  $15\ \mu\text{m}$  and the EBIC image b) shows that the doped area extends laterally as far as  $25\ \mu\text{m}$  with a depth of about  $5\ \mu\text{m}$ .

### 4.1.5 Transmission Electron Microscopy (TEM)

In a transmission electron microscope (TEM) the electron beam is defined by a condenser lens and directed onto a sample which has to be transparent for electrons. After passing the sample the electrons are collected by different electron optical elements and projected onto a two dimensional camera.

Samples have to be extremely thin. For low resolution a thickness of 100 nm is sufficient. High resolution TEM imaging is capable of resolving atomic distances. These images are not direct pictures of the sample. However, for the TEM analysis in this work, the electron beam is scanned over the sample in an imaging mode called scanning transmission electron microscopy (STEM). The resultant images can be interpreted directly, similar to SEM images [127].

In chapter 6 TEM imaging will be used to study a thin cross-sectional lamella of a laser treated line. This allows to verify epitaxial growth, detect crystal defects in the laser treated material, and estimate how far crystallites, which were observed using electron channeling contrast in SEM images (cf. Fig. 4.5), extend into the depth of the sample.

## 4.2 X-ray Photoelectron Spectroscopy (XPS)

The sampling depth of SEM imaging is at least several 10 nm if imaging is performed using SE. In the case of EDX elemental analysis the sampling depth is substantially increased <sup>1</sup>. In contrast to this, x-ray Photoelectron Spectroscopy

<sup>1</sup>For an electron beam with 1.5 keV the sampling depth of the EDX analysis is about 50 nm as determined by Casino simulation and discussed in detail in Sec. 6.2.4.

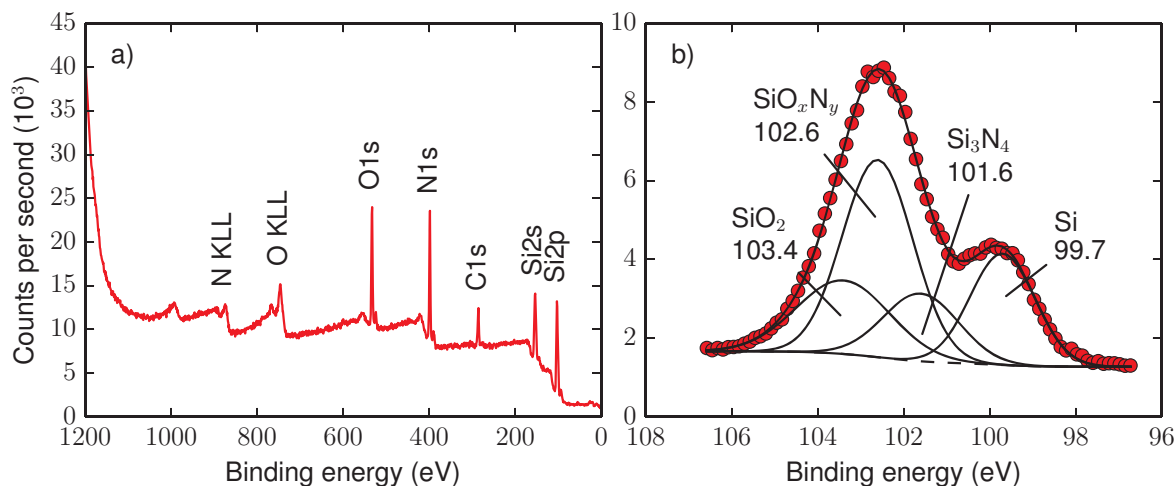


Figure 4.7: Survey spectrum of an XPS measurement on a laser processed surface (a) and corresponding detailed spectrum of the Si2p peak (b). The Survey spectrum shows the presence of N, O and C on the surface of the sample. The detailed spectrum of the Si2p peak reveals the composition of Si containing compounds of the surface. This spectrum will be discussed in detail in chapter 8.

(XPS) has a small sampling depth below 10 nm and thus allows to analyze the composition of the surface. A recommended textbook detailing on XPS is edited by Briggs and Seah [132].

In an XPS setup the surface under investigation is irradiated with x-rays from an anode made from a single element. In this work soft x-rays at 1254.6 eV from an Mg anode are used. The photons are absorbed by the material of the sample and cause ejection of electrons, the so-called photoelectrons. Since the exciting photon has a well defined energy, the kinetic energy of the photoelectron is the energy of the incident photon reduced by the binding energy which the photoelectron had within the atom. The photoelectrons emitted from the surface are guided by electron optics into an electron energy analyzer to measure their kinetic energy. Under the assumption that a photoelectron has not inelastically scattered in the sample the binding energy of this electron can be calculated from its kinetic energy and the known photon energy. The binding energy is not only element specific but also conveys information of the chemical state and electronic state of the surface. In Fig. 4.7 a) a so-called survey spectrum shows a wide range of binding energies from zero to the excitation photon energy <sup>2</sup>.

There is a significant background beneath the peaks in the survey spectrum. This background is caused by electrons that are inelastically scattered before leaving the sample surface. The inelastic scattering is also the mechanism that leads to the shallow sampling depth of the XPS method. The sampling depth is determined by the path length at which an electron can travel without being

<sup>2</sup>XPS spectra are usually plotted with an inverted x-axis so that the binding energy decreases from left to right. This originates from the display of the kinetic energy, which increases as the binding energy decreases. Although the kinetic energy is the primary value measured the binding energy is plotted since it describes the chemical composition of the surface in a generalized form which is independent of the excitation photon energy.

scattered or absorbed. This length depends on the electron energy and material. For photoelectrons in silicon this path length is a below three nanometers [133]. The background must be removed before the spectrum can be quantified.

Figure 4.7 b) shows a detailed scan of the binding energy range around the Si2p peak. Photoelectrons that originate from silicon in a compound are shifted with respect to the pure element (Si 99.7 eV). With the help of databases containing XPS peaks and corresponding elements or compounds the measured signal can be deconvoluted into contributions from different compounds<sup>3</sup>. Here the surface of a cw-laser treated silicon sample has been identified to contain, besides the expected bulk silicon (Si), its oxide (SiO<sub>2</sub>) and residues of the silicon nitride passivation (Si<sub>3</sub>N<sub>4</sub>), also a large quantity of a silicon oxynitride (SiO<sub>x</sub>N<sub>y</sub>) which will be shown in chapter 9 to be detrimental for device reliability.

### 4.3 Confocal Microscopy (LEXT)

A confocal microscope is capable of taking high resolution 3D images. The working principle relies on a the illumination of a single point of the sample and a pinhole aperture in front of the detector. Only an illuminated point which is confocal with the plane of the pinhole can pass the pinhole aperture and contributes to the measurement signal. A vast amount of information on optical microscopy, also detailing on confocal microscopy, is compiled at the web resource center of the Olympus company [135].

The Olympus LEXT OLS 4000 which was used for this work is capable of a magnification of up to 17,280x using a laser at the short wavelength end of the visible light (405 nm) for illumination. This allows to resolve the height of a sample with a precision of 10 nm and and lateral structures with a resolution of 120 nm. An example of a height mapping of a plated structure is shown in Fig. 4.8 a). In addition to this, the microscope is able to combine the laser based height measurement with color imaging to compose 3D color images with a quasi infinite depth of focus, as shown in the inset (b) [136]. The LEXT microscope will be used in chapter 6 to investigate the thickness of a liquid dopant layer on a textured silicon wafer. The method of extracting the liquid film thickness from LEXT images, developed in the course of this thesis, will be explained in the following.

#### 4.3.1 Film Thickness Analysis

The purpose of this analysis technique is to extract the thickness of a liquid film that is applied to the surface of a silicon wafer which is textured with random pyramids. With the LEXT microscope it is possible to acquire height maps of the surface. The liquid film is opaque for the violet light of the LEXT. An example of this is shown in Fig. 4.8 c). It is not possible to directly compare

---

<sup>3</sup>The database used for compound identification in this work is the NIST X-ray Photoelectron Spectroscopy Database [134]

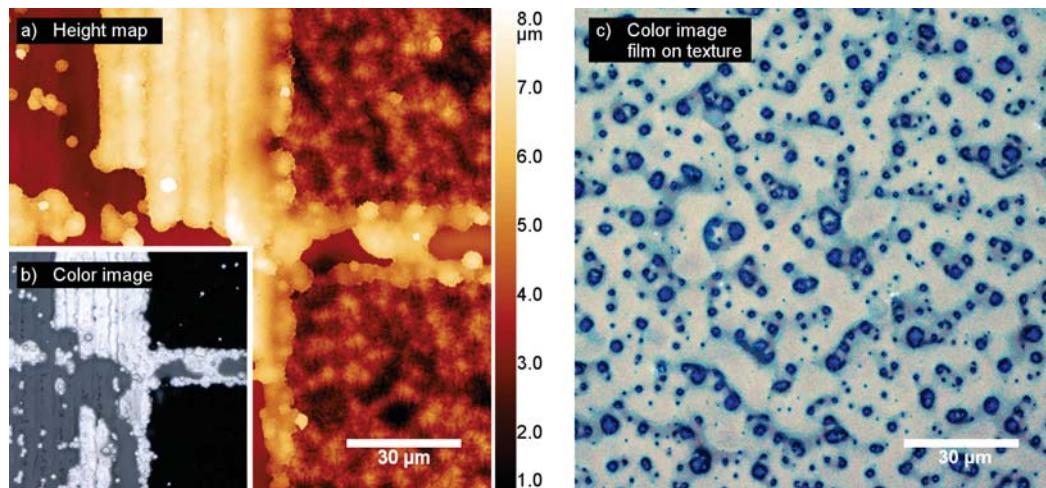


Figure 4.8: Height map (a) and color image (b) of metal plated structures measured with the LEXT confocal microscope. A liquid film applied to the surface of a textured and  $\text{SiN}_x$  coated wafer is opaque for the measurement (c). The tips of the pyramid texture break the surface of the liquid and appear as blue structures in the color image.

heightmaps of a sample before and after the application of the liquid film. The surface features are too small and a minute change in position between the measurements would alter the pixel-wise difference substantially. In addition to this, the height measurement of the LEXT is not absolute.

Instead, the statistical distribution of the relative height of the surface before and after the application of the liquid film is compared. The height distribution of the bare surface is represented by the red line in Fig. 4.9 a) and the coated surface is represented by the green line. The distribution narrows as the valleys of the random pyramid texture are filled with the liquid, but LEXT images reveal that the tips of the high pyramids are not covered with liquid. It can therefore be expected that the height distribution does not change in the region which represents these high tips. This region allows to match the distributions as shown in Fig. 4.9 a). The difference between the distribution of the bare surface and the coated surface which are matched by the uncovered pyramid tips gives the statistical distribution of film height shown in Fig. 4.9 b).

#### 4.4 Quasi-steady-state photoconductance (QSSPC)

The Quasi-steady-state photoconductance technique (QSSPC) is a simple method for determining the injection dependent minority charge carrier lifetime of semiconductor materials. From the charge carrier lifetime other parameters such as the surface recombination velocity can be extracted, as will be discussed in detail in the following. For detailed information on the QSSPC method the following references serve as a suitable starting point [46, 137].

## 4. Characterization Techniques

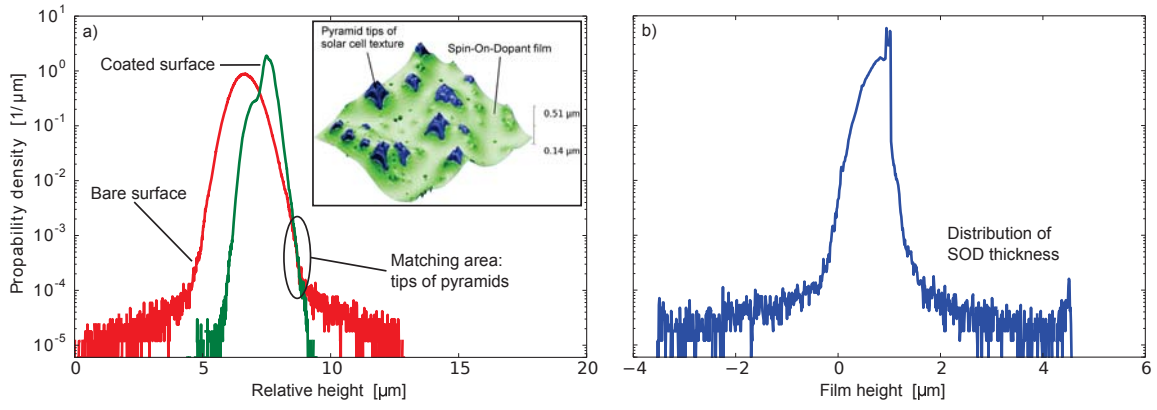


Figure 4.9: Distribution of the relative height of a bare wafer and a wafer covered with a liquid spin-on film (a) and the resulting distribution of the absolute film height (b). The inset of (a) is a perspective view on a heightmap acquired by the LEXT microscope. The color in the inset is intensified to allow differentiation of liquid film (green) and uncovered pyramid tips (blue).

### 4.4.1 Charge Carrier Lifetime

Important parameters of a solar cell, such as the saturation current density, depend on the recombination rate of excess minority charge carriers in the bulk and on the surface of the silicon crystal. This can be understood e.g., from the expression of the emitter saturation current density Eq. 2.35, where the  $S$  represents the surface recombination and the term  $D/L$  can be interpreted as the bulk recombination velocity. Neither the surface nor the bulk recombination rate can be directly measured. However, these recombination properties can be extracted from a measurement of the lifetime of the ensemble of excess charge carriers.

If the generation of excess charge carriers (e.g. by illumination) is switched off, the excess charge carriers recombine until the charge carrier density of the thermodynamic equilibrium  $np = n_i^2$  is reached. The loss of excess charge carriers with time equals the recombination rate:

$$\frac{d\Delta n}{dt} = -R. \quad (4.1)$$

A recombination rate  $R$  which is proportional to the concentration of the recombining species  $\Delta n$  results in an exponential decay of  $\Delta n(t)$ :

$$\Delta n(t) = \Delta n_0 \exp(-t/\tau) \quad (4.2)$$

with the initial charge carrier concentration  $\Delta n_0$  and the so called excess charge carrier recombination lifetime  $\tau$ . For semiconductors the assumption that all recombination processes are first order reactions (and thus  $R \propto \Delta n$ ) is not accurate. Recombination channels like the Auger recombination are of second order and proportional to  $(\Delta n)^2$ . Therefore, an injection dependent lifetime

$\tau(\Delta n)$  is defined by

$$\frac{d\Delta n}{dt} = -\frac{\Delta n}{\tau(\Delta n)}. \quad (4.3)$$

Due to diffusion in the crystal charge carriers can recombine via all of the recombination channels discussed in Sec. 2.3. However, the corresponding recombination rates are not spatially uniform and thus Eq. 4.3 does not represent a generally valid definition of the excess carrier lifetime. This leads to the concept of an effective lifetime  $\tau_{\text{eff}}$  which aggregates all recombination processes and presumes that excess carriers can reach any location within their diffusion length. Its definition depends on the dynamic of excess carrier generation.

After presenting the working principle of the QSSPC lifetime measurement, sections 4.4.3 and 4.4.4 will discuss two generation scenarios that allow the definition of an effective excess carrier lifetime.

#### 4.4.2 QSSPC Measurement

The determination of the injection dependent effective minority charge carrier lifetime using a quasi-steady-state photoconductance lifetime tester is based on a contactless and time resolved measurement of the excess carrier concentration of a wafer which is illuminated by a xenon flash with a peak light intensity exceeding 1000 suns. For the experiments conducted for this thesis the lab-type lifetime testers WCT-120 build by Sinton Consulting was used. The contactless measurement is done with a radio frequency coil that is coupled to the conductivity of the wafer and outputs a signal proportional to this conductivity. The photogenerated excess carrier density  $\Delta n$  ( $= \Delta p$ ) is connected to an increase in wafer conductance given by:

$$\Delta\sigma = q\Delta n(\mu_n + \mu_p)W \quad (4.4)$$

with the elemental charge  $q$ , the electron and hole mobilities  $\mu_n$  and  $\mu_p$  and the wafer thickness  $W$ . A reference solar cell measures the photon flux emitted from the xenon flash and allows the determination of the generation within the sample. The calculation of the effective charge carrier lifetime depends on the illumination mode.

Two distinct operating regimes can be defined according to the ratio of the time constants of carrier generation and carrier recombination:

- **Transient measurement:** In a transient measurement the illumination is turned off at  $t = 0$  and the effective lifetime is defined as the time constant of the fundamental decay mode as described in Sec. 4.4.3. Using the WCT-120 apparatus, a quasi-transient measurement condition is achieved by a short light pulse from a xenon flash with a decay time in the order of  $20 \mu\text{s}$ . Samples whose effective lifetime greatly exceeds the decay time of the flash ( $> 200 \mu\text{s}$ ) can be measured in this configuration. An example of a measurement of a well passivated wafer with an effective lifetime of  $630 \mu\text{s}$  is shown in Fig. 4.10 a).

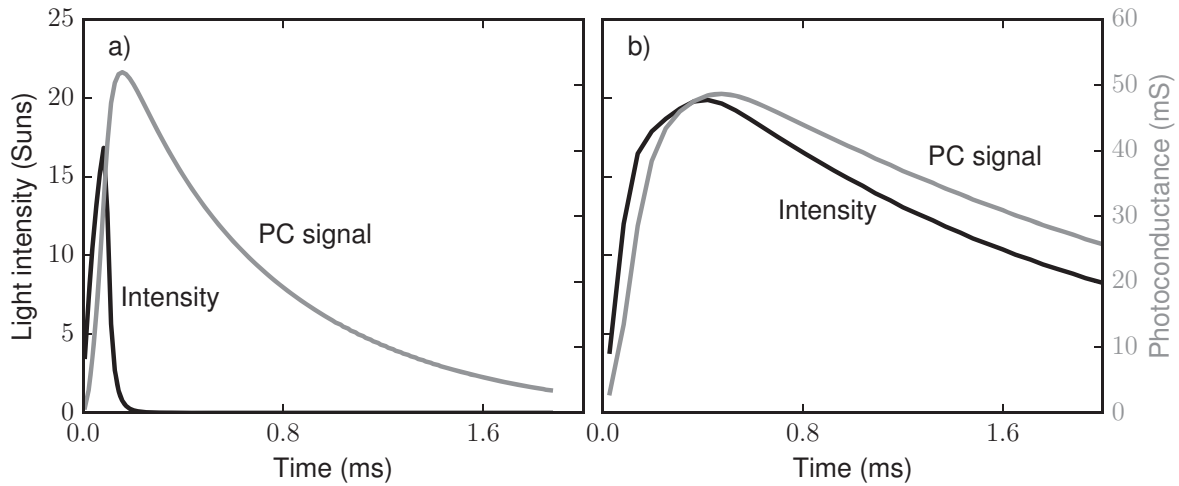


Figure 4.10: Light intensity and photoconductance (PC) signal of a transient QSSPC measurement (a) of a sample with a long lifetime of  $630 \mu\text{s}$  and a quasi-steady-state QSSPC measurement (b) of a sample with a short lifetime of  $60 \mu\text{s}$ .

- **Steady-state measurement:** If the illumination is constant, the time dependence of the continuity equation vanishes. This will be detailed in Sec. 4.4.4. Using the WCT-120 lifetime tester a quasi-steady state condition can be achieved by setting the decay time of the xenon flash to its maximum of about 2 ms. If the effective lifetime of the sample under investigation is small ( $< 200 \mu\text{s}$ ) compared to the decay of the light intensity, this is a so-called quasi-steady state measurement. An example of a measurement of a wafer with an effective lifetime of  $60 \mu\text{s}$  is shown in Fig. 4.10 b). The effective charge carrier lifetime under steady-state illumination is calculated as the ratio between the total number of excess charge carriers and the total generation.

Besides these presented scenarios a generalized analysis developed by Nagel et al. [138] closes the gap between these approximations and thus extends the applicability of the transient method and the steady-state method. The structures studied within this work are measured at quasi-steady-state conditions, where the difference between the steady-state method, as outlined above, and the generalized analysis is negligible.

#### 4.4.3 Effective Lifetime under Transient Excitation

The effective lifetime of the excess charge carriers in a sample can be measured by probing the average concentration of excess charge carriers as a function of time after a short burst of photons. The average excess charge carrier concentration can be measured using a lifetime tester, as discussed above. This section will follow the work of Luke et al. [139] and Otaredian et al. [140] to derive an analytic expression for the relationship between the effective lifetime ( $\tau_{\text{eff}}$ ) and the surface recombination velocity  $S$  under a transient excitation condition.

An expression for the average excess charge carrier concentration  $\Delta n$  after a short light pulse can be found by presuming a small perturbation of  $\Delta n$ . This reduces the problem to solving the continuity equation (cf. Eq. 2.16) of a laterally homogeneous sample:

$$\frac{d\Delta n}{dt} = D \frac{d^2(\Delta n)}{dz^2} - \frac{\Delta n}{\tau_B} + g \quad (4.5)$$

with the bulk lifetime  $\tau_B$ .

If the point of origin is set to the center of a wafer with thickness  $W$ , the generation from a short monochromatic light pulse is

$$g(z, t) = [k_1 \exp(-\alpha z) + k_2 \exp(\alpha z)] \delta(t) \quad (4.6)$$

where  $k_1$  and  $k_2$  are given as follows:

$$k_1 = \frac{N_0 \alpha \exp\left(-\frac{\alpha W}{2}\right)}{1 - \exp(-2\alpha W)}, \quad (4.7)$$

$$k_2 = k_1 \exp(-\alpha W). \quad (4.8)$$

The boundary conditions are given by the surface recombination at the front and rear surfaces:

$$D \frac{d\Delta n}{dz} \Big|_{W/2} = -S_1 \Delta n \Big|_{W/2} \quad (4.9)$$

$$D \frac{d\Delta n}{dz} \Big|_{-W/2} = S_2 \Delta n \Big|_{-W/2} \quad (4.10)$$

The solution of  $\Delta n$  can be obtained by the method of separating the variables. The corresponding general solution is a linear superposition of even and odd harmonic functions:

$$\Delta n(z, t) = e^{-t/\tau_B} \sum_{n=1}^{\infty} \left( A_n e^{-a_n^2 D t} \cos(a_n z) + B_n e^{-b_n^2 D t} \sin(b_n z) \right) \quad (4.11)$$

The coefficients  $A_n$  and  $B_n$  are determined by the initial concentration profile  $\Delta n(z, 0)$ , whereas the coefficients  $a_n$  and  $b_n$  are determined by the boundary conditions. If each coefficient  $a_n$  and  $b_n$  of each term in Eq. 4.11 is required to satisfy the boundary conditions Eq. 4.10 and 4.10 then the boundary conditions will also be satisfied by the superposition. The lifetime is commonly measured as the lifetime of the average carrier density. By integrating over the depth of the sample the contribution of the odd mode represented by the sin term in Eq. 4.11 vanishes. Only the coefficients  $a_n$  is of interest.  $a_n$  is determined by inserting the solution with mode index  $n$  into the boundary conditions. This results in the transcendental equation:

$$\tan(a_n W) = \frac{D a_n (S_1 + S_2)}{D^2 a_n^2 - (S_1 S_2)} \quad (4.12)$$

#### 4. Characterization Techniques

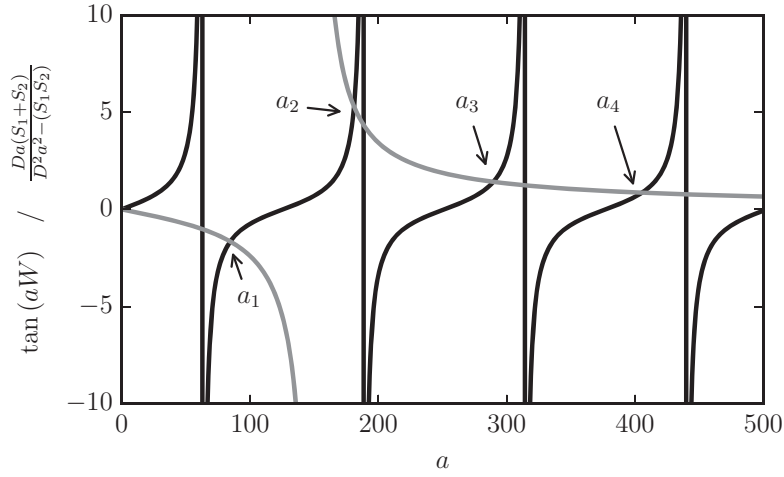


Figure 4.11: Graphical determination of the values of  $a_n$ .

According to Eq. 4.11 each mode  $n$  follows an exponential decay

$$\propto \exp\left(-\frac{t}{\tau_B} - a_n^2 D t\right). \quad (4.13)$$

A characteristic decay time  $\tau_n$  can be defined as the time after which the initial value is reduced to  $1/e$ :

$$\frac{1}{\tau_n} = \frac{1}{\tau_B} + a_n^2 D \quad (4.14)$$

In order to determine the values of  $a_n$ , Eq. 4.12 has to be numerically solved since in general, no analytic solution can be obtained. As can be seen from Fig. 4.11, which represents a graphical determination of the coefficients,  $a_{n-1} < a_n$  and thus  $a_{n-1}^2 \ll a_n^2$ . The decay of charge carriers consists of an infinitely large number of exponential decay processes, but the processes for large  $n$  are so fast that after a short amount of time only the first term in the summation is relevant. The exponential decay with  $\tau_1$  becomes dominant at the end of the process and is called the fundamental mode of recombination. The corresponding lifetime is called the fundamental lifetime and is the lifetime of the excess charge carriers after excitation by a short light pulse in the limit  $t \rightarrow \infty$ . In this context the effective lifetime can be defined to be identical to this fundamental lifetime. The effective lifetime  $\tau_{\text{eff}}$  can be split into the lifetime if recombination only occurs in the bulk  $\tau_B$  and a lifetime if recombination occurs only at the surfaces  $\tau_S$ :

$$\frac{1}{\tau_{n=1}} = \frac{1}{\tau_{\text{eff}}} = \frac{1}{\tau_B} + \frac{1}{\tau_S} \quad (4.15)$$

By combining Eq. 4.12 and 4.14 with  $n = 1$ , it can be shown that the surface lifetime can be calculated by determining the largest root of

$$\tan\left(\frac{W}{\sqrt{D\tau_S}}\right) = \sqrt{\frac{D}{\tau_S}} \frac{S_1 + S_2}{(D/\tau_S) - S_1 S_2}. \quad (4.16)$$

By measuring the decay of the average carrier density after a short light pulse the effective lifetime of charge carriers in a sample can be determined. The effective lifetime is composed of the bulk lifetime and of the surface lifetime. If the recombination rate in the bulk is known or assumed to be negligible compared to the surface recombination rate, Eq. 4.15 in combination with Eq. 4.16 allows to extract the surface recombination velocity from transient measurements of the effective excess charge carrier lifetime.

#### 4.4.4 Effective Lifetime under Steady-State Excitation

In the case of a steady-state excitation the sample is irradiated with a constant flux of photons. In this section an analytic expression for the relationship between the effective lifetime ( $\tau_{\text{eff}}$ ) and the surface recombination velocity  $S$  under a steady-state excitation condition is derived. The effective lifetime can then be defined as the ratio between cumulative excess carrier density and generation rate

$$\tau_{\text{eff}} = \frac{W \Delta n_{\text{av}}}{\int_0^d dz g(z)}. \quad (4.17)$$

In order to find the carrier density  $\Delta n(z)$  the steady-state continuity equation needs to be solved with the appropriate boundary conditions. In a steady-state the time derivative in the continuity equation (cf. Eq. 2.16) vanishes:

$$D \frac{d^2 \Delta n}{dz^2} - \frac{\Delta n}{\tau_B} = g \quad (4.18)$$

To find a general solution for this inhomogeneous linear differential equation a general solution for the homogeneous case and one particular solution for the inhomogeneous case must be found. The general solution for the homogeneous case is:

$$\Delta n_h = A_\lambda \exp(z/L) + B_\lambda \exp(-z/L) \quad (4.19)$$

with the diffusion length of the minority carriers  $L = \sqrt{D\tau_B}$ . For excitation with monochromatic light the generation rate is given by Eq. 2.2. With this exponential generation one particular solution of Eq. 4.18 is:

$$\Delta n_p = -\frac{j_\lambda \alpha_\lambda}{D(\alpha_\lambda^2 - L^{-2})} \exp(-\alpha_\lambda z). \quad (4.20)$$

From this the general solution of the excess charge carrier profile formed due to the steady-state excitation with monochromatic light can be constructed:

$$\Delta n_\lambda(z) = A_\lambda e^{z/L} + B_\lambda e^{-z/L} - \frac{j_\lambda \alpha_\lambda}{D(\alpha_\lambda^2 - L^{-2})} e^{-\alpha_\lambda z} \quad (4.21)$$

The coefficients  $A_\lambda$  and  $B_\lambda$  are determined by inserting Eq. 4.21 into the boundary conditions Eq. 4.10 and 4.10 given by the recombination rate at the

surfaces. The resulting system of equations is:

$$\begin{aligned} & \begin{pmatrix} S_0 - \frac{D}{L} & S_0 + \frac{D}{L} \\ (S_W + \frac{D}{L})e^{W/L} & (S_W - \frac{D}{L})e^{-W/L} \end{pmatrix} \begin{pmatrix} A_\lambda \\ B_\lambda \end{pmatrix} \\ & = \frac{\alpha_\lambda j_\lambda}{\alpha_\lambda^2 - L^{-2}} \begin{pmatrix} \frac{S_0}{D} + \alpha_\lambda \\ (\frac{S_W}{D} - \alpha_\lambda)e^{-\alpha_\lambda W} \end{pmatrix} \end{aligned} \quad (4.22)$$

Expression in terms of matrix elements <sup>4</sup>

$$\begin{pmatrix} a_{11} & a_{12} \\ a_{21} & a_{22} \end{pmatrix} \begin{pmatrix} A_\lambda \\ B_\lambda \end{pmatrix} = \begin{pmatrix} b_1 \\ b_2 \end{pmatrix} \quad (4.23)$$

yields the coefficients

$$A_\lambda = \frac{b_1 a_{22} - b_2 a_{12}}{a_{11} a_{22} - a_{21} a_{12}} \quad (4.24)$$

$$B_\lambda = \frac{b_1 a_{21} - b_2 a_{11}}{a_{21} a_{12} - a_{11} a_{22}}. \quad (4.25)$$

## 4.5 Other Characterization Techniques

Other characterization techniques that were used throughout this thesis are presented in this section. Although, they are discussed only briefly, references for further reading are provided.

### 4.5.1 Four-Point Probe

A four-point probe (4PP) can be used for measuring the sheet resistance  $R_{sh}$  of a semiconductor sample [46, 142]. In typical 4PP measurement setups four probes are equally spaced and arranged collinear. Passing a current through the two outer probes and measuring the voltage via the two inner probes allows to determine  $R_{sh}$  of the material using the relation [143]

$$R_{sh} = \frac{\pi}{\ln(2)} \frac{V}{I}. \quad (4.26)$$

The resistivity of the bulk  $\rho_B$  can be determined by measuring  $R_{sh}$  of an undiffused wafer and multiplying it with its thickness  $W$ :

$$\rho_B = R_{sh} W \quad (4.27)$$

In this work the four-point probe technique is used to measure the bulk resistivity as well as the sheet resistivity which is important for the characterization of emitters.

---

<sup>4</sup>this convenient notation is taken from [141]

### 4.5.2 Electrochemical C-V Profiling (ECV)

Electrochemical capacitance-voltage (ECV) profiling is a technique to determine the dopant concentration as a function of depth [46, 144]. In this work the technique is used to measure the dopant profile of the laser doped regions.

The ECV measurement relies on contacting the surface of the semiconductor via an electrolyte. By making use of a well defined electrochemical dissolution reaction, the material can be profiled to any depth at a controlled and calculated rate. The Schottky contact between electrolyte and semiconductor permits to measure the carrier concentration at the edge of the depletion layer below the successively etched surface. This is done by varying the applied voltage at a constant dc bias voltage and measuring the capacitance of the electrolyte semiconductor junction.

### 4.5.3 Quasi-Steady-State $V_{oc}$ Method (Suns- $V_{oc}$ )

The quasi-steady-state open-circuit voltage (Suns- $V_{oc}$ ) method allows the measurement of the I-V curve without the contribution of the series resistance. This method is used in this work for the determination of the open-circuit voltage ( $V_{oc}$ ) and pseudo fill-factor ( $pFF$ ) of test samples of solar cells at various stages during processing.

The method is based on the simultaneous measurement of the  $V_{oc}$  of the solar cells and the corresponding incident light intensity [145]. By using a flash lamp with a slow decay a  $V_{oc}$  vs. illumination curve can be taken quickly. The Suns- $V_{oc}$  measurements can be understood as a sequence of ordinary C-V measurements at different light intensities, where only the  $V_{oc}$  is recorded. Light intensity and the short-circuit current  $I_{sc}$  of the device are linearly proportional, which allows to construct a pseudo photovoltaic I-V curve.

### 4.5.4 Reverse Biased Electroluminescence (ReBEL)

Reverse biased electroluminescence (ReBEL) is a characterization technique that allows imaging of local breakdown spots on solar cells [146–148]. The solar cell is operated at a constant voltage in reverse bias and the emitted visible light is detected using a pixelated silicon detector.

The light emission under reverse bias originates from localized diode breakdowns. A breakdown can be classified by its breakdown voltage and reverse I-V characteristic into so-called early (type I), soft (type II) and hard (type III) breakdowns. Early breakdowns set on at a bias voltage of about -4 to -5 V and are presumably induced by surface defects [148]. Soft (type II) breakdowns set on at about -8 to -14 V and are put down to recombination active crystal defects. Kwapil and Kaseman showed that metal precipitates, presumably close to the space charge region, are found at these soft breakdown sites. Hard breakdowns set on at -14 to -16 V and are attributed to avalanche breakdowns due to high local electric fields, e.g., thin emitter sites.

## 4. Characterization Techniques

ReBEL measurements will be used in the course of this thesis to detect nickel-silicide growth induced shunts. Local deep silicide formation, penetrating the space charge region, causes soft (type II) breakdowns and light emission at a characteristic reverse bias.

### 4.5.5 Adhesion Tester

With the adhesion tester the adhesive strength of the connection between the silicon of the solar cell and the metallization grid is measured. Insufficient adhesion between the processed silicon surface and the nickel-copper metallization has been a major challenge of the work presented here.

For the adhesion test a cell connector ribbon is soldered onto the busbar of the solar cell. Before the ribbon is connected to a force gauge the sample is stored for 24 h to allow the solder joint to settle. After this, the soldered ribbon is peeled of under an angle of  $90^\circ$  by moving the cell on a table at a constant speed while recording the applied force. A detailed description of the test as well as the influence of the peel-angle can be found in the references [112, 149].

## 5 Experimental Setup

This section will present the basic process flow used throughout this thesis. It is the basis for the experiments conducted in the experimental chapters 6 to 9. In addition to the laser process, which has been developed within this thesis, the setup for the creation of front metal contacts using light-induced nickel plating will be explained in this chapter.

### 5.1 Laser Process

The process to create laser doped structures consists of three distinct steps: application of the dopant source, laser induced dopant incorporation, and wash-off of dopant source residues. Figure 5.1 depicts these processing steps.

#### 5.1.1 Dopant Source Application

The dopant source can be a dopant containing, preferably viscous, liquid or polymer film. A wide range of so-called spin-on dopants (SOD) is commercially available. However, as will be shown in chapter 6, phosphoric acid ( $\text{H}_3\text{PO}_4$ ) is a suitable and inexpensive SOD. In industrial processes dopant sources are typically applied via spray or roll-on coating. In this thesis a spin coater is used for the application of the SOD since it allows reproducible coating and the device is already available in the laboratory. As will be shown in the next chapter, a transfer to an industrially feasible coating method should be possible and straight forward. The wafer is held on the chuck of the spin coater by

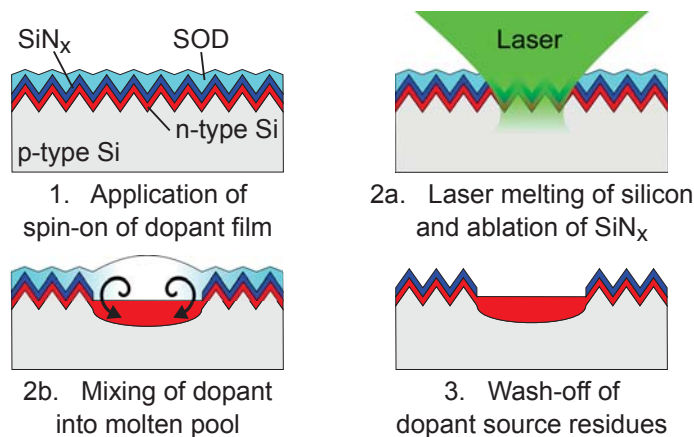


Figure 5.1: Schematic of the processing steps in laser doped selective emitter (LDSE) formation.

## 5. Experimental Setup

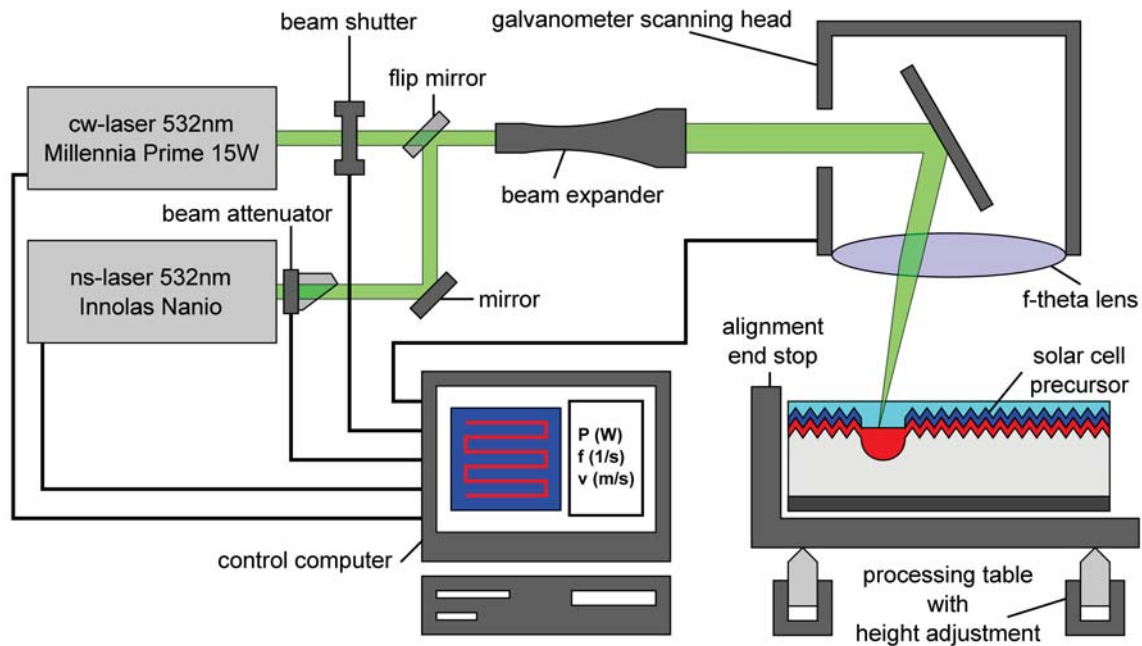


Figure 5.2: Schematic of the experimental setup used in this work for selective laser doping.

vacuum suction. An amount of SOD, sufficient to fully cover the front surface of the wafer, is applied onto the wafer using a pipette. Excess SOD is spun off at 3000 to 6000 RPM for 60 s.

The SOD has to be adequate for the surface that it is supposed to cover. In the most common case of a textured and  $\text{SiN}_x$  covered silicon wafer, a so-called solar cell precursor, almost all liquids can be spun on with satisfactory homogeneity. This is caused by the high surface roughness and the hydrophilicity of  $\text{SiN}_x$ . If planar or damage-etched wafers need to be covered, organic tensides can be added to lower surface tension [150]. Wafers without a  $\text{SiN}_x$  layer may need to be soaked in phosphoric acid prior to spin-coating to increase the hydrophilicity of the surface.

Polymeric SOD films may need to be pre-baked at temperatures of up to  $400^\circ\text{C}$  to start polymerization of the SOD on the surface of the precursor. For the experiments presented in this thesis, mainly  $\text{H}_3\text{PO}_4$  at 30 wt% was used to achieve n-type doping. A pre-baking of this SOD film is not necessary.

### 5.1.2 Laser Induced Dopant Incorporation

The experimental setup which was used to create locally doped silicon is shown in Fig. 5.2. The precursor covered with a SOD layer is loaded onto the processing table. Alignment of the wafer with the fixed optical setup is possible by pushing the wafer in  $x$  and  $y$  direction until the wafer edges hit the end-stops of the processing table. In this setup, end-stop-alignment was shown to have a lateral precision of  $16\ \mu\text{m}$  [151]. This allows to use the setup e.g., to create a selective emitter, unload the wafer for  $\text{SiN}_x$  deposition, and reload the wafer onto the

processing table for aligned laser ablation. To reduce the contamination of the sample with impurities a clean 1 mm thick silicon wafer can be placed between the processing table and sample wafer to prevent contact of the two.

Two laser systems are available for processing. Switching between the systems is possible by manually flipping a mirror into the beam path. The laser primarily used for deep and homogeneous laser doping is the Millenia Prime continuous wave (cw) laser built by Spectra-Physics which operates at 532 nm, emitting green light with a tuneable output power between 0.2 and 15 W. For selective ablation the 532 nm ns-pulsed laser Nanio 532-20-V built by Innolas can be used. Typical pulse lengths are between 40 and 160 ns at a repetition frequency of 100 to 500 kHz. The maximal pulse energy is between 20 and 160  $\mu\text{J}$  and depends on the repetition frequency. The intensity of the ns-pulsed laser which is delivered to the sample can be reduced with a variable attenuator.

The output of the laser systems is switched via a computer by directly controlling the pulsed laser and by opening and closing a beam shutter in the path of the cw-laser. The laser beam is then expanded by a beam expander with a variable expansion factor ranging from 1x to 8x. The parallel beam is directed into a galvanometer scanning head Intelliscan 20 built by Scanlabs. Here two computer controlled mirrors direct the beam through a f-theta lens with a focus length of 255 mm onto the sample surface. The pattern and travel speed of the laser spot on the surface is controlled by a computer program which allows design or import of the doping and ablation pattern.

Optimal focusing is achieved by changing the table height and minimizing the spot size on the wafer surface monitored with a magnifying digital camera. Thorough focusing is done at the start of every experimental session. If desired, the laser intensity can be measured using a powermeter in every section of the beam path.

### 5.1.3 Cleaning

After the laser process is finished, the wafer needs to be cleaned from residues of the SOD. The preferred procedure is to use a DI-water rinser. In the rinser the water is agitated by nitrogen bubbles to create a scrubbing action on the wafer surface. A quick exchange of DI-water removes the SOD before it can settle back on the surface. If the SOD is  $\text{H}_3\text{PO}_4$ , cleaning in this so-called quick dump rinser is sufficient. In the case of a polymeric SOD, dipping in diluted hydrofluoric acid (HF) may be necessary before DI-water rinsing. The laser doping process of the precursor wafers is finished after blow drying with a nitrogen gun.

## 5.2 Plating Process

By means of the cw-laser processing the  $\text{SiN}_x$  layer is ablated in the pattern of the contact grid. To create a nickel contact with low contact resistance and sufficient adhesion two steps are typically performed: Nickel deposition and

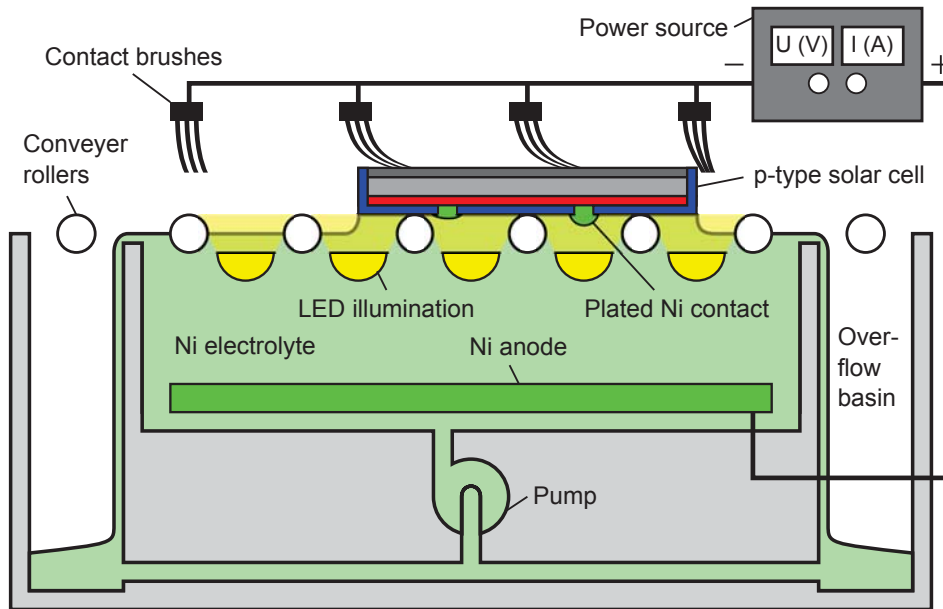


Figure 5.3: Schematic of the inline tool for single-sided bias-assisted light-induced nickel plating built by RENA company.

thermal nickel silicide formation. The details of these two steps of the front contact creation will be discussed in the following. For the subsequent copper and silver plating, established and well tested processes will be used as outlined e.g., by Jonas Bartsch [106], Andrew Mondon [112], or Achim Kraft [152].

### 5.2.1 Light-Induced Plating (LIP)

The benefit of metal plating for solar cells lays in the utilization of the dielectric layer. Here, the  $\text{SiN}_x$  layer acts as an anti-reflection coating, a passivation layer, and also as a mask for the metallization process. For metal deposition, nickel needs to be reduced from its ionic form in the electrolyte to elemental nickel on top of the processed and therefore exposed silicon surface. Since the nickel also serves as a barrier layer for the copper layer atop, the nickel layer needs to homogeneously cover all surfaces which are not covered with  $\text{SiN}_x$ . Only the exposed silicon surface should be suitable for nickel plating.

For light-induced plating (LIP) on a p-type solar cell, the rear contact is set to a negative potential and the cell is illuminated from the front. In this thesis LIP is mostly performed using an inline plating tool built by RENA which is depicted as a schematic in Fig. 5.3. After a 30 s dip in HF (1%) to remove native oxide, wafers are loaded onto transport rolls which carry the wafers slightly above the surface level of the agitated electrolyte through the plating tool. In Fig. 5.3 the direction of movement is to the right. When a wafer is above the electrolyte basin, it is wetted by the electrolyte from the front side. This is caused by a lowering of the surface energy by wetting the  $\text{SiN}_x$  compared to the electrolyte-air interface. Metal brushes contact the rear terminal of the solar cell and a voltage source sets it to a fixed negative potential relative to

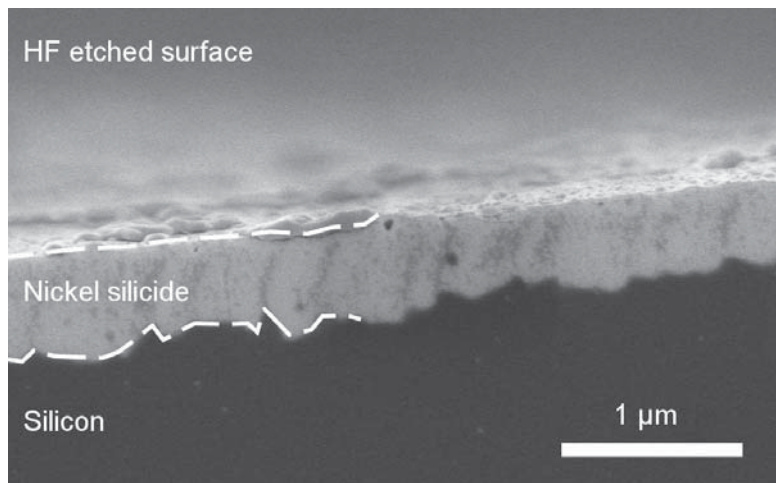


Figure 5.4: Cross-sectional SEM image of nickel silicide formed from LIP nickel on HF-etched silicon after annealing at 450° C for 10 min.

the nickel anode which is immersed in the electrolyte. LED arrays between the transport rolls illuminate the front surface of the wafer. Nickel ions from the electrolyte are reduced at a conductive surface, which is on a sufficiently high negative potential, such as the contact openings on the front side of the solar cell (the fundamentals of metal plating is detailed in Sec. 3.4.1). The nickel ions in the electrolyte are replenished by dissolving the nickel anode, which results in low maintenance and high lifetime of the electrolyte. At a bias voltage of 2.8 V the plating time (i.e. the time the wafer is in contact with the electrolyte) is adjusted to 60 s. These parameters result in a nickel layer with a typical thickness of 1  $\mu\text{m}$ .

### 5.2.2 Nickel Silicide Formation

Following the nickel deposition a nickel silicide layer is formed to reduce contact resistance and increase the mechanical adhesion of the metal contact. The silicide layer is formed at elevated temperatures in the range of 300° C to 450° C on a time scale of a few minutes (the fundamentals of nickel silicide formation is detailed in Sec. 3.4.2). This temperature is sufficient to allow the diffusion of nickel into silicon and to create a nickel silicide layer with a thickness of up to 600 nm [153]. For the formation of nickel silicide the diffusion of nickel into the silicon needs to be possible. A thin layer between nickel and silicon may act as a diffusion barrier and hinder the formation of nickel silicide.  $\text{SiN}_x$  acts as such a layer and thus prevents nickel silicide formation in regions where nickel is deposited on un-patterned surface. For example, this is the case at the edge of the laser lines where lateral growth during plating leads to a metal contact finger which is wider than the initial laser opening. On the other hand, a parasitic surface layer on the laser ablated silicon may hinder silicidation at the intended contact openings.

After light-induced nickel plating and subsequent Di-water rinse, the wafer is

## 5. Experimental Setup

immediately<sup>1</sup> loaded into an annealing oven to form the thin nickel silicide layer. The time gap between plating and thermal treatment is kept as short as possible since a preliminary study by Mondon et al. [112] indicated a reduction in the extend of silicide formation with the length of the time gap. A parasitic oxide layer that growths between silicon and nickel is suspected to impair silicidation.

The oven used for the formation of the silicide was either a conveyor belt furnace built by Centrotherm or a single wafer rapid thermal processor. In both cases the temperature profile was adjusted such that silicide formation was conducted at a temperature of 450° C for a length of 10 min under forming gas atmosphere. This process was proven to reliably produce silicides on reference samples with contact openings defined by ink-jet printing and HF etching [151, 154]. Figure 5.4 shows a cross-sectional SEM image of the nickel silicide formed on a solar cell precursor using this thermal process. The contacts of this sample have been opened by HF etching of the SiN<sub>x</sub> layer (mask and etch).

---

<sup>1</sup>with a maximum of 15 min between plating and thermal treatment

## 6 Evaluation of Suitable Laser Doping Parameters

At the beginning of this chapter the general requirements on an industrially feasible laser doping process will be discussed. In the main part, Sec. 6.2 and 6.3, the parameter space for laser processing using the cw and ns-pulsed laser will be swept to find suitable parameters for dielectric ablation, silicon doping, and epitaxial recrystallization. These parameters will be evaluated with respect to the formulated requirements in the last section. This will allow the selection of baseline parameter set that will be the basis of the detailed investigations conducted in the following chapters.

### 6.1 Requirements for Laser Doped Structures

A laser doping process suitable to enhance the cost effectiveness of industrial solar cell production needs to fulfill various requirements. In this section the prime requirements, summarized in Tab. 6.1, will be presented. They form the basis on which a process window for a laser doping process will be selected at the end of this chapter.

The main incentive to employ laser processing for patterning of the front side of the solar cell is to combine the formation of a selective emitter and the contact opening of the dielectric in a single processing step. The dielectric layer serve three purposes: passivation of the silicon surface, increasing of light coupling into the absorber, and defining a mask for subsequent front contact formation. The latter point holds the potential of great cost reduction by using a nickel-copper plating scheme as detailed in Sec. 3. To exploit this potential, the selective laser doping needs to be performed after dielectric deposition. The dielectric layer needs to be ablated in such a way that nickel plating as well as subsequent nickel silicide formation on the patterned contact openings is possible.

Process property	Effect
Complete dielectric ablation	Enables Ni-Cu plating
Simultaneous doping and ablation	Reduces process complexity
Narrow laser lines	Reduces shading loss
Deep, homogeneous, wide doping	Reduces risk of Ni induced shunting
High quality of doped material	Reduces recombination
High processing speed	Reduces processing cost per wafer

Table 6.1: Requirements for an industrially feasible laser doping process.

As pointed out in Sec. 2.5, a selective emitter brings about a number of advantages. For obvious reasons a suitable laser doping process should allow sufficient dopant incorporation. Optimization of the production process requires that the parameters of the dopant profile are controllable. With regard to subsequent nickel-copper plating the laser doped region needs to be sufficiently deep, homogeneous, and extend laterally beyond the ablated dielectric. This ensures that the emitter has a sufficient depth everywhere below the plated nickel layer and prevents the penetration of the p-n junction by deep nickel silicide growth.

The front side of efficient solar cells is usually textured. Despite the irregular textured wafer surface a laser processed line should be well defined and narrow. A fringed laser line with small contact openings adjacent to the main line, so-called satellites (cf. Fig. 6.1), are prone for nickel induced shunting. These satellites are presumed to have a shallow emitter which can easily be penetrated during nickel silicide formation. In addition to this, a well defined and narrow laser line brings the benefit of reduced shading loss and thus increased efficiency.

For maximum conversion efficiency the laser doped silicon material should be crystalline with a low defect density. The formation of macroscopic defects, such as voids within the resolidified doped silicon, needs to be avoided. The quality of the laser doped region can be characterized in terms of a corresponding emitter saturation current density, which is low if the quality of the laser doped region is high.

Last but not least, a suitable laser doping process needs to be viable for industrial mass production. Points that need to be considered here are the investment costs, the operating costs, and the lifetime of the production tools needed for laser processing [126]. For these reasons, simple processes are preferable to complex solutions. This includes the application of the dopant source, the laser process, as well as the cleaning of the dopant source residues. In addition to this, an industrial production tool is required to pattern the solar cells with high reproducibility, homogeneity, and at processing times that match the production rate of the manufacturing line. For the latter aspect, the speed with which the laser spot is moved across the wafer needs to be sufficiently high.

## 6.2 Laser Ablation

### 6.2.1 Beam Optics

The fundamental mode  $TEM_{00}$  of a laser has a Gaussian intensity distribution with a diameter defined by a drop in intensity to  $1/e$  of its maximum value. The diameter  $d$  of a laser beam widens from the waist diameter  $d_0$  of the beam at  $z = 0$  like [155]

$$d(z) = d_0 \sqrt{1 + \frac{z^2}{z_R^2}} \quad (6.1)$$

cw-laser								
Expansion	1x	2x	3x	4x	5x*	6x	7x	8x
Waist diameter ( $\mu\text{m}$ )	75	37	25	19	15	13	11	10
Rayleigh length ( $\mu\text{m}$ )	8326	2098	940	533	344	241	178	138
ns-pulsed laser								
Expansion	1x	2x	3x	4x*	5x	6x	7x	8x
Waist diameter ( $\mu\text{m}$ )	216	108	72	54	43	36	31	27
Rayleigh length ( $\mu\text{m}$ )	68800	17200	7650	4300	2750	1910	1400	1080

Table 6.2: Waist diameters and Rayleigh lengths of the cw and ns-pulsed laser beams after beam expansion. The beam diameters at the laser output are 0.8 mm (cw) and 2.3 mm (ns-pulsed) [156, 157], the focal length of the f-theta lens is 255 mm. The best suited parameters are marked with \*.

with the Rayleigh length  $z_R$ , which is the distance at which the beam diameter is increased by a factor of  $\sqrt{2}$ . The Rayleigh length is relevant in this context since it needs to be sufficiently high to account for texture and surface irregularities of the precursor. If  $z_R$  is too small the laser intensity at the edge of a wafer may be different to the intensity in the center, which would result in inhomogeneous doping across the wafer. The Rayleigh length is connected to the beam waist diameter and the wavelength  $\lambda$  through:

$$z_R = \frac{\pi d_0^2}{4\lambda}. \quad (6.2)$$

With the use of the beam expander the waist diameter  $d_0$  and thus the spot size on the work piece can be adjusted. Table 6.2 collects the possible  $d_0$  as well as the corresponding  $z_R$  values for the two laser systems.

Figure 6.3 a) displays the transmission of the cw-laser light through the setup. The laser power is measured at the position of the processing table as a function of the beam expansion factor. The drop in transmission starting at an expansion of 6x is caused by the aperture of the galvanometer scanning head which blocks out a significant part of the widely expanded laser beam. In addition to a reduction in maximum power output, the partial blocking of the Gaussian beam will result in an undesired Airy pattern.

The expansion factor has been chosen to 5x for the cw-laser and 4x for the ns-pulsed laser. For the cw-laser this results in a spot size of  $15 \mu\text{m}$  and a Rayleigh length of  $344 \mu\text{m}$ . This represents a compromise between a small spot size, sufficient Rayleigh length and optical properties of the laser drawn line, which will be explained in more detail in the following.

### 6.2.2 Optical Appearance of Laser Lines

If the laser spot is scanned across the surface of a sample, changes in the surface texture, reflectance and color can be observed optically. In order to perform a coarse scan of the parameter space, laser lines were drawn on textured and



$P$ (W)	15	15	15	6	6
$v$ (m/s)	1	5	8	1	8

Figure 6.1: Schematic of the different melt schemes observed using optical microscopy during parameter screening. The blue area represents unaffected  $\text{SiN}_x$ , the brown area represents partly ablated  $\text{SiN}_x$ , and the gray area is apparently fully ablated  $\text{SiN}_x$ . The laser ablated line is continuous and well defined at slow scanning speeds ( $v$ ) and high power ( $P$ ). With increase in speed and decrease in power the  $\text{SiN}_x$  is only partly ablated and the line breaks up into separated regions.

$\text{SiN}_x$  covered precursors at various travel speeds  $v$  and output powers  $P$ . The resultant lines were observed using the LEXT confocal microscope.

In the case of the cw-laser the resultant images have been categorized into five classes shown as schematics in Fig. 6.1. Beginning from left to right the surface area that has been optically affected by the laser irradiation is decreasing. At slow speeds and high power ( $v = 1$  m/s,  $P = 15$  W) the laser has flattened the texture in a line with a width of about  $20\ \mu\text{m}$ . If the scanning speed is increased ( $v = 5$  m/s) brown structures appear at the edge of the laser drawn line. SEM imaging of the edge of the laser line, shown in Fig. 6.2, reveals that this is  $\text{SiN}_x$  which has been partly decomposed and appears brown due to a change in the interference of this thinned layer. If the scanning speed is further increased ( $v = 8$  m/s) the area of incomplete ablation of  $\text{SiN}_x$  increases likewise. In addition to this, the occurrence of isolated spots of ablated  $\text{SiN}_x$  not connected to the main line increases. These so-called satellites can be put down to the geometry of the textures pyramid tips refracting the laser light. The geometry of the pyramids causes an intensification of the light as described by Knorz et al. [158]. Fast scanning speeds and wide laser spots lead to an increase in the density of these satellites. Satellites are considered undesirable due to their presumed shallow doping depths which is detrimental for reliability in a nickel-copper plating scheme. At slow speeds and intermediate power ( $v = 1$  m/s,  $P = 6$  W) the satellite density further increases up to the point where the main line disappears ( $v = 8$  m/s,  $P = 6$  W).

With the use of microscopy imaging the influence of the beam expansion factor on the linewidth and satellite density was studied. The data presented in Figs. 6.3 b) and c) have been extracted from LEXT images by using an appropriate color threshold and the particle analyzer in the image processor ImageJ [159]. Surprisingly, the data shown in Fig. 6.3 b) reveals that the line width (data points) correlates only slightly with the calculated spot size (solid

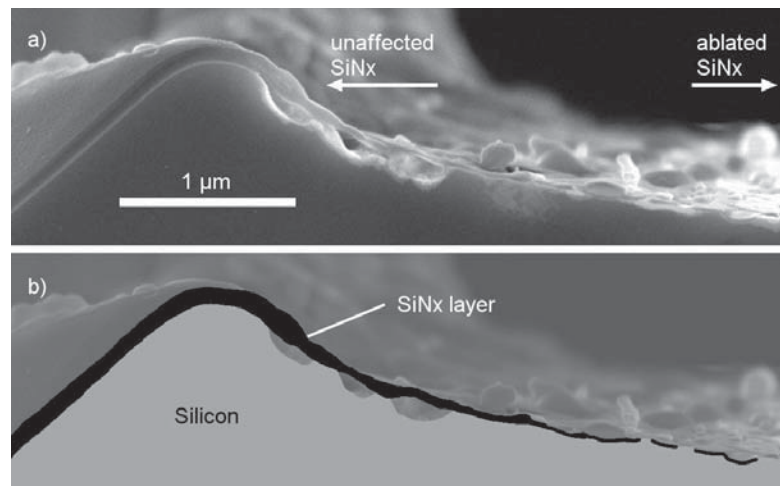


Figure 6.2: Cross-sectional SEM image of the edge region of a laser processed line (a) and a schematic indicating the  $\text{SiN}_x$  layer and the bulk silicon (b). The center of the corresponding laser line is to the right. The area to the left is not affected by the laser process.

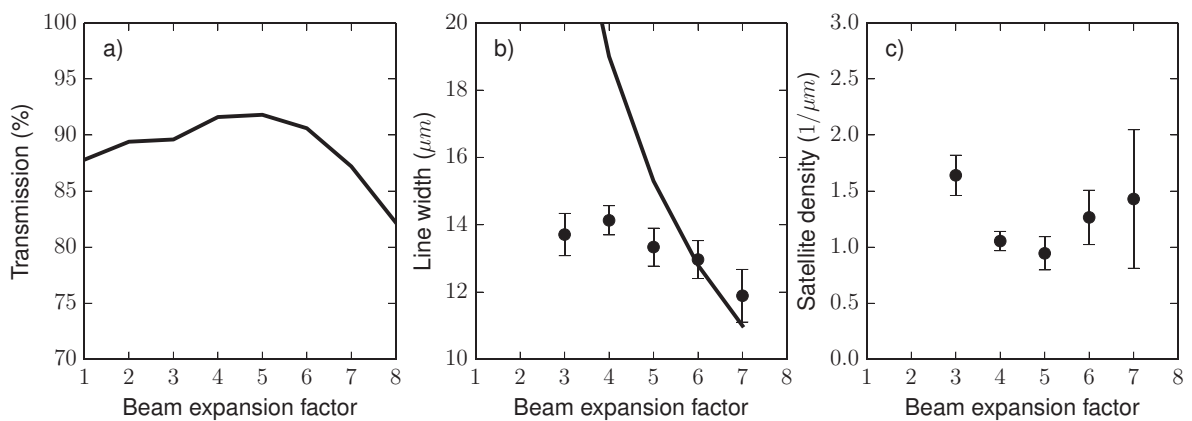


Figure 6.3: Transmission of the beam guiding system as a function of the beam expansion factor (a). Calculated spot size (solid line) and measured line width (points) as a function of the beam expansion factor (b). Number of ablation satellites (ablated areas not connected to the main laser line) per  $\mu\text{m}$  as a function of the beam expansion factor (c). The error in (b) and (c) represents the RMS of the respective value determined at different positions on the wafer.

## 6. Evaluation of Suitable Laser Doping Parameters

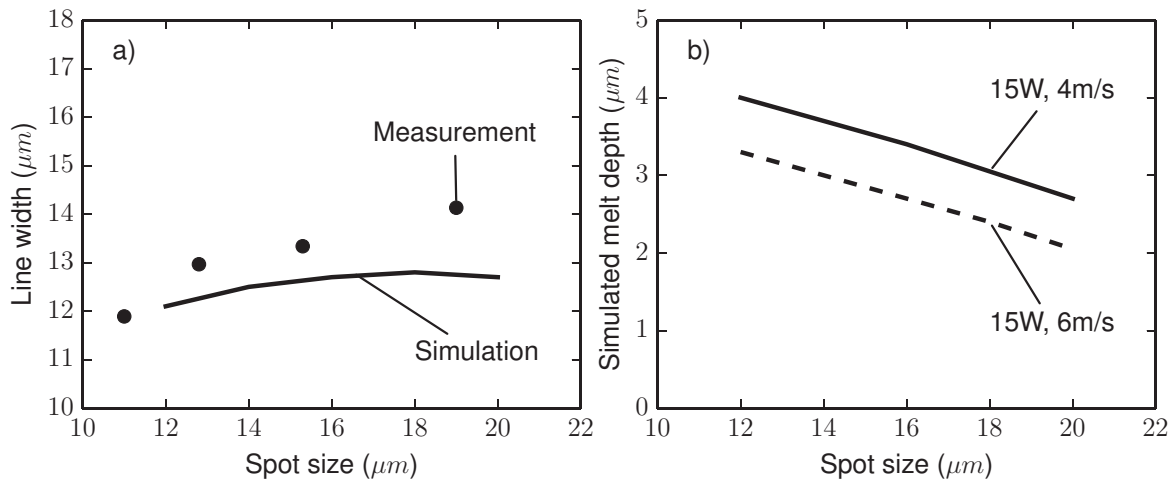


Figure 6.4: Measured laser line width (points) and the result of the simulation conducted by Blecher et al. [90] as a function of the laser spot size (a). Simulated melt depth [90] as a function of the spot size for two different scanning speeds (b).

line).

The beam expansion factor has a significant impact on the satellite density as shown in Fig. 6.3 c). The error bar represents the root mean square (RMS) of the satellite density determined at nine positions distributed evenly on a silicon wafer with a side length of 156 mm. This error is therefore a measure of the homogeneity of the shape of the laser drawn line. With increasing beam expansion the spot size as well as the Rayleigh length decreases (cf. Tab. 6.2). At a beam expansion larger than 5x the Rayleigh length is so small, that at the edges of the wafer the laser beam is not focused properly. This may be caused by an imperfect f-theta lens or a slight bow in the processed wafer. The results are an inhomogeneous line shape, as well as an increase in satellite density. The homogeneous line shape, the low satellite density, the peak in transmission, and the small line width lead to the chosen beam expansion factor of 5x which will be used throughout this work.

Numerical simulations of the LDSE process using a cw-laser source have been conducted by Blecher et al. [89, 90] (detailed discussion in Sec. 3.3.3). They predicted relevant parameters, such as the width and depth of the molten zone, for a planar silicon wafer covered with a 75 nm  $\text{SiN}_x$  layer and  $0.5 \mu\text{m}$  of SOD. Figure 6.4 a) shows the measured line width and the result of the simulation as a function of the spot size. The measured line width and the value determined from the simulation are in good agreement, considering that the measured data was determined from textured samples. The line width is only weakly correlated with the spot size. However, the simulated depth of the molten zone exhibits a linear relationship with the spot size, as shown in Fig. 6.4 b). This suggests the presumption that a line drawn by the cw-laser at relatively high speeds (similar to the two left most schematics of Fig. 6.1) has been molten to a depth exceeding one micrometer. The influence of scanning speed on the doping profile will be discussed in detail later in this chapter.

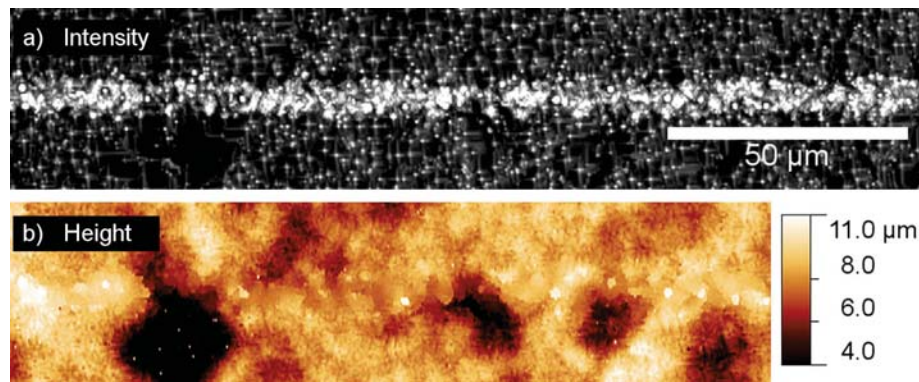


Figure 6.5: Confocal microscope images of a ns-pulsed laser ablated line using 80 ns long pulses at a pulse energy of  $5 \mu\text{J}$ . The laser reflection image (a) shows that the resultant laser line has a width of about  $13 \mu\text{m}$ . The height map (b) shows little change of the random pyramid surface texture. Sauaia-Lopes has found these laser parameters best suited for laser ablation [160].

### ns-Pulsed Laser Ablation

The extended heat-affected zone of cw-laser processing limits the suitability of this technique for damage free ablation of dielectric layers. On the other hand, its primal advantage is the extended depth of the molten zone in selective doping, which will be discussed in the next section. Instead, ns-pulsed laser processing has been found to be a suitable tool for selective  $\text{SiN}_x$  ablation by various researchers [23, 66, 77]. Lopes-Sauaia [160] studied ablation using the same experimental setup with the ns-pulsed laser and found optimal ablation conditions using a beam expansion of 4x and 80 ns long pulses at a pulse energy of  $5 \mu\text{J}$ . These ablation parameters result in a laser line width of about  $13 \mu\text{m}$  as shown in Fig. 6.5.

### 6.2.3 Nickel Plating on Laser Lines

There is a variety of electrolytes for nickel plating commercially available. Three electrolytes which differ in their chemical deposition mechanism have been tested for the suitability of metal deposition on cw-laser doped lines.

#### Electroless Electrolyte

At first a so-called electroless nickel electrolyte has been used. Here the electrons needed for the reduction of nickel ions are delivered by a reducing agent added to the electrolyte. Laser structured areas should expose a bare silicon surface which acts as a catalyst allowing the redox reaction to form elemental nickel. On  $\text{SiN}_x$  covered surfaces this redox reaction is hindered and elemental nickel is not deposited.

LDSE process has been used to create single lines on  $\text{SiN}_x$  covered solar cell precursors. The scanning velocity  $v$  and the cw-laser power  $P$  have been varied

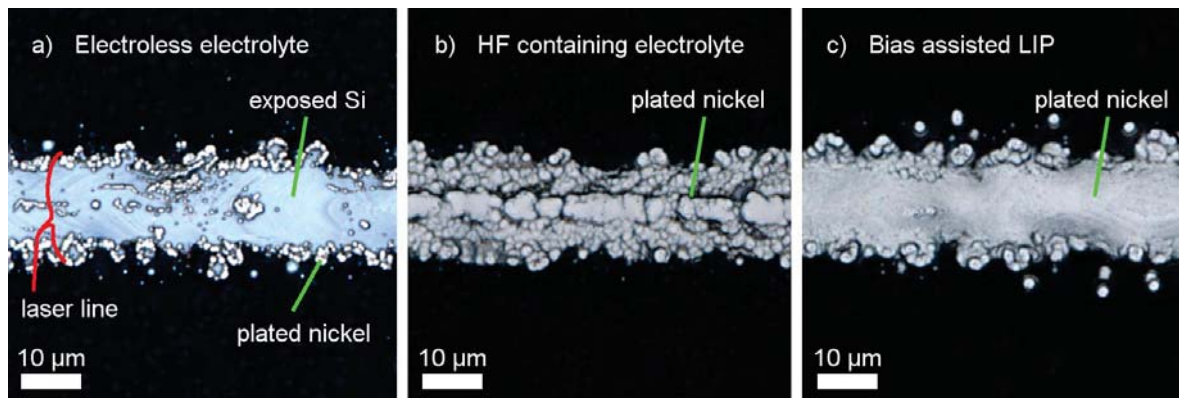


Figure 6.6: Microscopy images of nickel deposition on cw-laser lines using three different plating processes: Electroless nickel plating (a), plating with electroless electrolyte containing HF (b), and bias-assisted light-induced plating (c). The light blue area in (a) is silicon not covered with nickel. (b) and (c) are fully covered with plated nickel.

between 0.5 – 7m/s and 6 – 15 W. After a 30 s dip in HF (1%) and DI-rinse the samples have been immersed in the electroless electrolyte NIPOSIT<sup>1</sup> for 90 s.

The quality of the nickel deposition was examined using the LEXT microscope. An representative example of the deposition is shown in Fig. 6.6 a). For all parameters tested the deposition was meager and inhomogeneous. This poor result can usually put down to inadequate surface properties of the exposed silicon [114]. This presumption is supported by good plating results on similar samples processed using the same electrolyte but photo lithography and chemical etching for SiN<sub>x</sub> structuring [160]. This prolonged etching with HF creates a clean and reactive silicon surface well suited for nickel plating.

### Electroless HF-containing Electrolyte

This experimental procedure has been repeated with a different electroless electrolyte. The used NICKELEX electrolyte<sup>2</sup> contains a small amount of HF (< 1 wt%) to promote plating by etching the native silicon oxide covering the catalytic silicon. The samples have been immersed in the hot electrolyte (95° C) for 90 s.

An example of the nickel deposition is shown in Fig. 6.6 b). For all process parameters nickel deposition was increased and more homogeneous compared to the previous experiment. Deposition at 15 W using a scanning speed of 3 and 5 m/s resulted in the best results. It is presumed that this can be put down to the etching effect of HF which acts on the surface and removes process induced species that hinders metal deposition.

However, industrial implementation of electroless plating is not without problems because the reducing agent in the electrolyte must be carefully controlled. Additionally, a hot electrolyte containing HF complicates handling, raises health

<sup>1</sup>NIPOSIT 162 PM-988 manufactured by Dow Chemical Company

<sup>2</sup>NICKELEX manufactured by Transene Company

and safety issues and affects the quality of the SiN<sub>x</sub> passivation.

### Light-Induced Plating

In bias-assisted light-induced plating (LIP) the electrons for the reduction of the nickel ions are supplied from an external current source via the conducting surface of the sample as discussed in Sec. 5.2.1. The screening of the relevant LDSE parameters has been repeated a third time, now with the use of LIP.

The most homogeneous nickel deposition was observed using a laser power  $P$  between 9 and 15 W and a scanning speed  $v$  of 3 to 5 m/s. An example of the nickel deposition at a suitable parameter ( $v = 5$  m/s,  $P = 15$  W) is shown in Fig. 6.6 c). At scanning speeds below 1 m/s nickel deposition is limited to the edges of the laser line, similar to the result presented in Fig. 6.6 a). With increasing  $v$  the coverage increases likewise. Homogeneous nickel deposition was also observed on laser lines that were presumably covered with a only partly ablated layer of SiN<sub>x</sub>, similar to the case  $P = 15$  W,  $v = 8$  m/s in Fig. 6.1. Apparently, LIP is not as sensitive to the condition of the surface as the electroless nickel plating methods.

### 6.2.4 Surface Characterization

The nickel deposition using electroless electrolytes was meager and inhomogeneous for all tested LDSE process parameters. However, the homogeneity of the plated layer increased if a HF containing electrolyte was employed. Although LIP created nickel layers with sufficient quality at intermediate scanning speeds, the deposition at low scanning speeds was severely hindered. All these observations can be put down to an inadequate surface condition after the LDSE process. Only by HF induced etching of the surface by the NICKELX electrolyte or the stimulation of nickel reduction from the electrolyte by the bias voltage in LIP nickel deposition on the laser lines was possible.

In this section the surface of laser lines created with the LDSE process using the cw-laser will be studied using energy-dispersive X-ray spectroscopy (EDX). For this purpose a sample with laser lines processed at various speeds ranging from 0.5 to 10 m/s at 15 W has been prepared. A Czochralski (CZ) grown p-type silicon wafer was covered with 75 nm PECVD SiN<sub>x</sub><sup>3</sup>. After dopant application, laser processing, and cleaning, the sample has been dipped in HF (1%) for 30 s to treat the surface as it would be for nickel LIP. The EDX measurements are performed on a spot in the center of the laser lines as illustrated in Fig. 6.7 a). A shallow sampling depth of the SEM analysis is achieved by setting the energy of the primary electrons to 1.5 keV. The maximum depth of emitted characteristic x-rays was estimated to about 50 nm by using the Monte Carlo simulation program CASINO [129]. The measured spectrum was fitted using three Gaussian peaks on top of a background modeled as linear convoluted

---

<sup>3</sup>The same experiment was also conducted using multicrystalline material. The results are identical to the ones presented here.

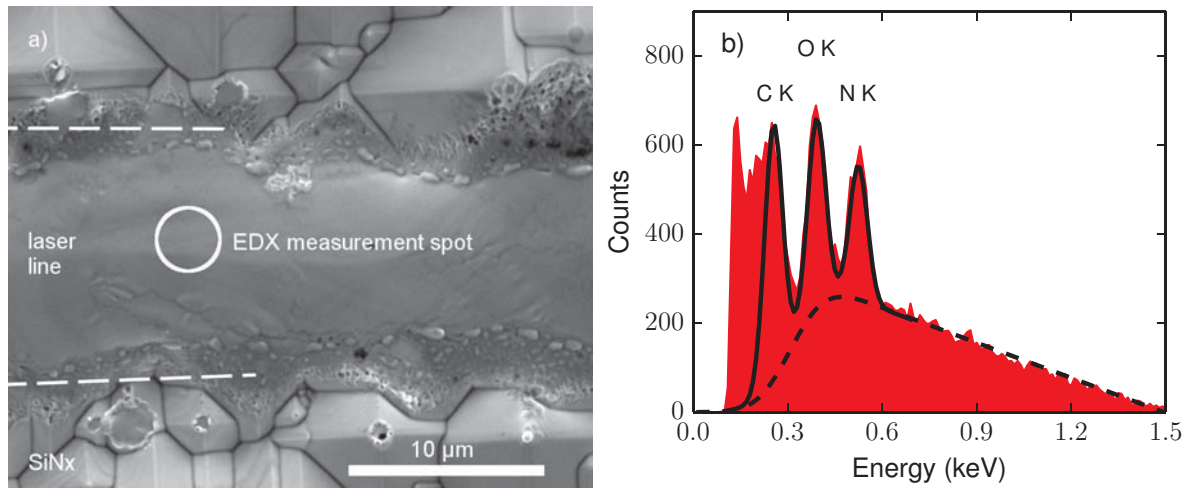


Figure 6.7: Top view SEM image of a laser line (a) indicating the position of EDX measurements conducted for surface analysis. The corresponding x-ray spectrum (b) is fitted with a background (dashed line) and three Gaussian curves ( $\sigma = 0.028$  keV) at  $\mu = 0.26$ ,  $0.39$ , and  $0.52$  keV corresponding to the  $CK\alpha$ ,  $OK\alpha$ , and  $NK\alpha$  x-ray lines (solid line). The fitted data is used to construct Fig. 6.3.

with a shifted error function<sup>4</sup>. The Gaussian peaks represent the x-ray lines of carbon ( $CK\alpha$ :  $0.26$  keV), nitrogen ( $NK\alpha$ :  $0.39$  keV), and oxygen ( $OK\alpha$ :  $0.52$  keV) and have a width of  $\sigma = 0.028$  keV representing the spectral resolution of the x-ray detector. A representative example of the measured as well as the fitted spectrum is shown in Fig. 6.7 b).

Figure 6.8 displays the peak heights of the  $OK\alpha$  and  $NK\alpha$  extracted from the fit as a function of the linear energy density. The linear energy density

$$\varepsilon = \frac{P}{v} \quad (6.3)$$

is used as the abscissa because it is proportional to the total energy a point on the surface receives during processing. With increasing energy density the intensity of the nitrogen signal decreases rapidly to a constant value at scanning speeds slower than about  $3$  m/s. On the other hand, after a slight decrease at very fast  $v$  and a signal minimum at about  $5$  m/s the oxygen signal increases linearly with the energy density. The measured peak heights can be compared to the peak height measured on a pure silicon reference sample dipped in HF (1%) prior to EDX measurement. In comparison to this reference, the intensity of the nitrogen peak from the LDSE surfaces is significantly increased for all processing parameters. The intensity of the oxygen peak is on par with the intensity from the reference at a scanning speed faster than  $3$  m/s.

These measurements suggest the assumption that the optimal scanning speed is a trade-off between  $SiN_x$  ablation and the formation of silicon oxide species,

<sup>4</sup>In theory, the continuum can be expected to extend from the maximum energy of the primary beam electrons and increase exponentially to zero keV energy. In reality, the background goes to zero at the low end of the energy spectrum due to absorption by the detector window and the detector dead layer [161].

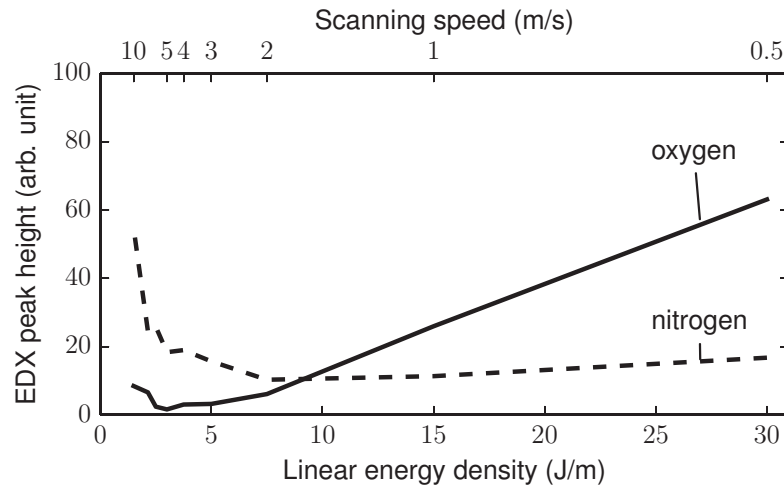


Figure 6.8: Intensity of the  $O K\alpha$  (oxygen) and  $N K\alpha$  (nitrogen) x-ray emission from cw-laser  $\text{SiN}_x$  ablated silicon ( $P = 15 \text{ W}$ ). The intensity is shown as a function of the linear energy density ( $\epsilon$ ), which is inversely proportional to the scanning speed  $v$ . The primary electron energy is 1.5 keV resulting in a sampling depth of about 50 nm.

both of which hinder nickel deposition and prevents nickel silicide formation (which will be in the focus of chapter 8). Although a quantitative evaluation of the data is not possible since the surface cannot be treated as homogeneous throughout the sampling depth, the best processing parameters determined by evaluating the plating quality in the previous section (3 m/s and 5 m/s at 15 W) are in agreement with the results of the EDX measurement. At these intermediate scanning speeds the oxygen content of the surface layer is minimal and the nitrogen content is approaching its plateau value.

## 6.3 n-Type Laser Doping

The LDSE process with the cw-laser is optimally suited for creating deep and homogeneous laser doped lines due to a melt depth of a few micrometers even at reasonable fast scanning speeds (cf. Fig. 6.4 b). This section will discuss the influence of the processing parameters on the dopant profile of the laser doped silicon. These processing parameters are primarily the type and thickness of the spin-on dopant (Sec. 6.3.1) and the laser scanning speed (Sec. 6.3.2). Scanning and transmission electron microscopy will be used to study macroscopic and microscopic defects in the recrystallized silicon (Sec. 6.3.3).

### 6.3.1 Spin-On Dopant Type and Thickness

While there is a variety of spin-on dopant sources (SOD) commercially available, phosphoric acid ( $\text{H}_3\text{PO}_4$ ) with or without additives is an inexpensive alternative which has shown good results as a n-type dopant source in inline-diffusion and laser doping processes [18, 150]. In this section the suitability of  $\text{H}_3\text{PO}_4$  as a SOD will be tested. After that, the influence of the thickness of the SOD on

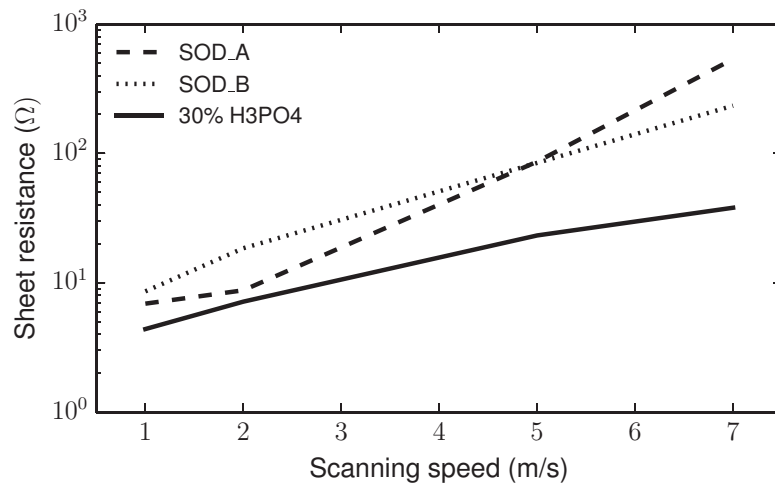


Figure 6.9: Sheet resistance of cw-laser doped silicon as a function of the scanning speed for the three different dopant sources.

the sheet resistance will be examined.

### SOD Type

In this section two commercially available phosphorous dopant sources as well as 30 wt% H<sub>3</sub>PO<sub>4</sub> will be evaluated using sheet resistance measurements.

Three p-type wafers have been coated with two commercially available phosphorous dopant sources SOD\_A and SOD\_B according to the instructions supplied by the manufacturer as well as with 30 wt% H<sub>3</sub>PO<sub>4</sub> at a rotational speed of 3000 RPM. The samples have been prepared using different scanning speeds ranging from 1 to 7 m/s at a laser output power of 15 W. Squares with an edge length of 3 cm were hatched using laser lines. These laser lines had a center to center distance of 9 μm at a linewidth of about 14 μm resulting in an effective overlap of 5 μm or about a 35%. After DI-water rinsing the sheet resistance of the laser hatched fields was measured using the four-point-probe technique.

Figure 6.9 displays the measured sheet resistance as a function of the scanning speed for the three different dopant sources. For all SOD the sheet resistance increases with the scanning speed. Surprisingly the H<sub>3</sub>PO<sub>4</sub> results in the lowest sheet resistance at all speeds. Low sheet resistance is the result of effective dopant incorporation and thus doping is most effective when H<sub>3</sub>PO<sub>4</sub> is used. At the optimal parameters for LDSE processing as determined in the previous section (15 W, 5 m/s) the sheet resistance is as low as 23 Ω. If necessary, a higher sheet resistance of the laser doped region, i.e., reduced dopant concentration, should be achievable by diluting the H<sub>3</sub>PO<sub>4</sub> with DI-water [150, 162]. In addition to the benefit of effective dopant incorporation, the residue from the H<sub>3</sub>PO<sub>4</sub> SOD is easy to clean off after laser processing, whereas the other SODs need to be dipped in HF to remove the residue from the wafer surface. In conclusion, commercially available SOD may be useful if an un-textured or

shiny etched wafer needs to be coated with a SOD. In that case the  $\text{H}_3\text{PO}_4$  is not homogeneously wetting the wafer surface and a polymerizing SOD needs to be used. However, for all applications that will be studied in this thesis  $\text{H}_3\text{PO}_4$  at 30 wt% is working well because all samples under investigation were textured.

### SOD Thickness

The  $\text{H}_3\text{PO}_4$  SOD can be applied using spray-on, roll-on, or spin coating [19, 150]. In this thesis only spin-on coating is used since it represents a highly reproducible coating method. The slow processing time and manual handling is acceptable because the experiments conducted used a limited number of wafers. However, for industrial implementation spin-coating is not a viable coating method due to single wafer processing, long processing times and complex wafer loading and unloading.

In this section the thickness of the  $\text{H}_3\text{PO}_4$  SOD applied at different rotational speeds  $\omega$  using a spin coater will be studied. Furthermore, the influence of the SOD thickness on the sheet resistance will be evaluated. The presented data may be valuable for the development of other coating methods.

For this experiment wafers have been coated at different  $\omega$  ranging from 3000 to 6000 RPM using  $\text{H}_3\text{PO}_4$  at 30 wt%. The wafers differed in texture and passivation coating. Three textures have been tested. Two of which were random pyramid textures, one processed at ISE and the other one at Bosch Solar. The third texture was developed at RENA under the name KI+ (Kantenisolation Plus). It was developed for edge isolation by chemical etching of the back side. In addition to this,  $\text{SiN}_x$  covered as well as bare silicon surfaces have been spin coated. The thickness distribution of the SOD on the coated wafers was measured using confocal microscopy as explained in Sec. 4.3. Additionally, the average thickness has been determined by weighing the wafer before and after coating. After the determination of the SOD thickness, squares hatched with laser lines as described in the previous section were created on the different wafers using a scanning speed of 5 m/s at 15 W with a line overlap of 64%. The sheet resistance of these laser hatched fields was measured using the four-point-probe technique.

Figure 6.10 displays height distributions of the dopant film above the wafer surface. The distributions start at a film height of  $0 \mu\text{m}^5$  which is caused by the pyramid tips which are not covered with SOD. The distributions have a width of 2 – 3  $\mu\text{m}$  and are rather similar. The largest influence on the SOD thickness is the rotational speed. From the data displayed in Fig. 6.10 a) it becomes evident that the thickness of the SOD decreases as  $\omega$  increases. The influence of the texture is shown in Fig. 6.10 b). The average pyramid height of the wafer textured by Bosch Solar is larger than the other textures which

---

<sup>5</sup>Negative values as well as sharp peaks are likely caused by artifacts in the measurement and extraction methods.

## 6. Evaluation of Suitable Laser Doping Parameters

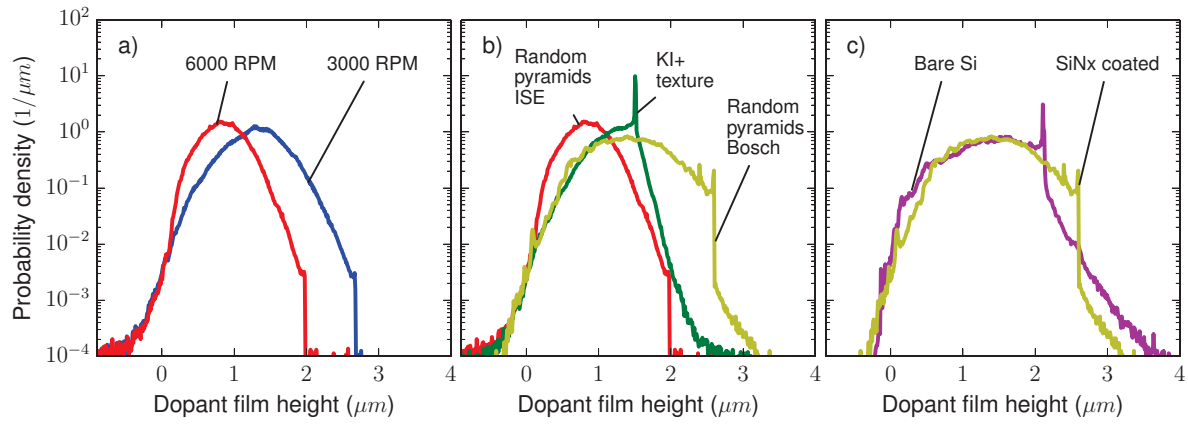


Figure 6.10: Height distributions of  $\text{H}_3\text{PO}_4$  dopant film above the wafer surface. The plots show the influence of different rotational speeds during application (a), different surface textures (b), and  $\text{SiN}_x$  dielectric coating.

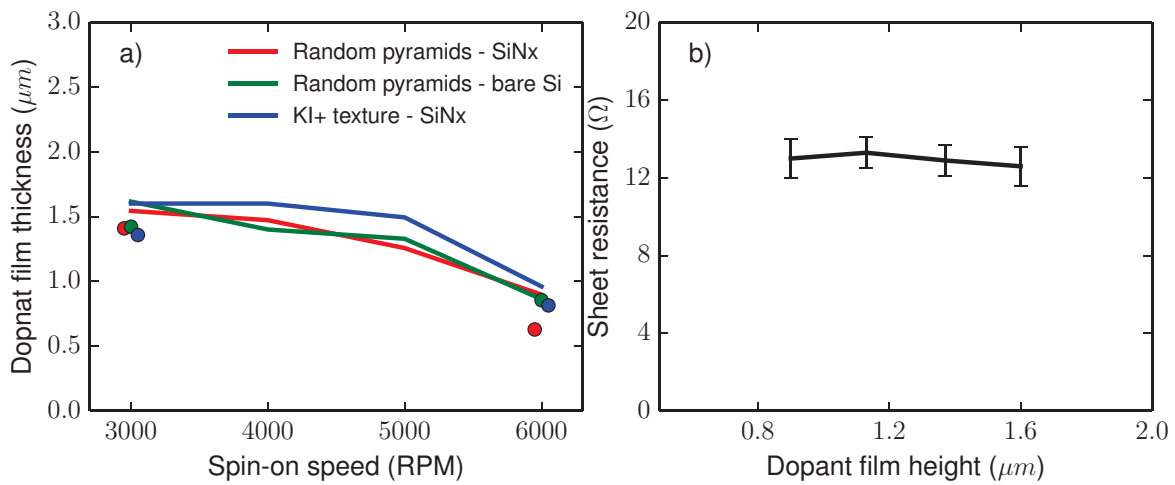


Figure 6.11: Average dopant film thickness as a function of the rotational speed during application for different surfaces (a). The sheet resistance of cw-laser doped silicon as a function of the average film thickness is shown in (b).

results in an increase in dopant film height. The influence of the passivation coating on textured wafers is negligible as shown in Fig. 6.10 c).

The average dopant film thickness is extracted from the height distributions and displayed as a function of  $\omega$  in Fig. 6.11 a). Additionally, the average thickness determined from weighing the wafers is shown in the same plot (solid lines). The two measurement methods are in good agreement and show that the dominating influence on the film thickness is  $\omega$ . By varying  $\omega$  between 3000 and 6000 RPM the average film thickness can be adjusted between 1.6 and 0.9  $\mu\text{m}$ . Figure 6.11 b) shows the sheet resistance of the laser hatched fields as a function of the average dopant film height. From the constant sheet resistance of 13  $\Omega$  it is evident that the dopant incorporation is not dependent on the film thickness in the tested range.

Spin coating of  $\text{H}_3\text{PO}_4$  at 30 wt% allows to adjust the dopant film thickness

in a range of 0.9 to 1.6  $\mu\text{m}$ . At these speeds the tips of a random pyramid texture are not covered with the dopant source. This may present a problem for doping processes with a low linear energy density that only melt pyramid tips (cf. Fig. 6.1 ( $P = 6\text{ W}$ ,  $v = 8\text{ m/s}$ )). In that case the availability of the SOD for doping may be reduced. On the other hand, at intermediate linear energy densities doping is independent of the film thickness. This result shows that a transfer to an industrial coating process should not be limited by a reduced film homogeneity if high throughput tools are used to apply the SOD. The sheet resistance can be adjusted by using higher scanning speeds or by diluting the phosphoric acid with DI-water [162].

### 6.3.2 Depth and Width of Laser Doping

It was shown in the previous section that laser doping with phosphoric acid as a dopant source can create highly doped regions with sheet resistivities as low as  $4\ \Omega$ . In this section the depth profile of the dopant concentration after the LDSE process with the cw-laser and the ns-pulsed laser will be discussed. Furthermore, the junction shape of n-type laser doped lines on a p-type bulk will be analyzed using the electron beam induced current (EBIC) technique.

#### Dopant Profile

In order to measure the dopant depth profile of laser doped silicon two samples have been processed with the cw-laser as well as with the ns-pulsed laser.

A Czochralski (CZ) grown p-type silicon wafer with a random pyramid texture (without  $\text{SiN}_x$  passivation) was spin-coated at 3000 RPM. Two laser doped fields were created on the sample. One was processed using the cw-laser at a scanning speed of 5 m/s at 15 W which results in 14  $\mu\text{m}$  wide lines. The used hatch distance of 5  $\mu\text{m}$  thus corresponds to an line overlap of 64%. The other field was processed using the ns-pulsed laser at a scanning speed of 0.7 m/s, repetition rate of 200 kHz, pulse length 80 ns, and a pulse energy of 20  $\mu\text{J}$ <sup>6</sup>. At a linewidth of 13  $\mu\text{m}$  the hatch distance of 4  $\mu\text{m}$  corresponds to an line overlap of 69%. These values are chosen so that the overlap of the two laser processes is comparable. The dopant profile has been determined for both laser doped fields using the electrochemical capacity-voltage (ECV) profiling technique.

The depth profile of the electrically active dopant concentration is shown in Fig. 6.12. The ns-doping profile has a peak dopant concentration of  $2 \cdot 10^{19}\ \text{cm}^{-3}$  and creates a junction at a depth of 1.5  $\mu\text{m}$  in  $0.5\ \Omega$  material. The sheet resistance calculated from this profile is  $41\ \Omega$  which is in acceptable agreement with the  $51\ \Omega$  measured using the four-point-probe. The cw-doped field has a peak dopant concentration of  $5 \cdot 10^{19}\ \text{cm}^{-3}$  and creates a junction at 4.2  $\mu\text{m}$ . The calculated sheet resistivity of  $11\ \Omega$  is also in acceptable agreement with the measured  $13\ \Omega$  using the four-point-probe.

---

<sup>6</sup>This doping parameter has been determined from a screening test where it appeared optically smooth and had a low sheet resistivity ( $51\ \Omega$ ).

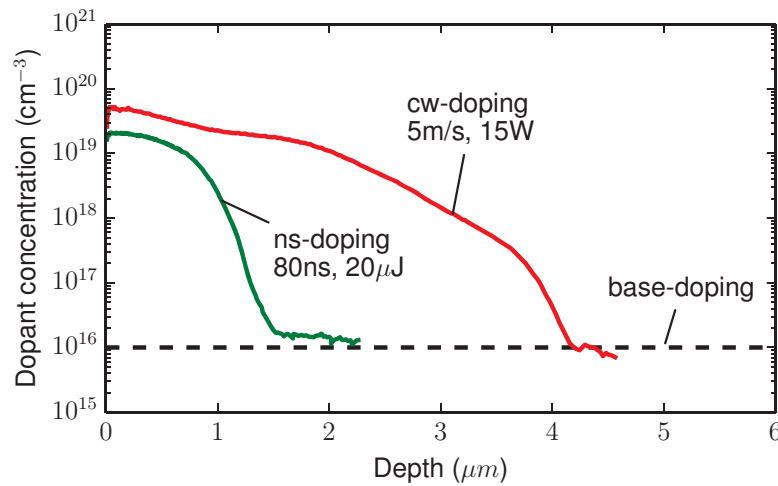


Figure 6.12: Depth profile of the electrically active dopant concentration of cw and ns-pulsed laser doped silicon measured using the ECV technique. From the dopant profile a sheet resistance of  $11 \Omega$  (cw) and  $41 \Omega$  (ns-pulsed) is calculated.

Both laser processes lead to planarization of the pyramid texture due to sufficiently long melt times and allow dopant incorporation to a depth exceeding one micrometer. Nevertheless, the cw-laser driven LDSE process is suitable to create deeper junctions with a higher peak dopant concentration at a faster scanning speed. This is one of the reasons why the cw-laser process is primarily used for selective doping in this work. The second advantage of a cw-laser is connected to the homogeneity and shape of the laser doped structures which will be in the focus of the following section.

### Junction Shape

In order to analyze the cross-sectional shape of the p-n junction after selective cw-laser doping EBIC and microscopy imaging has been employed.

A generic study of the junction shape is complicated by a random pyramid texture. For this reason damage etched wafers with a relatively smooth surface coated with 75 nm  $\text{SiN}_x$  have been used in this experiment. The damage etched surface is sufficiently rough to allow a homogeneous application of the  $\text{H}_3\text{PO}_4$  SOD at 3000 RPM but smooth enough on the micrometer scale to allow a precise measurement of the junction shape. Single laser lines have been drawn with the cw-laser at various scanning speeds ranging from 1 to 9 m/s at 15 W. After this, a cross section of the laser line was prepared and measured using the EBIC technique (cf. Sec. 4.1.4). The corresponding width of the ablated  $\text{SiN}_x$  was measured using the LEXT confocal microscope.

The junction depth created at the different scanning speeds as a function of the lateral position is shown in Fig. 6.13 a). The junction depth decreases from the maximal depth of  $9 \mu\text{m}$  at a slow scanning speed of 1 m/s as the scanning speed increases. The width of the doped area at surface level decreases from its maximum value of  $33 \mu\text{m}$  at  $v = 1 \text{ m/s}$  to  $22 \mu\text{m}$  at  $v = 9 \text{ m/s}$ .

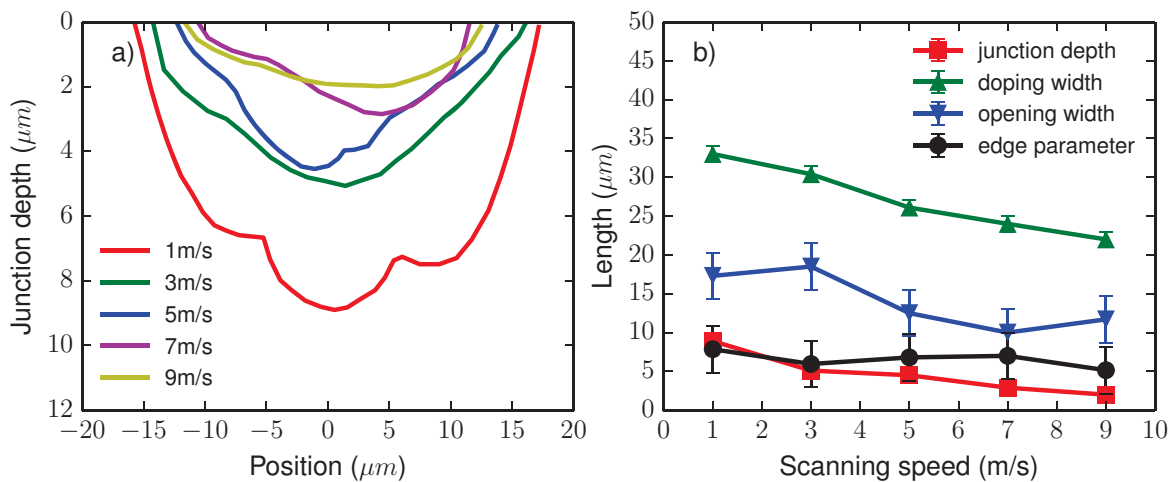


Figure 6.13: Cross-sectional shape of the p-n junction created by cw-laser doping at various scanning speeds (a). The shape of the p-n junction has been determined from EBIC measurements. By comparing the width of the p-n junction at the surface level and microscopic imaging of the  $\text{SiN}_x$  ablation width, a measure of the how far the laser doping extends below the un-ablated  $\text{SiN}_x$  can be defined (cf. Eq. 6.4). This edge parameter (black circles), along with the maximum junction depth (red squares), the doping width at surface level (green triangles), and the width of the ablation opening (inverted blue triangles), is shown as a function of the scanning speed in (b).

Figure 6.13 b) collects a variety of length parameters extracted from the EBIC and LEXT measurements. The red squares represent the maximum depth of the junction and decreases from  $9 \mu\text{m}$  as  $v$  increases. The green triangles represent the width of the doped area on surface level, whereas the blue inverted triangles represent the corresponding  $\text{SiN}_x$  opening width as measured with the microscope. The rather large estimated error of  $3 \mu\text{m}$  in the measurement of the opening width is caused by the fact that the transition from un-irradiated  $\text{SiN}_x$  to complete (optical) ablation is not abrupt, as shown in Fig. 6.2. In all cases the doped width exceeds the width of the  $\text{SiN}_x$  ablation. From the difference between the doping width  $w_d$  and the opening width  $w_o$  the so-called edge parameter is defined by:

$$\Delta_{\text{edge}} = \frac{w_d - w_o}{2}. \quad (6.4)$$

It is a measure of how far below the edge the silicon is doped while still being covered with  $\text{SiN}_x$ . In Fig. 6.13 b)  $\Delta_{\text{edge}}$  is represented by the black circles. In the  $v$  range tested  $\Delta_{\text{edge}}$  is well above  $5 \mu\text{m}$  for all speeds.

The edge parameter is an important measure for a cell concept that relies on simultaneous selective emitter doping, opening of the dielectric layer, and subsequent nickel-copper plating for contact formation. As discussed in detail in Sec. 3.4 the contact resistance and adhesion between silicon and nickel is improved by the formation of a nickel silicide at elevated temperatures. The forming silicide grows into the silicon and if the emitter is not sufficiently deep the p-n junction is shunted. This results in a significant degradation of

cell performance [58]. A deep selective emitter that extends below all contact opening, and thus has a  $\Delta_{\text{edge}} > 0$ , is presumed to prevent this degradation. This point will be in the focus of chapter 9.

Up to fast scanning speeds of 9 m/s the cw-laser driven LDSE process allows doping depths exceeding one micrometer and doping incorporation that extends laterally at least  $5 \mu\text{m}$  below the ablated  $\text{SiN}_x$  layer. These properties, which are desirable for nickel-copper plated solar cells, as well as for cell concepts that benefit from deep selective doping, are driven by melt circulation in the laser molten pool as discussed in Sec. 3.3.

### 6.3.3 Recrystallization Defects

In order to investigate macroscopic as well as microscopic defects in cw-laser treated silicon, samples have been prepared for SEM and TEM analysis. A Czochralski (CZ) grown p-type silicon wafer with a random pyramid texture (without  $\text{SiN}_x$  passivation) was spin-coated at 3000 RPM with  $\text{H}_3\text{PO}_4$ . Individual laser lines have been drawn using the cw-laser at scanning speeds in the range between 1 to 7 m/s and laser output power in the range from 9 to 15 W. All laser lines have been imaged from the top using SEM. For imaging of the cross-section of the laser doped region, selected samples have been prepared using an ion-beam cross-section polisher. For a detailed investigation of crystallographic defects a cross-sectional lamella of a laser line processed at 1 m/s was prepared for TEM analysis. The preparation as well as the TEM measurement was conducted at the Australian National University in the course of a joint research project.

#### Macroscopic Cavity Defects

The top-view SEM investigations using BSE imaging as detailed in Sec. 4.1 allowed to detect buried structures within the remolten silicon. At slow scanning speeds below 3 m/s the formation of cavities in the center of the laser line was observed. An example of the formed cavities at 2 m/s and 15 W is shown in Fig. 6.14 as a cross-sectional view (a) and as a top-view (b). These cavities have a diameter of several micrometers and are fully covered with silicon. Only at scanning speeds below 0.5 m/s the cavities break through the surface and form pits on the laser line. The large cavities are accompanied by smaller sub-micrometer sized cavities which appear closer to the surface. From the top-view (b) a periodicity of the cavity formation is evident. A large number of micrometer sized cavities is observed at scanning speeds of 0.5 m/s at 15 W ( $\varepsilon = 30 \text{ J/m}$ ). With a decrease of the linear energy density ( $\varepsilon$ ) the quantity and size of cavities is reduced. At a scanning speed faster than 2 m/s at 11 W ( $\varepsilon = 5.5 \text{ J/m}$ ) no large cavities in the center of the laser line are observable. Cw-laser doping should be performed at  $\varepsilon$  below this threshold.

The formation of characteristic cavities similar to the ones described above have been observed during keyhole laser welding by many researchers as reviewed

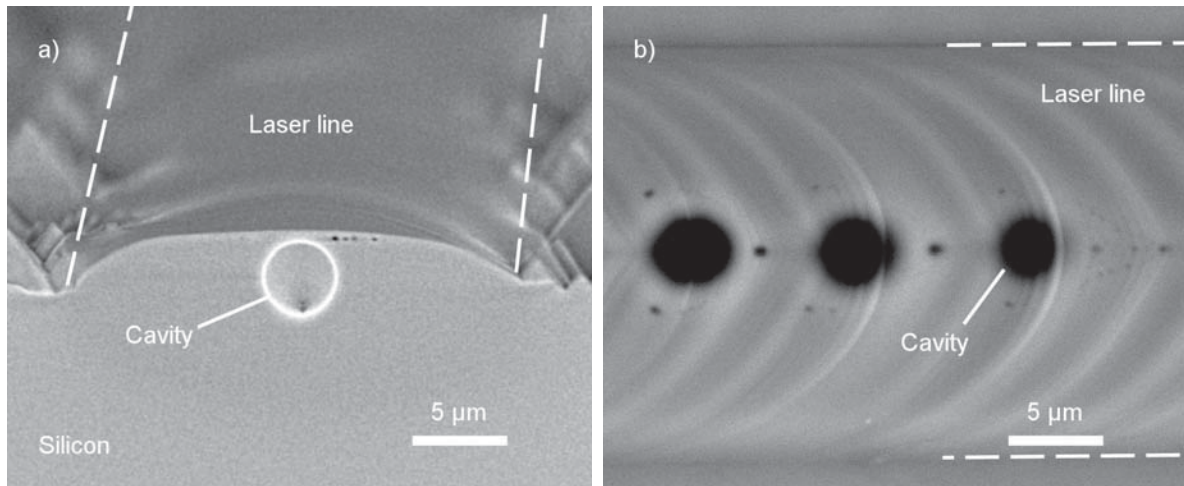


Figure 6.14: Cross-sectional SEM image of a laser line produced at high power (15 W) and slow scanning speed (2 m/s) (a). A micrometer sized cavity is formed in the center of the laser line. A top view SEM analysis (b), using back scatter electron imaging with a primary electron energy of 30 keV, reveals a periodic occurrence of this cavity defect.

in Sec. 3.3.3. In keyhole laser welding the surface is molten by laser irradiation and intense evaporation of the hot metal depresses the molten pool and forms a keyhole. Matsunawa et al. [91] found that large cavities are formed because the evaporation site in the keyhole changes its position with time. They concluded that the vaporization of material induces a recoil pressure which leads to a strong perturbation of the keyhole as well as the whole molten pool and results in the entrapment of gas into the resolidified material.

This conclusion is in agreement with the observed formation of large cavities during laser doping in this work. However, calculations of the surface temperature during LDSE processing by Blecher et al. [89, 90] predict temperatures that are below the boiling point of silicon. It is therefore presumed that surface evaporation is not the only mechanism that causes the keyhole. As discussed in Sec. 3.3.2 also the Marangoni force causes a depression of the molten pool. This depression may serve as a beam trap, effectively decreasing reflection and causing stronger heating than calculated by Blecher et al., who did not include surface deformation into their computer model. The increased heating increases silicon evaporation, deepens the depression, and causes reduced reflection. This runaway effect may lead to perturbations of the keyhole similar to the ones observed by Matsunawa et al. and explain the observed macroscopic cavities in the center of the cw-laser doped line.

Micrometer sized defects are detrimental for the performance of a solar cell. The unpassivated surface of a cavity in the proximity of the p-n junction increases the emitter saturation current of the device. For this reason cw-laser doping should be performed at linear energy densities below  $\varepsilon = 5.5 \text{ J/m}$ . This estimation of the threshold value of cavity formation is independent of the used SOD and valid for an experimental setup with a 532 nm cw-laser with a spot size of about  $15 \mu\text{m}$ .

## TEM Analysis

For the TEM analysis a thin lamella with a thickness of about 100 nm was prepared from a laser line drawn at  $v = 1$  m/s and  $P = 15$  W. For handling of the lamella platinum was deposited on the front side of the sample. The preparation was done using fast gallium ions which lead to the amorphization of the silicon surface up to a depth of about 50 nm. Imaging was performed in the scanning transmission electron microscopy mode of a Philips CM300 TEM at 300 keV yielding a resolution of up to 0.2 nm.

The cross-sectional shape of the p-n junction has been determined in Sec. 6.3.2 and is shown as a schematic in Fig. 6.15 a). In this schematic the position of the  $10 \times 5 \mu\text{m}^2$  lamella, covering half of the laser line width and about  $5 \mu\text{m}$  of the depth of the doped region, is highlighted. An overview<sup>7</sup> of the lamella is shown in (b). The diffraction pattern measured at the point marked “D1” proves that the recrystallized silicon has the same orientation as the crystalline bulk ( $\langle 110 \rangle$ ). Irregularities in the silicon crystal appear in the center of the laser line up to a depth of about  $1 \mu\text{m}$ . Figure 6.15 c) shows a close-up of this region. Here four dislocation loops (marked “L”) are located at depths between 0.5 and  $1.1 \mu\text{m}$ . A thin area close to the surface that is separated by an irregular boundary from the silicon bulk exhibits a change in contrast. Close-ups of the surface region are shown in (d). Analysis of the diffraction pattern at the point “D2” proves that the region between the “T” marks is twinned with respect to the bulk. The twinned region exhibits a channeling contrast compared to the bulk, due to the difference in crystal orientation. The inset in (d) shows that the boundary between the twinned regions is decorated with tear drop shaped voids (marked “V”). The larger voids have a length of about 135 nm and a width of about 65 nm. EDX measurements did not show a significant difference in composition between the twinned surface region (marked “E1”) and the bulk silicon (marked “E2”).

## Twinning

Twinning in the recrystallized silicon could be observed for all recrystallization velocities up to scanning speeds of 7 m/s by channeling contrast imaging using top-view SEM. Single laser lines were produced on CZ grown silicon covered with 75 nm  $\text{SiN}_x$ <sup>8</sup> using a cw-laser spot with  $P = 15$  W traveling in a direction equivalent to the  $\langle 100 \rangle$  crystal orientation.

An example of the channeling contrast image for a laser line produced at  $v = 3$  m/s is shown in Fig. 6.16 a). The schematic presented in (b) illustrates the contrast in the SEM image (a) to improve the readability of the channeling contrast information. The experimental data schematically summarized in Fig. 6.17 indicates that the twin quantity and quality of twinning depends

<sup>7</sup>Figure 6.15 b) and (c) are composed from multiple TEM images by image stitching.

<sup>8</sup>pre-tests showed that the formation of twins is independent of the presence of a  $\text{SiN}_x$  layer during laser doping

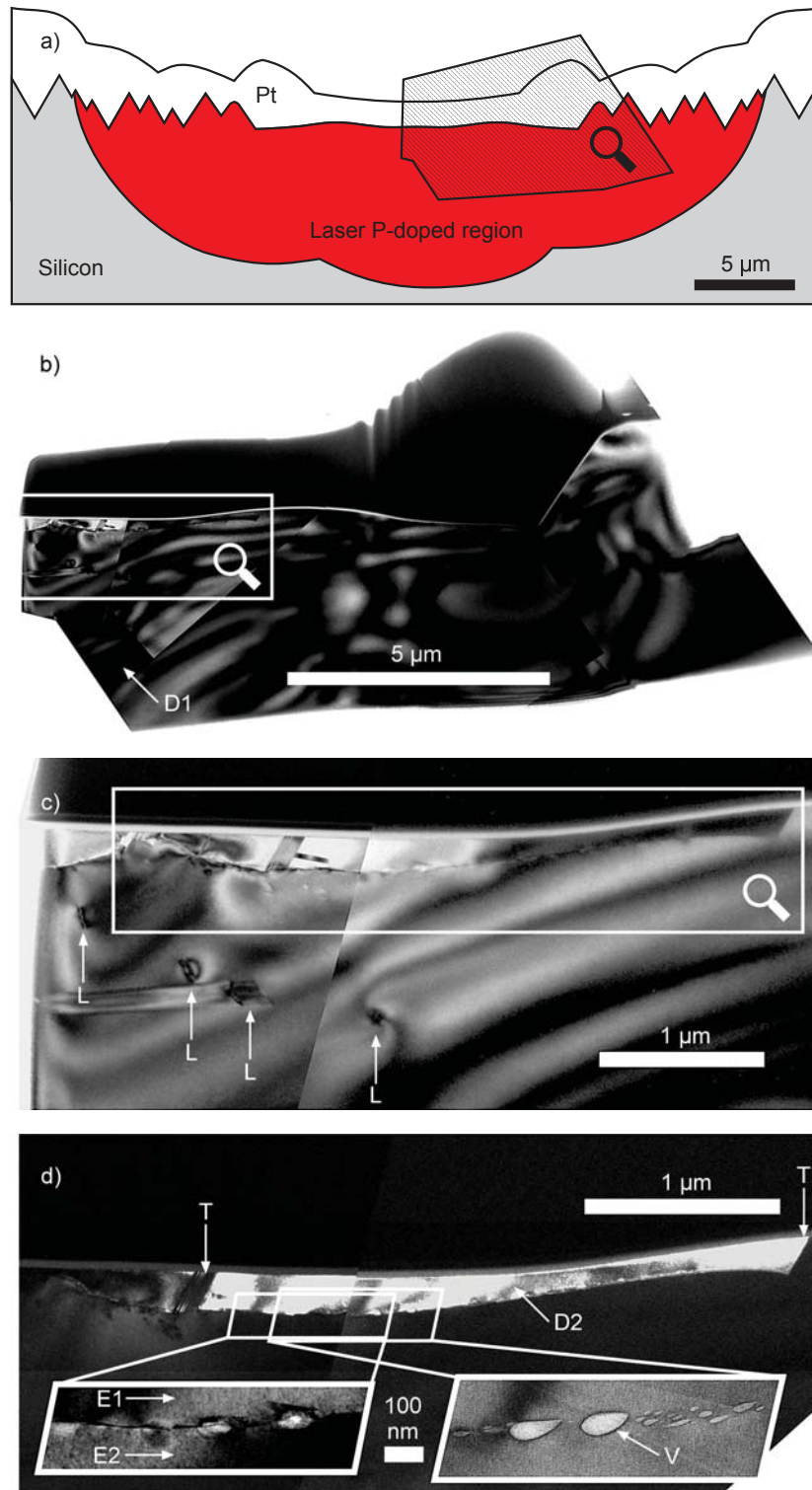


Figure 6.15: Schematic of cross-section of a laser doped line (a), highlighting the region from which a TEM lamella (b) was prepared. The analysis of the diffraction pattern at the point “D1” showed epitaxial recrystallization. A close-up of the central region (c) reveals four dislocation loops (“L”) and a thin surface region exhibiting a channeling contrast. Diffraction pattern taken from point “D2” in the close-up on the surface region (d) reveals that the bright region between the “T” marks is twinned with respect to the bulk. The insets in (d) are magnifications (100 nm scale bar) of the boundary between the twinned regions. This boundary is decorated with voids (“V”). EDX measurements at “E1” and “E2” showed no significant difference in composition.

## 6. Evaluation of Suitable Laser Doping Parameters

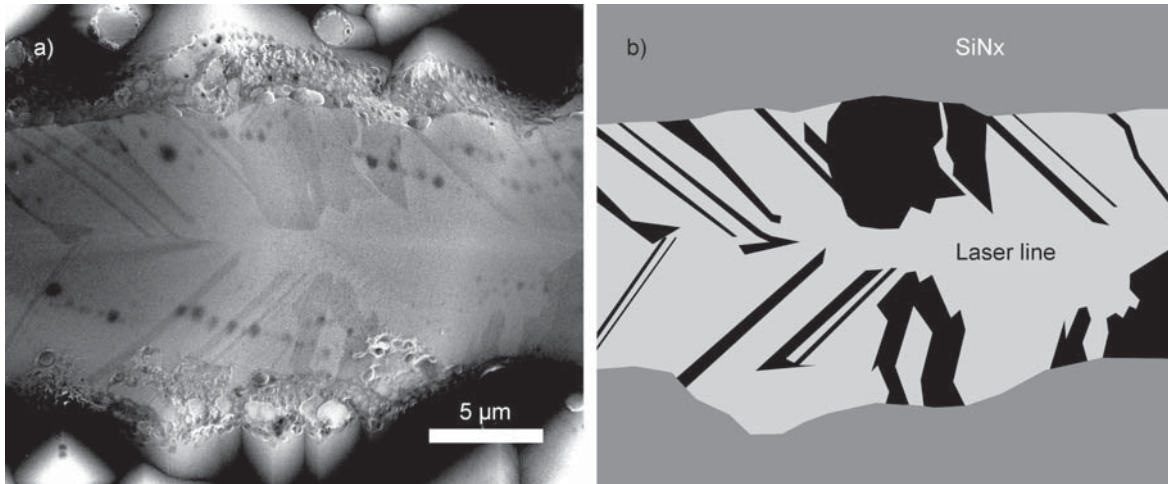


Figure 6.16: Top view SEM image of a laser line produced at intermediate scanning speed ( $v = 3 \text{ m/s}$ ,  $P = 15 \text{ W}$ ) exhibiting a channeling contrast (a). Illustration of this contrast to improve readability (b).

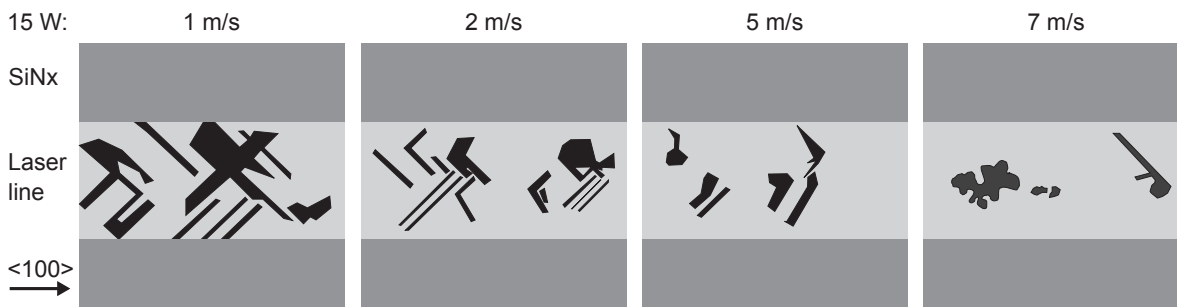


Figure 6.17: Schematic of the change in the quantity and quality of formed twin boundaries due to a change in the cw-laser scanning speed. The schematics have been extracted from SEM images similar Fig. 6.16. The lines were processed on CZ silicon with an output power of 15 W. The scanning direction was to the right, equivalent to the  $\langle 100 \rangle$  crystal direction. Regions that appeared darker in the SEM image (due to channeling contrast) have been redrawn black in this schematic.

on the scanning speed. Slow  $v$  produce more twin boundaries than fast  $v$ . On the other hand, the twin boundaries at fast  $v$  appear not as ordered and symmetrical. The contrasting regions, having a different crystal orientation, at  $v = 7$  m/s do not have straight boundaries parallel to crystal orientations of high symmetry. From the channeling contrast imaging alone these fringed crystallites at high  $v$  cannot be decisively identified as twins.

The orientation of the elongated twinned crystallites similar to the direction of the recrystallization. This can be compared to the observation of elongated polycrystalline growth by Gat et al. [101] using laser remelting of amorphous silicon. By using particular beam shapes, such as a doughnut-shaped beam, the occurrence of twinning or the formation of crystallites in general may be reduced, as detailed in Sec. 3.3.4

However, the TEM analysis presented in the previous section showed that at  $v = 1$  m/s twinning appears in the top 200 nm of the recrystallized material. It is presumed that also at higher  $v$  twinning is restricted to shallow regions of the recrystallized silicon. These twinning defects close to the highly recombinative surface, which will be the surface of the metal plated contacts, should have a minute effect on the emitter saturation current density.

## 6.4 Suitable Laser Doping Parameters

At the beginning of this chapter a list of requirements on an industrial laser doping process has been outlined. The investigations presented in the main part of this chapter allow pointing out process parameters that are especially suited for the production of solar cells with laser doped contacts openings and nickel-copper plated contacts.

One requirement for a suitable laser process is that the dielectric is fully ablated and that the underlying surface is well conditioned for nickel plating. Effective  $\text{SiN}_x$  ablation and reliable nickel deposition using a ns-pulsed laser was shown by Sauaia-Lopes [160] using the same setup. However, solar cells produced by Sauaia showed severe degradation after thermal nickel silicide formation. To circumvent nickel induced shunting of the p-n junction, the investigations focused on using a cw-laser for dielectric ablation and selective doping.

Using this cw-laser, well defined and narrow lines of ablated  $\text{SiN}_x$  were produced using a spot size of  $15 \mu\text{m}$  at linear energy densities above  $3 \text{ J/m}$  ( $v = 5$  m/s,  $P = 15$  W). After difficulties with electroless plating, bias-assisted light-induced plating on laser lines created at intermediate scanning speeds ( $3 - 5$  m/s) and a moderate to high output power ( $9 - 15$  W) resulted in homogeneous coverage of the  $\text{SiN}_x$  ablated silicon with nickel. A surface analysis indicated that at higher scanning speeds the  $\text{SiN}_x$  dielectric is not fully ablated, whereas an oxidized species on the silicon surface hinders nickel deposition at slow scanning speeds. The existence and composition of such a parasitic surface layer will be investigated in chapter 8.

Laser doping with phosphoric acid as a dopant source resulted in sheet resistances as low as  $11 \Omega$  at an intermediate scanning speed ( $v = 5 \text{ m/s}$ ,  $P = 15 \text{ W}$ ). It was shown that the thickness of this dopant source has little influence on the resultant sheet resistivity, which facilitates industrial implementation of the dopant application. Due to convection driven dopant mixing in the molten silicon pool during cw-laser processing, p-n junction depths of up to  $9 \mu\text{m}$  have been measured. At a scanning speed of  $5 \text{ m/s}$  and  $P = 15 \text{ W}$  the p-n junction had a depth of about  $4 \mu\text{m}$ . The convective fluid flow and the indirect ablation of the  $\text{SiN}_x$  layer results in doping of silicon which is still covered with  $\text{SiN}_x$ . Independent on the scanning speed, the laser doped region extends at least  $5 \mu\text{m}$  below the edge of the  $\text{SiN}_x$  opening. It is presumed that this property may prevent device degradation by deep nickel silicide growth. This point will be in the focus of chapter 9.

Macroscopic and microscopic defects introduced by laser doping have been observed using SEM and TEM imaging. Micrometer sized cavities probability introduced by fluctuating keyhole formation appear at linear energy densities above  $\varepsilon = 5.5 \text{ J/m}$ . TEM imaging showed that cw-laser treated silicon recrystallized mostly single crystalline with dislocation defects and twinning in the center of the laser line up to a depth of  $1 \mu\text{m}$ . Twinning is found to decrease with scanning speed. Due to the proximity of these crystal imperfections to the highly recombinative metal contact the impact on device performance is presumed to be minute. A detailed investigation in terms of the emitter saturation current density of a laser doped emitter will be conducted in the following chapter.

Considering the aforementioned requirements, a process based on a cw-laser seems a promising tool for the creation of highly doped contact openings for solar cells with nickel-copper plated contacts. Laser doping of silicon from phosphoric acid (30 wt%) at a scanning speed of  $5 \text{ m/s}$  and an output power of  $15 \text{ W}$  using a spot size of  $15 \mu\text{m}$  appears to be a suitable baseline parameter set for the detailed investigations conducted in the following chapters.

## 7 Cavity Defects in Laser Doped Silicon

In this chapter the  $\text{SiN}_x$  ablation mechanism of cw-laser processing and the impact of the simultaneous doping on effective charge carrier lifetimes will be investigated.

During cell production laser doping is usually performed after the deposition of the  $\text{SiN}_x$  dielectric [18, 23, 77] but can alternatively be performed before  $\text{SiN}_x$  deposition [124, 125]. In recent years many groups have combined the selective laser doping and selective laser ablation into a single process step [77, 78, 163]. Doing so, Hameiri et al. [16] have observed that emitter quality is reduced if  $\text{SiN}_x$  ablation and doping are combined into a single step. It is assumed that this is caused by a thermal expansion mismatch between  $\text{SiN}_x$  and silicon. The advantage of laser processing after dielectric deposition is simultaneous and self-aligned selective dielectric ablation and laser doping. If the laser doping is performed before dielectric deposition an additional process step for the patterning of the dielectric is needed. In order to calculate which processing sequence yields higher solar cell efficiencies or better cost-effectiveness, the impact of the presence of a dielectric coating during laser doping on the emitter recombination needs to be understood and precisely measured.

In the following the  $\text{SiN}_x$  ablation mechanism and its impact on emitter recombination will be studied. It will be shown that great care needs to be taken if recombination properties are to be measured using asymmetric samples and lifetime-testers based on xenon flash illumination, which are common in laboratory and production environments. It will be demonstrated that the presence of a  $\text{SiN}_x$  layer promotes the formation of cavities within the re-solidified silicon and significantly increases the emitter saturation current density. As a last point a model will be presented that explains the observed cavity formation and lifetime reduction in cw-laser processing. The proposed mechanism explains the dielectric ablation and considers defect formation beyond induced stress by a thermal expansion mismatch.

### 7.1 Development of a Precise Method for $j_{0e}$ Determination

In this section a method is developed that allows the precise determination of rather high emitter saturation current densities  $j_{0e}$  from QSSPC measurements on asymmetrical lifetime samples. For this, the continuity equation of the steady-state excitation by a xenon spectrum is solved. This newly developed method will be called “CESS-method”. At first, the proposed method is checked for self-consistency and validated by comparison of the calculated values to experimental data and device simulation. After that, the CESS-method will be

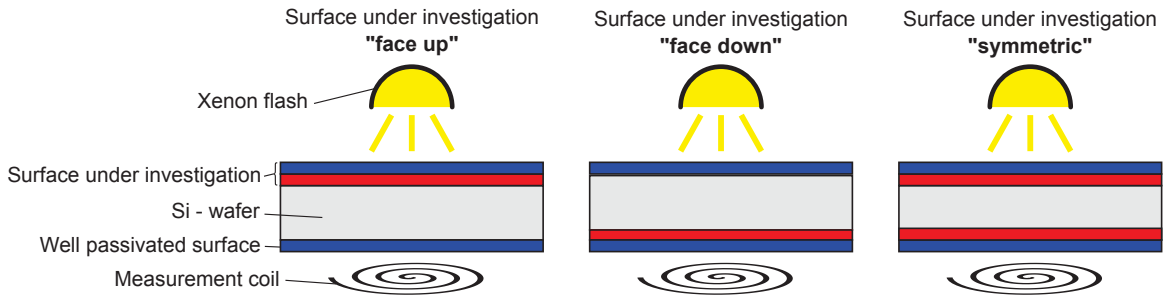


Figure 7.1: Schematic and notation of QSSPC measurement configurations.

compared to widely used approximations. The new method will then be used in the Sec. 7.3 to determine the  $j_{0e}$  of the laser doped emitters.

### 7.1.1 Asymmetric Lifetime Samples

The samples that will be studied in detail in this chapter have different emitters on the front and on the rear side of the wafer. Some of the samples have surfaces that are passivated with a dielectric layer. In the context of this recombination analysis the contributions to the recombination from the volume of the emitter and from the surface of the semiconductor are expressed via a single parameter. This is either the emitter saturation current density  $j_{0e}$  or the associated surface recombination velocity  $S$ .

For wafers with an emitter the surface recombination velocity at an imaginary surface at the base side of the space charge region is equivalent to the recombination current density in the emitter [164]:

$$S = j_{0e} \frac{N_a + \Delta n}{qn_i^2}. \quad (7.1)$$

Since the excess charge carrier concentration is known from the QSSPC measurement (cf. Sec. 4.4) and  $N_a$  can be determined from the base resistivity of the wafer material, the  $j_{0e}$  and  $S$  carry the same information and can therefore be used interchangeably. As a result the asymmetric samples can be thought of having two different surface recombination velocities  $S_0$  and  $S_W$  representing the front and the back, respectively.

The intention of using asymmetrical samples is to increase the effective lifetime of the excess charge carriers. This is achieved because one of the surfaces can be a well passivated high-efficiency emitter with a low (and possibly known)  $S$  while the other side is the surface under investigation. Although the recombination at the surface under investigation may be substantial, the effective lifetime is still rather long since the other surface contributes little to the recombination of charge carriers.

Figure 7.1 shows three different measurement configurations for the determination of the recombination properties of the surface under investigation. The

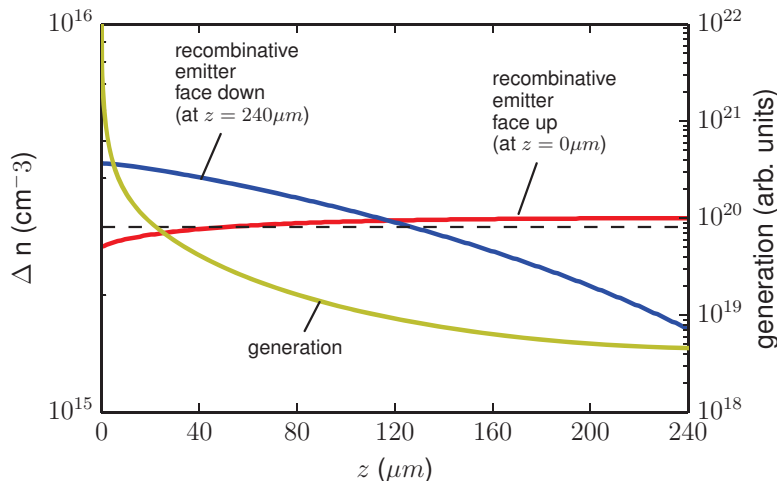


Figure 7.2: Excess charge carrier density (red and blue line) and the generation caused by a xenon lamp (yellow line) as a function of the distance from the surface top, as simulated using PC1D [165]. The red line represents the charge carrier profile if the recombinative surface is face-up and the blue line represents the face-down case. If a high generation rate coincides with high recombination, as in the face-up case, the charge carrier profile is fairly constant at a level of  $3 \cdot 10^{15} \text{ cm}^{-3}$  (dashed line). If the sample is measured face-down the assumption of a constant profile becomes inaccurate.

sample is measured “face-up” if the highly recombinative surface under investigation is facing the xenon flash and “face-down” if the sample is flipped around so the well passivated surface faces the flash. If the sample is symmetrically processed and the surface at the front and the rear have similar properties the measurement configuration will be denoted “symmetric”.

### Excess Charge Carrier Profile

Figure 7.2 displays  $\Delta n(z)$  profiles simulated using PC1D [165] of a sample in the “face-up” and “face-down” measurement condition that is illuminated with a xenon light source. For both configurations the intensity of the steady-state illumination is chosen in a way that an average excess charge carrier concentration  $\Delta n_{av}$  of  $3 \cdot 10^{15} \text{ cm}^{-3}$  is achieved. The red line in Fig. 7.2 represents the configuration where the recombinative structure ( $S = 1800 \text{ cm/s} \hat{=} j_{0e} = 1100 \text{ fA/cm}^2$ ) is facing the xenon flash. This  $\Delta n$  profile is relatively constant throughout the depth of the sample. In contrast to this, the  $\Delta n$  profile of the sample in the “face-down” configuration, represented by the blue line, decreases from  $4.3 \cdot 10^{15} \text{ cm}^{-3}$  at the front to  $1.6 \cdot 10^{15} \text{ cm}^{-3}$  at the rear side. This is the configuration where the well passivated structure is facing the flash and the recombinative structure is at the rear.

### Orientation Dependent Effective Lifetime

The effective minority charge carrier lifetime ( $\tau_{\text{eff}}$ ) during steady-state excitation is given by the ratio between the cumulative excess charge carrier density and

the generation rate.

$$\tau_{\text{eff}} = \frac{\int_0^W dz \Delta n(z)}{\int_0^W dz g(z)}. \quad (7.2)$$

The resulting lifetimes of the two samples, shown in Fig. 7.2, differ substantially with apparent longer lifetime in the sample with the well passivated structure facing the flash ( $18 \mu\text{s}$  vs.  $31 \mu\text{s}$ ). The reason for this can be put down to the non-uniform generation profile  $g(z)$ . Generation at the front  $g(0)$  is significantly larger than  $g(W)$ . If the highly recombinative surface is at the front,  $\tau_{\text{eff}}$  will be reduced compared to the case where most of the charge carriers are generated at the front side but need to diffuse through the bulk to recombine at the recombinative surface at the rear.

### 7.1.2 CESS-Method

Measuring the cumulative excess charge carrier concentration of a sample under steady-state photoexcitation allows to determine the effective lifetime. This is commonly done by using a QSSPC lifetime tester as described in Sec. 4.4.2. The relation between effective charge carrier lifetime, bulk and surface recombination was detailed in Sec. 4.4.4 by solving the transport equation of excess charge carrier under monochromatic steady-state illumination. In the following this relation will be used to extract recombination properties of interest from QSSPC measurements.

The continuity equation for the steady-state excitation with a monochromatic light source was solved in Sec. 4.4.4. With the use of Eq. 4.21 the excess charge carrier density ( $\Delta n_\lambda$ ) can be calculated for monochromatic excitation with a given ambipolar diffusion constant  $D$ , bulk lifetime  $\tau_B$ , absorption coefficient  $\alpha_\lambda$ , photon flux  $j_\lambda$ , sample thickness  $W$  as a function of the surface recombination velocities  $S_0$  and  $S_W$ :

$$\Delta n_\lambda(z) = \Delta n_\lambda(z, S_0, S_W). \quad (7.3)$$

In order to determine  $\Delta n(z)$  during illumination with a broad spectrum of wavelengths, as it is the case in the QSSPC measurement setup, the monochromatic solutions can be superposed:

$$\Delta n(z, S_0, S_W) = \sum_\lambda \Delta n_\lambda(z, S_0, S_W). \quad (7.4)$$

Accordingly, the total generation becomes:

$$g(z) = \sum_\lambda g_\lambda(z), \quad (7.5)$$

where  $g_\lambda(z)$  is given by the Beer-Lambert law (cf. Sec. 2.2). The absorption coefficient  $\alpha_\lambda$  is a material property and  $j_\lambda$  can be found from spectral irradiance

measurements of the light source. By solving the continuity equation for steady-state excitation the effective lifetime can be calculated for any combination of  $S_0$  and  $S_W$ :

$$\tau_{\text{eff}}(S_0, S_W) = \frac{\int_0^W dz \Delta n(z, S_0, S_W)}{\int_0^W dz g(z)}. \quad (7.6)$$

This calculation incorporates the finite mobility of the minority charge carriers as well as the inhomogeneous generation profile. The method of relating the surface recombination velocity to effective charge carrier lifetime measurements by solving the continuity equation under steady-state excitation will be denoted “CESS-method” in the following.

In the case of a symmetric sample ( $S_0 = S_W$ )  $\tau_{\text{eff}}$  can be determined from a simple QSSPC measurement. In the case of an asymmetric sample, the sample may be measured twice, in the face-up and in the face-down configuration. This is equivalent to exchanging  $S_0$  and  $S_W$  in Eq. 7.6. Adjusting  $S_0$  and  $S_W$  until the analytic calculation matches the measured  $\tau_{\text{eff}}$  allows to determine  $S_0$  and  $S_W$ . In the recombination analysis in Sec. 7.3.1,  $S$  of the well passivated emitter is determined from a symmetrical sample as a first step. Then  $S$  of the emitter under investigation is determined from a measurement on an asymmetric sample, where one surface is the well passivated emitter with the known  $S$  from the first step.

### Validation of the CESS-Method

In this section the CESS-method, described above, is validated by comparison of  $\tau_{\text{eff}}$  values calculated with the method to numerical simulation using PC1D [165] and experimental data.

At first, the effective lifetime  $\tau_{\text{eff}}$  of a sample with one perfectly passivated surface ( $S = 0$  cm/s) and one imperfect surface ( $S > 0$  cm/s) has been simulated under low level injection (LLI) conditions with PC1D and is compared to the calculated values using the CESS-method. The result is shown in Fig. 7.3 for the face-down and face-up measurement configurations. The simulated values were precisely reproduced with the largest deviation between the simulated and the calculated  $\tau_{\text{eff}}$  values being 4% at  $S=256$  cm/s.

Figure 7.4 displays the injection dependent effective charge carrier lifetime of an existing sample, measured using the QSSPC technique. One side of the sample was covered with a laser doped emitter and the other side was well passivated. The well passivated side had a low surface recombination velocity of 30 cm/s<sup>1</sup>. The laser doped side, which is the surface under investigation, will be characterized by the surface recombination velocity  $S$ .

As mentioned before the apparent lifetime varies depending on the orientation of the sample. The sample measured face-up (face-down) has a effective lifetime of 18.9  $\mu\text{s}$  (30.9  $\mu\text{s}$ ) at  $\Delta n_{\text{av}}$  of  $3 \cdot 10^{15}$  cm<sup>-3</sup>. This orientation dependence is

---

<sup>1</sup>This value was extracted from symmetric lifetime samples.

## 7. Cavity Defects in Laser Doped Silicon

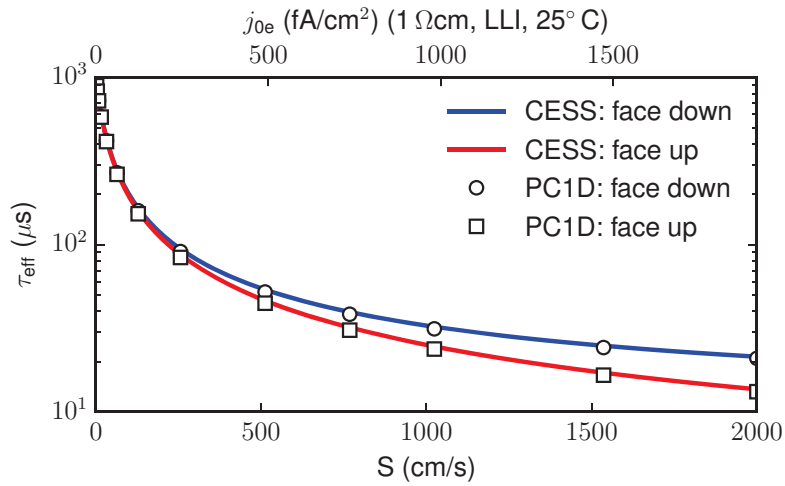


Figure 7.3: Effective lifetime  $\tau_{\text{eff}}$  of an asymmetric lifetime sample simulated using PC1D [165] and the CESS-method. One side of the sample is well passivated ( $S = 0 \text{ cm/s}$ ), the other side is characterized by the surface recombination  $S$  plotted on the abscissa. The sample has been simulated (calculated) using  $1 \Omega\text{cm}$  p-type material under low level injection (LLI) conditions. The corresponding emitter saturation current density  $j_{0e}$  was calculated at  $25^\circ\text{C}$ .

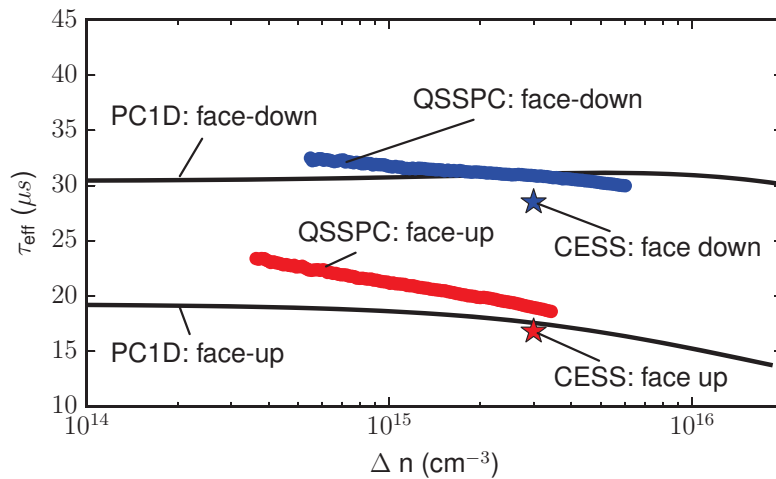


Figure 7.4: Injection dependent effective lifetime  $\tau_{\text{eff}}$  determined from measurement (colored data points), PC1D simulation (solid lines), and from calculation using the CESS-method (stars) for the case of a face-up (red) and face-down (blue) sample orientation. The calculated  $\tau_{\text{eff}}$  are within an error margin of 10% from the measured data and simulation.

also observed in the simulated data using the xenon spectrum for illumination. The reflection and absorption properties of the anti-reflection coating as well as other effects of the random pyramid texture is incorporated into the simulation. The  $j_{0e}$  of the simulated laser doped emitter is tuned to match the measured data as close as possible. The best match is achieved at with  $S = 1800\text{cm/s}$  at the laser doped surface. The simulation with this  $S$  value returned  $\tau_{\text{eff}} = 17.6\ \mu\text{s}$  ( $31.1\ \mu\text{s}$ ) for the face-up (face-down) configuration. The effective lifetime of a sample with  $S = 1800\text{cm/s}$  calculated with the CESS-method is  $\tau_{\text{eff}} = 16.8\ \mu\text{s}$  ( $28.5\ \mu\text{s}$ ) for the face-up (face-down) configuration. The orientation dependence of the calculated  $\tau_{\text{eff}}$  is consistent with the measured values.

This discussion indicates that the CESS-method is fairly reliable even in the case of highly recombinative surfaces with  $S$  as high as  $2000\text{cm/s}$  and small charge carrier lifetimes. The calculation of the emitter saturation current from the effective lifetime using the continuity equation is within an error of 10% from the simulated and measured data, which is considered acceptable. In Sec. 7.3.2, this method will be used to extract the emitter saturation current density of laser doped emitters from QSSPC measurements.

### 7.1.3 Uniform Charge Carrier Approximation

In order to extract the emitter saturation current density  $j_{0e}$  from QSSPC measurements of the effective lifetime  $\tau_{\text{eff}}$  the following simplified relation is commonly used [166]:

$$\frac{1}{\tau_{\text{eff}}} = \frac{1}{\tau_B} + \frac{N_a (j_{0e,0} + j_{0e,W})}{qWn_i^2}, \quad (7.7)$$

with  $j_{0e}$  of the front ( $j_{0e,0}$ ) and rear side ( $j_{0e,W}$ ). This expression is accurate if the excess charge carrier density is independent of the position within the wafer:  $\Delta n(z) \approx \text{const.}$  [167]. Equation 7.7 can be expressed in terms of  $S$  using Eq. 7.1:

$$\frac{1}{\tau_{\text{eff}}} = \frac{1}{\tau_B} + \frac{N_a}{N_a + \Delta n} \frac{(S_0 + S_W)}{W}, \quad (7.8)$$

For the experimental data analyzed in this chapter the error introduced by this approximation turned out to be significant, exceeding 30%. If the uniform charge carrier approximation is used to determine  $S$  from the measurements presented in Fig. 7.4 the result would be  $S = 1216\text{cm/s}$  if the sample is measured in the “face-up” configuration and  $S = 723\text{cm/s}$  if the sample is measured “face-down”. These values are not self-consistent and significantly smaller than the  $S = 1800\text{cm/s}$  determined by comparing measured  $\tau_{\text{eff}}$  with PC1D simulations.

The systematic error introduced by Eq. 7.7 can be circumvented by solving the continuity equation (Eq. 4.18) for the case of steady-state excitation as shown above. However, due to the common usage and simple application of Eq. 7.7 the deviation between the CESS-method and this approximation will be examined in the following.

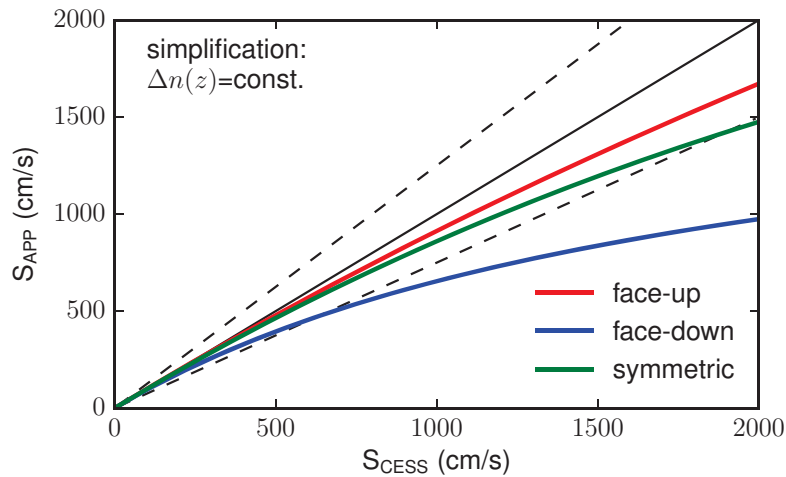


Figure 7.5: Calculated surface recombination velocity ( $S_{APP}$ ) using the constant charge carrier approximation as a function of  $S$  used in the solution of the continuity equation ( $S_{CESS}$ ). For every  $S_{CESS}$  the effective lifetime is calculated from Eq. 7.2, and from this  $S_{APP}$  is determined using Eq. 7.7. As  $S_{CESS}$  increases, the approximation of  $S_{APP}$  assuming a constant charge carrier profile becomes increasingly inaccurate.

### Difference Between Approximation and Analytic Solution

If emitter recombination is analyzed with QSSPC lifetime measurements that are evaluated according to Eq. 7.7, neither the finite mobility of the minority charge carriers nor the breakage in symmetry by the one sided illumination is accounted for. As a result of the finite mobility the  $S$  value of the recombinative emitter under investigation is underestimated in any measurement configuration (face-up, face-down, or symmetric). The asymmetry in illumination increases this effect if the structures are measured face-down.

Figure 7.5 shows this systematic deviation between the uniform charge carrier approximation and the CESS-method as a function of the surface recombination velocity of the surface under investigation. The plotted data has been calculated by solving the continuity equation as described in Sec. 4.4.4 with the generation profile of a xenon light source and the boundary conditions according to the measurement configuration (face-up, down, or symmetric). The surface recombination velocity of the surface under investigation is plugged into the according boundary condition as an independent variable. This is the  $S_{CESS}$  of the CESS-method. In the following  $S_{CESS}$  will be treated as an unbiased method to determine the true surface recombination velocity, hence serving as a benchmark for simpler approximation. From the resultant  $\Delta n(z)$  profile the effective charge carrier lifetime  $\tau_{eff}$  has been calculated according to equation 7.2. Then  $S$  of the surface under investigation has been calculated from  $\tau_{eff}$  using the approximation Eq. 7.7. This is denoted  $S_{APP}$ . The black diagonal represents the case where the approximated  $S_{APP}$  is accurate. The dashed lines represent a measurement error of 25%.

From the calculation it is evident that the relative error increases with the recombination velocity. In all measurement configurations the  $S_{APP}$  has an

error less than 25% if  $S_{CESS}$  is below 500 cm/s (300 fA/cm<sup>2</sup>). If surfaces with a higher surface recombination velocity are measured facing down, the approximation of a constant  $\Delta n(z)$  profile is not suitable to determine  $S$  (or  $j_{0e}$ ). The domain where the approximation is valid is extended by measuring face-up or processing the wafer symmetrically. In these cases high generation and high recombination appear at the same surface. The proximity of creation and recombination of charge carriers partly compensates the effect of finite mobility of the minority charge carriers and leads to a  $\Delta n(z)$  profile which is relatively constant. This effect has been shown for the sample measured face-up in Fig. 7.2. As a result the sample measured face-up shows the smallest deviation from the CESS-method.

### Validity Domain of the Approximation

The  $\Delta n(z)$  profile depends on a variety of material, wafer, and measurement parameters that influence the domain in which the simplified relation of Eq. 7.7 is applicable. For the data in figure 7.5 a 240  $\mu\text{m}$  thick 1  $\Omega\text{ cm}$  p-type fz-silicon wafer with a diffusion coefficient  $D$  of 21.9 cm<sup>2</sup>/s at  $\Delta n_{av}$  of  $3 \cdot 10^{15}\text{ cm}^{-3}$  has been assumed. The bulk lifetime  $\tau_B = 1\text{ ms}$  is determined by the auger recombination [168] in the doped base material. The light source has been an unfiltered xenon lamp [169].

By altering these base line parameters in the calculation the influence of  $D$ ,  $\tau_B$ ,  $W$ , and the spectrum of the light source were studied. In the following the primal findings are summerized:

- The influence of the diffusion coefficient is small. Although the finite mobility is the primal cause for the failure of Eq. 7.7, the range of the ambipolar diffusion coefficient in silicon is limited to about 10 – 25 cm<sup>2</sup>/s. Nevertheless, a high value of  $D$  slightly reduces the systematic error.
- The effect of the bulk lifetime  $\tau_B$  is also small for ranges typical for silicon wafers.  $\tau_B$  has to be reduced to 50  $\mu\text{s}$  to observe a significant effect. At this short bulk lifetime the generated charge carrier within the depths of the sample cannot reach the surfaces. As a side effect, the measurement face-up improves slightly.
- The thickness of the sample  $W$  influences the accuracy of the calculation substantially. For very thin samples of 120  $\mu\text{m}$  the domain of acceptable error (< 25 %) extends up to  $S = 1000\text{ cm/s}$ . Accordingly, the systematic error increases with the thickness of the wafer.
- The spectrum of the excitation source has only a minute effect on the accuracy of the estimation of  $S$  from  $\tau_{\text{eff}}$ . As mentioned above, not the inhomogeneous illumination is the primal cause for the systematic error but the finite mobility of the minority charge carriers. For samples measured face-up, the inhomogeneous illumination is rather beneficial.

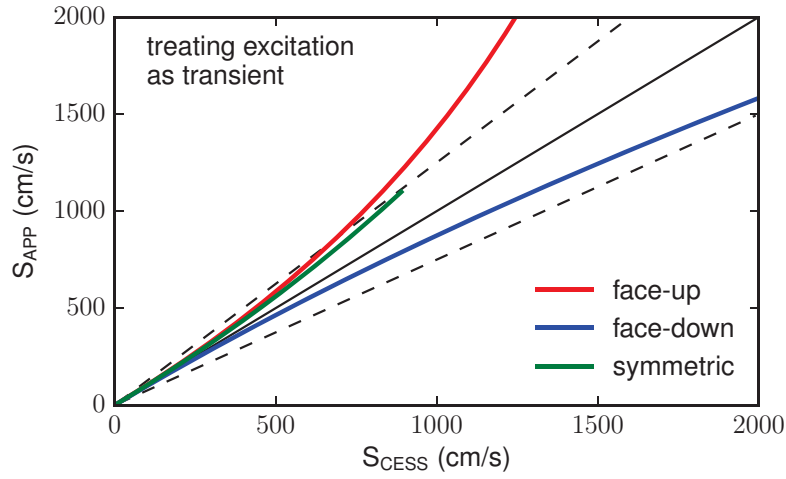


Figure 7.6: Calculated surface recombination velocity ( $S_{APP}$ ) using the transient excitation approximation as a function of  $S$  used in the solution of the continuity equation ( $S_{CESS}$ ). For every  $S_{CESS}$  the effective lifetime is calculated from Eq. 7.2 and from this  $S_{APP}$  is determined using Eq. 7.9. In the case of a symmetric measurement configuration the numerical solving algorithm is not converging due to very small  $\tau_{eff}$ . As this approximation incorporates a finite charge carrier mobility, the calculation results not always in a systematic underestimation of  $S_{APP}$ , in contrast to the uniform charge carrier profile approximation shown in Fig. 7.5. In the case of measuring the sample face-up  $S_{APP}$  is considerably overestimated.

Therefore, if the sample is illuminated with a IR-filtered xenon source, the more homogeneous generation causes a reduced precision of the measurement.

In conclusion, the simplified evaluation of the recombination at a surface under the assumption  $\Delta n(z) = \text{const.}$  is valid if the surface under investigation has a recombination velocity  $S < 500$  cm/s and the sample is thin. If a sample has a well passivated and a recombination active surface, it is best if the sample is measured face-up, i.e. with the recombinative side facing the flash. In any case the solution of the continuity equation for steady state excitation should be used if measurement precision is important.

#### 7.1.4 Transient Excitation Approximation

It has been shown in the previous section that it is the finite mobility of the minority charge carriers that permits a simple expression connecting the effective lifetime and the surface recombination velocity (or emitter saturation current density). However, the treatment of the effective lifetime after a transient excitation which has been discussed in detail in Sec. 4.4.3 includes the finite mobility of the charge carriers. In this section the systematic error connected to using

$$\frac{1}{\tau_{eff}} = \frac{1}{\tau_B} + \frac{1}{\tau_S} \quad (7.9)$$

and the largest root of

$$\tan\left(\frac{d}{\sqrt{D\tau_s}}\right) = \sqrt{\frac{D}{\tau_s}} \frac{S_1 + S_2}{(D/\tau_s) - S_1 S_2} \quad (7.10)$$

(cf. Sec. 4.4.3) will be discussed.

Similar to the previous section,  $S_{CESS}$  is defined as the  $S$  in the solution of the continuity equation and  $S_{APP}$  is the value determined by combining Eq. 7.9 and 7.10. The parameters of the calculation are the same as in the previous section.

From the data displayed in Fig. 7.6 it becomes evident that this treatment is also defective. Especially, the sample measured face-up and the symmetrically processed sample show substantial and systematic overestimation of the  $S$  (or  $j_{0e}$ ) value. It appears that samples evaluated with this technique should be measured face-down. That way the domain of acceptable measurement error extends to fairly high recombination velocities.

## 7.2 Experimental

In this section the quality of a laser doped silicon is examined by measuring the emitter saturation current density of laser-doped (LD) emitters. Additionally, samples were treated with a delineation etch to expose crystal defects. A distinction was made between doping of bare silicon wafers (LD-bare) and doping of silicon wafers with a  $\text{SiN}_x$  coating present during the laser process (LD- $\text{SiN}_x$ ).

### 7.2.1 Sample Preparation

A  $120\ \Omega$  and  $1.2\ \mu\text{m}$  deep emitter was created on both sides of alkaline textured  $240\ \mu\text{m}$  thick  $1\ \Omega\ \text{cm}$  p-type 4" fz-silicon wafers using a  $\text{POCl}_3$  furnace diffusion process. Subsequently, a  $75\ \text{nm}$  thick  $\text{SiN}_x$  film was deposited by plasma-enhanced chemical-vapor deposition (PECVD). The batch of wafers was split into two groups "LD- $\text{SiN}_x$ " and "LD-bare". The front side of the "LD- $\text{SiN}_x$ " wafers were spin-coated with 30%  $\text{H}_3\text{PO}_4$  for 60 s at 3000 RPM resulting in a  $1.5\ \mu\text{m}$  thick liquid phosphorous dopant layer. The cw-laser was used to locally dope and pattern the sample using the setup described in chapter 5. The 15 W laser spot with a diameter of  $15\ \mu\text{m}$  was scanned across the sample at velocity of 5 m/s. As shown in chapter 6 the laser power is sufficient to simultaneously ablate the  $\text{SiN}_x$  and create  $14\ \mu\text{m}$  wide and  $4\ \mu\text{m}$  deep highly doped lines with a sheet resistance of  $13\ \Omega$ . Each wafer was subdivided into four quadrants ( $4\ \text{cm} \times 4\ \text{cm}$ ) with varying coverage of laser treated area: unprocessed reference, 4 % coverage (resembling the average coverage of a solar cell with a selective emitter structure), 20 % line-coverage and full coverage using a line to line hatch distance of  $5\ \mu\text{m}$ . With the exception of the unprocessed reference quadrant the single sided laser processing created asymmetrical samples, regarding front and

rear side of the sample. In order to remove the dopant film residue after laser doping the wafers were cleaned in a DI-water rinser. Subsequently, the  $\text{SiN}_x$  film was removed using 20 % HF from all wafers of both groups. The "LD-bare" group was laser doped after  $\text{SiN}_x$  removal in the same fashion as described above. After that the samples were coated on both sides with a silicon rich oxynitride (SiriON)[170] layer by PECVD and fired at  $650^\circ\text{C}$  to enhance the hydrogen passivation. An overview of the processing sequence used for groups in this experiment is shown in Fig. 7.7.

### 7.2.2 Emitter Saturation Current Densities

The injection dependent effective charge carrier lifetime  $\tau_{\text{eff}}$  was measured at low level injection by means of the quasi-steady-state photoconductance (QSSPC) method [137]. The optical properties of the planar laser treated and the textured furnace diffused surfaces have been corrected for by using OPAL [171]. With (without) the SiriON dielectric the light coupling into the planar sample is a factor of 0.94 (0.68) lower than the reference solar cell and the coupling of the textured sample is a factor of 1.06 (0.93) higher (lower). From  $\tau_{\text{eff}}$  at  $\Delta n_{av} = 3 \cdot 10^{15} \text{ cm}^{-3}$  the  $j_{0e}$  of the laser-doped emitter is calculated as described in detail below. Subsequently, the SiriON layer was removed using 20 % HF and the  $j_{0e}$  measurement of the unpassivated emitter was repeated. After this the laser-doped emitter dopant profile has been measured using the electrochemical capacitance-voltage (ECV) technique.

### 7.2.3 Delineation Etch and Microscopy Study

Cross sections of laser processed lines from the "LD-SiNx" and the "LD-bare" group have been examined using a scanning electron microscope (SEM). Additionally, the samples have been etched in Secco etchant [172] for 15 s to delineate crystal defects and examined using SEM.

## 7.3 Results and Discussion

At first a short recapitulation of the employed method to extract  $j_{0e}$  of laser doped emitters is presented. In the second section  $j_{0e}$  values of the samples produced according to the scheme shown in Figure 7.7 are discussed. After that laser induced defects are studied using delineation etching and SEM analysis. These observations lead to a model for indirect  $\text{SiN}_x$  ablation and cavity formation which is presented at the end of this chapter.

### 7.3.1 Methodology of $j_{0e}$ Determination

In Sec. 7.1 the steady-state continuity equation which describes the distribution of excess charge carriers  $\Delta n(z)$  is solved to accurately extract the  $j_{0e}$  of the laser doped structures. The excess charge carrier density  $\Delta n_\gamma$  can be calculated

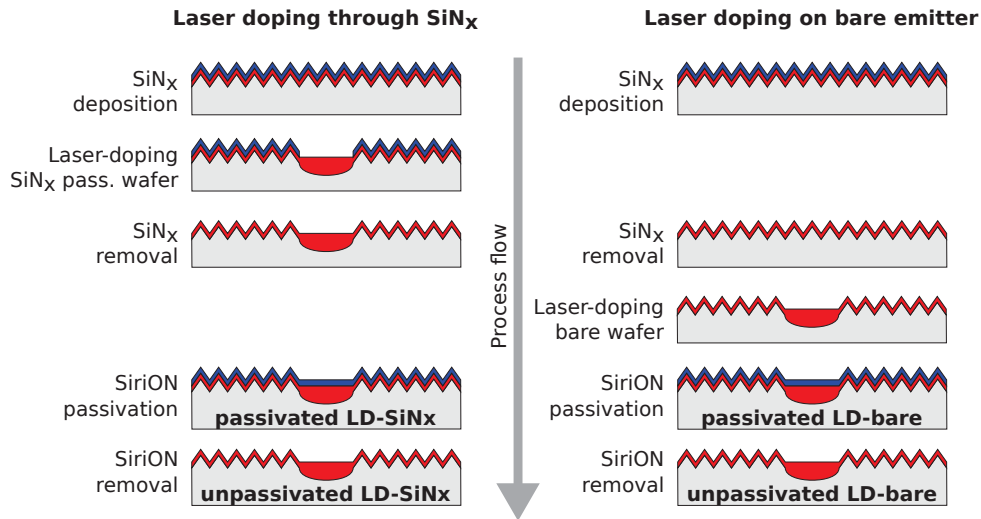


Figure 7.7: Processing scheme for the samples produced in order to study the emitter quality and the influence of the presence of a dielectric layer during laser doping.

for a given  $D$ ,  $\tau_B$ ,  $W$ ,  $S_0$ ,  $S_W$ , and spectral irradiance. With a known  $\Delta n_{av}$  ( $= 3 \cdot 10^{15} \text{ cm}^{-3}$ ), ambipolar diffusion coefficient  $D$  ( $= 21.9 \text{ cm}^2 \text{ s}^{-1}$ ), and a bulk lifetime  $\tau_B$  ( $= 10^{-3} \text{ s}$ ), the effective lifetime  $\tau_{\text{eff}}$  can now be calculated as a function of  $S_0$  and  $S_W$  using spectral irradiance data for the xenon flash.

In the case of the symmetrical furnace diffused sample both surfaces have the same recombination velocity ( $S_0 = S_W$ ) which allows the determination of  $S_W$  ( $= 30 \text{ cm/s}$  for the SiriON passivated sample) from the measured effective lifetime  $\tau_{\text{eff}}$  ( $= 290 \mu\text{s}$ ). According to Eq. 7.1, for the base doping concentration  $N_a$  ( $= 1.5 \cdot 10^{16} \text{ cm}^{-3}$ ), elementary charge  $q$ , and intrinsic charge carrier concentration  $n_i$  ( $= 8.3 \cdot 10^9 \text{ cm}^{-3}$  at  $25^\circ \text{C}$ ),  $S_W$  of the SiriON passivated furnace diffused emitter corresponds to an emitter saturation current of  $j_{0e,W} = 18 \text{ fA/cm}^2$ , which is in good agreement with earlier experiments conducted by Reichel et al. [173], applying the same thermal diffusion recipe for emitter formation. This value is now used to determine the surface recombination velocity  $S_0$  and emitter saturation current density  $j_{0e}$  of the laser processed surfaces of the asymmetrical samples from the measured  $\tau_{\text{eff}}$ .

### 7.3.2 Emitter Recombination Analysis

Figure 7.8 shows the  $j_{0e}$  of the laser treated surface as a function of the coverage with laser lines. The plot collects  $j_{0e}$  of the passivated as well as unpassivated samples from the "LD-bare" and "LD-SiNx" group.

The  $j_{0e}$  of the passivated laser doped emitters were determined by fitting a line through 0%, 4% and 20% coverage (green and blue triangles) and extrapolating to full coverage. Details on this extrapolation method can be found in the references [125, 174]. The  $j_{0e}$  value determined from this fitting is with  $195 \pm 3 \text{ fA/cm}^2$  for the "LD-bare" group significantly smaller than the

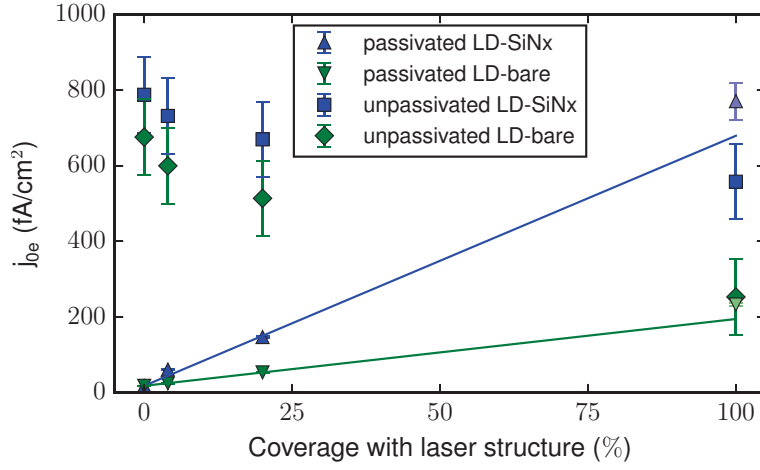


Figure 7.8: Effective  $j_{0e}$  as a function of the coverage with laser-doped emitter of the "LD-bare" (green) and the "LD-SiNx" (blue) group (schematic of process groups cf. Fig. 7.7). Triangles represent  $j_{0e}$  of SiriON passivated samples whereas squares represent the corresponding  $j_{0e}$  with unpassivated surfaces. In the case of the SiriON samples  $j_{0e}$  increases rapidly with laser-doped emitter coverage, whereas in the unpassivated case the laser-doped emitter has a lower  $j_{0e}$  than the high efficiency furnace diffused emitter.

$233 \pm 5 \text{ fA/cm}^2$  which was measured at full coverage. This can be explained by the following: Full coverage is achieved by a narrow hatch of  $5 \mu\text{m}$  that is smaller than the laser line width of  $12 \mu\text{m}$ . As a result every point on the surface is molten and re-crystallized at least two times. This additional re-crystallization is expected to be the cause for an increased amount of imperfections and increased  $j_{0e}$  [15]. Also in the "LD-SiNx" group the  $j_{0e}$  from the fit is with  $680 \pm 58 \text{ fA/cm}^2$  smaller than the measured  $771 \pm 49 \text{ fA/cm}^2$  at full coverage, however this difference is not significant.

In either case the emitter recombination is strongly increased if a  $\text{SiN}_x$  dielectric was present during laser treatment, which will be discussed in detail in the following section. In the unpassivated case i.e. after the removal of the SiriON dielectric using HF, the measured lifetime decreased dramatically ( $\approx 10 \mu\text{s}$ ) mostly due to the increased recombination of the unpassivated furnace diffused emitter to  $j_{0e,W}^{\text{unpass}} \approx 750 \text{ fA/cm}^2$ . Due to enhanced charge carrier shielding  $j_{0e}^{\text{unpass}}$  decreases with the laser-doped emitter coverage. The underlying mechanism has been discussed in detail in Sec. 2.5.

The benefit of deep p-n junctions with regard to shielding charge carriers from a recombinative surface becomes evident if  $j_{0e}$  calculated using EDNA [48] from the laser doped emitter profile for a well passivated case ( $S_{\text{surf}} = 10 \text{ cm/s}$ )  $j_{0e} = 120 \text{ fA/cm}^2$  is compared to  $j_{0e}$  for the unpassivated case ( $S_{\text{surf}} = 10^7 \text{ cm/s}$ )  $j_{0e}^{\text{unpass}} = 180 \text{ fA/cm}^2$ . In comparison to the furnace diffused emitter the quality of the passivation layer has only a minor influence on the emitter recombination. It needs to be noted that the trend of decreasing  $j_{0e}^{\text{unpass}}$  with laser-doped emitter coverage is also present in  $\tau_{\text{eff}}$  but due to high  $j_{0e,W}^{\text{unpass}}$  the absolute values of  $j_{0e}^{\text{unpass}}$  calculated from  $\tau_{\text{eff}}$  are of reduced precision as indicated by the large error bars in Fig. 7.8.

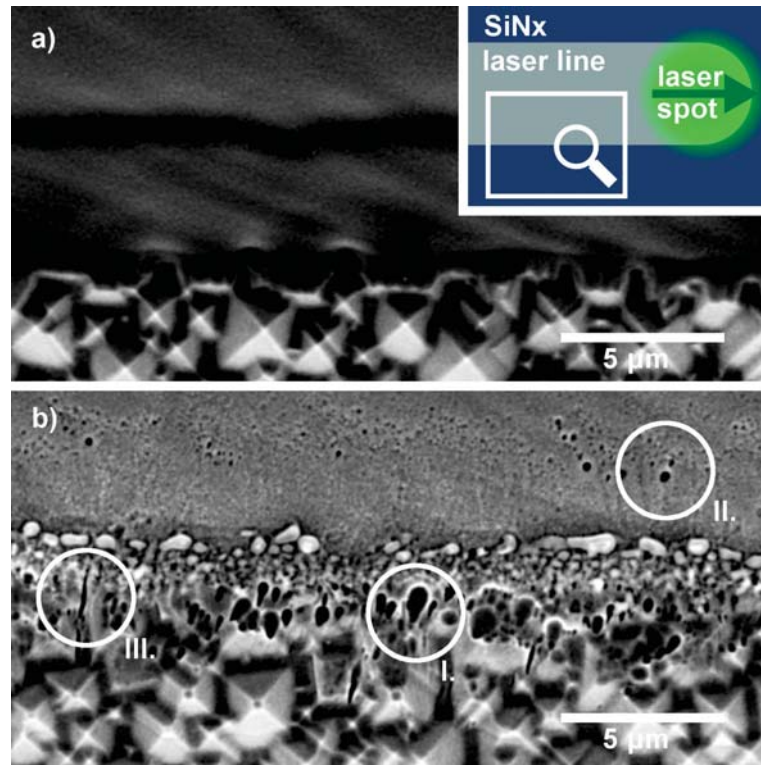


Figure 7.9: Top view SEM images of the edge of a laser line from the "LD-bare" (a) and "LD-SiNx" (b) group after secco delineation etching. The inset shows a schematic of a laser line and indicates the area imaged in (a) and (b) as well as the moving direction of the laser spot. Only the "LD-SiNx" sample (b) shows a large number of etch pits which are categorized into three classes. I: large round or tear-shaped pits at the edge of the laser line; II: round etch pits in the center of the line; III: cracks at the edge and region of low irradiation.

### 7.3.3 Delineation Etch and Microscopy Study

Figure 7.9 shows SEM images of laser line edges of the "LD-bare" and "LD-SiNx" group after delineation etching. In the "LD-bare" case (a), where laser doping was performed on a bare surface, no etch pits are observed indicating a low crystal defect density. This is in agreement with the measured  $j_{0e}$  ( $195 \text{ fA/cm}^2$ ) which is on a similar level as the  $j_{0e}$  determined from the ECV profile ( $120 \text{ fA/cm}^2$ ) using EDNA. As this EDNA calculation included only Auger recombination the difference to the measured value is an indicator of increased Shockley-Read-Hall recombination, which is likely caused by crystal damage in the emitter. In the "LD-SiNx" case (b) the additional SiNx layer present during laser treatment lead to a high etch pit density which is in agreement with the increased measured  $j_{0e}$  ( $680 \text{ fA/cm}^2$ ) and the high difference to the  $j_{0e}$  calculated ( $120 \text{ fA/cm}^2$ ) using EDNA. Most of the etched pits are round or tear-shaped and are located at the edge of the laser line, in the transition region between full SiNx ablation and non-irradiated SiNx (cf. Fig. 7.9 (b) type I.).

This crystal damage on the edge of the laser line was observed before and is

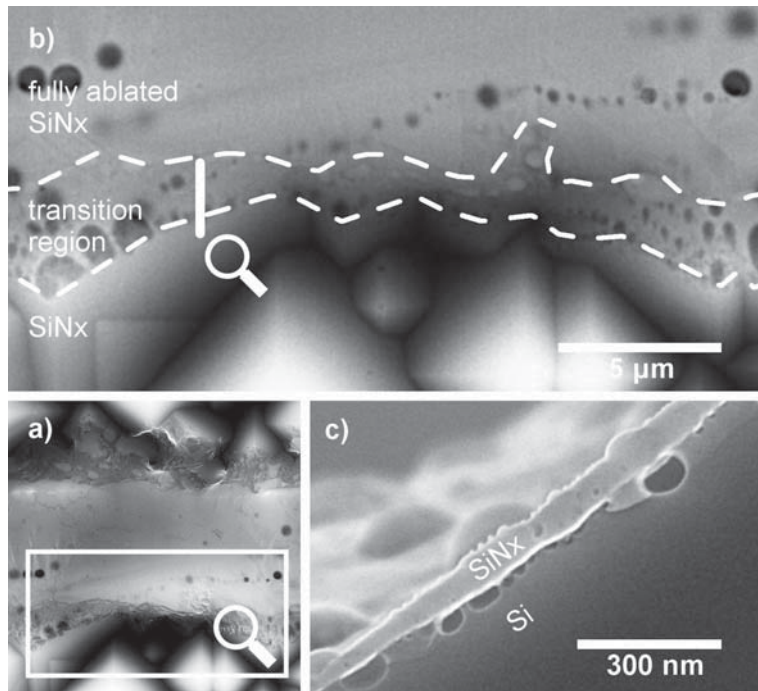


Figure 7.10: Top view SEM image of a laser line from the "LD-SiN<sub>x</sub>" group using secondary electrons (a). In this imaging mode three regions can be identified by their respective surface morphology: un-irradiated SiN<sub>x</sub>, partly ablated transition region, and fully ablated SiN<sub>x</sub>. These regions have been mapped from (a) to close-up (b) showing the corresponding features using back-scatter electrons. A sampling depth of 1.5 μm allows detection of cavities within the silicon in the transition region and in the fully ablated region. At a position similar to the vertical bar in (b) a cross section was polished in the transition region (c). The cavities in this region are located remarkably close to the SiN<sub>x</sub> layer.

attributed to the thermal expansion mismatch between SiN<sub>x</sub> and silicon [15, 18, 175, 176]. The referenced works suggest that during heating, the SiN<sub>x</sub> layer puts the underlying silicon under tensile stress and induces crystal defects. Hameiri et al. [16] showed that a SiO<sub>2</sub>/ SiN<sub>x</sub> double layer reduces this detrimental effect. They argue that the thermal expansion mismatch between SiO<sub>2</sub> and silicon puts the underlying silicon under compression which induces fewer defects during cooling. The expansion mismatch may explain the observed etch pits and cracks in the transition region but Fig. 7.9 also reveals defects in the center of the laser line (cf. Fig. 7.9 (b) type II.), which cannot solely be caused by a thermal expansion mismatch.

To investigate the origin of the defects in the edge region SEM imaging was performed on a "LD-SiN<sub>x</sub>" sample directly after the laser treatment. Using a primary electron energy of 30 keV and a backscatter electron detector (BSD) resulted in a sampling depth of 1.5 μm which allowed to image material properties up to this depth (the principle of this particular SEM imaging is detailed in Sec. 4.1.2). Figure 7.10 (a) shows an overview of the laser line using secondary electron imaging. In this imaging mode three regions of varying SiN<sub>x</sub> ablation can be identified: un-irradiated SiN<sub>x</sub>, partly ablated transition region, and fully ablated SiN<sub>x</sub>. These regions have been mapped to the close-up (b). The image

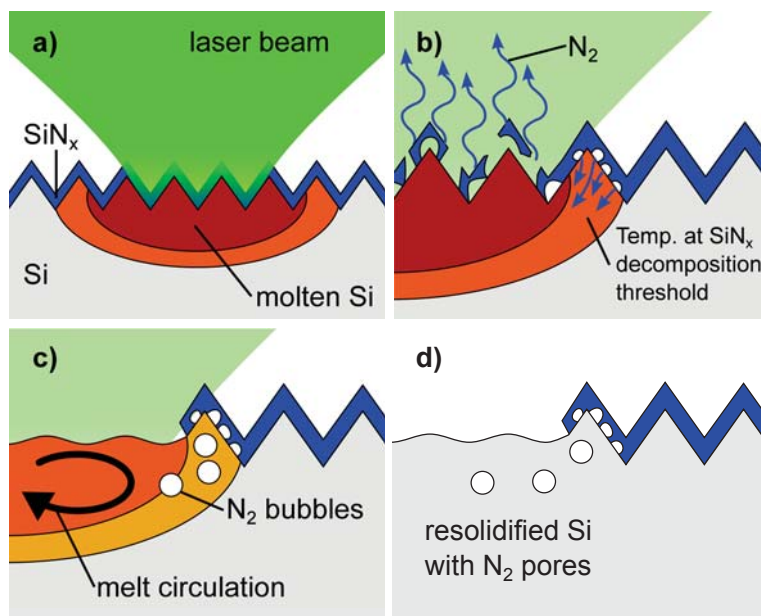


Figure 7.11: Scheme of SiN<sub>x</sub> ablation using laser processing. Laser melting of silicon (a) leads to indirect heating and decomposition of SiN<sub>x</sub> layer atop the molten pool (b). Due to reduced temperature of the pool in the transition region the SiN<sub>x</sub> layer is only partly decomposed. N<sub>2</sub> from the decomposition of SiN<sub>x</sub> is released as bubbles into the molten silicon where they are transported by melt circulation (c). After re-solidification the bubbles are frozen in place (d).

from the BSD reveals that the pits which were exposed by the delineating etch were already present as cavities within the silicon in the edge region as well as the central area of the laser line. Cavities appear in the BSD image as regions with reduced signal due to increased material penetration depth and thus reduced backscattering probability. A SEM image of a cross-section in the transition region is shown in Fig. 7.10 (c). On top of the silicon the thin SiN<sub>x</sub> passivation layer is visible. This layer is slightly bulged and deformed indicating that it has been exposed to temperatures close to its decomposition temperature. A string of cavities is located just below the SiN<sub>x</sub> layer, which suggests the assumption that the cavities originate from decomposed SiN<sub>x</sub> at the underside of the SiN<sub>x</sub> passivation layer. This leads to a model of the ablation and defect formation which will be discussed in the following.

## 7.4 Development of a Model of SiN<sub>x</sub> Ablation and Cavity Formation

The observation of the strongly increased recombination as well as the formation of cavities in the laser-doped emitter lead to a model of the SiN<sub>x</sub> ablation mechanism using laser processing as depicted in Fig. 7.11. This model relies on the indirect ablation of the SiN<sub>x</sub>. As such, it should be valid for a process employing laser pulses with a duration exceeding a nanosecond and cw-lasers.

### 7.4.1 General Case for Indirect Ablation

The  $\text{SiN}_x$  dielectric is transparent at wavelengths down to the UV regime. At wavelengths laser processing is typically performed, only a minute fraction of irradiation is absorbed directly within the thin  $\text{SiN}_x$  layer. For green lasers at 532 nm this fraction is 0.3% and for UV laser processing at 355 nm it is 2.8%<sup>2</sup>. The laser irradiation is mostly absorbed in the underlying silicon. At sufficient laser power the silicon is molten in a pool shape with the highest temperature in the center and decreasing to the sides. This is illustrated in Fig. 7.11 (a). Conductive heat transfer results in an indirect heating of the  $\text{SiN}_x$  atop the molten pool. If the  $\text{SiN}_x$  exceeds a temperature of 2150 K it decomposes into liquid silicon and gaseous  $\text{N}_2$  [178, 179]. In the center region the energy input into the  $\text{SiN}_x$  layer is sufficient to fully decompose the  $\text{SiN}_x$  and the released  $\text{N}_2$  can freely escape into the atmosphere. The temperature of the molten silicon pool decreases laterally and at some distance from the center the heat conducted to the  $\text{SiN}_x$  is insufficient to fully decompose the  $\text{SiN}_x$ . In this transition region only a fraction of the  $\text{SiN}_x$  layer which is in direct contact with the molten silicon may be decomposed as illustrated in (b). As the remaining solid  $\text{SiN}_x$  is still atop the decomposed part the gaseous  $\text{N}_2$  is released as a bubble into the molten silicon. The width of this transition region and thus the extent of bubble formation depends on the wavelength and shape of the laser spot as well as the effective irradiation duration. A lateral temperature gradient at the surface of the molten pool causes a gradient in surface tension. This surface tension gradient leads to a circular mass transfer of the molten silicon within the molten pool as illustrated in (c). The dynamic of the molten pool is detailed in Sec. 3.3.3. The flow of molten silicon transports the bubbles away from the transition region towards the center of the laser line. As the laser processed area cools down the bubbles are frozen within the re-solidified silicon. This is illustrated in (d).

### 7.4.2 cw-Laser Ablation

In this work cw-laser doping serves as an example with a Gaussian intensity profile and an effective irradiation dwell time of about  $3 \mu\text{s}$ <sup>3</sup>. For this case Blecher et al. [89] have predicted strong melt circulation which are in agreement with high junction depths and the proposed bubble transport. The presence of cavities leads to additional unpassivated surface area within the emitter which is particularly detrimental if these recombination active surfaces are close to the space charge region. These unpassivated surfaces within the emitter would explain the observed increases in recombination if the  $\text{SiN}_x$  layer is ablated using the cw-laser process.

---

<sup>2</sup>These values have been calculated assuming linear absorption from the data published by Baker-Finch et al. [177].

<sup>3</sup>Simple estimation: 15  $\mu\text{m}$  laser spot scanned at 5 m/s results in a irradiation length of 3  $\mu\text{s}$ .

### 7.4.3 Reduction of Cavity Formation

Bubble formation depends on the temperature distribution on the surface of the molten pool and can be reduced, if the transition region with incomplete  $\text{SiN}_x$  ablation is narrowed. This can be achieved by shorter irradiation duration, which reduces heat transfer to the  $\text{SiN}_x$  layer in the transition region. Using a laser system with a flat-top intensity profile will also narrow the transition region. Melt circulation, which causes the transport of bubbles within the molten pool, increases with the temperature gradient at the surface of the molten pool and with the duration of irradiation. Like bubble formation melt circulation is reduced if short laser pulses and flat-top intensity profiles are used.

In earlier experiments using green laser pulses with a Gaussian intensity profile and a pulse duration of 80 ns no cavities in the center region of the laser line have been observed. Applying the proposed model for cavity formation, this can be explained by shorter melt duration and reduced melt circulation. However, at present it is not clear at exactly what process parameters the bubble formation becomes substantial and significantly reduces the emitter quality. The experiment shown in this chapter merely represents a case that clearly is affected by process induced cavities in the laser doped emitter.

## 7.5 Conclusion

The discussion of the recombination quality of laser-doped emitters presented in this work is based on the solution of the steady-state continuity equation for excess charge carriers. This method of extracting  $j_{0e}$  values exceeding  $\approx 100 \text{ fA/cm}^2$  from QSSPC lifetime measurements circumvents systematic errors introduced by commonly used approximations. It was found that  $j_{0e}$  of a laser-doped emitter with a  $\text{SiN}_x$  layer present during laser processing is more than three times as high as the  $j_{0e}$  of a laser-doped emitter which was created before the deposition of the  $\text{SiN}_x$  layer. Furthermore, it was shown that laser-doped emitters are effectively shielding charge carriers from unpassivated or metallized surfaces which results in lower recombination compared to a homogeneous emitter formed via furnace diffusion.

Using SEM imaging and delineation etching, defects have been located at the edge of the laser line. In earlier publications these defects have been attributed to a thermal expansion mismatch between silicon and  $\text{SiN}_x$ . SEM imaging using backscatter electrons at high energies revealed that the majority of defects are already present after the laser process in the form of micro cavities. This cannot result from a mere expansion mismatch. SEM imaging on a cross section of a laser line suggests a model of  $\text{SiN}_x$  ablation for laser processing where the  $\text{SiN}_x$  layer is indirectly heated from the molten silicon. At the edge of the laser line the  $\text{SiN}_x$  is only partly decomposed into gaseous  $\text{N}_2$  which is released into the liquid silicon as bubbles. Circulation currents driven by a temperature gradient at the surface transports these bubbles within the molten pool. The

detrimental effect of the  $\text{SiN}_x$  layer can be put down to the fact that these micro cavities introduce additional unpassivated surfaces to the laser-doped emitter or additional recombination active defects within the emitter.

The precise influence of the laser process parameters on cavity formation, transport and emitter quality is not fully understood. Compared to laser processing using pulsed lasers, the pool depth as well as the irradiation length is rather large for the experimental parameters presented in this work. However, the findings suggest that large melt pools and long irradiation lengths can create emitters with excellent charge carrier shielding properties if cavity formation can be prevented, as can be seen for samples that were laser-doped before  $\text{SiN}_x$  deposition. The optimal trade-off between bubble formation and charge carrier shielding may be achieved by increasing the scanning speed of a laser spot with a flat-top intensity profile or by creating the laser-doped emitter before  $\text{SiN}_x$  deposition. The latter approach is investigated in detail in chapter 9.

## 8 Analysis of Detrimental Surface Layer on Laser Doped Silicon

Meager nickel deposition after laser patterning using the cw-laser process to simultaneously dope and ablate the dielectric was reported in the chapter 6. This finding suggests that a parasitic barrier layer on the surface hinders nickel deposition onto the silicon. In this chapter the presence of such a detrimental layer after cw-laser processing will be verified by surface sensitive x-ray photoelectron spectroscopy.

A detailed description of the sample preparation in the first section is followed by an examination of nickel plating and nickel silicide formation on the processed areas in Sec. 8.2. XPS measurements conducted on the surface allow a detailed analysis of the surface composition. Nickel deposition, nickel silicide formation, XPS measurement and high resolution SEM imaging are related to prove the formation of a parasitic silicon oxynitride surface layer which hinders nickel deposition and prevents nickel silicide formation. In Sec. 8.3, a row of simple follow-up experiments are aimed to investigate the laser induced formation mechanism of the silicon oxynitride. From these results, implications for solar cell laser processing are drawn before summarizing all findings in the final section of this chapter.

### 8.1 Experimental

The composition of the silicon surface after cw-laser ablation is studied by means of x-ray photoelectron spectroscopy (XPS) which allows to analyze the top few nanometers of the laser treated area (XPS is detailed in Sec. 4.2). Additionally, the nickel deposition, nickel silicide formation and the surface of the laser treated surface is imaged using scanning electron microscopy (SEM) (detailed in Sec. 4.1).

A 1  $\Omega$  cm industrial grade CZ-grown p-type silicon wafer with random pyramid texture and a thickness of 250  $\mu\text{m}$  was covered with a silicon nitride ( $\text{SiN}_x$ ) layer with a thickness of 75 nm using plasma-enhanced chemical vapor deposition (PECVD). Subsequently, the front side was spin-coated with 30 wt%  $\text{H}_3\text{PO}_4$  at 3000 rpm for 60 s, creating a 1.5  $\mu\text{m}$  thick liquid phosphorous dopant layer. The cw-laser was used to locally dope and pattern the wafer with 2 mm wide fields of touching laser lines (hatch 12  $\mu\text{m}$ ) using the setup described in chapter 5. The 15 W laser spot with a diameter of 15  $\mu\text{m}$  was scanned across the sample at a speed of 5 m/s. As shown in chapter 6 the laser power is sufficient to simultaneously ablate the  $\text{SiN}_x$  and create 14  $\mu\text{m}$  wide and 4  $\mu\text{m}$  deep highly

doped lines. In order to remove the SOD residue the wafer was cleaned in a DI-water rinser. With a dicing saw the wafer was divided into six samples in three groups with varying surface treatment. Two samples were etched for 30 s in buffered oxide etchant (BHF 10:1  $\approx$  HF 7%), another two were etched for 60 s in BHF and the other two were not treated with BHF. After this, all sample were deglaced in 1 % HF for 30 s.

In order to check the quality of nickel deposition and nickel silicide ( $\text{Ni}_x\text{Si}_y$ ) formation on the cw-laser treated surface one sample from each group (treated with BHF for 0, 30, 60 s) was plated with nickel using LIP and annealed in a rapid thermal processor for 10 min at 450° C. The plating quality was analyzed using SEM. After that, the elemental nickel was removed from the surface using piranha etchant [180, 181], which allowed imaging the silicide formation with the SEM.

The surfaces of two samples were analyzed with XPS. One sample was etched in BHF for 60 s the other was not treated with BHF. Both samples were deglaced in diluted HF as described above and were not plated with nickel. The XPS analysis was performed at a photoemission angle of 45° on a Perkin Elmer PHI 5600 system using a Mg anode to generate X-rays. The sampling depth in silicon is in the range of 3 to 7 nm. For quantitative analysis, the correction factors supplied by the manufacturer were used. Charge referencing was performed using the C 1s line (284.8 eV) of the adventitious carbon.

The influence of buffered oxide etchant (BHF 10:1  $\approx$  HF 7%) on the laser structured surface was studied using high resolution SEM imaging. For this the BHF etching time was varied between 30 s and 120 s. The samples were measured after cw-laser processing, BHF etching and deglazing in 1 % HF.

## 8.2 Results and Discussion

### 8.2.1 Nickel Plating and Silicidation

The experiments conducted in chapter 6 showed that nickel deposition on cw-laser ablated silicon is not always successful. The metal deposition using an electroless nickel electrolyte was meager and inhomogeneous. Homogeneous deposition was achieved with nickel LIP (cf. Sec. 6.2.3) which was therefore used in this experiment. In this section the influence of BHF etching on nickel plating and nickel silicide ( $\text{Ni}_x\text{Si}_y$ ) formation is analyzed.

Figure 8.1 shows a top view SEM image of the laser structured surface after nickel plating of the three groups with varying BHF etching time. In the case of the untreated sample (a) the nickel deposition is inhomogeneous. The plating quality is substantially worse compared to the plating quality observed in earlier experiments. The inhomogeneity can be explained by the current distribution during the nickel LIP. Whereas the homogeneous plated case presented in chapter 6 (cf. Fig. 6.6 c) was a single laser line 14  $\mu\text{m}$  thick, the inhomogeneous case presented here is a laser treated field with a width of 2 mm. In the case of the thin line, the excess electrons in the emitter below the  $\text{SiN}_x$  covered

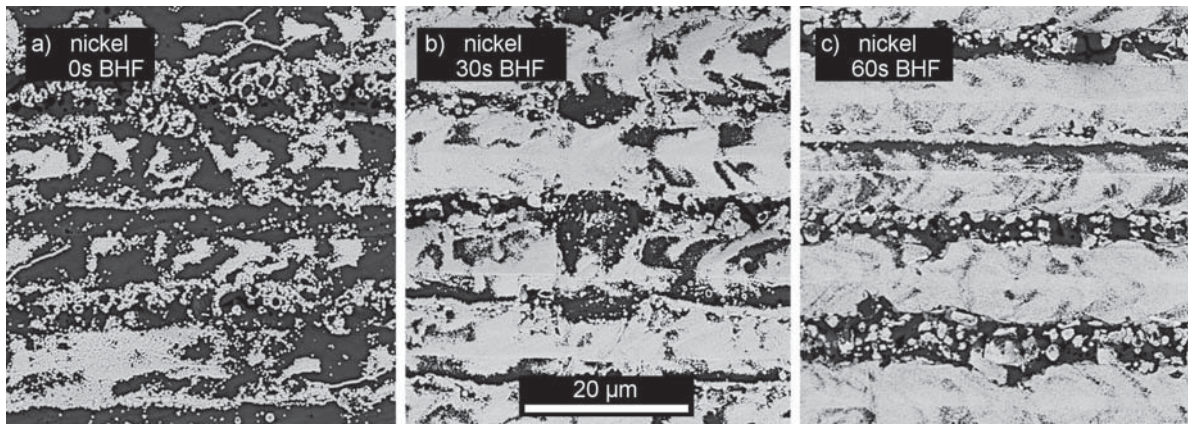


Figure 8.1: Top view SEM images of laser treated area after nickel LIP at different BHF etching times (0, 30, 60 s). The light gray areas correspond to deposited nickel, the dark areas correspond to the laser treated silicon surface.

surroundings of the line also contribute to the reduction of nickel from the electrolyte. In the case of the laser processed field such contributions are reduced to the edge region of the field and the plating rate is effectively reduced. This is a known effect and is explained in detail for copper plating e.g., by Bartsch et al. [182]

BHF etching increases the nickel deposition quantity and homogeneity as can be seen in Fig. 8.1 (b) and (c). The horizontal pattern in (b), and (c) with stripes of little, and stripes of high nickel deposition corresponds to the spacing of the processed laser lines. This suggests the presumption that the horizontal stripes with little nickel deposition were not fully ablated by the laser process. The thickness of the nickel layer is significantly reduced compared to the thickness of the nickel layer on a single laser line. This can be put down to the current distribution effect discussed above.

After annealing at 450° C and etching-off the elemental nickel the formed  $\text{Ni}_x\text{Si}_y$  was imaged using SEM. Figure 8.2 shows the formed  $\text{Ni}_x\text{Si}_y$  (gray structures) for the reference sample (a) and the two BHF etched samples (b) and (c). In the case of the reference process (a)  $\text{Ni}_x\text{Si}_y$  formation is minute. With the length of the BHF treatment the  $\text{Ni}_x\text{Si}_y$  formation increases to a coverage of about 50 % in the 60 s case (c).

### 8.2.2 XPS Surface Characterization

Figure 8.3 shows the Si2p region of the XPS measurement on a sample that was laser processed and solely deglaced in 1 % HF. After background subtraction [183] and deconvolution of the peaks (assuming Gaussian shape) three species can be identified: silicon at a binding energy of 99.7 eV [184–186],  $\text{SiN}_x$  at 101.6 eV [186–188] and  $\text{SiO}_2$  at 103.4 eV [185, 187, 188]. A fourth peak at 102.6 eV can be attributed to the formation of a silicon oxynitride ( $\text{SiO}_x\text{N}_y$ ) phase, with a Si2p binding energy intermediate to  $\text{SiO}_2$  and  $\text{SiN}_x$  [188–190]. The relative signal intensities can be attributed to photoelectrons from bulk

## 8. Analysis of Detrimental Surface Layer on Laser Doped Silicon

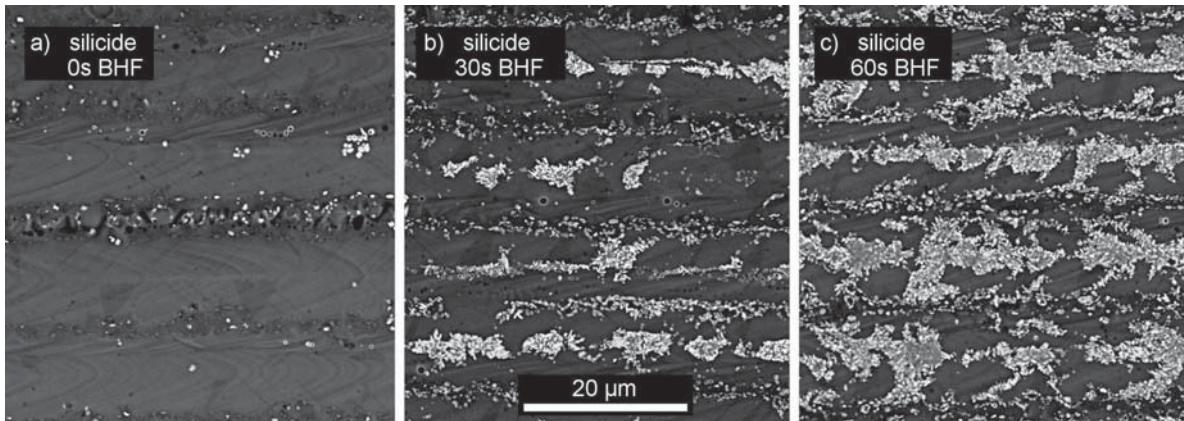


Figure 8.2: Top view SEM images of laser treated area after nickel silicide formation at  $450^{\circ}\text{C}$  and nickel etch-back for different BHF etching times (0, 30, 60 s). The light gray areas correspond to formed nickel silicide, the dark areas correspond to the laser treated silicon surface.

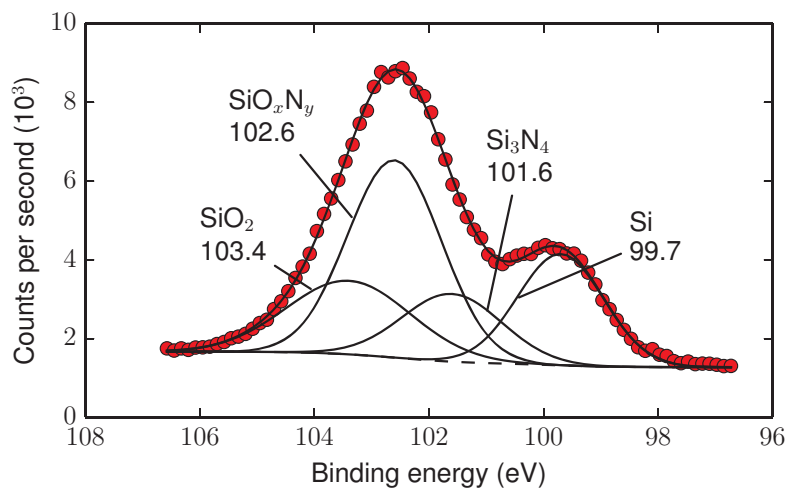


Figure 8.3: XPS signal of the Si2p region (dotted curve) from the cw-laser treated surface. The Shirley background (dashed line) was subtracted prior to deconvolution using four Gaussian curves (solid lines) representing silicon,  $\text{Si}_3\text{N}_4$ ,  $\text{SiO}_x\text{N}_y$  and  $\text{SiO}_2$ .

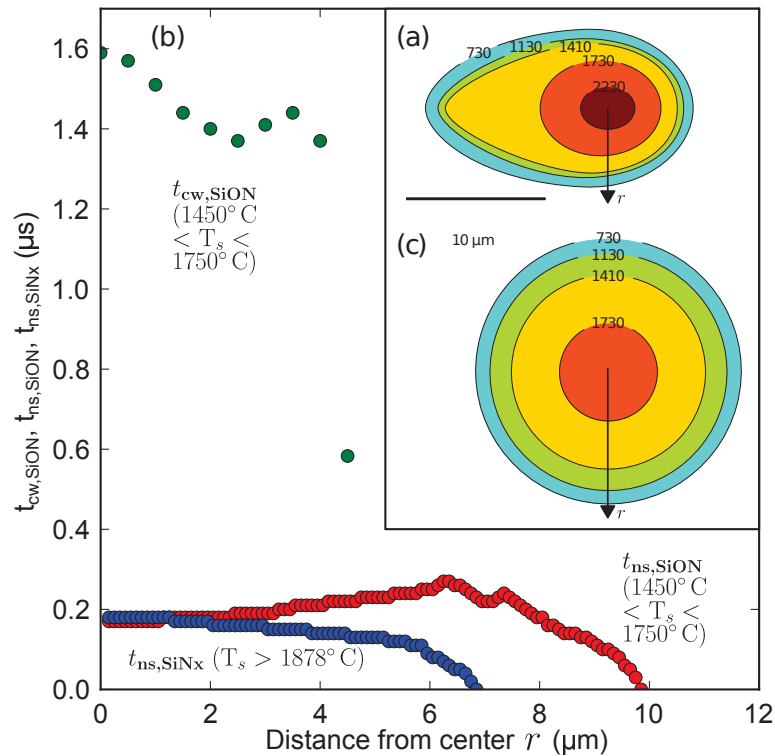


Figure 8.4: Insert (a) shows the surface temperature distributions of cw-laser processing as simulated by Blecher et al. [89] (travel direction to the right). Graph (b) plots the time span of SiO<sub>x</sub>N<sub>y</sub> formation and SiN<sub>x</sub> ablation as a function of distance from the center for cw-laser and ns-pulsed laser ablation. The values are calculated from simulations published by Blecher et al. [89] for the cw-laser and from simulations conducted using LCPSim [85] for the ns-pulsed case. Insert (c) exemplarily shows the surface temperature distribution 200 ns after the onset of a 80 ns laser pulse as simulated with LCPSim.

silicon (23%), native SiO<sub>2</sub> (16%) and small patches of residual SiN<sub>x</sub> dielectric (21%). The SiO<sub>x</sub>N<sub>y</sub> which accounts for 40% of the signal is assumed to have formed during the cw-laser process from the interaction of the SiN<sub>x</sub> layer with oxygen from the atmosphere, the SOD, or the native oxide. A XPS measurement on a sample etched for 60 s in BHF showed a reduced SiO<sub>x</sub>N<sub>y</sub> signal of 33% compared to the 40% without the BHF treatment.

### 8.2.3 Silicon Oxynitride (SiO<sub>x</sub>N<sub>y</sub>) Formation

Since the absorption of the green laser light within the dopant source and the SiN<sub>x</sub> is negligible almost all the energy is deposited within the top few μm of the silicon substrate. Blecher et al. have developed a numerical model for selective emitter formation of the employed process sequence [89, 90]. Figure 8.4 a) shows the simulated temperature distribution on a planar silicon surface during the passage of a laser spot. The simulation parameters (spot size 14 μm, laser power 13.5 W, scan speed 4 m/s) are closely matching the experimental parameters of this work. The peak temperature of the silicon surface exceeds 2200°C at the center of the laser line. The energy from the heated silicon is

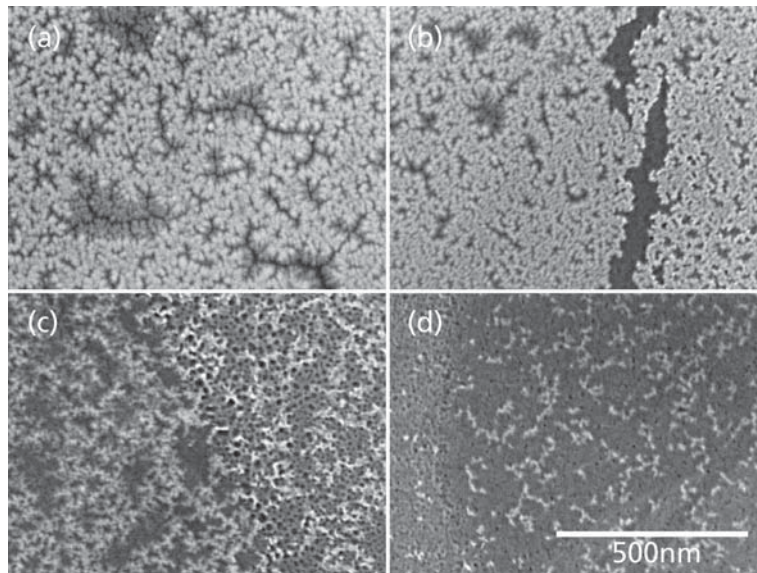


Figure 8.5: Top view SEM images of the surface of a laser doped line (a). The light gray dendritic structure is attributed to  $\text{SiO}_x\text{N}_y$  formation during laser doping. Immersion in BHF 10:1 gradually etches the dendrites as seen after 30 s (b), 60 s (c) and 120 s (d) etching.

transferred via thermal conduction to the capping dielectric and the dopant source layer.

Ablation of the dielectric occurs if the temperature is sufficient to decompose the dielectric film. In the case of  $\text{SiN}_x$  significant decomposition into liquid silicon and gaseous  $\text{N}_2$  starts at about  $1675^\circ\text{C}$  [191] and at  $1878^\circ\text{C}$   $\text{SiN}_x$  is fully instable [178, 179]. This indirect and decomposition driven ablation process is discussed in detail in chapter 7.

The  $\text{SiO}_x\text{N}_y$  forms while the temperature of the surface is lower than  $1750^\circ\text{C}$  and higher than  $1450^\circ\text{C}$ , with the kinetics of  $\text{Si}_2\text{N}_2\text{O}$  formation being highest at  $1700^\circ\text{C}$  [192] ( $\text{SiO}_x\text{N}_y$  formation and its structure will be detailed in Sec. 8.3.1). Using the surface temperature distribution shown in Fig. 8.4 a) the time span  $t_{\text{cw},\text{SiON}}$  during which the temperature is between  $1450^\circ\text{C}$  and  $1750^\circ\text{C}$  is calculated as a function of the distance from the center perpendicular to the traveling direction and plotted in Fig. 8.4 b). Throughout most of the width of the heat-affected zone  $t_{\text{cw},\text{SiON}}$  is at about  $1.5\ \mu\text{s}$ .

Similar to  $\text{SiO}_2$  and  $\text{SiN}_x$ ,  $\text{SiO}_x\text{N}_y$  is a diffusion barrier for nickel and therefore hinders the formation of  $\text{Ni}_x\text{Si}_y$ . BHF etching improves nickel deposition as well as  $\text{Ni}_x\text{Si}_y$  formation. Figure 8.5 shows the effect of BHF etching on a dendritic microstructure visible on the surface of cw-laser doped lines in high resolution SEM images. The diameter of the dendrites was measured to about 20 nm. As the etching time is increased from 30 s to 60 s and 120 s the microstructure is gradually removed. This microstructure is not present in the absence of the  $\text{SiN}_x$  dielectric which was checked on a laser processed sample without  $\text{SiN}_x$  coating. The etch rate of  $\text{SiO}_x\text{N}_y$  in BHF is with 3-40 nm/min [193] higher than the  $\text{SiN}_x$  (0.5-1 nm/min) and lower than the  $\text{SiO}_2$  (100 nm/min)

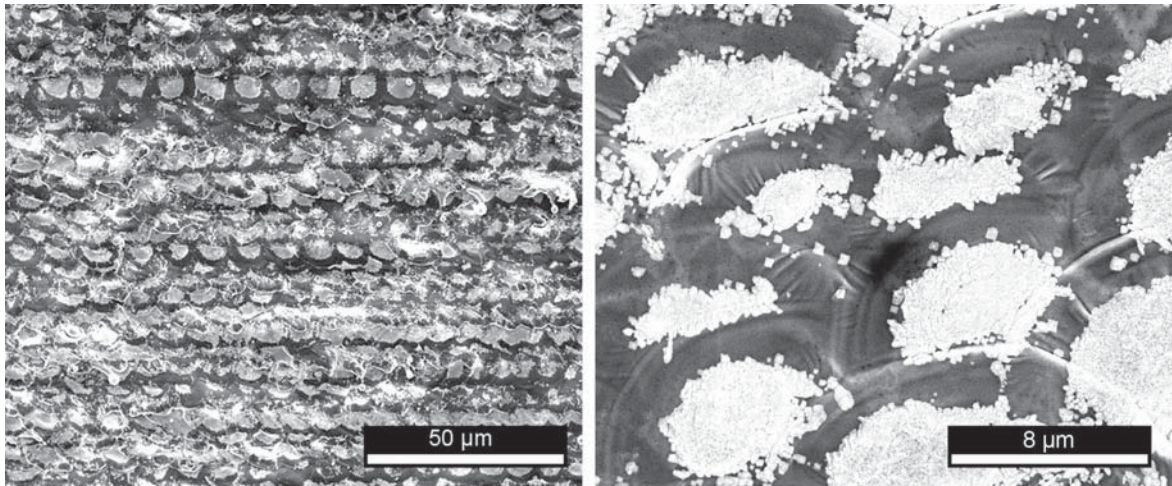


Figure 8.6: Top view SEM image (a) and close-up (b) of ns-pulsed laser treated area after nickel silicide formation at  $450^{\circ}\text{C}$  and nickel etch-back. The light gray areas correspond to formed nickel silicide, the dark areas correspond to "bare" silicon. The  $\text{SiN}_x$  dielectric was ablated with a ns-pulsed laser process which is the sole difference to the sample shown in Fig. 8.2 a).

etch rate [180, 193] and matches well with the observed removal of the 20 nm structure after 2 min. Here it is assumed that the dendrites have a circular cross-section and that the observed lateral dimension of 20 nm corresponds to a similar depth. Therefore, it is presumed that this microstructure is comprised of  $\text{SiO}_x\text{N}_y$ .

### 8.2.4 ns-Pulsed Laser Ablation

The results presented above suggest the assumption that the irradiation time during  $\text{SiN}_x$  ablation is crucial to prevent  $\text{SiO}_x\text{N}_y$  and allow nickel silicide formation. To test this assumption additional samples were produced using the ns-pulsed laser instead of the cw-laser. The formation of  $\text{Ni}_x\text{Si}_y$  as well as the dendritic microstructure were studied as described above.

Figure 8.6 shows the  $\text{Ni}_x\text{Si}_y$  formation on the ns-pulsed laser treated surface after annealing and etching of elemental nickel at two different SEM magnifications. The bright leaf-shaped areas represent  $\text{Ni}_x\text{Si}_y$  as discussed in the previous section. The  $\text{Ni}_x\text{Si}_y$  coverage after the ns-pulsed ablation has significantly increased in comparison to the cw-laser ablation. However, the coverage is not uniform but circular pattern stemming from the ns-pulsed ablation are observable. It is presumed that during ns-pulsed laser irradiation a formation of  $\text{SiO}_x\text{N}_y$  hinders  $\text{Ni}_x\text{Si}_y$  formation in the perimeter of the ablation pattern. With the help of LCPSim [85] the surface temperature distribution of a single laser shot matching the experimental parameters (spot size:  $20\ \mu\text{m}$ ,  $E_{pulse} = 10\ \mu\text{J}$ ,  $\tau_{pulse} = 80\ \text{ns}$ ) was simulated. Figure 8.4 c) exemplary shows the temperature distribution after 200 ns. From this simulation the time during which  $\text{SiO}_x\text{N}_y$  is formed ( $t_{ns,\text{SiON}}$ ) and during which  $\text{SiN}_x$  is ablated ( $t_{ns,\text{SiNx}}$ ) was calculated

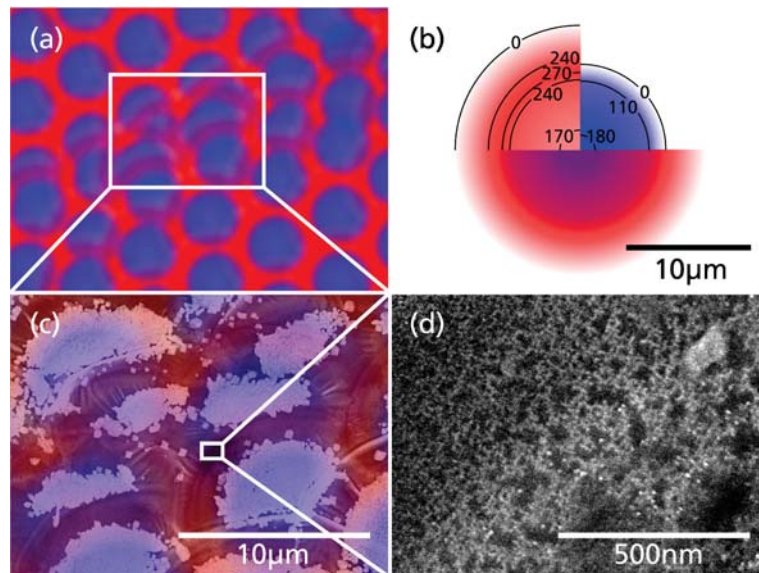


Figure 8.7: Schematic of overlapping laser pulses for  $\text{SiN}_x$  ablation (a). Single pulses are color-coded indicating time spans of  $\text{SiO}_x\text{N}_y$  formation (red) and  $\text{SiN}_x$  ablation (blue) in ns (b). SEM image of a ns-pulse ablated busbar after  $\text{Ni}_x\text{Si}_y$  formation overlaid with the color pattern indicating the position and  $\text{SiO}_x\text{N}_y$  formation regions of laser pulses (c). Close-up SEM image of a dendritic microstructure on the surface of the perimeter region of ablation spots (d).

and is shown in Fig. 8.4 b) as a function of the radius. The  $\text{SiO}_x\text{N}_y$  formation time peaks at about 300 ns at a distance of  $6 \mu\text{m}$  from the center of the ablation spot. At this distance  $t_{\text{ns},\text{SiN}_x}$  is already declining which leads to incomplete  $\text{SiN}_x$  ablation. In this area  $\text{SiO}_x\text{N}_y$  formation is promoted.

Figure 8.7 a) shows a schematic of the composition of single overlapping laser pulses to ablate  $\text{SiN}_x$  from a larger area, e.g., patterning of the busbar. The color of a single spot represents  $t_{\text{ns},\text{SiON}}$  (red) and  $t_{\text{ns},\text{SiN}_x}$  (blue). Figure 8.7 b) shows detailed contour lines of  $t_{\text{ns},\text{SiON}}$  (red) and  $t_{\text{ns},\text{SiN}_x}$  (blue) as well as the corresponding superimposition (bottom) of a single laser pulse.  $\text{SiO}_x\text{N}_y$  formation is expected in areas where red is dominant. Figure 8.7 c) shows a SEM image of a ns-pulsed laser ablated field after  $\text{Ni}_x\text{Si}_y$  formation overlaid with the color pattern indicating the position and  $\text{SiO}_x\text{N}_y$  formation regions of the laser pulses. The pattern in (c) is shown without the overlay in Fig. 8.6 b). It becomes apparent that  $\text{Ni}_x\text{Si}_y$  formation is hindered in a halo stretching from about  $4 \mu\text{m}$  to about  $6 \mu\text{m}$  around an ablation spot. In this area high resolution SEM imaging shown in Fig. 8.7 d) reveals a dendritic microstructure similar to the structures presented in Fig. 8.5 and attributed to  $\text{SiO}_x\text{N}_y$ . A subsequent overlapping laser pulse will partly decompose this  $\text{SiO}_x\text{N}_y$  and lead to the observed leaf-shaped  $\text{Ni}_x\text{Si}_y$  patches. The color pattern overlaid on Fig. 8.7 c) reproduces this consecutive formation and decomposition process by stacking the single laser spots on top of each other according to their temporal order. In areas toned blue decomposition of  $\text{SiN}_x$  and  $\text{SiO}_x\text{N}_y$  dominates and  $\text{Ni}_x\text{Si}_y$  is formed, in regions toned red formation of  $\text{SiO}_x\text{N}_y$  dominates decomposition

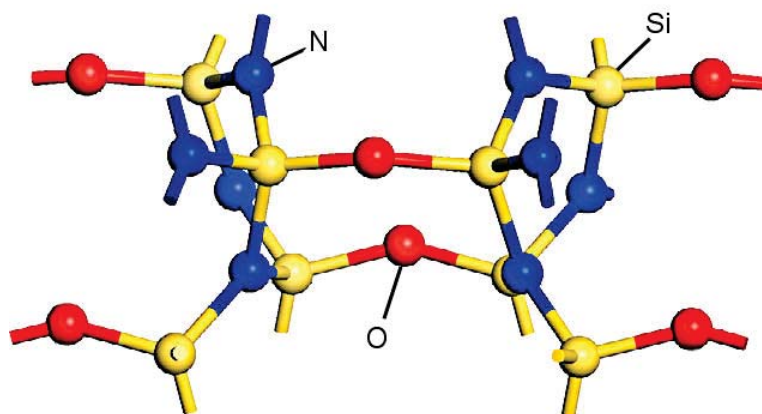


Figure 8.8: Unit cell structure ball-and-stick model of  $\text{Si}_2\text{N}_2\text{O}$  (adapted from [197]).

which hinders nickel diffusion.

### 8.3 Laser Induced $\text{SiO}_x\text{N}_y$ Formation

The investigations in the previous section have shown that a parasitic surface layer comprised of silicon oxynitride ( $\text{SiO}_x\text{N}_y$ ) is formed when  $\text{SiN}_x$  is ablated from silicon using a ns-pulsed or cw-laser process. In this section a row of simple experiments will be conducted that follow-up the main results of the previous section. These experiments show how microstructures can be created using the laser formed  $\text{SiO}_x\text{N}_y$  layer as a diffusion or etching mask, and on the other hand, help to understand the laser induced  $\text{SiO}_x\text{N}_y$  formation mechanism.

#### 8.3.1 Formation and Structure of $\text{SiO}_x\text{N}_y$

Crystalline  $\text{Si}_3\text{N}_4$  is an important material for high performance structural applications such as gas turbines and engines. Amorphous  $\text{Si}_3\text{N}_4$  is an important material in the microelectronics industry due to its chemical stability, high structural density, and excellent dielectric properties [194]. However,  $\text{Si}_3\text{N}_4$  is thermodynamically unstable when exposed to an oxidizing environment. This lead to extensive oxidation studies, designed to gain a fundamental understanding of the oxidation behavior of  $\text{Si}_3\text{N}_4$ , e.g., [192, 194–196]. In this section these findings will be briefly summarized.

Silicon oxynitride in the composition  $\text{Si}_2\text{N}_2\text{O}$  is the only stable compound in the  $\text{Si}_3\text{N}_4$ – $\text{SiO}_2$  system. The formation of  $\text{Si}_2\text{N}_2\text{O}$  occurs via a liquid phase from  $\text{Si}_3\text{N}_4$  and  $\text{SiO}_2$  in a system without molecular oxygen [198]. The investigations of Huang et al. [192] found that below  $1450^\circ\text{C}$  no  $\text{Si}_2\text{N}_2\text{O}$  was detected. They observed gradual decomposition of  $\text{Si}_2\text{N}_2\text{O}$  to  $\text{Si}_3\text{N}_4(\text{s})$ , silicon(l),  $\text{SiO}(\text{g})$ , and  $\text{N}_2(\text{g})$  above  $1750^\circ\text{C}$ . They found the kinetics of  $\text{Si}_2\text{N}_2\text{O}$  formation from  $\text{Si}_3\text{N}_4$  and  $\text{SiO}_2$  is highest at  $1700^\circ\text{C}$ . Thermodynamic calculations of the Si–N–O

## 8. Analysis of Detrimental Surface Layer on Laser Doped Silicon

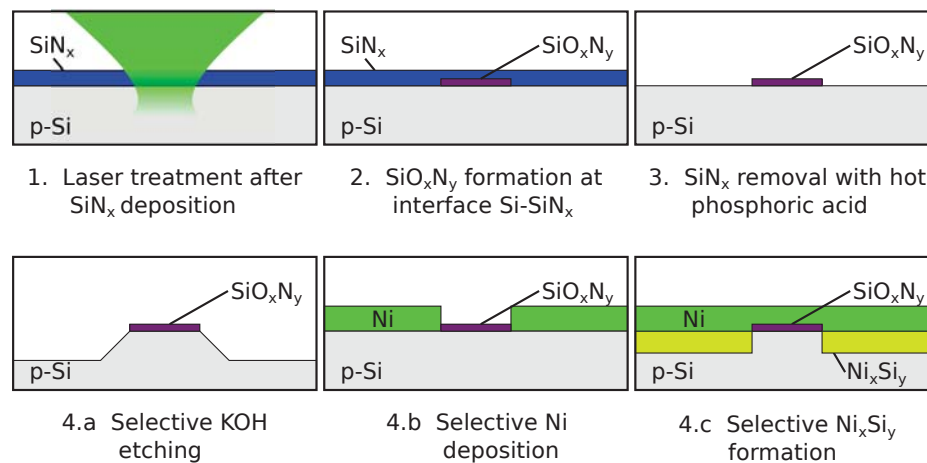


Figure 8.9: Schematic of the sample preparation with a laser formed  $\text{SiO}_x\text{N}_y$  layer (1-3). The  $\text{SiO}_x\text{N}_y$  can be used as a mask for microstructuring (4a), selective nickel deposition (4b), or selective nickel silicide formation (4c).

system conducted by Du et al. [195] indicated that  $\text{Si}_2\text{N}_2\text{O}$  and  $\text{SiO}_2$  should be formed when  $\text{Si}_3\text{N}_4$  is oxidized at temperatures between  $1200^\circ\text{C}$  and  $1400^\circ\text{C}$ . By using a kinetic model, the molecular oxygen diffusivity in  $\text{Si}_2\text{N}_2\text{O}$  is found to be significantly lower than in  $\text{SiO}_2$ . Du et al. concluded that the structurally dense  $\text{Si}_2\text{N}_2\text{O}$  is a diffusion barrier superior to  $\text{SiO}_2$ .

The  $\text{Si}_2\text{N}_2\text{O}$  layer in oxidation studies of crystalline  $\text{Si}_3\text{N}_4$  was identified as a single-phase material rather than a physical mixture of  $\text{Si}_3\text{N}_4$  and  $\text{SiO}_2$  [194]. The  $\text{Si}_2\text{N}_2\text{O}$  structure is built up of  $\text{SiN}_3\text{O}$  tetrahedra joined together by sharing corners. The orthorhombic crystal structure consists of irregular, but parallel, sheets of covalently bonded silicon and nitrogen atoms linked by Si-O-Si bonds [197, 199]. The unit cell structure of  $\text{Si}_2\text{N}_2\text{O}$  is shown in Fig. 8.8. Because of the similarities between the structure of  $\text{Si}_3\text{N}_4$  and  $\text{Si}_2\text{N}_2\text{O}$ , there is some limited solubility and a solid solution ( $\text{SiO}_x\text{N}_y$ ) can be formed without a change of structure.

### 8.3.2 Microstructuring using Silicon Oxynitride

In Sec. 8.2 it was shown that a parasitic  $\text{SiO}_x\text{N}_y$  layer is created during cw-laser ablation of  $\text{SiN}_x$ . In this section the cw-laser will be used to intentionally form  $\text{SiO}_x\text{N}_y$  on a  $\text{SiN}_x$  covered silicon wafer. This laser patterned  $\text{SiO}_x\text{N}_y$  layer can be used for microstructuring, selective metal plating or selective nickel silicidation.

#### Sample Preparation

For the following experiment FZ silicon wafer were covered with a 75 nm thick  $\text{SiN}_x$  layer from a PECVD system (Roth & Rau SiNA XS). Figure 8.9 shows a schematic of the sample preparation. The wafer was irradiated using the

laser setup described in chapter 5. The laser power was varied between 5 and 9 W and the laser scanning speed was varied between 0.5 and 10 m/s. These parameters correspond to linear energy densities  $\varepsilon$  (cf. Eq. 6.3) between 0.5 and 18 J/m. Individual lines were drawn using a laser spot size of 15  $\mu\text{m}$ . A change of the optical appearance of the laser treated area was observed at  $\varepsilon$  above 2 J/m, using the LEXT confocal microscope. Below this threshold value a decomposition of the SiN<sub>x</sub> layer was not visible and no distinction could be made between the processed and unprocessed SiN<sub>x</sub> covered silicon wafer.

After the laser process the SiN<sub>x</sub> layer was removed by immersing the wafer in an agitated bath of hot phosphoric acid (160° C) for 4 min. After this step (cf. Fig. 8.9 step 3.) the SiN<sub>x</sub> layer is fully removed from the surface whereas silicon oxide containing species are not etched [180].

The masking effect of SiO<sub>x</sub>N<sub>y</sub> was tested in three separate followup experiments depicted as 4.a), 4.b), and 4.c) in Fig. 8.9:

- 4.a) Silicon ridges: Silicon ridges were created by etching the exposed silicon of the sample in heated KOH (80° C).
- 4.b) Selective plating: After a 30 s deglaze in 1 % HF, Nickel was plated selectively on the exposed silicon using Enpat electroless nickel electrolyte (produced by Transene Company).
- 4.c) Selective silicidation: After a 30 s deglaze in 1 % HF, the wafer surface was sputter coated with nickel and annealed at 450° C for 5 min in a rapid thermal processor. After that, the elemental nickel was removed using piranha etchant [180].

### Ridge Microstructure

By anisotropic etching of the laser treated wafer silicon ridges were produced. The silicon surface is masked with a SiO<sub>x</sub>N<sub>y</sub> layer that formed along the laser drawn line. The SiO<sub>x</sub>N<sub>y</sub> layer was found to be an effective mask at linear energy densities  $\varepsilon$  above 0.7 J/m. Figure 8.10 a) shows a SEM image of the 5  $\mu\text{m}$  wide and 2  $\mu\text{m}$  high silicon ridge created at 0.7 J/m ( $P=7\text{ W}$ ,  $v=10\text{ m/s}$ ). If  $\varepsilon$  is increased to 2.3 J/m ( $P=7\text{ W}$ ,  $v=3\text{ m/s}$ ) the ridge widens to 15  $\mu\text{m}$  as shown in (b). If  $\varepsilon$  is further increased the SiO<sub>x</sub>N<sub>y</sub> in the central area of the laser drawn line is heated above its decomposition temperature, which leads to porosities in the SiO<sub>x</sub>N<sub>y</sub> mask. At  $\varepsilon$  above 10 J/m ( $P=5\text{ W}$ ,  $v=0.5\text{ m/s}$ ) the central area of the laser drawn line is not fully protected from the silicon etchant, which results in the 20  $\mu\text{m}$  wide double-ridge microstructure shown in (c).

### Selective Plating

Nickel was deposited solely on the bare silicon surface of the samples. The reduction reaction of the electroless nickel electrolyte was not possible on areas

## 8. Analysis of Detrimental Surface Layer on Laser Doped Silicon

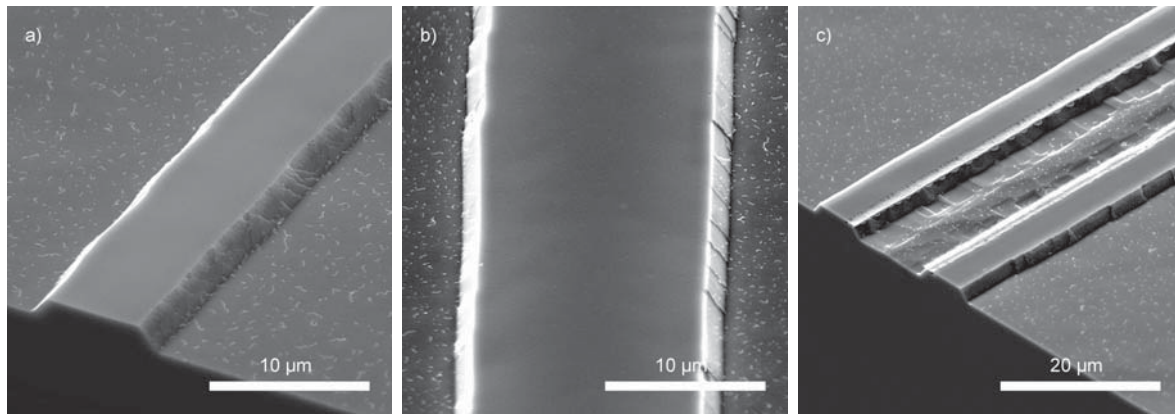


Figure 8.10: SEM images of silicon ridge structures formed by selective KOH etching. The  $\text{SiO}_x\text{N}_y$  etching mask was created at different laser parameters:  $P=7\text{ W}$ ,  $v=10\text{ m/s}$  (a);  $P=7\text{ W}$ ,  $v=3\text{ m/s}$  (b);  $P=5\text{ W}$ ,  $v=0.5\text{ m/s}$  (c)

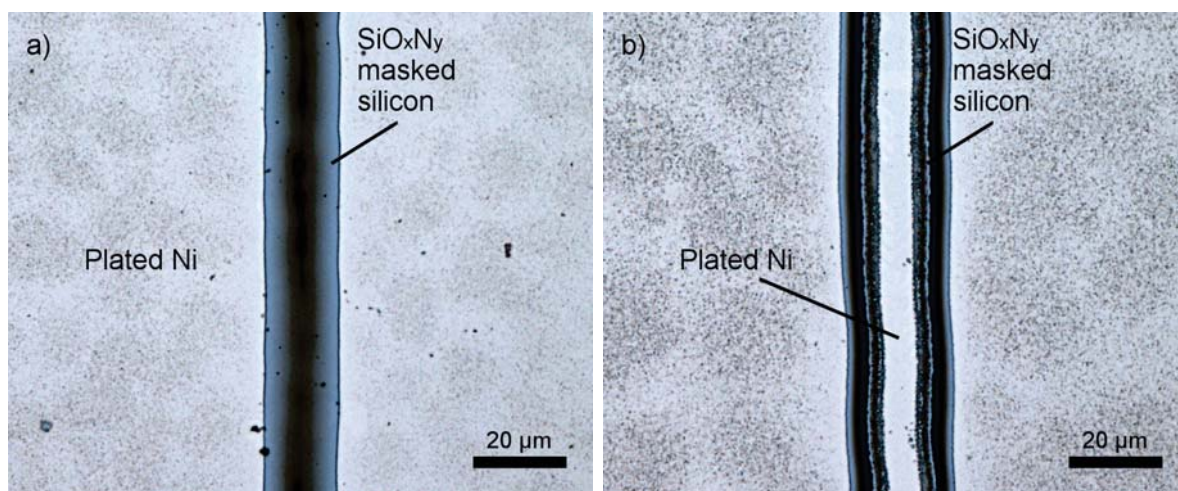


Figure 8.11: Microscopy images of selective nickel plating on a silicon wafer masked with laser formed  $\text{SiO}_x\text{N}_y$ . After electroless plating the only area not covered with nickel is the laser processed area. The  $\text{SiO}_x\text{N}_y$  layer was created at different laser parameters:  $P=5\text{ W}$ ,  $v=3\text{ m/s}$  (a);  $P=9\text{ W}$ ,  $v=3\text{ m/s}$  (b)

covered with laser patterned  $\text{SiO}_x\text{N}_y$ . Similar to the reported results in the previous section, the  $\text{SiO}_x\text{N}_y$  layer was found to be effective as a plating mask at  $\epsilon$  above  $0.7\text{ J/m}$ . Figure 8.11 a) shows a microscopy image of a  $15\text{ }\mu\text{m}$  wide area which is not covered with plated nickel. This laser line was created with  $\epsilon=1.7\text{ J/m}$  ( $P=5\text{ W}$ ,  $v=3\text{ m/s}$ ). This sample was cut perpendicular to the laser line into  $5\text{ mm}$  wide strips. With a multimeter the resistance across the separating laser line was measured to  $0.15\text{ M}\Omega$ . If  $\epsilon$  is increased to  $3\text{ J/m}$  the  $\text{SiO}_x\text{N}_y$  layer in the center of the laser line is partly decomposed which results in a fine strip of plated nickel along the laser processed line as shown in (b). The corresponding resistance across the nickel gap of a  $5\text{ mm}$  wide sample strip was measured to  $0.05\text{ M}\Omega$ . The decrease of the resistance is further prove for the nickel formed in the center of the laser line.

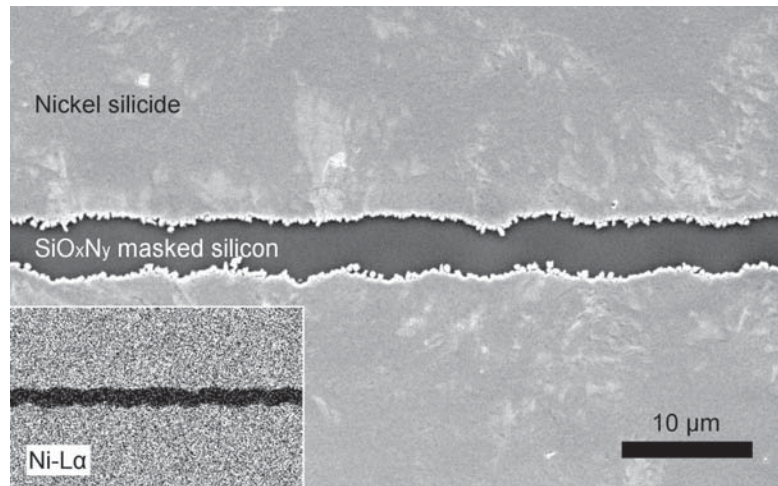


Figure 8.12: Top view SEM image of nickel silicide on a silicon wafer and corresponding EDX mapping of the Ni-L $\alpha$  peak (inset). The silicide was produced by nickel sputtering and annealing at 450° C for 5 min. After annealing the elemental nickel was etched away. Along a laser processed line a SiO $_x$ N $_y$  layer was formed which prevents nickel silicide formation.

### Selective Silicidation

The structurally dense SiO $_x$ N $_y$  also acts as a barrier for nickel diffusion into the underlying silicon. During in the annealing step nickel silicide was formed in all areas with the exception of the laser treated line. Figure 8.12 shows a SEM image of the laser treated sample at  $\varepsilon=0.9$  J/m ( $P=9$  W,  $v=10$  m/s) after annealing and etching of the elemental nickel. The inset shows the corresponding EDX signal of the Ni-L $\alpha$  peak. The material contrast of the SEM image and the EDX signal mapping proves that nickel has formed exclusively in regions not irradiated by the cw-laser.

Microscopy imaging directly after the cw-laser process showed that the SiN $_x$  layer exhibits no signs of decomposition below a threshold  $\varepsilon$  of about 2 J/m. Nevertheless, all followup experiments discussed above showed that a barrier layer is formed even below this threshold value. This observation can be explained if the SiO $_x$ N $_y$  layer is formed at the interface between the silicon bulk and the SiN $_x$  as indicated in Fig. 8.9 2.). At  $\varepsilon$  below the threshold SiO $_x$ N $_y$  could be formed while the surface temperature of the molten silicon is still below the decomposition temperature of SiN $_x$ . In that case, the source of oxygen for the formation of SiO $_x$ N $_y$  may be a native SiO $_2$  layer on the wafer surface before SiN $_x$  deposition. By cw-laser processing such a Si–SiO $_2$ –SiN $_x$  stack is presumed to be transformed into a Si–SiO $_x$ N $_y$ –SiN $_x$  stack.

## 8.4 Implications for Solar Cell Laser Processing

The SiO $_x$ N $_y$  layer formed during cw-laser ablation of a SiN $_x$  layer has a number of detrimental and few advantageous consequences for the production of solar

cells with nickel-copper plated contacts. These effects are discussed in the following.

### 8.4.1 Consequences of $\text{SiO}_x\text{N}_y$ Formation

As shown in this chapter and in chapter 6 the nickel deposition, especially from electroless electrolytes, but to some extent also for LIP, is severely hindered by the  $\text{SiO}_x\text{N}_y$  layer. Whereas on individual laser lines an acceptable nickel deposition quality was achieved, on laser treated areas comprised of overlapping laser lines it was not possible to form a homogeneous and dense nickel layer. In a nickel-copper plating scheme such a homogeneous and dense layer, which covers all areas where the  $\text{SiN}_x$  was ablated, is essential to prevent the diffusion of copper into the silicon and prevent performance degradation of the solar cell.

In addition to this, the results presented above show clearly that a  $\text{SiO}_x\text{N}_y$  layer also acts as a barrier for nickel diffusion into the silicon, thereby preventing the formation of nickel silicide. Deep nickel silicide growth can lead the degradation of solar cell performance as detailed in Sec. 3.4.2. The formation of a  $\text{SiO}_x\text{N}_y$  barrier layer on areas with a shallow emitter, e.g., at the edge of a laser line where satellite ablation occurs, may thus be desirable. On the other hand, silicide formation is elemental for the creation of a low contact resistance as well as the mechanical adhesion between the silicon and the metal contact, as detailed in Sec. 3.4. The latter is seen as a primal challenge in the production of solar cells with nickel-copper plated contacts and will be in the focus of the next chapter.

### 8.4.2 Overcoming $\text{SiO}_x\text{N}_y$ Connected Challenges

One way to overcome the challenges presented above is to effectively prevent the formation of  $\text{SiO}_x\text{N}_y$ . The other way relies on removing the parasitic layer after cw-laser processing.

#### Preventing Formation of $\text{SiO}_x\text{N}_y$

As shown in Sec. 8.2.4 shorter irradiation length for  $\text{SiN}_x$  ablation results in reduced  $\text{SiO}_x\text{N}_y$  formation. Ultra short laser pulse processing, such as ps-pulsed laser ablation, results in  $\text{SiN}_x$  ablation directly suitable for nickel plating[31, 32]. On the one hand, short pulse lengths decrease  $\text{SiO}_x\text{N}_y$  formation. On the other hand, shorter irradiation results in a reduction of the laser doping quality. The predominance of diffusive dopant mixing in ns-pulsed laser doping results in shallow emitter depths at the edges of the laser doped areas [72], which are thus prone for nickel silicide growth induced degradation. In this regard, cw-laser doping is better suited for laser doping since it allows deep and homogeneous doping at high processing speed. Due to melt convection the laser doped region extends beyond the width of  $\text{SiN}_x$  ablation, producing a deep emitter below every  $\text{SiN}_x$  ablated area. The edge-parameter ( $\Delta_{\text{edge}}$ ) characterizing

this beneficial lateral excess doping is discussed in detail in Sec. 6.3.2. With cw-laser doping, doping depths on the order of micrometers can be produced at scanning speeds of meters per second.

If laser doping and laser ablation are split into separate processes cw-laser doping can be performed before  $\text{SiN}_x$  deposition and ns-pulsed or ps-pulsed laser processing can be used for the ablation of the  $\text{SiN}_x$  dielectric. On the one hand, this would combine the benefits of the individual processes, prevent the formation of  $\text{SiO}_x\text{N}_y$ , and results in mechanically and electrically stable nickel-copper cells. On the other hand, this processing sequence, employing two laser systems, significantly increases process complexity and reduces the maximum solar cell efficiency. This sequence will be studied in detail in the next chapter.

It can be assumed that  $\text{SiO}_x\text{N}_y$  formation is also prevented if the source of oxygen needed for the oxidation of  $\text{SiN}_x$  is removed. The removal of native oxide before  $\text{SiN}_x$  deposition and processing in a oxygen free ambient would be possible alterations to the processing sequence in order to hinder  $\text{SiO}_x\text{N}_y$  formation. Unfortunately, these alterations are beyond the scope of this work. To this point, the source of oxygen as well as the detailed mechanics of  $\text{SiO}_x\text{N}_y$  formation are not fully understood.

### Removal of $\text{SiO}_x\text{N}_y$

$\text{SiO}_x\text{N}_y$  can be chemically etched using HF as shown above. The etch rate of  $\text{SiO}_x\text{N}_y$  in BHF is higher than the etch rate of  $\text{SiN}_x$ . Nevertheless, BHF etching for a duration sufficient to remove the  $\text{SiO}_x\text{N}_y$  layer results in a color change of the  $\text{SiN}_x$  layer as well as an increase in parasitic nickel plating. In the next chapter the consequences of BHF removal of the  $\text{SiO}_x\text{N}_y$  layer for contact adhesion and device performance will be investigated.

Like the  $\text{SiN}_x$  layer, also the  $\text{SiO}_x\text{N}_y$  layer can be ablated using ns-pulsed or ps-pulsed laser processing. In a processing sequence that employs two laser systems, laser doping can be performed using the cw-laser. The cw-laser spot is directly followed by a pulsed laser spot which ablates the freshly formed  $\text{SiO}_x\text{N}_y$ . In this setup the increase in process complexity is limited since laser doping and  $\text{SiO}_x\text{N}_y$  ablation can be housed in a single tool. The next chapter will present and discuss the advantages of this sequence in detail.

## 8.5 Conclusion

Meager nickel deposition on cw-laser ablated  $\text{SiN}_x$  passivated silicon suggested the assumption that a detrimental surface layer is formed during laser processing. In this chapter the presence of such a layer was proven by nickel plating and silicide formation, both of which improved after harsh chemical surface etching. The surface layer was identified as silicon oxynitride ( $\text{SiO}_x\text{N}_y$ ) by means of XPS measurements. The effect of BHF etching on the dendritic structure of the  $\text{SiO}_x\text{N}_y$  was imaged using SEM imaging. This microstructure is to a lesser

extend also present after ns-pulsed laser ablation. Numerical simulation of the surface temperature during laser ablation agreed with the extend of  $\text{SiO}_x\text{N}_y$  formation during cw and ns-pulsed irradiation.

Follow-up experiments were conducted in order to study the laser induced  $\text{SiO}_x\text{N}_y$  formation mechanism. It was shown that the laser formed  $\text{SiO}_x\text{N}_y$  can be used for microstructuring, selective nickel deposition, and nickel silicide formation.  $\text{SiO}_x\text{N}_y$  formation at laser intensities insufficient to cause optical change of the  $\text{SiN}_x$  layer allowed the presumption that  $\text{SiO}_x\text{N}_y$  forms on the Si– $\text{SiN}_x$  interface, with native  $\text{SiO}_2$  serving as the source of oxygen.

From these findings implications for solar cell laser processing were drawn. These include complications that arise from the formation of a  $\text{SiO}_x\text{N}_y$  layer, as well as alterations to the standard process sequence of cw-laser doping which are presumed to overcome these complications. These alterations are aimed to either circumvent  $\text{SiO}_x\text{N}_y$  formation or include measures to remove it before nickel plating. In the next chapter some of the suggested alterations to the standard process sequence proposed here will be evaluated. This will be done by producing test cells and characterizing them in terms of electrical and mechanical stability.

## 9 Overcoming Mechanical Challenges for Ni-Cu Plated Contacts

The experiment presented in the first part of this chapter will prove, that LDSE doped contact openings, in its original form, are not suitable for silicidation and exhibit low adhesion to plated metal front contacts. In Sec. 9.3 alternative processing sequences are presented that overcome this limitation and prevent mechanical and electrical device failure. The chapter will be concluded with a comparison between efficient solar cells produced with the proposed laser processing sequences, based on computer simulations.

Besides electrical performance, processes for industrial production have tight constraints on processing speed, process stability, parasitic plating and long-term stability. Especially the adhesion of the plated front metal contact was identified as a challenge [26, 33, 34, 108]. Poor adhesion can cause problems during automated module manufacturing, leads to detachment of contact fingers and reduces long-term module stability. The adhesion of silicon and nickel can be promoted by mechanical interlocking of the metal within surface keying features [36, 200, 201]. A more commonly used approach is based on the creation of a nickel silicide ( $\text{Ni}_x\text{Si}_y$ ) layer jointing silicon and nickel by chemical bonding [109–111]. In the latter approach plated nickel diffuses into the underlying silicon wafer and forms a nickel silicide layer during an annealing step at elevated temperatures. Here silicon and silicide are bound by covalent bonding and silicide and nickel by metal bonding [202]. Details regarding nickel diffusion and silicide formation can be found in Sec. 3.4.2.

Mondon et al. [111] have demonstrated excellent contact adhesion between solar cell and front side metallization using this method. However, the growth of nickel silicide into the emitter involves the risk of metal-induced shunting of the p-n junction lowering cell fill-factor and efficiency [77, 109, 203]. For this reason forming a deep emitter under the contacts by using a long pulse or cw-laser process seems particularly interesting. However, in the previous chapter it was shown, that the cw-laser treated surface is not suitable for silicide formation due to a blocking silicon oxynitride ( $\text{SiO}_x\text{N}_y$ ) layer. This layer has been identified by means of x-ray photoelectron spectroscopy (XPS) measurements on the laser treated surface.

In the following the implications of different surface treatments on nickel silicide formation are studied using scanning electron microscopy (SEM) and energy-dispersive X-ray spectroscopy (EDX). Different process sequences will be suggested that allows to form a selective emitter using cw-laser doping that proves to produce electrically and mechanically stable nickel-copper plated solar

cells. This process creates a deep p-n junction which effectively reduces the occurrences of metal-induced shunts shown using pseudo light current-voltage measurements (Suns  $V_{oc}$ ) measurements.

### 9.1 Experimental

The samples for this experiment have been fabricated using common industrial silicon material and processes, with the exception of the front contact system which has been produced by laser processing and single sided light-induced plating (LIP), as detailed in Chapter 5.

#### 9.1.1 Basic Sample Design

1-3  $\Omega$  cm industrial grade CZ  $156 \times 156 \text{ mm}^2$  p-type silicon wafers with random pyramid texture and a thickness of  $200 \mu\text{m}$  were used. A  $90 \Omega$  emitter was created with a  $\text{POCl}_3$  process in a tube furnace. After phosphosilicate glass removal and chemical edge isolation a silicon nitride ( $\text{SiN}_x$ ) with a thickness of  $75 \text{ nm}$  was deposited on the front side using a plasma-enhanced chemical vapor deposition (PECVD) system (Roth & Rau SiNA XS). Using screen printing and firing at  $880^\circ \text{C}$ , an aluminum back surface field (Al-BSF) was formed on the rear side.

Subsequently, the front side was spin-coated with 30 wt%  $\text{H}_3\text{PO}_4$  at 3000 RPM for 60 s, creating a  $1.5 \mu\text{m}$  thick liquid phosphorous dopant layer. The cw-laser was used to locally dope and pattern the wafers using the setup described in Chapter 5. The 15 W laser spot with a diameter of  $15 \mu\text{m}$  was scanned across the sample at velocity of 5 m/s. As shown in Chapter 6, the laser power is sufficient to simultaneously ablate the  $\text{SiN}_x$  and create  $14 \mu\text{m}$  wide and  $4 \mu\text{m}$  deep highly doped lines with a sheet resistance of about  $13 \Omega$ . In order to remove the SOD residue the wafers were cleaned in a DI-water rinser.

#### 9.1.2 Front Contact Formation

In order to study the influence of the surface condition of the laser treated region, regarding silicide formation, electrical properties, and metal contact adhesion,  $48 \times 48 \text{ mm}^2$  test cells were produced with a finger spacing of 1.5 mm and a single 1.5 mm wide busbar.

This batch was divided into three groups (20 samples each) following different processing sequences to alter the surface condition of the laser treated areas. Also a fourth group has been produced without a selective emitter as a reference. The different process sequences are outlined in Fig. 9.1.

##### **Group: $\text{SiN}_x \rightarrow \text{open+dope}$**

In the first group the laser doping takes place after the  $\text{SiN}_x$  deposition. This is the standard LDSE process, where the ablation of the  $\text{SiN}_x$  and the local

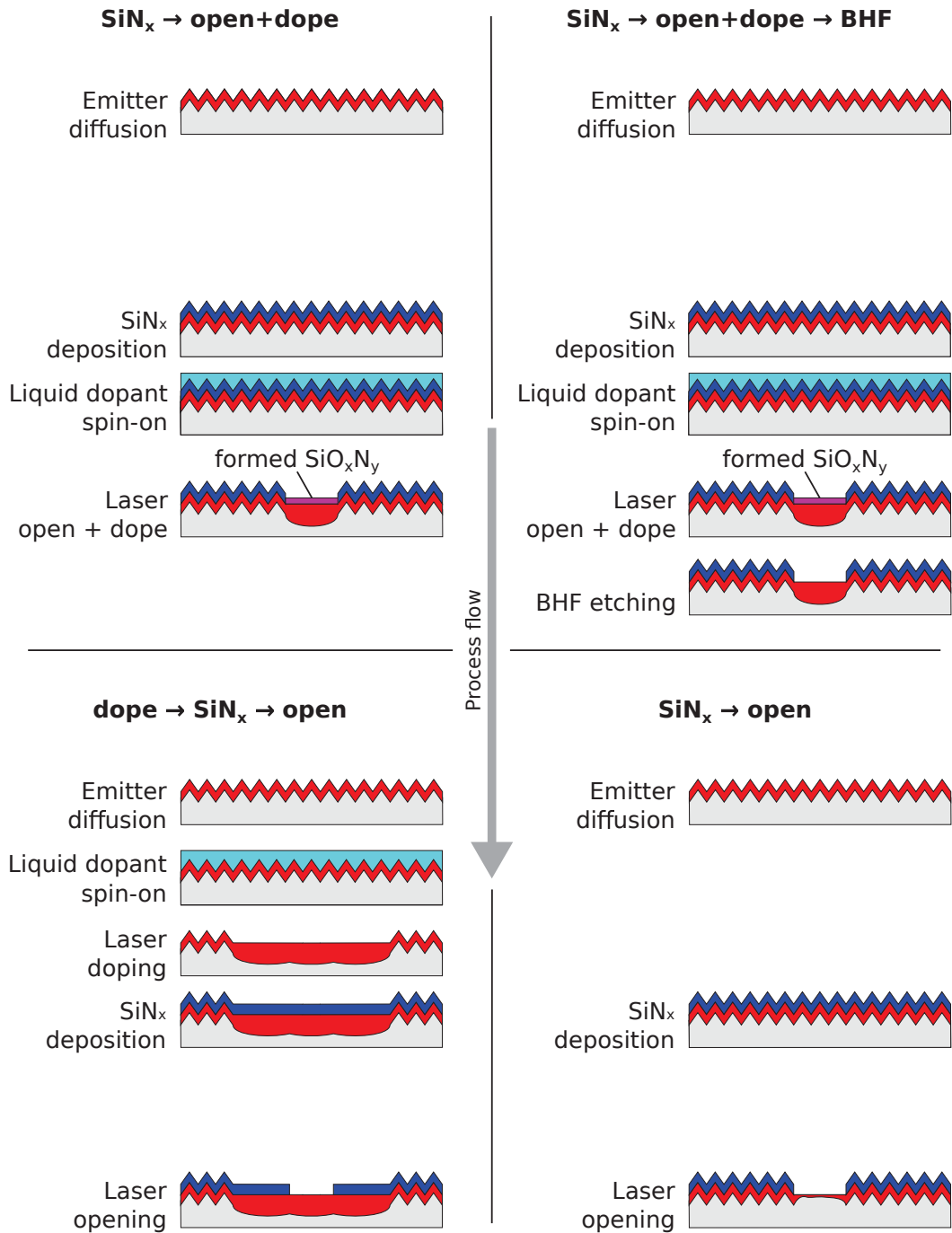


Figure 9.1: Schematic of the process sequences used in this chapter to create selective emitter structures with a cw-laser doping process. The " $\text{SiN}_x \rightarrow \text{open+dope}$ " sequence is a straight forward approach where the local dopant diffusion and  $\text{SiN}_x$  ablation is combined into one step, this is also referred to as the LDSE process. Using an additional BHF treatment in the " $\text{SiN}_x \rightarrow \text{open+dope} \rightarrow \text{BHF}$ " sequence alters the surface condition of the laser doped lines. The " $\text{dope} \rightarrow \text{SiN}_x \rightarrow \text{open}$ " sequence splits the dopant diffusion and  $\text{SiN}_x$  ablation into separate processing steps. The sequence denoted " $\text{SiN}_x \rightarrow \text{open}$ " is a ns-pulsed laser ablation of the  $\text{SiN}_x$  layer without additional doping.

dopant diffusion occurs simultaneously during the passage of the laser spot. This sequence is denoted as "SiN<sub>x</sub> → open+dope" and has proven to produce Al-BSF cells exceeding efficiencies of 19 % [18, 25].

**Group: SiN<sub>x</sub> → open+dope → BHF**

In the second group the silicon wafer is immersed in buffered oxide etch (BHF 10:1 ≈ HF 7 %) for 60 s after the laser doping in order to remove the SiO<sub>x</sub>N<sub>y</sub> surface layer and allow nickel diffusion into the silicon, during an annealing step. This extended LDSE sequence will be denoted "SiN<sub>x</sub> → open+dope → BHF".

**Group: dope → SiN<sub>x</sub> → open**

It is expected that the increased etch rate of the BHF leads to an increased amount of etched pinholes in the passivation layer resulting in parasitic nickel plating. To address this limitation the third group employs two laser processing steps. One before and one after the SiN<sub>x</sub> deposition. The laser doping takes place directly after the furnace diffusion. The SOD is spun onto the phosphorus silicate glass (PSG). The laser doping was performed using the same parameters (15 W, 5 m/s) as in the "SiN<sub>x</sub> → open+dope" and "SiN<sub>x</sub> → open+dope → BHF" cases, which leads to similar doping depths. After the subsequent PSG etching and SiN<sub>x</sub> deposition the dielectric patterning is performed with the ns-pulse laser (Innolas Nanio). The laser doped area needs to be wider than the 14 μm ns-laser ablation width due to imperfect alignment of the two laser systems. The doping width was set to 150 μm using overlapping laser lines. Figure 9.1 illustrates this sequence denoted as "dope → SiN<sub>x</sub> → open".

**Group: SiN<sub>x</sub> → open**

As a reference two test cells have been produced without laser doping and SiN<sub>x</sub> patterning by ns-laser pulses ("SiN<sub>x</sub> → open"). The spot size (20 μm), pulse energy (10 μJ), and the pulse duration (80 ns) have been adjusted to fully ablate the SiN<sub>x</sub> layer in a circular area of about 14 μm. The overlap (about 50 %) has been chosen such that the busbar can be fully ablated.

**Nickel Plating and Silicide Formation**

A 1 μm thin layer of nickel was deposited on the laser pattern using light-induced plating in a Watts type nickel electrolyte [114] after a 30 s deglaze in HF (1 %) using the RENA inline plating tool described in Chapter 5. A subsequent rather harsh annealing step at 450 °C for 5 minutes in forming gas atmosphere was employed to create a nickel silicide layer and to provoke shunting. As explained in detail in Sec. 5.2.2 this process was shown to form a homogeneous nickel silicide layer in earlier experiments [154]. The process sequence "dope →

SiN<sub>x</sub> → open” proved to be electrically stable to annealing so that a prolonged time of 10 minutes was chosen to test this sequence in even harsher conditions.

### 9.1.3 Electrical and Mechanical Characterization

In order to characterize the electrical properties of the fabricated test cells a Sinton Instruments Suns-V<sub>oc</sub> stage (cf. Sec. 4.5.3) was used to determine the pseudo light IV curves. Silicidation induced shunting was characterized using the pseudo fill factor (*pFF*) calculated from the these curves measured after annealing, which proves to be particularly sensitive to this defect mechanism [77, 203]. Piranha etchant [180] was used to etch off elemental nickel from the front side of the solar cell. Using SEM and EDX (cf. Sec. 4.1) the silicide coverage of the laser doped lines was measured. Reverse biased electroluminescence (ReBEL) (cf. Sec. 4.5.4) studies were performed with a PIXIS 1024 camera and with a confocal laser scanning microscope ( $\mu$ -ReBEL) as described by Gundel et al. [204]. The shown  $\mu$ -ReBEL images are the pixel-wise integrated count rates of photon energies between 1.85 eV and 2.35 eV (530-670 nm). At a reverse bias of 16 V diode breakdowns are found to appear at recombination active defects (type II breakdown) in solar cells [146] and emit photons in the visible to mid-infrared range [205]. It is assumed that nickel silicide growth causes these shunts as metallic precipitates have been identified to cause type II breakdowns [203, 206].

Following the nickel-copper-silver front side metallization scheme employed by Mondon et al. [111] nickel light-induced plating was used to deposit a 1  $\mu$ m thin nickel layer on the silicide covered pattern, which was defined by the laser process. This is followed by light-induced copper and silver plating.

In order to characterize the mechanical adhesion of the front side metallization a standard metal ribbon was soldered to the silver capped busbar using a manual solder station. The force needed to peel off the ribbon under 90° angle was recorded with a pull-tester (cf. Sec. 4.5.5). The peel force is normalized to a busbar width of 1 mm. As a last point the failing interface was studied using SEM imaging of the fractured contact area of the test cells.

## 9.2 Results and Discussion

In the following the results from the experiment are presented. At first, the shunting of the p-n junction during the front contact formation is studied. Then the position of a localized shunt is determined and the shunting mechanism is derived. At last, the contact adhesion is measured and correlated to the coverage of the busbar with nickel silicide.

### 9.2.1 Front Contact Formation

After the laser process and nickel plating, right before annealing, the *pFF* of the test cells were measured. All groups had *pFF* values well above 83%.

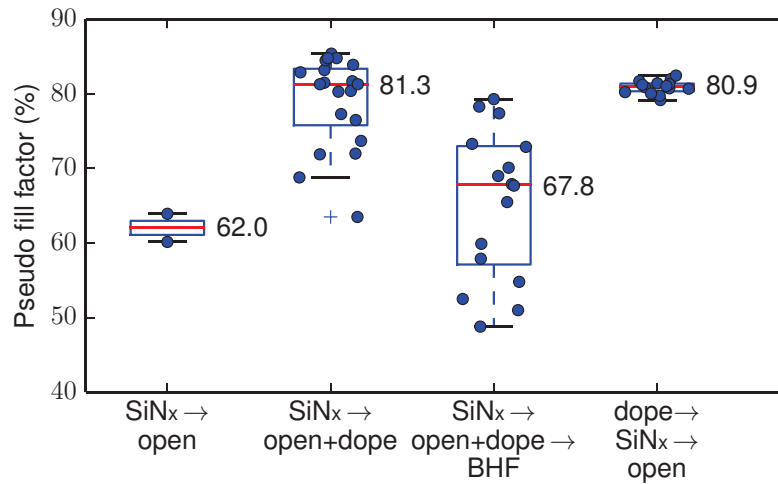


Figure 9.2: Box plot of pseudo fill factor values after annealing at 450° C. The numbers within the plot represent the median values. Ni<sub>x</sub>Si<sub>y</sub> growth has penetrated the p-n junction resulting in  $pFF$  values below 80 % in the case without the selective emitter ("SiN<sub>x</sub> → open") and in the case with the additional harsh BHF treatment ("SiN<sub>x</sub> → open+dope → BHF"). "SiN<sub>x</sub> → open+dope" and "SiN<sub>x</sub> → open+dope → BHF" groups show significant scattering as compared to "dope → SiN<sub>x</sub> → open" which hints at a degradation mechanism with low probability.

However, after annealing at 450° C the picture changed. Figure 9.2 shows the  $pFF$  values of the cells after the thermal process intended to form a nickel silicide layer. After annealing, the samples without the laser doped emitter show the highest degradation. In the "SiN<sub>x</sub> → open" group, the shallow p-n junction is severely shunted by silicide growth which results in a low median  $pFF$  value of 62 %. The  $pFF$  of the laser doped emitter designs are generally higher, whereas only the "SiN<sub>x</sub> → open+dope" and the "dope → SiN<sub>x</sub> → open" sequence yields acceptable  $pFF$  values above 80 %. In these cases the laser doping seems to prevent the shunting of the p-n junction.

However, SEM imaging of the formed nickel silicide reveals that the cause for the stability of the "SiN<sub>x</sub> → open+dope" group to annealing can be put down to a different reason. Figure 9.3 shows the nickel silicide formed on the laser lines after the different sequences. In the case of "SiN<sub>x</sub> → open+dope", shown (a), little to none silicide is formed due to the SiO<sub>x</sub>N<sub>y</sub> nickel-diffusion barrier (cf. Chapter 8). If the SiO<sub>x</sub>N<sub>y</sub> is removed using BHF ("SiN<sub>x</sub> → open+dope → BHF") the silicide coverage increases as seen in (b) but at the same time the  $pFF$  rapidly decreases to a value below 70 %.

Both processes which employ the cw-laser to simultaneously dope and open the SiN<sub>x</sub> layer exhibit unusual variations of the  $pFF$  value. The loss in the pseudo fill factor  $\Delta_{pFF}$ , defined as the difference between the  $pFF$  measurement before and after the annealing step, varies in the "SiN<sub>x</sub> → open+dope → BHF" case between 3 and 35 %. In the "SiN<sub>x</sub> → open+dope" case the deviation from the median value is reduced, however the distribution of  $pFF$  is severely skewed, with a tail extending to low  $pFF$  values. The fact that the  $pFF$  values have

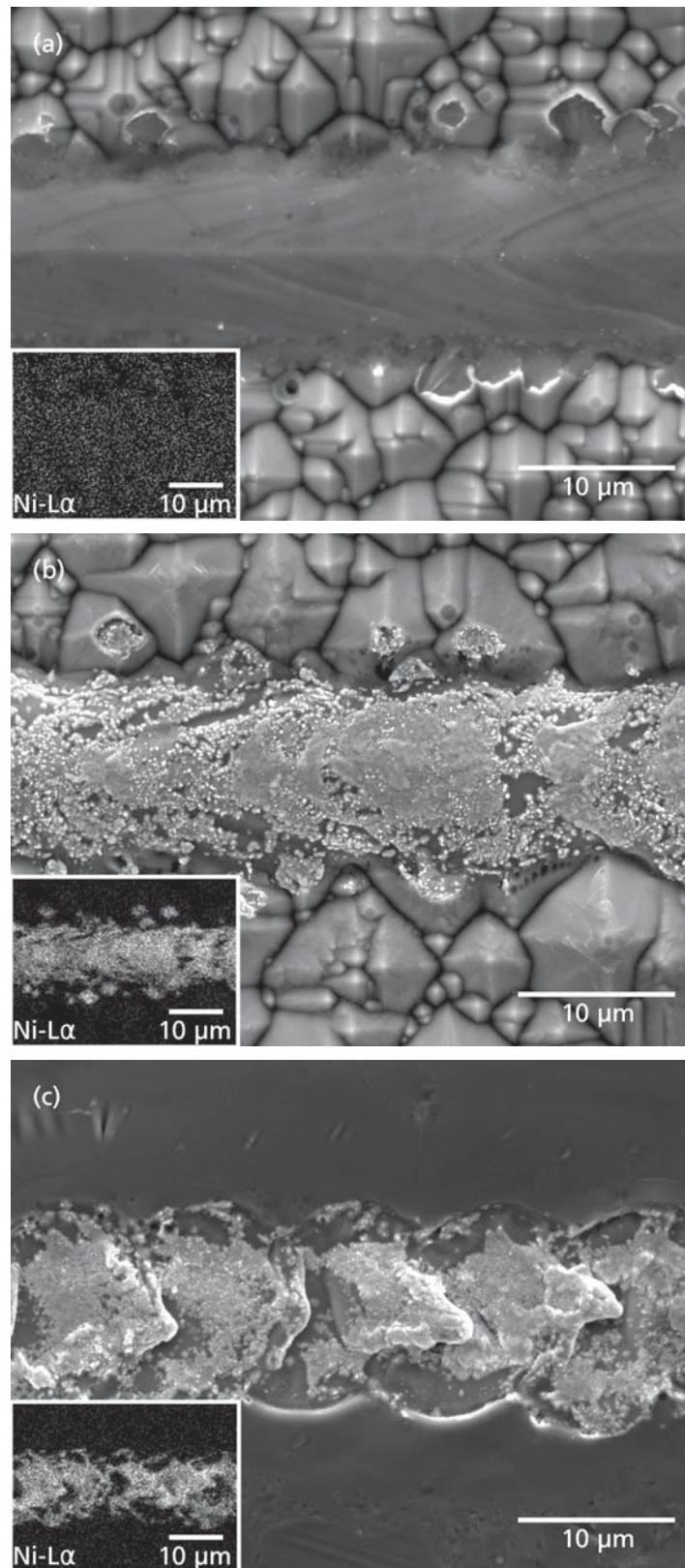


Figure 9.3: SEM images of laser processed fingers (horizontal structure) after etching off the elemental nickel. (a) "SiN<sub>x</sub> → open+dope", (b) "SiN<sub>x</sub> → open+dope → BHF", (c) "dope → SiN<sub>x</sub> → open". The inserts show the corresponding Ni L<sub>α1,2</sub> EDX mapping of the laser lines. With the EDX mapping the light gray areas in (b) and (c) have been identified as Ni<sub>x</sub>Si<sub>y</sub>.

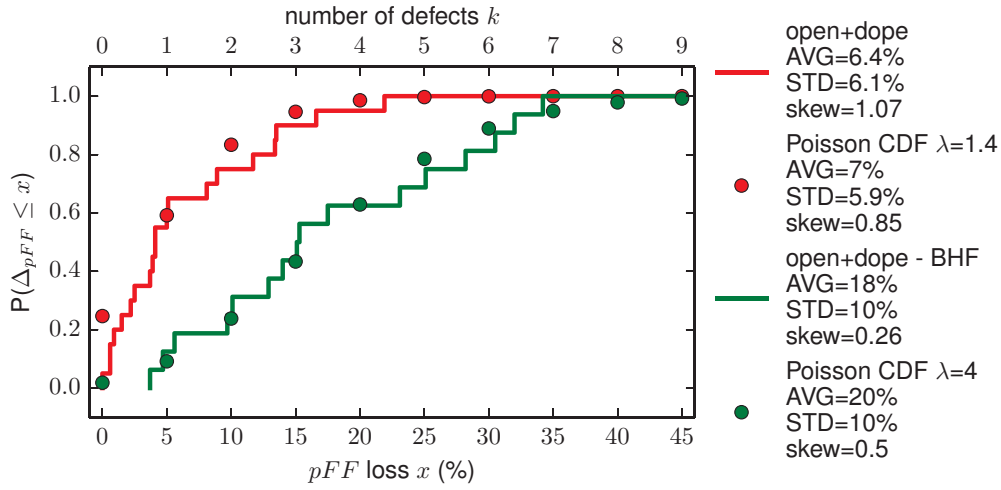


Figure 9.4: Cumulative Poisson distribution functions (circles) fitted to the measured distributions of  $pFF$  values (solid lines) of the "SiN<sub>x</sub> → open+dope" and "SiN<sub>x</sub> → open+dope → BHF" process sequences, assuming that every "defect site" reduces the  $pFF$  by 5%. The fitted Poisson parameters are  $\lambda = 1.4$  and  $\lambda = 4$ , accordingly. In the legend the mean (AVG), standard deviation (STD) and skew values of the corresponding distributions are given.

a wide spread and that the  $pFF$  distribution is skewed hints at a poisson-like failure mechanism with a low probability. Figure 9.4 shows the cumulative distribution function of the measured  $\Delta_{pFF}$  for both process sequences. The "SiN<sub>x</sub> → open+dope" process has an average  $pFF$  loss and standard deviation of about 6%abs and the distribution has a skew value of about 1. If the SiO<sub>x</sub>N<sub>y</sub> layer is removed with BHF the average loss as well as the standard deviation increases to 18% and 10%. On the other hand, the skew is reduced to 0.26. A poisson distribution has been fitted to the data under the simplified assumption, that the number of defect sites (e.g., nickel-induced shunts) on a test cell is proportional to its  $\Delta_{pFF}$  value. As can be seen in Fig.9.4, the fitted distributions describe the data well, despite the crude assumption that every shunt reduces the  $pFF$  by 5%. The expected number of shunts per test cell ( $\lambda$ ) extracted from the fit to the "SiN<sub>x</sub> → open+dope" data is 1.4. In the case of the BHF treated cells the expected number of shunts increases to 4. Under the assumption that the shunts are only occurring along the laser lines this number corresponds to about one shunt per meter of laser line for the untreated and about three shunts per meter of laser line for the BHF treated samples<sup>1</sup>. This is in agreement with the observed increase in Ni<sub>x</sub>Si<sub>y</sub> formation after BHF treatment.

The pseudo fill factor of the test cells which were broadly doped with the cw-laser and opened with ns-pulsed laser ablation is at a sufficiently high level of about 81% with a standard deviation below 1%abs. As can be seen from Fig.9.3 c), in the "dope → SiN<sub>x</sub> → open" group nickel silicid has formed in the ns-pulsed laser ablated area. It appears that the formation of SiO<sub>x</sub>N<sub>y</sub> is

<sup>1</sup>length of laser patterned fingers on test cell:  $32 \times 48 \text{ mm} \approx 1.5 \text{ m}$

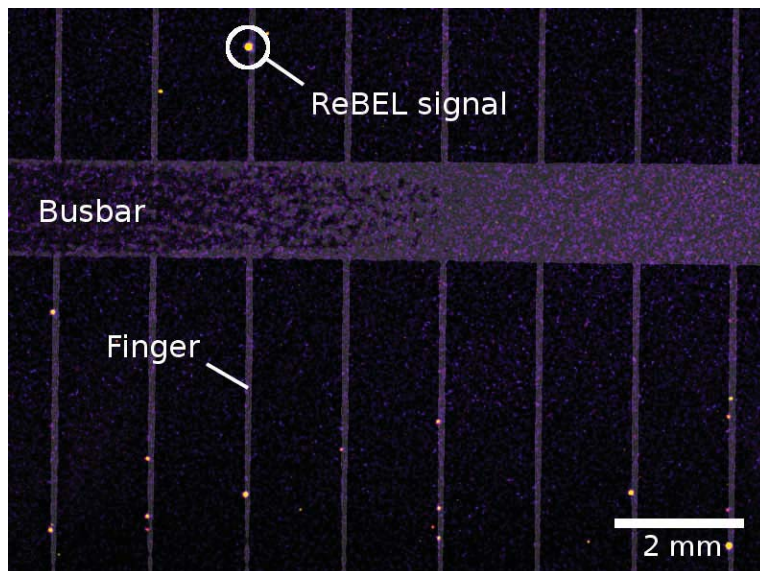


Figure 9.5: Photograph with overlaid ReBEL image of " $\text{SiN}_x \rightarrow \text{open+dope} \rightarrow \text{BHF}$ " cell after nickel plating, annealing and subsequent nickel etch off. Bright spots along the laser structured fingers represent light emission from non-ohmic shunts caused by  $\text{Ni}_x\text{Si}_y$  penetrating the p-n junction.

suppressed when short laser pulses are used for  $\text{SiN}_x$  ablation instead of cw-laser processing. This agrees well with the findings presented in the previous chapter (cf. Sec. 8.2.4), where nickel silicide formation on ns-pulsed laser ablated silicon was observed.

From these results it can be concluded that in the case of " $\text{SiN}_x \rightarrow \text{open+dope}$ ", which represents the standard LDSE process, it is not the p-n junction shaping but the  $\text{SiO}_x\text{N}_y$  formation hindering the silicide formation, which leads to the stability of the  $pFF$  to annealing. At the same time, little nickel silicide is formed in the standard LDSE process, which is likely to be the cause of the observed low adhesion of the plated contacts.

### 9.2.2 Microscopic Localization of Ni Induced Shunts

A ReBEL measurement on a " $\text{SiN}_x \rightarrow \text{open+dope} \rightarrow \text{BHF}$ " cell is shown in Fig. 9.5. The bright spots, indicating light emission from breakdown sites, appear exclusively along the laser doped fingers. This suggests the presumption that it is not parasitic plating that causes the observed degradation of the devices  $pFF$ . It seems that nickel from the front contact grid has formed deep  $\text{Ni}_x\text{Si}_y$  which penetrates the p-n junction and causes nickel-induced shunts. The total length of laser line fingers imaged in Fig. 9.5 is about 64 mm. With a total of about 13 imaged shunts this results in a about 0.2 shunts per mm of laser line (or  $200 \text{ m}^{-1}$ ). This number is a factor 50 higher than expected from the statistical analysis of the  $pFF$  measurements. This discrepancy may be resolved if not all shunts contribute to the  $pFF$  loss to the same extend. The large variance in  $pFF$  may be caused by just the few shunts that have

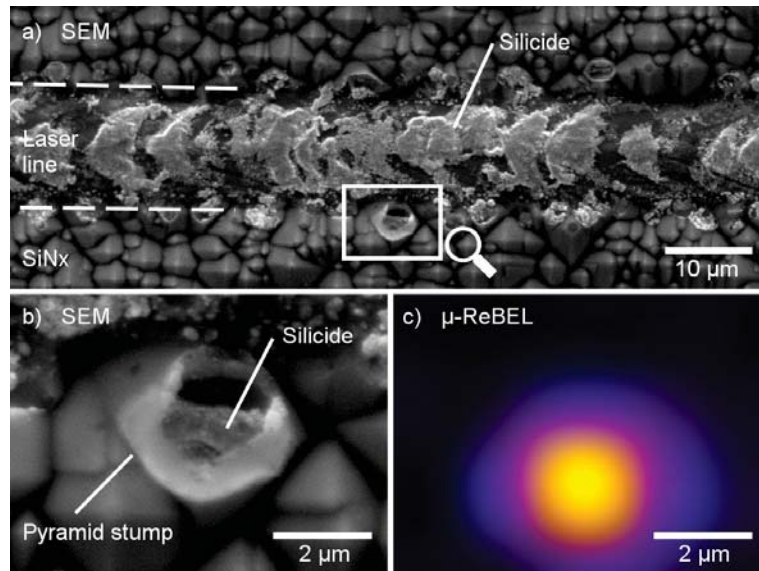


Figure 9.6: SEM overview (a), closeup (b) and corresponding signal (black  $\leftrightarrow$  low, light  $\leftrightarrow$  high signal) from  $\mu$ -ReBEL measurement (c) of a finger from a "SiN<sub>x</sub>  $\rightarrow$  open+dope  $\rightarrow$  BHF" cell after nickel plating, annealing and subsequent nickel etch off. The light emission from a metal-induced shunt originates from the outer edge of a pyramid stump on the edge of the laser line.

a significant impact on the  $pFF$  because they are especially severe, e.g., by being unusually deep.

A microscopic localization of a shunt by means of a  $\mu$ -ReBEL measurement shown in Fig. 9.6 reveals that the edge of the laser line, where pyramid stumps appear, is prone for nickel silicide growth induced shunting. By means of standard ReBEL measurement a position on a laser line with a shunt has been located. SEM images of this laser line, shown in (a) and (b), have been aligned to the microscopic position of the shunt determined using the  $\mu$ -ReBEL measurement (c). Figure 9.6 (a) and (b) are the SEM image and the corresponding aligned  $\mu$ -ReBEL measurement. The shunt can be localized to appear at the outer edge of the laser line, in a pyramid stump where nickel silicide has formed.

On the edge of the laser line only the tips of pyramids receive sufficient laser energy to create a silicon melt. This effect is caused by the focussing of the laser light into the pyramid tips due to the pyramid geometry and a high refractive index of SiN<sub>x</sub> and silicon as explained by Knorz et al. [158]. On the outer edge of such pyramid stumps the laser irradiation is just high enough for ablation of the SiN<sub>x</sub> but insufficient to create a deep melt and a sufficient doping depth. The high variance of the  $pFF$  values of the "SiN<sub>x</sub>  $\rightarrow$  open+dope" and "SiN<sub>x</sub>  $\rightarrow$  open+dope  $\rightarrow$  BHF" cases may be explained by the low probability for the unfavorable combination of pyramid geometry and relative position to the irradiated area which leads to sites with SiN<sub>x</sub> ablation but shallow laser doping. The "SiN<sub>x</sub>  $\rightarrow$  open+dope" group is on a  $pFF$  level above 80 % because the SiO<sub>x</sub>N<sub>y</sub> formation hinders nickel diffusion and silicide formation, thus the

Table 9.1:  $\text{Ni}_x\text{Si}_y$  coverage as determined by SEM imaging and corresponding peel force for the different process sequences. The measured coverage is relative to the area of the last selective contact opening step. In addition the  $pFF$  values of Fig. 9.2 are listed. Only the "dope  $\rightarrow$   $\text{SiN}_x \rightarrow$  open" sequence produces  $pFF$  above 80 % and a front contact adhesion exceeding 1 N/mm.

Process sequence	$\text{Ni}_x\text{Si}_y$ coverage		$pFF$ median (%)	peel force	
	finger (%)	busbar (%)		mean (N/mm)	max (N/mm)
" $\text{SiN}_x \rightarrow$ open+dope"	<1	<1	81.3	0.03	0.66
" $\text{SiN}_x \rightarrow$ open+dope $\rightarrow$ BHF"	49	67	67.8	0.49	1.25
"dope $\rightarrow$ $\text{SiN}_x \rightarrow$ open"	53	68	80.9	0.33	1.37

probability for a severe shunt decreases. In the case of the "dope  $\rightarrow$   $\text{SiN}_x \rightarrow$  open" group the laser doped area is designed to be significantly wider than the  $\text{SiN}_x$  ablation (doping width: 150  $\mu\text{m}$ , opening width: 14  $\mu\text{m}$ ). This results in a sufficient deep p-n junction for all sites with silicide growth and leads to a narrow distribution of  $pFF$  values above 80 % (cf. Fig. 9.2).

### 9.2.3 Adhesion of Ni-Cu Contacts

Table 9.1 collects the coverage of the laser doped fingers and busbars with nickel silicide as well as the median and maximum of the force needed to peel of the front metal contact from the cell. Figure 9.7 shows the corresponding detailed peel force measurements of the three studied sequences. By evaluating this data the relation between nickel silicide formation and adhesion becomes evident. In the " $\text{SiN}_x \rightarrow$  open+dope" case little to none silicide formation leads to minute peel forces, whereas the process sequences with a silicide coverage higher than 60 % exhibit significantly higher peel forces. The mean peel force for the " $\text{SiN}_x \rightarrow$  open+dope  $\rightarrow$  BHF" and "dope  $\rightarrow$   $\text{SiN}_x \rightarrow$  open" laser processes are averaging at 0.49 N/mm and 0.33 N/mm and peaking at 1.37 N/mm. The data collected in table 9.1 also reveals that only the "dope  $\rightarrow$   $\text{SiN}_x \rightarrow$  open" laser process produces test cells which are electrically stable with a  $pFF$  of about 81 %, as well as mechanically stable with sufficient adhesion.

Figure 9.8 shows top view SEM images of the test cells after the solder ribbon has been peeled off. In the " $\text{SiN}_x \rightarrow$  open+dope  $\rightarrow$  BHF" as well as in the " $\text{SiN}_x \rightarrow$  open+dope" case the point of failure is mostly the silicide–nickel interface with only little sites where the silicide–nickel adhesion surpasses the fracture strength of the silicon wafer. The breakage within the silicon material is the so-called chipping. The chipping sites occur along tracks of silicide formation which in turn run along the path of the laser spot during laser doping. Laser damage may be responsible for microcracks in the molten and recrystallized silicon. Wendt et al. [207] states microcracks as the main cause for microchipping.

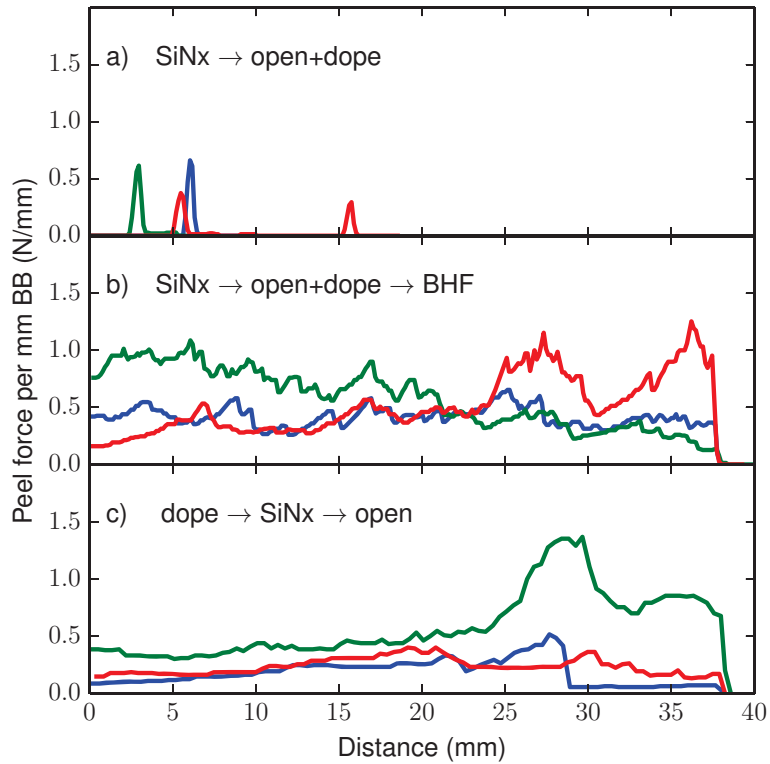


Figure 9.7: Peel force diagrams of Ni-Cu-Ag stack for the three process sequences "SiN<sub>x</sub> → open+dope" (a), "SiN<sub>x</sub> → open+dope → BHF" (b) and "dope → SiN<sub>x</sub> → open" (c). For each sequence the forces for three exemplary cells are shown (red, green, blue).

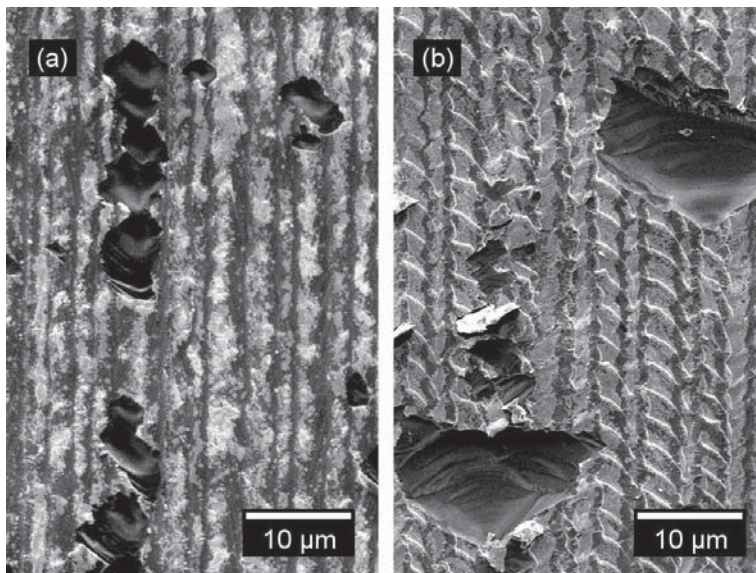


Figure 9.8: SEM images of laser processed busbars of the "SiN<sub>x</sub> → open+dope → BHF" (a) and "dope → SiN<sub>x</sub> → open" (b) sequence after peeling of the solder ribbon. The predominant adhesion failure is between Ni<sub>x</sub>Si<sub>y</sub> and nickel. These images have been selected since they also show sites with silicon chipping.

The adhesion presented here ( $\approx 1 \text{ N/mm}$ ) is about a factor two lower than the results which have been demonstrated by Mondon et. al. [111] ( $\approx 2 \text{ N/mm}$ ). It is assumed that this difference is caused by the difference in surface morphology, nickel silicide coverage and nickel silicide growth. The surface of a random pyramide textured area is 1.4 times as large as a planarized area present after cw-laser doping. This increase in relative surface area may already account for about 40 % difference in the measured peel force normalized to the busbar width. A second point may be found in the incomplete removal of  $\text{SiO}_x\text{N}_y$  in the " $\text{SiN}_x \rightarrow \text{open+dope} \rightarrow \text{BHF}$ " case (and to a lesser extend in the " $\text{dope} \rightarrow \text{SiN}_x \rightarrow \text{open}$ " case). Here the surface is still covered with porous residues of  $\text{SiO}_x\text{N}_y$  and silicide growth may start at a nm-scaled site free of  $\text{SiO}_x\text{N}_y$ , grow into the silicon and continue lateral growth below the thin  $\text{SiO}_x\text{N}_y$  layer. In this case only a nm-sized silicide island would form a metallic bond to nickel although EDX measurements would suggest full coverage of the laser line with nickel silicide. The third point is found in the imperfect silicide coverage of the busbar of about 70 %. Especially in the " $\text{dope} \rightarrow \text{SiN}_x \rightarrow \text{open}$ " case the coverage may be increased by the use of an optimized  $\text{SiN}_x$  ablation process e.g. by using a ps-pulsed UV process. This process allows ablation of  $\text{SiN}_x$  with a smaller heat affected zone and reduced  $\text{SiO}_x\text{N}_y$  formation time due to higher UV absorptivity of silicon and the ultra short laser pulse.

## 9.3 Overcoming Failure Mechanisms

In the previous section it was shown that cw-laser doping creates sufficiently deep p-n junctions that effectively prevent nickel induced shunting, if it were not for the pyramids of the texture at the edge of the laser line. The problem was addressed by wide doping before  $\text{SiN}_x$  deposition and subsequent laser ablation. This necessitates the alignment of the doping and the ablation pattern, which complicated the process sequence and required wide laser doped fingers.

In this section alternative processing sequences designed to create electrically stable solar cells with good mechanical adhesion are studied. The basic sample design and the front contact formation is identical to the processes presented in the previous section.

### 9.3.1 Alternative Processing Sequences

The two alternative process sequences presented here addresses these issues, a) by using planar material and subsequent chemical etching and b) by using the laser ablation process for the selective removal of the  $\text{SiO}_x\text{N}_y$  barrier layer. In both process sequences the laser processing is performed using a single process tool after the  $\text{SiN}_x$  deposition, omitting inter-tool alignment. In accordance with the previous experiment, after laser processing the samples were nickel plated, annealed at  $450^\circ \text{C}$  for 5 min, piranha etched, and re-plated with light-induced nickel plating. The  $pFF$  was measured and the adhesion of the nickel-copper-silver stack was determined using the adhesion tester, as described above. The

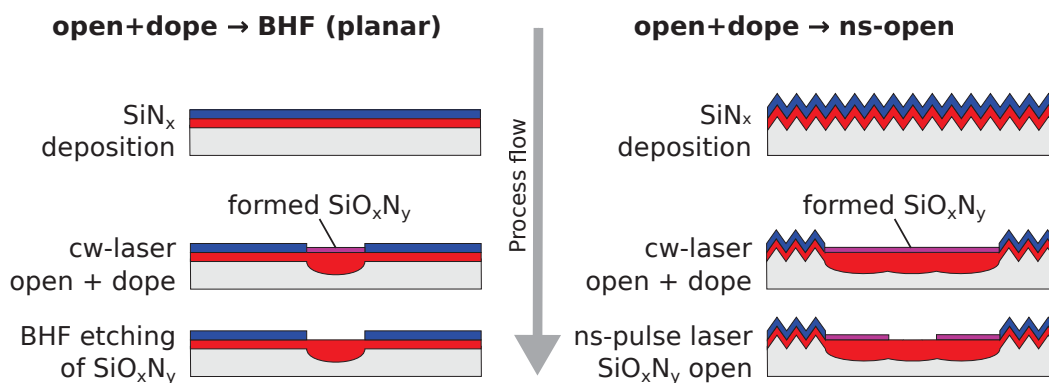


Figure 9.9: Schematic of alternative process sequences to create electrically stable solar cells with good mechanical adhesion. The "open+dope → BHF (planar)" sequence represents the LDSE process on a planar wafer with the addition of a BHF treatment to remove the  $\text{SiO}_x\text{N}_y$  formed during laser doping. The "open+dope → ns-open" sequence employs two laser systems within the same processing tool. A cw-laser allows selective doping and a ns-pulsed laser ablates the formed  $\text{SiO}_x\text{N}_y$ .

alternative laser process sequences are outlined in Fig. 9.9 and described in the following.

### Group: open+dope → BHF (planar)

The samples in this group are produced using the LDSE process on solar cell precursors without a light trapping texture. The wafer material for the samples has only received a saw damage etch [61] resulting in a rather planar surface. After the cw-laser doping using the same parameters as detailed in the previous section, a 60 s BHF etch is performed to remove the parasitic  $\text{SiO}_x\text{N}_y$  layer.

### Group: open+dope → ns-open

In this group the  $\text{SiO}_x\text{N}_y$  formed by cw-laser doping is removed using ns-pulsed laser ablation. As described in Chapter 5, the laser processing tool that was used in this thesis houses two laser systems. Switching from the one to the other is possible by flipping a mirror. Both laser beams can be adjusted to propagate on the same optical axis before they enter the galvanometer scanner. This allows aligned processing without adjusting the position of the wafer. An example of the precision achievable is given in Fig. 9.10 a) and (b), where a microscopy image and its schematic representation shows that a  $20\ \mu\text{m}$  wide cw-laser doped line can be treated by the  $14\ \mu\text{m}$  sized spot of the ns-pulsed laser without crossing the edge of the cw-laser doped line.

Although this precision is achievable in principle, with the research laser tool used in this thesis this precision cannot be ensured across a wafer with 156 mm edge length. Therefore the cw-laser treated area was extended to a doping width of  $45\ \mu\text{m}$ . Figure 9.10 c) shows a microscopy image of the intersection of the busbar with a finger. The ns-pulsed laser treated area is well within the cw-laser doped area.

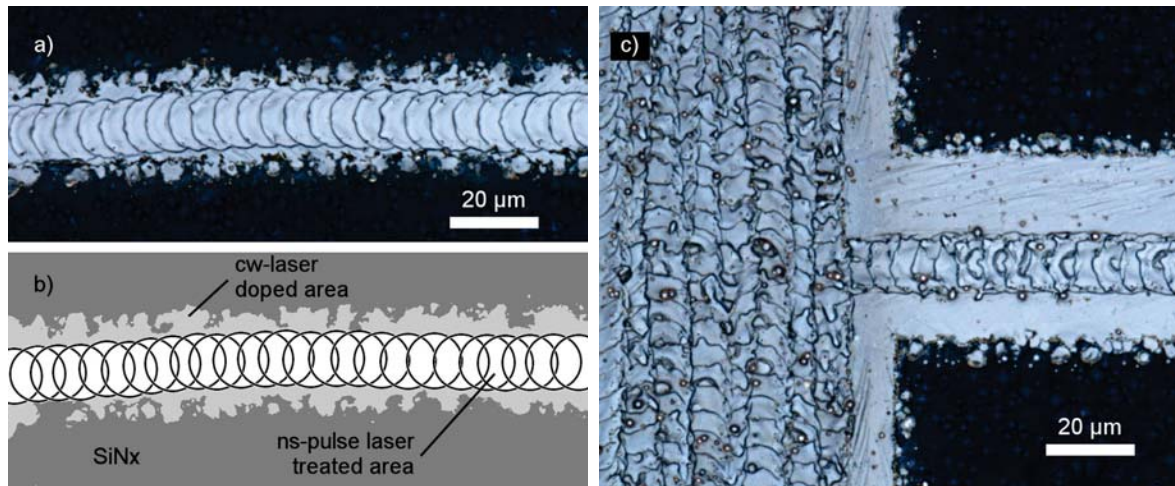


Figure 9.10: Microscopy images of consecutive laser treated silicon. ns-pulsed laser spots placed within the center of a  $20\ \mu\text{m}$  wide laser doped line (a) and the corresponding schematic (b). An intersection of the busbar and a finger of the solar cell test structures produced (c), where the laser doped area is extended to a width of  $45\ \mu\text{m}$ . This ensures that the ns-pulsed laser spots are within the doped area at all places on a  $156\times 156\ \text{mm}^2$  wafer.

The ns-pulsed laser ablation has been performed at three different laser parameters. At a scanning speed of  $0.5\ \text{m/s}$  and a pulse energy of  $5\ \mu\text{J}$  the laser remelting produces planar surfaces (cf. Fig. 9.10 a). If the scanning speed is doubled to  $1\ \text{m/s}$  the spacing between the ablation spots doubles. At a scanning speed of  $1\ \text{m/s}$  and a pulse energy of  $10\ \mu\text{J}$  the silicon is partly evaporated or expelled, producing a shallow groove. The pulse duration is kept constant at  $80\ \text{ns}$ .

### 9.3.2 $\text{SiO}_x\text{N}_y$ Removal

From the results obtained in Chapter 8 and the previous section, it is presumed that the absence of a  $\text{SiO}_x\text{N}_y$  interface layer is a necessity for the formation of nickel silicide. Thus, if silicide formation after annealing is detected the absence of  $\text{SiO}_x\text{N}_y$  can be concluded.

Figure 9.11 shows SEM and EDX measurements of laser structured fingers after etching off the elemental nickel for the two alternative process sequences. The material contrast of the SEM image and the EDX measurement proves that a nickel silicide has formed on both fingers. Although almost full coverage with silicides was observed on the fingers, the coverage of the busbar is reduced to about 70% in the case of the BHF treated sample. For the "open+dope → ns-open" sequence the silicide coverage depends on the ablation parameters. Figure 9.12 shows microscopy images of an intersection of the busbar and a finger after silicide formation and elemental nickel etching off. In (a) the pulse energy was set to  $10\ \mu\text{J}$  allowing the formation of a  $20\ \mu\text{m}$  wide area fully covered with silicide, whereas in (b) the pulse energy was set to  $5\ \mu\text{J}$  resulting in circular silicide spots with about  $5\ \mu\text{m}$  diameter.

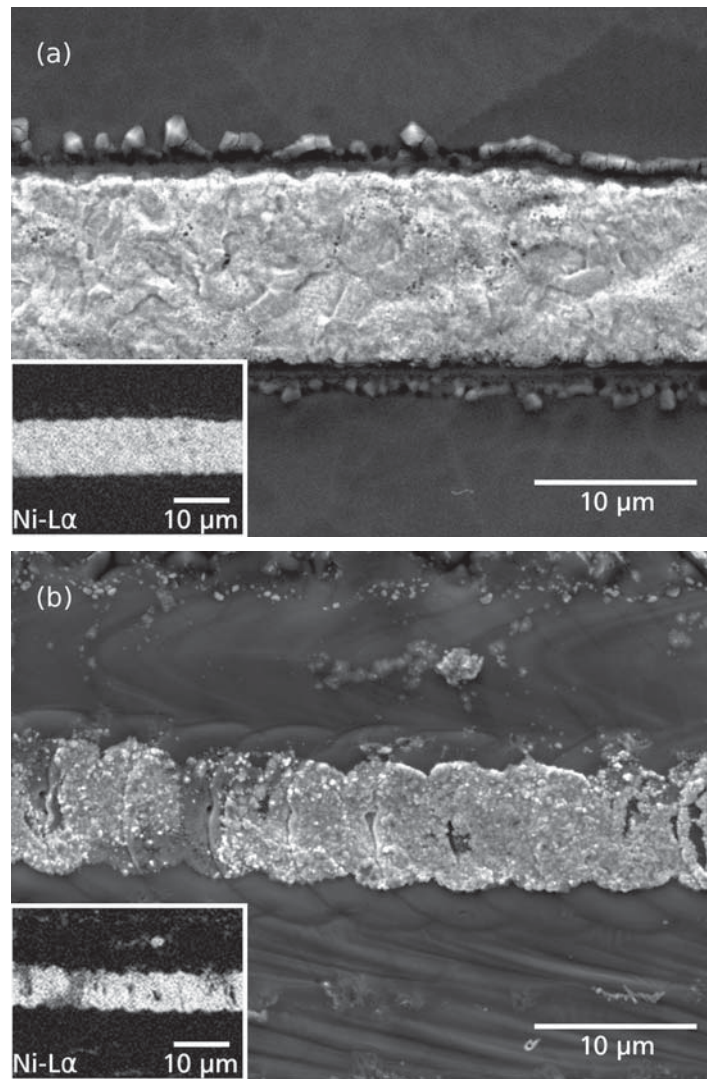


Figure 9.11: SEM images of laser processed fingers (horizontal structure) after etching off the elemental nickel. (a) "open+dope → BHF (planar)", (b) "open+dope → ns-open". The inserts show the corresponding Ni  $L\alpha_{1,2}$  EDX mapping of the laser lines.

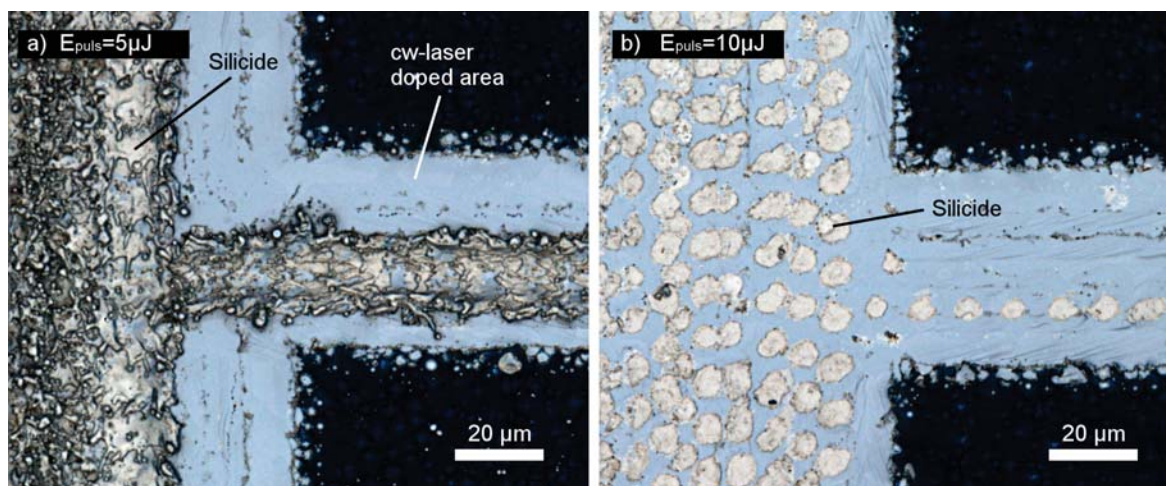


Figure 9.12: Microscopy images of busbar-finger intersections after the "open+dope → ns-open" sequence, silicide formation and etching off the elemental nickel. At high pulse energy (a) the ns-pulsed laser ablated area is fully covered with nickel silicide. At low pulse energy (b) only small patches of silicide are formed.

The formation of silicides shows that the removal of  $\text{SiO}_x\text{N}_y$  can be achieved by both, harsh chemical etching and ns-pulsed laser ablation.

### 9.3.3 Prevention of $\text{Ni}_x\text{Si}_y$ Shunting

After nickel silicide formation the  $pFF$  of the test structures have been determined. Alongside the samples that employ the alternative laser process sequences, two additional groups have been tested for nickel silicide growth induced shunting and its characteristic  $pFF$  drop. To serve as a reference, four test cells produced from a planar wafer using the standard LDSE process and which were not etched in BHF are measured. In addition to this, an alternative plating and annealing sequence, denoted "post-anneal", has been tested.

#### Group: Post-anneal

To test an alternative contact formation, which is a simplified process for silicide formation and copper-silver contact build-up, additional twelve samples were produced using the "open+dope → ns-open" sequence. After a 30 s HF dip, these samples were nickel plated using LIP. Directly after that, copper and silver were plated to finish the metallization stack. A subsequent annealing step at  $275^\circ\text{C}$  for 5 min was intended to produce a thin nickel silicide layer and thus provide the electrical and mechanical contact between silicon and nickel metallization. Since the plating of the metallization stack is fully completed before the silicide formation during annealing, this process is denoted "post-anneal" in the following. Mondon et al. have shown contact adhesion exceeding  $2\text{ N/mm}$  using ps-pulsed laser ablation and the post-anneal front contact formation route [32].

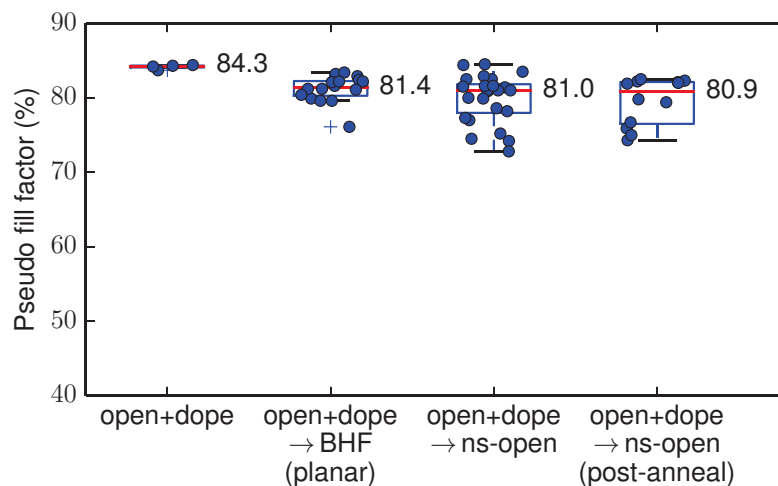


Figure 9.13: Box plot of pseudo fill factor values after laser processing and annealing. The first three groups from the left have been annealed for 5 min at 450° C. The “post-anneal” group was annealed for 5 min at 275° C. The numbers within the plot represent the median values.

### pFF Measurements

Figure 9.13 displays the measured  $pFF$  data of the different process sequences. The reference “open+dope” sequence has excellent  $pFF$  values above 84% and the highest median value in comparison to the other groups. This is caused by the  $\text{SiO}_x\text{N}_y$  hindering the formation of a nickel silicide and thus preventing the test cell from nickel induced shunting.

The “open+dope → BHF (planar)” group has a median  $pFF$  of 81.4%, despite the harsh annealing and extensive silicide formation. The only difference between this group and the BHF treated group presented in the previous section is the random pyramid texture. The textured samples were severely degraded after annealing and  $pFF$  values were at about 70%. In contrast to these, the planar samples have a deep and homogeneous p-n junction stretching below the  $\text{SiN}_x$  covered edge, thereby effectively preventing the penetration of the space charge region by silicide growth. This confirms the earlier observation that the pyramid tips at the edge of the laser line are detrimental for annealing stability, supports the presumption that cw-laser doping is well suited for producing nickel-copper plated solar cells (cf. Sec.6.4), and results in the observed high  $pFF$  values.

The “open+dope → ns-open” sequence produces test cells stable to harsh annealing. The measurement of the  $pFF$  values results in a median value of 81.0% and a standard deviation of about 3%abs. While the maximum  $pFF$  measured exceeds 84%, the smallest values is as low as 73%. The three different laser parameter sets for the ns-pulsed ablation resulted in median values of 81% ( $5\ \mu\text{J}$ , 0.5 m/s), 77% ( $5\ \mu\text{J}$ , 1 m/s), and 83% ( $10\ \mu\text{J}$ , 1 m/s). However, considering a deviation of about 3%abs., this difference is of arguable significance. Instead, it is presumed that this variation is a result of improper

alignment between the cw-laser doping and the ns-pulsed laser ablation. This misalignment can occur globally on individual wafers, if the wafer is moved on the processing table in between the laser doping and the laser ablation step, or if the path of the two laser beams is not perfectly aligned due to minimal variations of the flip mirror position after manual beam switching. Misalignment can also occur locally on all wafers in edge regions, where the optical quality of the f-theta lens declines. A correlation of the measured  $pFF$  values with the order of processing and the position on the processing table revealed that the  $pFF$  drop is caused by a combination of slight global and local misalignment of the laser doping and laser ablation. There are always four samples with a size of  $48 \times 48 \text{ mm}^2$  that were produced from the same wafer. Two test cell positions produced systematically smaller  $pFF$  values than the other two processed on the same wafer. This effect increases with the amount of processed wafers.

The  $pFF$  values of the “post-anneal” group are distributed with a median of 80.9% and a standard deviation of about 3%abs. The difference in  $pFF$  between the laser ablation parameters is with median values of 82% ( $5 \mu\text{J}$ , 0.5 m/s), 76% ( $5 \mu\text{J}$ , 1 m/s), and 82% ( $10 \mu\text{J}$ , 1 m/s) is of arguable significance. Again, it is presumed that misalignment errors dominate the observed variation in  $pFF$ . The  $pFF$  values of this group are similar to the “open+dope  $\rightarrow$  ns-open” group, indicating that the annealing mode does not have a substantial impact on the  $pFF$ .

#### 9.3.4 Contact Adhesion

The contact adhesion between silicon and the metallization stack has been determined by peeling a soldered ribbon from the test cells under  $90^\circ$ . The required force was recorded and is displayed in Fig. 9.14 for the groups “open+dope  $\rightarrow$  BHF (planar)”, “open+dope  $\rightarrow$  ns-open”, and “post-anneal”. The group without the BHF treatment is not included into the figure since the contact adhesion was so little that most of the metall contacts fell off before attaching the adhesion tester to the solder ribbon. The mean and maximum forces, the coverage of the fingers and busbars with silicide, as well as the median  $pFF$  are compiled in Tab. 9.2.

In the “open+dope” case only minimal peel forces could be measured. This can be put down to the absence of a nickel silicide interlayer. In contrast to this, the sequences “open+dope  $\rightarrow$  BHF (planar)” and “open+dope  $\rightarrow$  ns-open”, which resulted in a significant coverage with nickel silicide, produced well adhering contacts with mean peel forces above 1 N/mm and maximum values of 2.14 N/mm and 2.79 N/mm. In these two cases, the adhesion of the nickel-copper plated contacts exceeded the wafer breakage force and resulted in ripping apart the silicon wafer below the busbar contact, as shown exemplarily in Fig. 9.15.

Although the laser process used for the “post-anneal” samples produces silicon surfaces that are suitable for nickel silicide formation, microscopy imaging of the busbar and fingers revealed that only little silicide has formed. As a result

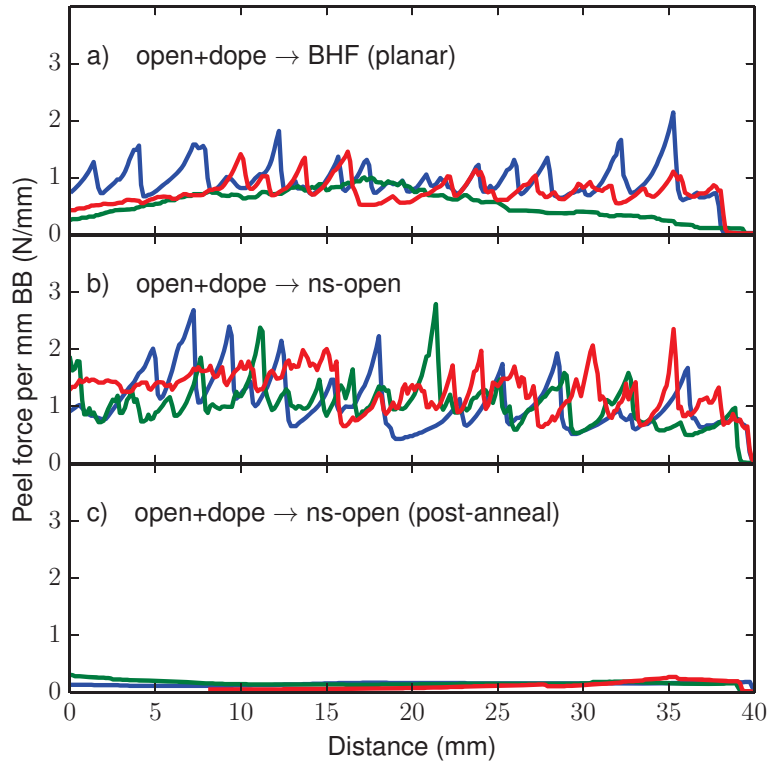


Figure 9.14: Peel force diagrams of the metallization stack for the process sequences "open+dope → BHF (planar)" (a), "open+dope → ns-open" (b) and "post-anneal" (c). For each sequence the forces for three exemplary cells are shown (red, green, blue).

Table 9.2:  $\text{Ni}_x\text{Si}_y$  coverage as determined by SEM and optical microscopy imaging and corresponding  $pFF$  median value and peel force for the different alternative process sequences. The measured coverage is relative to the area of the last selective contact opening step. The  $pFF$  measurement is detailed in Fig. 9.13 and the peel force is detailed in 9.14.

Process sequence	$\text{Ni}_x\text{Si}_y$ coverage		$pFF$ median (%)	peel force	
	finger (%)	busbar (%)		mean (N/mm)	max (N/mm)
"open+dope"	<1	<1	84.3	0.00	0.21
"open+dope → BHF (planar)"	≈100	≈70	81.4	1.09	2.14
"open+dope → ns-open"	31 - 100	46 - 100	81.0	1.12	2.79
Post-anneal					
"open+dope → ns-open"	<1	<6	80.9	0.14	0.31

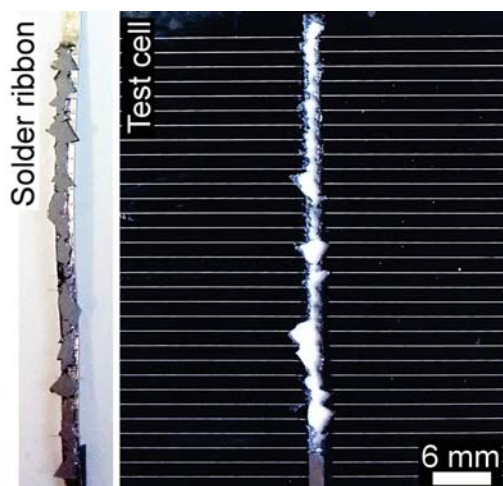


Figure 9.15: Solder ribbon and test cell after the peel test. The excellent contact adhesion caused ripping out of silicon from the test cell. The cell was produced with the "open+dope → ns-open" laser processing sequence.

of this, the contact adhesion is with a mean value of  $0.14 \text{ N/mm}$  unsatisfactory. Up to this point the reason for the minute silicide formation is not clear. The reason may be found in a silicon oxide interlayer formed during copper and silver plating, hindering nickel diffusion into the silicon. Also the relatively low temperature of  $275^\circ \text{ C}$  of the "post-anneal" process may be insufficient to form silicides, although the formation on a clean surface should be possible at this temperature in principle [118].

## 9.4 Simulation of Solar Cell Efficiency Potential

Throughout this thesis the characteristics of a cw-laser doped emitter have been studied in great detail. In Chapter 7 the emitter saturation current density of passivated and unpassivated laser doped emitter were measured. It was found that a parasitic surface layer forms during cw-laser ablation. Unsuccessful contact adhesion caused by this layer necessitates alterations to the standard LDSE process sequence. The process sequences proposed in this chapter allow to produce solar cells which are stable to annealing and have well adhering nickel-copper contacts. In this section the Quokka solar cell simulator [208] will be used to estimate the efficiency potential of these process sequences.

### 9.4.1 Setup

Quokka allows two dimensional simulations of a solar cells. The following results are based on a solar cell design referred to as LBSF cells (local back surface field) [209]. The LBSF solar cells are realized using a selective emitter at the front and a local back surface field at the rear side. The used simulation parameters are collected in Tab. 9.3 and briefly described in the following. The rear contact of the simulated solar cell is established by line openings of the rear

Table 9.3: Simulation parameters kept constant throughout the simulation runs.

Parameter	
Simulation engine	Quokka2 (2D) [208]
Auger model	Richter [43]
Mobility model	Klaasen [210]
Temperature	300 K
Material	p-type Si, 1 $\Omega\text{cm}$
Bulk lifetime	500 $\mu\text{s}$
Wafer thickness	160 $\mu\text{m}$
Rear side	Local back surface field (LBSF)
LBSF geometry	lines
LBSF width	50 $\mu\text{m}$
LBSF pitch	1.3 mm
LBSF sheet resistance	20 $\Omega$
LBSF contact resistance	1 $\text{m}\Omega\text{cm}^2$
$j_{01}$ of LBSF	250 $\text{fA}/\text{cm}^2$
$S$ of pass. rear	10 $\text{cm}/\text{s}$
Front side	Selective emitter with Ni-Cu contacts
Finger pitch	1.3 mm
Contact opening width	14 $\mu\text{m}$
$j_{01}$ of blanket emitter	18 $\text{fA}/\text{cm}^2$
Blanket emitter junction depth	1.2 $\mu\text{m}$
Blanket emitter sheet resistance	120 $\Omega$
Blanket emitter collection efficiency	99 %
$j_{02}$ of blanket emitter	5 $\text{nA}/\text{cm}^2$
$j_{02}$ of laser patterned emitter	20 $\text{nA}/\text{cm}^2$

Table 9.4: Laser process sequence specific simulation parameters.

Process sequence	contact shading width ( $\mu\text{m}$ )	laser doping width ( $\mu\text{m}$ )	$j_{0e}$ of cont. emitter ( $\frac{\text{fA}}{\text{cm}^2}$ )	$j_{0e}$ of pass. emitter ( $\frac{\text{fA}}{\text{cm}^2}$ )	collection efficiency (%)	$\rho_c$ ( $\Omega\text{cm}^2$ )
"SiN <sub>x</sub> → open"	34		750	18	99	10 <sup>-3</sup>
"SiN <sub>x</sub> → open+dope"	34	14	770		60	10 <sup>-5</sup>
"dope → SiN <sub>x</sub> → open"	34	150	253	233	60	10 <sup>-5</sup>
"open+dope → ns-open"	65	45	770	770	60	10 <sup>-5</sup>

side dielectric passivation and firing a screen printed aluminium paste to form LBSF lines. The design and recombination of the rear side is in accordance with industrial feasible processes as recently shown by researchers from Schott Solar [62].

The design parameters of the front side of the simulated cell are varied to study the influence of the different process sequences on the cell performance. However, the finger pitch, the blanket emitter<sup>2</sup>, the passivation system and the contact opening width are the same for all simulation runs. The parameters for the blanket emitter as well as the effect of the passivation layer are taken from measurements of the furnace diffused emitter in Chapter 7. The contact opening has been measured in Chapter 6. All parameters which are kept constant throughout the runs are collected in Tab. 9.3, whereas the parameters that are specific for the tested laser processing sequences are collected in Tab. 9.4. These are the shading width of the metall finger, which is  $34\ \mu\text{m}$  for all sequences, except for the "open+dope  $\rightarrow$  ns-open" sequence where it is  $65\ \mu\text{m}$  wide. The extended finger width is caused by the  $45\ \mu\text{m}$  wide cw-laser ablation of the dielectric layer and  $20\ \mu\text{m}$  plating overgrowth. However, nickel silicide is only formed along the narrow ns-laser treated line, thus the contact opening width is still  $14\ \mu\text{m}$ . The width of the laser doped area below the contact fingers depends on the laser processing sequence. It varies between zero in the case of the "SiN<sub>x</sub>  $\rightarrow$  open" process and the  $150\ \mu\text{m}$  required for proper alignment in the case of the "dope  $\rightarrow$  SiN<sub>x</sub>  $\rightarrow$  open" sequence. The emitter saturation current densities  $j_{0e}$  for the passivated and contacted areas have been measured in Chapter 7. The collection efficiency represents the fraction of the minority carriers generated in the laser patterned emitter that contribute to the photo current. A high collection efficiency implies a high blue response. In the case of pure laser ablation ("SiN<sub>x</sub>  $\rightarrow$  open") no additional dopants are brought into the emitter, resulting in an excellent blue-response. In the case of the highly doped  $4\ \mu\text{m}$  deep emitter the blue response is substantially reduced. For the laser doped emitter, the collection efficiency was estimated to be identical to the internal quantum efficiency at  $500\ \text{nm}$  ( $\approx 0.6$ ) which was calculated using EDNA [48]. Due to the low surface dopant concentration of the blanket emitter, the specific contact resistance  $\rho_c$  is increased ( $10^{-3}\ \Omega\text{cm}^2$ ) in the "SiN<sub>x</sub>  $\rightarrow$  open" case in comparison to the other cell designs with laser doped emitters below the contacts ( $10^{-5}\ \Omega\text{cm}^2$ ).

## 9.4.2 Results and Discussion

In the following the results from seven simulation runs with different front side designs are compared. The "SiN<sub>x</sub>  $\rightarrow$  open" process can be understood as a reference process without a selective emitter design. The narrow contact opening can be achieved for example with a ps-pulsed laser, which is assumed

---

<sup>2</sup>The simulated blanket emitter parameters correspond to the parameters of the blanket emitter described and measured in chapter 7: depth  $1.2\ \mu\text{m}$ , surface doping density  $8.5 \cdot 10^{18}\ \text{cm}^{-3}$ , sheet resistance  $120\ \Omega$ , and  $j_{0e}$   $18\ \text{fA}/\text{cm}^2$ .

Table 9.5: Electrical properties of the simulated solar cells with different laser processed front sides. Additionally the stability to annealing and the strength of the contact adhesion is indicated. The asterisked "SiN<sub>x</sub> → open" process is considered the reference processing route.

Process sequence	$V_{oc}$ (mV)	$j_{sc}$ ( $\frac{mA}{cm^2}$ )	$FF$ (%)	$\eta$ (%)	annealing stable	contact adhesion
"SiN <sub>x</sub> → open"	702	37.4	81.6	21.5*	–	+
"SiN <sub>x</sub> → open+dope"	702	37.4	81.9	21.6	+	–
"SiN <sub>x</sub> → open+dope (planar)"	700	34.5	81.9	19.8	+	+
"dope → SiN <sub>x</sub> → open"	694	36.7	82.1	21.0	+	+
"open+dope → ns-open"	694	36.6	82.0	20.9	+	+
<b>Optimized sequence</b>						
"dope → SiN <sub>x</sub> → open (opt.)"	702	37.3	81.9	21.5	+	+
"open+dope → ns-open (opt.)"	700	37.2	81.9	21.4	+	+

to be free of laser damage. However, this design is prone to nickel silicide growth induced shunting, as shown in Sec. 9.2.1. The deep emitter of the LDSE process ("SiN<sub>x</sub> → open+dope") prevents this degradation and decreases the contact resistance. Unfortunately, this process results in low contact adhesion. Performing the LDSE process on planar wafers ("SiN<sub>x</sub> → open+dope (planar)") followed by a harsh BHF treatment allowed to overcome the adhesion problem. Excellent adhesion could also be achieved by laser doping before the SiN<sub>x</sub> deposition and subsequent pulsed laser ablation ("dope → SiN<sub>x</sub> → open"), as well as by a wide laser doping using the LDSE process and narrow ablation of the formed SiO<sub>x</sub>N<sub>y</sub> layer using a ns-pulsed laser ("open+dope → ns-open"). In addition to the five designs which have been experimentally tested in the previous section, two designs are simulated, which feature layouts, that are presumed to be achievable after process optimization.

Table 9.5 compiles the results from the simulation runs. The "SiN<sub>x</sub> → open" reference process achieves an excellent short circuit voltage  $V_{oc}$  and a high short circuit current density  $j_{sc}$ , resulting in a cell efficiency  $\eta$  of 21.5%. This is due to the driven in emitter, the effective surface passivation, and the narrow contact shading width. With the additional doping below the contact fingers ("SiN<sub>x</sub> → open+dope")  $\rho_c$  decreases, which has a small influence on the  $FF$ , resulting in an  $\eta$  of 21.6%. The necessary planarity of the surface ("SiN<sub>x</sub> → open+dope (planar)") to avoid adhesion problems results in a significant decrease of  $j_{sc}$  and a severe reduction of  $\eta$  to 19.8%. Separating the doping and the contact opening into two separate laser processes ("dope → SiN<sub>x</sub> → open" and "open+dope → ns-open") yields a mildly reduced  $V_{oc}$  and increased  $FF$  due to the extended highly doped region. Mostly due to the reduced  $j_{sc}$  the efficiency of these cells (21.0% and 20.9%) is significantly lower than  $\eta$  of the reference process. In the "dope → SiN<sub>x</sub> → open" case this is caused by the wide laser doped area (150  $\mu$ m) which has a low blue response

and a high  $j_{0e}$ . Extended cw-laser ablation ( $45\ \mu\text{m}$ ) causes wide metal plated contacts and current loss due to increased contact shading in the "open+dope  $\rightarrow$  ns-open" case.

In the two additional runs, optimized processes were assumed. For the "dope  $\rightarrow$  SiN<sub>x</sub>  $\rightarrow$  open (opt.)" sequence, the width of the laser doped region has been reduced to  $45\ \mu\text{m}$ , which is achievable by state-of-the-art inter tool alignment. This results in a significant increase of efficiency to 21.5 %, caused by higher  $V_{oc}$  and  $j_{sc}$ , can be put down to a better blue response of the cell. Similar improvements are found in the "open+dope  $\rightarrow$  ns-open" case, with an optimized  $22\ \mu\text{m}$  wide laser doped region. The resultant increase in  $j_{sc}$  and  $V_{oc}$  produced a significant increase in cell efficiency to 21.4 %. With this reasonable optimization both processes produce cells which are on par with the reference sequence.

These results indicate that control of silicide growth is imperative to exploit the full efficiency and cost reduction potential of plated nickel-copper contacts. The basic concept of the selective emitter, which is to increase the  $FF$  and the  $V_{oc}$ , resulted in only a minor increase in  $\eta$  of 0.1 % in the best case. Using laser doping processes, which produced cells with adhering contacts, resulted in simulated solar cell efficiencies that were severely reduced compared to the pure laser ablation process. Nevertheless, laser doping increases the process window for silicide formation and allows the combination of this technology with any emitter design, whether it is a high efficiency driven in emitter or a lowly doped and shallow industrial emitter, to produce cells with adhering contacts. Despite the additional processing steps, a reasonable optimization of the alignment procedures promises efficiencies that are on par with the efficiency of purely laser ablated cells.

The pure laser ablation without additional selective doping using a fast pulsed laser appears to be the best option, yielding high efficiency potential and minimal process complexity. However, device degradation and insufficient adhesion is a challenging issue. Extensive research effort is directed towards understanding the nickel-silicide formation on laser contact openings and great progress has been made in the last few years [31, 32, 62]. Also laser ablation produces damage in the silicon crystal, thereby reducing the emitter quality and efficiency potential [66, 211, 212]. This aspect has not been included into the device simulation and for this reason  $\eta = 21.5\%$  represents merely the upper limit of the pure ablation process. In contrast to this, the laser damage produced by laser doping has been measured in chapter 7 and is incorporated into the simulation. In the end, pure laser ablation may only be the second best option to produce nickel-copper plated solar cells. With the best option being a laser doping process that produces stable cells across a wide process window for contact formation bringing only little gain in device efficiency.

## 9.5 Conclusion

The cw-laser process was employed to create solar cell test structures with a selective emitter. It was shown, that a  $\text{SiO}_x\text{N}_y$  layer which results from  $\text{SiN}_x$  cw-laser ablation hinders nickel silicide formation during annealing. This resulted in poor mechanical adhesion between front metal contact and silicon. Wet chemical etching of the  $\text{SiO}_x\text{N}_y$  resulted on the one hand in a substantial increase of mechanical adhesion but on the other hand, the produced test cells were severely degraded by metal-induced shunts. By means of ReBEL imaging the position of a prominent localized shunt could be determined. Scanning electron microscopy in conjunction with  $\mu$ -ReBEL measurements allowed to identify a pyramid tip at the edge of the laser processed line to coincide with this shunt. It was presumed that texture tips at the edge of the laser line receive sufficient energy for dielectric ablation, but that the laser doping below this opening is too shallow to prevent penetration of the p-n junction by nickel silicide growth. With a combination of two laser processes, using a cw-laser to produce a  $4\ \mu\text{m}$  deep p-n junction before  $\text{SiN}_x$  deposition and a ns-pulsed laser to remove the  $\text{SiN}_x$  layer, solar cell test structures with nickel-copper contacts have been created that were stable even to harsh thermal nickel silicidation processes and showed good mechanical adhesion. However, splitting the laser processes into a doping step before  $\text{SiN}_x$  deposition and a contact opening step after  $\text{SiN}_x$  deposition is disadvantageous. The necessary alignment between laser doped region and contact opening pattern increases the complexity of the process sequence, and the wide doping widths required for proper alignment reduces the efficiency potential.

Building upon the knowledge of the  $\text{SiO}_x\text{N}_y$  diffusion barrier and the nickel-induced shunting mechanism, two alternative processing sequences have been developed. These were based on either avoiding the shunting at the pyramid tips by processing on planar wafers, or on the selective removal of the  $\text{SiO}_x\text{N}_y$  layer using a ns-pulsed laser. Whereas the former method is not beneficial for cell efficiency, the high stability to annealing proved that the primal cause for the electrical failure of the test cells after chemical removal of the  $\text{SiO}_x\text{N}_y$  layer was the random pyramid texture. Selective removal of the  $\text{SiO}_x\text{N}_y$  layer using a ns-pulsed laser resulted in test cells with a median  $pFF$  of 81 % and excellent peel forces averaging above 1 N/mm.

Detailed characterization of the laser processes allowed numerical simulations of solar cell performance. By assuming a well designed rear side the cell efficiency was limited by the performance of the front side. That way the proposed sequences have been compared in terms of the simulated cell efficiency. If annealing induced device degradation and insufficient adhesion can be prevented by well controlled silicide growth on a laser contact opening with a shallow emitter, the pure laser ablation route surpasses the selective laser doping, yielding high efficiency potential and minimal process complexity. However, it was found that an optimized selective emitter process produces cell efficiencies that are on par with a defect free pure laser ablation process. Although

a selective emitter does not necessarily improve the cell efficiency, it allows decoupling the emitter design from the contact formation, while ensuring the production of stable solar cells with adhering metal contacts.



## 10 Summary and Outlook

The combination of localized laser doping and light-induced plating is treated as a promising technology to increase efficiency beyond that of standard screen-printed silicon solar cells while keeping the cost of production low.

The major scope of this work is to understand the fundamental physical and chemical mechanisms that govern the laser doping process, identify the technological challenges that hinder the commercial success of innovative laser doped cells with nickel-copper plated contacts, and to develop options to overcome these problems. Furthermore, the suitability of these newly developed processes needs to be experimentally verified and their industrial feasibility needs to be assessed.

The combination of a lowly doped blanket emitter and a highly doped emitter below the metal contacts, forming a selective emitter, yields benefits with regard to charge carrier recombination and contact resistance, which were discussed in detail on a theoretical basis. Likewise, the physical processes relevant to laser doping were reviewed and related to analogous processes found in the field of laser welding.

In the course of this thesis, a laser doping process, which has already proven to produce efficient solar cells with nickel-copper plated contacts on an industrial scale, has been implemented into a versatile research tool. By performing dedicated experiments to find suitable parameters for dielectric ablation, silicon doping, and epitaxial recrystallization, a set of baseline parameters was determined. Using a green continuous wave (cw) laser at an output power of 15 W and a processing speed of 5 m/s resulted in 14  $\mu\text{m}$  wide and highly doped lines. The high processing speed and narrow line width qualifies this parameter set for industrial implementation. However, meager and inhomogeneous deposition of plated nickel layers across the suitable parameter space indicated an imperfect condition of the laser treated surface after silicon nitride ( $\text{SiN}_x$ ) ablation.

Consequently, the mechanism of  $\text{SiN}_x$  ablation as well as the condition of the silicon surface was studied. At first, the ablation with a cw-laser was investigated. For this purpose, a precise method to determine the emitter saturation current density ( $j_{0e}$ ) from photoconductivity measurements, based on the analytic solution of the transport equations for free charge carriers, was developed. Using this method, the detrimental effect of a  $\text{SiN}_x$  layer present during laser doping was shown and could be precisely quantified. Whereas  $j_{0e}$  of the laser doped emitter was as low as 253  $\text{fA}/\text{cm}^2$ , if the emitter was created

before  $\text{SiN}_x$  deposition,  $j_{0e}$  increased by a factor of three if the laser doping was combined with  $\text{SiN}_x$  ablation ( $j_{0e} \approx 750 \text{ fA/cm}^2$ ). This detrimental effect of the  $\text{SiN}_x$  layer on the emitter quality was reported before and has been attributed to a thermal expansion mismatch between silicon and  $\text{SiN}_x$ . However, void formation at the edge of the laser line just below a partly decomposed  $\text{SiN}_x$  layer, which was observed with scanning electron microscopy (SEM), suggested an alternative explanation. A descriptive ablation model was proposed that explains the formation of void defects from gaseous nitrogen released from partly decomposed  $\text{SiN}_x$  into the molten silicon pool. These voids form recombinative surfaces close to the p-n junction and are thus likely to cause the reduction of the emitter quality.

The composition of the laser ablated silicon surface was analyzed using x-ray photoelectron spectroscopy. The decomposition of the measured Si2p signal peak allowed the identification of a silicon oxynitride ( $\text{SiO}_x\text{N}_y$ ) species. The structurally dense  $\text{SiO}_x\text{N}_y$ , which is similar to  $\text{SiN}_x$ , is a dielectric layer that serves as an effective diffusion barrier. It was experimentally verified that this surface layer hinders nickel plating and prevents the formation of a nickel silicide. With the help of computer simulations the dwell time during which the surface is at the temperature of  $\text{SiO}_x\text{N}_y$  formation was estimated. In the case of cw-laser doping this dwell time ( $1.5 \mu\text{s}$ ) is a factor five larger than in the case of a ns-pulsed laser process ( $0.3 \mu\text{s}$ ). This difference is also reflected in extensive formation of nickel silicide on ns-pulsed laser ablated silicon. Additionally, SEM imaging was utilized to estimate the thickness of the  $\text{SiO}_x\text{N}_y$  layer, formed on cw-laser ablated silicon, to about 20 nm, and to demonstrate the resilience of the detrimental layer to chemical etching. It was observed that the  $\text{SiO}_x\text{N}_y$  layer is mostly removed after etch times as long as 120 s in 7% hydrofluoric acid. From these findings, implications for solar cell laser processing are drawn, which form the basis of alterations to the original laser process as well as newly developed process sequences.

Various alterations to the baseline process sequence were evaluated based on electrical and mechanical characterization of solar cell test samples. Whereas the baseline process was stable to the annealing step needed for nickel silicide formation, this original sequence resulted in negligible contact adhesion. After chemical removal of the  $\text{SiO}_x\text{N}_y$  layer, nickel silicide was formed during annealing and the contact adhesion increased significantly. Unfortunately, these cells were severely degraded after the annealing step. In this way it is demonstrated, that on the one hand nickel silicide formation is a necessity to achieve sufficient contact adhesion, but that on the other hand nickel silicide growth can penetrate the space charge region and cause heavy shunting.

By means of reverse biased electroluminescence microcharacterization (ReBEL) nickel silicide growth induced shunts were investigated. By correlating ReBEL and SEM imaging the shunting mechanism is attributed to refraction at the

light trapping texture, concentrating the laser light into the tips of the random pyramids. At the edge region of the Gaussian laser spot, the laser intensity is insufficient to form a deep emitter, but due to the concentration effect the intensity is sufficient for  $\text{SiN}_x$  ablation at pyramid tips. During silicide formation this leads to the observed device degradation. This failure mechanism can be circumvented by laser processing on planar wafers, which is admittedly disadvantageous for the short circuit current of the device. Nevertheless, electrically stable test cells with excellent contact adhesion exceeding  $1 \text{ N/mm}$  could be achieved on chemically etched planar samples.

Two alternative laser process sequences were devised, both of which were shown to produce stable test cells with adhering contacts. The first sequence is based on selective cw-laser doping before the deposition of the  $\text{SiN}_x$  layer, which prevents the formation of the  $\text{SiO}_x\text{N}_y$  in the first place. Using an additional dedicated short pulsed laser ablation step the contact opening is then performed above the highly doped emitter. In the other sequence the cw-laser doping is performed after  $\text{SiN}_x$  deposition. The formed  $\text{SiO}_x\text{N}_y$  layer is subsequently removed using a short pulsed laser that can be housed in the same processing tool. Whereas the first approach brings benefits with regard to the laser doped emitter quality, a reduced process complexity and simplified alignment qualify the latter approach.

The detailed characterization of the laser processes, as well as the gained insight into the design constraints were used to perform two-dimensional solar cell simulations. This allowed to assess the proposed process sequences based on their efficiency potential. Under the assumption of a well designed cell rear side, a defect free contact opening, exposing the blanket emitter to the nickel-copper contact, yields a simulated efficiency of 21.5%. If a laser doped selective emitter is introduced to increase the tolerance to deep silicide growth, laser doping and laser ablation needs to be performed using separate laser sources. Mediocre precision of alignment between doping and contact opening, that could be achieved with the available equipment, reduced the efficiency to about 21%. However, optimized alignment, which is assumed to be realizable with a dedicated processing tool, resulted in a substantial increased of the simulated efficiency to 21.5%, thereby being on par with a defect free contact opening.

## 10.1 Outlook

It appears that future research and development should be directed at either optimizing a selective emitter approach to increase the tolerance of solar cells to nickel induced shunting, or at producing stable cells with adhering contacts using laser contact opening.

The combination of a deep and lowly doped blanket emitter and a defect free contact opening yields a high efficiency potential. However, a contact opening free of defects cannot be achieved with a rapid laser process [66, 211, 212]. A reduced efficiency can therefore be expected, with the loss depending on the specific implementation of the laser contact opening process. The efficiency gain, achieved by using a selective emitter below a screen printed metallization, seems to be overcome by nickel-copper contacts. A nickel-silicide interlayer allows contacting even lowly doped emitters with reasonable contact resistance. At the same time, the laser contact opening surpasses the selective emitter approach in terms of industrial feasibility. However, to achieve stable cells with well adhering metal contacts, the formation of nickel silicide on laser contact openings needs to be further investigated. In recent years important advances have been made leading to novel approaches where the adhesion relies on mechanical interlocking as well as on controlled silicide formation [31, 32]. In approaches without a silicide interlayer the contact resistance may yet reoccur as the limiting factor of efficient solar cells.

Although a selective emitter does not necessarily improve the cell efficiency, it allows decoupling the blanket emitter design from the contact formation, while ensuring the production of stable solar cells with adhering metal contacts. The combination of a laser source for doping and a laser source dedicated for contact opening effectively trades process simplicity for three things: (a) a reduction of the design constraints on the blanket emitter, (b) a wide process window for silicide formation, and (c) a low contact resistance. Increasing the alignment precision will reduce the required width of the laser doped region. This will result in a reduction of shading loss and an increased blue response, further paving the way for industrial production of efficient solar cells with nickel-copper contacts.

## References

- [1] L. Mastny (editor). REN21: Renewables global status report, 2011.
- [2] Z. Shi, S. Wenham, and J. Ji. Mass production of the innovative PLUTO solar cell technology. In *Conference Proceedings of the IEEE Photovoltaic Specialists Conference*, pages 1922–1926, 2009.
- [3] S. R. Wenham and M. A. Green. Patent: Self aligning method for forming a selective emitter and metallization on a solar cell, 2002.
- [4] A. Lennon, Y. Yao, and S. Wenham. Evolution of metal plating for silicon solar cell metallisation. *Progress in Photovoltaics: Research and Applications*, 21(7):1454–1468, 2013.
- [5] A. Morales. Suntech says it received notice of default on bonds due. BloombergBusiness, 18th March 2013.
- [6] J. Zhao, A. Wang, P. P. Altermatt, S. R. Wenham, and M. A. Green. 24% efficient silicon solar cells. In *24th IEEE Photovoltaic Specialists Conference*, volume 2, pages 1477–1480, 1994.
- [7] J. Zhao, A. Wang, P. P. Altermatt, S. R. Wenham, and M. A. Green. 24% Efficient perl silicon solar cell: Recent improvements in high efficiency silicon cell research. *Solar Energy Materials and Solar Cells*, (41-42): 87–99, June 1996.
- [8] J. Zhao, A. Wang, M. A. Green, and F. Ferrazza. 19.8% efficient "honeycomb" textured multicrystalline and 24.4% monocrystalline silicon solar cells. *Appl. Phys. Lett.*, 73(14):1991–1993, 1998.
- [9] J. Zhao, Wang A., and Green M. 24.5% efficiency silicon PERT cells on MCZ substrates and 24.7% efficiency PERL cells on FZ substrates. *Progress in Photovoltaics*, 7:471–474, 1999.
- [10] M. A. Green, K. Emery, Y. Hishikawa, W. Warta, and E. Dunlop. Solar cell efficiency tables (Version 45). *Progress in Photovoltaics*, 23:1–9, 2015.
- [11] A. Sugianto, J. Bovatsek, S. Wenham, B. Tjahjono, G. Xu, Y. Yao, B. Hallam, X. Bai, N. Kuepper, C. Mun Chong, and R. Patel. 18.5% laser-doped solar cell on CZ p-type silicon. In *Conference Proceedings of the IEEE Photovoltaic Specialists Conference*, pages 689–694, 2010.

- [12] K. S. Wang, B. S. Tjahjono, J. Wong, A. Uddin, and S. R. Wenham. Sheet resistance characterization of laser-doped lines on crystalline silicon wafers for photovoltaic applications. *Solar Energy Materials and Solar Cells*, 95(3):974–980, March 2011.
- [13] Z. Hameiri, L. Mai, and S. R. Wenham. Laser-doped local back surface field. In *Conference Proceedings of the IEEE Photovoltaic Specialists Conference*, pages 1054–1057, 2011.
- [14] B. Tjahjono, J. Guo, Z. Hameiri, L. Mai, A. Sugianto, S. Wang, and S. R. Wenham. High efficiency solar cells structures through the use of laser doping. In *Conference Proceedings of the 22nd European Photovoltaic Solar Energy Conference*, pages 966–969, 2007.
- [15] A. Sugianto, B. Tjahjono, J. Guo, and S. Wenham. Impact of laser induced defects on the performance of solar cells using localised laser doped regions beneath the metal contacts. In *22nd European Photovoltaic Solar*, pages 1759–1762, 2007.
- [16] Z. Hameiri, T. Puzzer, L. Mai, A. Sproul, and S. R. Wenham. Laser induced defects in laser doped solar cells. *Progress in Photovoltaics: Research and Applications*, 19(4):391–405, 2011.
- [17] Z. Hameiri, L. Mai, T. Puzzer, and S. R. Wenham. Influence of laser power on the properties of laser doped solar cells. *Solar Energy Materials and Solar Cells*, 95(4):1085–1094, April 2011.
- [18] B. Hallam, S. Wenham, A. Sugianto, L. Mai, C. Chong, M. Edwards, D. Jordan, and P. Fath. Record large-area p-type CZ production cell efficiency of 19.3% based on LDSE technology. *IEEE Journal of Photovoltaics*, 1(1):43–48, 2011.
- [19] J.M. Bovatsek, A. Sugianto, B. Hallam, B. Tjahjono, S. Wenham, and R.S. Patel. High-Speed Fabrication of Laser Doping Selective Emitter Solar Cells Using 532Nm Continuous Wave (Cw) and Modelocked Quasi-Cw Laser Sources. In *26th European Photovoltaic Solar Energy Conference and Exhibition*, volume 1, pages 895–900, 2011.
- [20] B. Tjahjono, H. Haverkamp, V. Wu, H. T. Anditsch, W. H. Jung, J. Cheng, J. Ting, M. J. Yang, D. Habermann, T. Sziptalak, C. Buchner, C. Schmid, B. Beilby, and K. C. Hsu. Optimizing Selective Emitter Technology in One Year of Full Scale Production. In *Proceedings of the 26th EU PVSEC*, pages 901–905, 2011.
- [21] B. Tjahjono, M. Yang, C. Lan, and J. Ting. 18.9% efficient laser doped selective emitter solar cell on industrial grade p-type Czochralski wafer. In *Conference Proceedings of the 25th European Photovoltaic Solar Energy Conference and Exhibition, Valencia, Spain*, pages 6–10, 2010.

- [22] X. Wang, V. Allen, V. Vais, Y. Zhao, B. Tjahjono, Y. Yao, S. Wenham, and A. Lennon. Laser-doped metal-plated bifacial silicon solar cells. *Solar Energy Materials and Solar Cells*, pages 1–9, June 2014.
- [23] Z. Hameiri, L. Mai, A. Sproul, and S. R. Wenham. 18.7% efficient laser-doped solar cell on p-type Czochralski silicon. *Applied Physics Letters*, 97(22):222111, November 2010.
- [24] E. Lee, H. Lee, I. Kim, J. Choi, D. Oh, J. Shim, K. Cho, J. Kim, H. Seok Lee, S. Lee, B. Hallam, and S. R. Wenham. The potential efficiency of laser doped solar cells using photoluminescence imaging. In *Conference Proceedings of the IEEE Photovoltaic Specialists Conference*, pages 1436–1439, 2010.
- [25] E. Lee, H. Lee, J. Choi, D. Oh, J. Shim, K. Cho, J. Kim, S. Lee, B. Hallam, S. R. Wenham, and H. Lee. Improved LDSE processing for the avoidance of overplating yielding 19.2% efficiency on commercial grade crystalline Si solar cell. *Solar Energy Materials and Solar Cells*, 95(12):3592–3595, December 2011.
- [26] Z. Hameiri, L. Mai, and S. R. Wenham. Advantages of photoplatting for laser doped solar cells. *Progress in Photovoltaics: Research and Applications*, 19(5):511–516, 2011.
- [27] B. Hallam, S. Wenham, H. Lee, E. Lee, H. Lee, J. Kim, and J. Shin. Effect of edge junction isolation on the performance of laser doped selective emitter solar cells. *Solar Energy Materials and Solar Cells*, 95(12):3557–3563, December 2011.
- [28] G. Xu, B. Hallam, Z. Hameiri, C. M. Chong, and S. Wenham. Progress in laser doped perl solar cell on p-type CZ silicon wafer. In *Conference Proceedings of the 27th European Photovoltaic Solar Energy Conference*, pages 1550–1552, 2012.
- [29] S. Flynn and A. Lennon. Copper penetration in laser-doped selective-emitter silicon solar cells with plated nickel barrier layers. *Solar Energy Materials and Solar Cells*, 130:309–316, 2014.
- [30] B. Hallam, A. Urueña, R. Russell, M. Aleman, M. Abbott, C. Dang, S. Wenham, L. Tous, and J. Poortmans. Efficiency enhancement of i-PERC solar cells by implementation of a laser doped selective emitter. *Solar Energy Materials and Solar Cells*, 134:89–98, 2015.
- [31] L. Tous, M. Aleman, R. Russell, E. Cornagliotti, P. Choulat, A. Uruena, S. Singh, J. John, F. Duerinckx, J. Poortmans, and R. Mertens. Evaluation of advanced p-PERL and n-PERT large area silicon solar cells with 20.5% energy conversion efficiencies. *Progress in Photovoltaics: Research and Applications*, 20:6–11, 2014.

- [32] A. Mondon, J. Bartsch, M. Kamp, A. Brand, B. Steinhauser, N. Bay, J. Horzel, M. Glatthaar, and S. W. Glunz. Plated nickel-copper contacts on c-Si: from microelectronic processing to cost effective silicon solar cell production. In *Conference Proceedings of the 29th European Photovoltaic Solar Energy Conference, Amsterdam, Netherlands*, 2014.
- [33] Y. Yao, J. Rodriguez, J. Cui, A. Lennon, and S. Wenham. Uniform plating of thin nickel layers for silicon solar cells. *Energy Procedia*, 38: 807–815, 2013.
- [34] M. D. Abbott, J. E. Cotter, F. W. Chen, T. Trupke, R. Bardos, and K. C. Fisher. Application of photoluminescence characterization to the development and manufacturing of high-efficiency silicon solar cells. *Journal of Applied Physics*, 100(11):114514, 2006.
- [35] Eicke R. Weber. Transition metals in silicon. *Applied Physics A - Solids and Surfaces*, 30:1–22, 1983.
- [36] A. M. Wenham, M. A. Green, and S. R. Wenham. Patent: Improved metal adhesion, 2010.
- [37] M. A. Green. Self-consistent optical parameters of intrinsic silicon at 300 K including temperature coefficients. *Solar Energy Materials and Solar Cells*, 92(11):1305–1310, November 2008.
- [38] K. Misiakos and D. Tsamakis. Accurate measurement s of the silicon intrinsic carrier density from 78 to 340K. *Journal of Applied Physics*, 74 (1993):3293–3297, 1993.
- [39] W. Van Roosbroeck and W. Shockley. Photon-radiative recombination of electrons and holes in germanium. *Physical Review*, 94(6):1558–1560, 1954.
- [40] H. Schlangenotto, H. Maeder, and W. Gerlach. Temperature dependence of the radiative recombination coefficient in silicon. *Physica Status Solidi (a)*, 21(1):357–367, 1974.
- [41] M. A. Green. *Silicon solar cells: advanced principles and practice*. Centre for Photovoltaic Devices and Systems, 1995. ISBN 0-733-40994-3.
- [42] J. Dziewior and W. Schmid. Auger coefficient for highly doped and highly excited silicon. *Applied Physics Letters*, 31(5):346–348, September 1977.
- [43] A. Richter, S. W. Glunz, F. Werner, J. Schmidt, and A. Cuevas. Improved quantitative description of Auger recombination in crystalline silicon. *Physical Review B - Condensed Matter and Materials Physics*, 86(16): 165202, 2012.

- [44] W. Shockley and W. T. Read. Statistics of the Recombination of Holes and Electrons. *Physical Review*, 87(5):835–842, 1952.
- [45] R. N. Hall. Electron-hole recombination in germanium. *Physical Review*, 87(2):387, 1952.
- [46] D.K. Schroder. *Semiconductor material and device characterization*. John Wiley & Sons, 2nd edition, 2006. ISBN 0-471-73906-7.
- [47] H. Ibach and H. Lüth. *Festkörperphysik: Einführung in die Grundlagen*. Springer Verlag, 7th edition, 2009. ISBN 3-540-58575-3.
- [48] K. R. McIntosh and P. P. Altermatt. A freeware 1D emitter model for silicon solar cells. In *Conference Proceedings of the IEEE Photovoltaic Specialists Conference*, pages 2188–2193, 2010.
- [49] J. del Alamo, J. van Meerbergen, F. D’Hoore, and J. Nijs. High-low junctions for solar cell applications. *Solid-State Electronics*, 24:533–538, 1981.
- [50] C. Chang and S. Sze. Carrier transport across metal-semiconductor barriers. *Solid-State Electronics*, 13:727–740, 1970.
- [51] N. Stavitski, M. van Dal, A. Lauwers, C. Vrancken, A. Kovalgin, and R. Wolters. Systematic TLM measurements of NiSi and PtSi specific contact resistance to n- and p-type Si in a broad doping range. *IEEE Electron Device Letters*, 29(4):378–381, 2008.
- [52] S. Braun, E. Emre, B. Raabe, and G. Hahn. Electroless Nickel and Copper Metallization: Contact Formation on Crystalline Silicon and Background Plating Behaviour on PECVD SiNx: H Layers. In *25th European Photovoltaic Solar Energy Conference and Exhibition. Valencia, 2006*.
- [53] L. Tous and M. Recaman-Payo. Evaluating contact resistance using epitaxially grown phosphorous emitters. In *Conference Proceedings of the 26th European Photovoltaic Solar Energy Conference, Hamburg, Germany, pages 1–3, 2011*.
- [54] G. Schubert. *Thick film metallisation of crystalline silicon solar cells - Mechanisms, models and applications*. PhD thesis, Universität Konstanz, Fachbereich Physik, 2006.
- [55] M. Hörteis. *Fine-Line Printed Contacts on Crystalline Silicon Solar Cells*. PhD thesis, Universität Konstanz, Fachberich Physik, 2009.

- [56] I. B. Cooper, K. Tate, A. F. Carroll, K. R. Mikeska, R. C. Reedy, and A. Rohatgi. Low Resistance Screen-Printed Ag Contacts to POCl<sub>3</sub> Emitters with Low Saturation Current Density for High Efficiency Si Solar Cells. In *Proceedings of the 38th IEEE Photovoltaic Specialists Conference*, pages 3359–3364. IEEE, 2012.
- [57] A. Yu. Electron tunneling and contact resistance of metal-silicon contact barriers. *Solid-State Electronics*, 13:239–247, 1970.
- [58] S. Kluska. *Development and characterization of laser chemical processes for high efficiency silicon solar cells*. PhD thesis, Albert-Ludwigs-Universität Freiburg im Breisgau, 2013.
- [59] G. Hahn. Status of selective emitter technology. In *Proceeding of the 25th European Photovoltaic Solar Energy Conference and Exhibition, Valencia, Spain*, pages 1091–1096, 2010.
- [60] P. P. Altermatt, J. Schumacher, A. Cuevas, M. J. Kerr, S. W. Glunz, R. King, G. Heiser, and A. Schenk. Numerical modeling of highly doped Si:P emitters based on Fermi-Dirac statistics and self-consistent material parameters. *Journal of Applied Physics*, 92(6):3187–3197, 2002.
- [61] T. Markvart and L. Castañer. *Practical Handbook of Photovoltaics: Fundamentals and Applications: Fundamentals and Applications*. Elsevier, 2003. ISBN 1-856-17390-9.
- [62] A. Metz, D. Adler, S. Bagus, H. Blanke, M. Bothar, E. Brouwer, S. Dauwe, K. Dressler, R. Droessler, T. Droste, M. Fiedler, Y. Gassenbauer, T. Grahl, N. Hermert, W. Kuzminski, A. Lachowicz, T. Lauinger, N. Lenck, M. Manole, M. Martini, R. Messmer, C. Meyer, J. Moschner, K. Ramspeck, P. Roth, R. Schönfelder, B. Schum, J. Sticksel, K. Vaas, M. Volk, and K. Wangemann. Industrial high performance crystalline silicon solar cells and modules based on rear surface passivation technology. *Solar Energy Materials and Solar Cells*, 120:417–425, 2013.
- [63] S. W. Glunz and E. Schneiderlöchner. Laser-fired contact silicon solar cells on p-and n-substrates. In *19th European Photovoltaic Solar Energy Conference, Paris*, pages 1–4, 2004.
- [64] F. Colville. PV’s 20/20 Vision Demands Cost-Efficiency Duality. *PV Society, Reed Business Information*, 2009.
- [65] D. W. Bäuerle. *Laser processing and chemistry*. Springer Science & Business Media, 2011. ISBN 3-642-17613-5.
- [66] S. Hermann, N. Harder, R. Brendel, D. Herzog, and H. Haferkamp. Picosecond laser ablation of SiO<sub>2</sub> layers on silicon substrates. *Applied Physics A*, 99(1):151–158, April 2010.

- [67] John Perlin. The silicon solar cell turns 50. Technical report, National Renewable Energy Lab., Golden, CO.(US), 2004.
- [68] S. R. Wenham, C. B. Honsberg, and M. A. Green. Buried contact silicon solar cells. *Solar Energy Materials and Solar Cells*, 34(1-4):101–110, September 1994.
- [69] T. M. Bruton, K. C. Heasman, J. P. Nagle, D. W. Cunningham, N. B. Mason, R. Russell, and M. A. Balbuena. Large area high efficiency silicon solar cells made by the laser grooved buried grid process. In *Proceedings of the 12th European PV Solar Energy Conference*, pages 761–762, 1994.
- [70] T. M. Bruton, G. Luthardt, K. D. Rasch, K. Roy, I. Dorrity, B. Garrard, L. Teale, J. Alonso, U. Ugalde, K. Declerq, J. Nijs, J. Szlufcik, A. Rauber, W. Wettling, and A. Vallera. A study of the manufacture at 500 MWp p.a. of crystalline silicon photovoltaic modules. In *Proceedings of the 14th European Photovoltaic Solar Energy Conference and Exhibition*, pages 11–16, 1997.
- [71] B. D. Clark. Lasers in solar cell production. *Photonics Spectra*, pages 11–14, 2009.
- [72] A. Fell. *Modelling and Simulation of Laser Chemical Processing (LCP) for the Manufacturing of Silicon Solar Cells*. PhD thesis, Universitat Konstanz, 2010.
- [73] S. Kluska, M. K. Cinkowski, and F. Granek. Boron LCP Local Back Surface Fields for High Efficiency Silicon Solar Cells. In *Proceedings of the 37th IEEE Photovoltaic Specialists Conference*, pages 1468–1473, 2011.
- [74] B. Steinhauser, M. B. Mansoor, U. Jager, J. Benick, and M. Hermle. Firing-stable PassDop passivation for screen printed n-type PERL solar cells based on a-SiNx:P. *Solar Energy Materials and Solar Cells*, 126: 96–100, 2014.
- [75] D. Kray, N. Bay, G. Cimiotti, S. Kleinschmidt, N. Kosterke, A. Losel, M. Sailer, A. Trager, H. Kuhnlein, H. Nussbaumer, C. Fleischmann, and F. Granek. Industrial LCP selective emitter solar cells with plated contacts. In *Conference Proceedings of the IEEE Photovoltaic Specialists Conference*, pages 667–671, 2010.
- [76] S. Kluska and F. Granek. High-efficiency silicon solar cells with boron local back surface fields formed by laser chemical processing. *IEEE Electron Device Letters*, 32(9):1257–1259, 2011.
- [77] S. Kluska, C. Fleischmann, A. Buchler, W. Hordt, C. Geisler, S. Hopman, and M. Glatthaar. Micro characterization of laser structured solar cells with plated Ni-Ag contacts. *Solar Energy Materials and Solar Cells*, 120: 323–331, January 2014.

- [78] B. Hallam, C. Chan, A. Sugianto, and S. Wenham. Deep junction laser doping for contacting buried layers in silicon solar cells. *Solar Energy Materials and Solar Cells*, 113:124–134, June 2013.
- [79] Z. Wang, P. Han, H. Lu, H. Qian, L. Chen, Q. Meng, N. Tang, F. Gao, Y. Jiang, J. Wu, W. Wu, H. Zhu, J. Ji, Z. Shi, A. Sugianto, L. Mai, B. Hallam, and S. Wenham. Advanced PERC and PERL production cells with 20.3 % record efficiency for standard commercial p-type silicon wafers. *Progress in Photovoltaics: Research and Applications*, pages 260–268, 2012.
- [80] Vijay V. Vaitheeswaran. The Economist: Beyond Profit – Suntech’s bankruptcy, 21th march 2013.
- [81] M. von Allmen. *Laser-Beam Interactions with Materials - Physical principles and applications*. Springer Verl., 2nd edition, 1995.
- [82] C. J. Smithells. *Smithells Metals Reference Book, (E. A. Brandes and G. B. Brook, Eds.)*. Oxford: Butterworth-Heinemann, 7th edition, 1992. ISBN 0-7506-1020-4.
- [83] J. Straub, A. Weinzierl, and M. Zell. Thermokapillare Grenzflächenkonvektion. *Wärme- und Stoffübertragung*, 25:281–288, 1990.
- [84] T. R. Anthony and H. E. Cline. Surface rippling induced by surface-tension gradients during laser surface melting and alloying. *Journal of Applied Physics*, 48(9):3888–3894, 1977.
- [85] A. Fell and G. P. Willeke. Fast simulation code for heating, phase changes and dopant diffusion in silicon laser processing using the alternating direction explicit (ADE) method. *Applied Physics A: Materials Science and Processing*, 98(2):435–440, February 2010.
- [86] J. R. Köhler and S. Eisele. Influence of precursor layer ablation on laser doping of silicon. *Progress in Photovoltaics: Research and Applications*, 18(April):334–339, 2010.
- [87] G. Poulain, D. Blanc, B. Semmache, Y. Pellegrin, and M. Lemiti. Finite Element Simulation Of Laser-Induced Diffusion In Silicon. *Energy Procedia*, 8:587–591, 2011.
- [88] W. Zhang, G. G. Roy, J. W. Elmer, and T. DebRoy. Modeling of heat transfer and fluid flow during gas tungsten arc spot welding of low carbon steel. *Journal of Applied Physics*, 93(5):3022–3033, 2003.
- [89] J. J. Blecher, T. Palmer, E. W. Reutzler, and T. Debroy. Laser-silicon interaction for selective emitter formation in photovoltaics. II. Model applications. *Journal of Applied Physics*, 112(11):114906, 2012.

- [90] J. J. Blecher, T. Palmer, T. DebRoy, and E. Reutzel. Laser-silicon interaction for selective emitter formation in photovoltaics. I. Numerical model and validation. *Journal of Applied Physics*, 112(11):114906, 2012.
- [91] A. Matsunawa, J. Kim, N. Seto, M. Mizutani, and S. Katayama. Dynamics of keyhole and molten pool in laser welding. *Journal of Laser Applications*, 10:247, 1998.
- [92] J. Lee, S. Ko, D. Farson, and C. Yoo. Mechanism of keyhole formation and stability in stationary laser welding. *Journal of Physics D: Applied Physics*, 35:1570–1576, 2002.
- [93] H. Ki, J. Mazumder, and P. S. Mohanty. Modeling of laser keyhole welding: Part I. mathematical modeling, numerical methodology, role of recoil pressure, multiple reflections, and free surface evolution. *Metallurgical and Materials Transactions A*, 33(June):1817–1830, 2002.
- [94] S. Pang, L. Chen, J. Zhou, Y. Yin, and T. Chen. A three-dimensional sharp interface model for self-consistent keyhole and weld pool dynamics in deep penetration laser welding. *Journal of Physics D: Applied Physics*, 44:025301, 2010.
- [95] W. Cho, S. Na, M. Cho, and J. Lee. Numerical study of alloying element distribution in CO<sub>2</sub> laser-GMA hybrid welding. *Computational Materials Science*, 49(4):792–800, 2010.
- [96] W. Cho, S. Na, C. Thomy, and F. Vollertsen. Numerical simulation of molten pool dynamics in high power disk laser welding. *Journal of Materials Processing Technology*, 212(1):262–275, 2012.
- [97] W. Tan, S. Neil, and C. Yung. Investigation of keyhole plume and molten pool based on a three-dimensional dynamic model with sharp interface formulation. *Journal of Physics D: Applied Physics*, 46:55501, 2013.
- [98] M. Courtois, M. Carin, P. Masson, S. Gaied, and M. Balabane. A new approach to compute multi-reflections of laser beam in a keyhole for heat transfer and fluid flow modelling in laser welding. *Journal of Physics D: Applied Physics*, 46:505305, 2013.
- [99] F. F. Abraham and J. Q. Broughton. Pulsed melting of silicon (111) and (100) surfaces simulated by molecular dynamics. *Physical Review Letters*, 56(7):734–737, 1986.
- [100] A. G. Cullis. Microstructure and Topography. In *Laser annealing of semiconductors*, pages 147–196. 1982.
- [101] A. Gat, L. Gerzberg, J. F. Gibbons, T. J. Magee, J. Peng, and J. D. Hong. Cw laser anneal of polycrystalline silicon: Crystalline structure, electrical properties. *Applied Physics Letters*, 33(1978):775–778, 1978.

- [102] E. I. Givargizov. *Oriented crystallization on amorphous substrates*. Springer, 1991. ISBN 1-489-92562-6.
- [103] Y. Kawamura, K. Toyoda, and S. Namba. Effective deep ultraviolet photoetching of polymethyl methacrylate by an excimer laser. *Appl. Phys. Lett.*, 40(1982):374–375, 1982.
- [104] N. Aizaki. Recrystallization of silicon film on insulating layers using a laser beam split by a birefringent plate. *Applied Physics Letters*, 44(1984): 686–688, 1984.
- [105] M. Robert Pinnel and James E. Bennett. Qualitative observations on the diffusion of copper and gold through a nickel barrier. *Metallurgical Transactions A*, 7(May):629–635, 1976.
- [106] J. Bartsch, V. Radtke, C. Schetter, and S. W. Glunz. Electrochemical methods to analyse the light-induced plating process. *Journal of Applied Electrochemistry*, 40(4):757–765, April 2010.
- [107] A. Kraft, C. Wolf, J. Bartsch, M. Glatthaar, and S. Glunz. Long term stability of copper front side contacts for crystalline silicon solar cells. *Solar Energy Materials and Solar Cells*, 136:25–31, 2015.
- [108] A. Karpour, B. S. Tjahjono, and S. R. Wenham. Advanced electroless plating of high efficiency silicon solar cells. In *Proceedings of the 24th European Photovoltaic Solar Energy Conference, Hamburg, Germany*, pages 1465–1468, 2009.
- [109] M. G. Coleman, R. Pryor, and T. G. Sparks. The Pd<sub>2</sub>Si - Pd - Ni - solder plated metallization system for silicon solar cells. In *Photovoltaic Specialists Conference, 13th, Washington, D.C.*, pages 597–602, 1978.
- [110] J. Jensen, P. Møller, T. Bruton, N. Mason, R. Russell, J. Hadley, P. Verhoeven, and A. Matthewson. Electrochemical Deposition of Buried Contacts in High-Efficiency Crystalline Silicon Photovoltaic Cells. *Journal of The Electrochemical Society*, 150(1):G49–G53, 2003.
- [111] A. Mondon, M. N. Jawaid, J. Bartsch, M. Glatthaar, and S. W. Glunz. Microstructure analysis of the interface situation and adhesion of thermally formed nickel silicide for plated nickel-copper contacts on silicon solar cells. *Solar Energy Materials and Solar Cells*, 117:209–213, October 2013.
- [112] A. Mondon. *Nickel silicide from plated nickel for high adhesion of fully plated solar cell metallization*. PhD thesis, Albert-Ludwig-Universität Freiburg, 2015.
- [113] G. O. Mallory. *Electroless plating: fundamentals and applications*, chapter 1. The fundamental aspects of electroless nickel plating, pages 1–56. Noyes Publications/William Andrew Publishing, LLC: Norwich, NY, USA, 1990.

- [114] N. Kanani. *Galvanotechnik: Grundlagen, Verfahren und Praxis*, volume 2. Hanser Verlag, 2009. ISBN 978-3-446-41738-0.
- [115] L. Tous, J.F. Lerat, T. Emeraud, R. Negru, K. Huet, A. Uruena, M. Aleman, J. Meersschaut, H. Bender, R. Russell, et al. Nickel silicide contacts formed by excimer laser annealing for high efficiency solar cells. *Progress in Photovoltaics: Research and Applications*, 21(3):267–275, 2013.
- [116] A. Lauwers, J. Kittl, M. Van Dal, O. Chamirian, M. Pawlak, M. de Potter, R. Lindsay, T. Raymakers, X. Pages, B. Mebarki, T. Mandrekar, and K. Maex. Ni based silicides for 45nm CMOS and beyond. *Materials Science and Engineering: B*, 114-115:29–41, 2004.
- [117] D. J. Coe and E. H. Rhoderick. Silicide formation in Ni-Si Schottky barrier diodes. *Journal of Physics D: Applied Physics*, 9:965–972, 2001.
- [118] L. J. Chen. *Silicide technology for integrated circuits*, volume 5. Institution of Engineering and Technology, London, 2004. ISBN 0-863-41352-0.
- [119] G. Finstad. A Xe marker study of the transformation of Ni<sub>2</sub>Si to NiSi in thin films. *Physica Status Solidi (a)*, 63(1):223–228, 1981.
- [120] E. O. Kirkendall and A. D. Smigelskas. Zinc Diffusion in Alpha Brass. *Aime Trans*, 171:130–142, 1947.
- [121] P. S. Lee, D. Mangelinck, K. L. Pey, J. Ding, J. Y. Dai, C. S. Ho, and A. See. On the Ni-Si phase transformation with/without native oxide. *Microelectronic Engineering*, 51:583–594, 2000.
- [122] K. Bullis. Why We Need More Solar Companies to Fail. *MIT Technology Review*, March 18th:9–10, 2013.
- [123] Suntech. Letter to Suntech Customers, September 2nd, 2011.
- [124] T. C. Röder, S. J. Eisele, P. Grabitz, C. Wagner, G. Kulushich, J. R. Köhler, and J. H. Werner. Add-on laser tailored selective emitter solar cells. *Progress in Photovoltaics: Research and Applications*, 18(7):505–510, 2010.
- [125] U. Jäger, S. Mack, C. Wufka, A. Wolf, D. Biro, and R. Preu. Benefit of selective emitters for p-Type silicon solar cells with passivated surfaces. *IEEE Journal of Photovoltaics*, 3(2):621–627, April 2013.
- [126] F. Geyer. Einzel- und Gesamtprozesskosten der direktgalvanischen Metallisierung für kristalline Silicium-Solarzellen. Master’s thesis, Karlsruher Institut für Technologie(KIT), 2014.

- [127] J. I. Goldstein, D. E. Newbury, P. Echlin, et al. *Scanning electron microscopy and X-ray microanalysis – A text for biologists, materials scientists, and geologists*. Plenum Publishing Corporation, 2nd edition, 1992. ISBN 0-306-44175-6.
- [128] R. Waser. *Nanoelectronics and Information Technology*. Wiley-VCH Verlag, Weinheim, 2012.
- [129] D. Drouin, A. R. Couture, D. Joly, X. Tastet, V. Aimez, and R. Gauvin. CASINO V2.42 - A fast and easy-to-use modeling tool for scanning electron microscopy and microanalysis users. *Scanning*, 29(3):92–101, 2007.
- [130] A. J. Wilkinson and P. B. Hirsch. Electron diffraction based techniques in scanning electron microscopy of bulk materials. *Micron*, 28(4):279–308, August 1997.
- [131] J. I. Hanoka and R. O. Bell. Electron-Beam-Induced Currents in Semiconductors. *Annual Review of Materials Science*, 11(4):353–380, 1981.
- [132] D. Briggs and M.P. Seah. *Practical surface analysis: Volume 1 – Auger and X-ray Photoelectron Spectroscopy*. John Wiley & Sons, 2nd edition, 1990.
- [133] C. J. Powell and A. Jablonski. *NIST Electron Inelastic-Mean-Free-Path Database- Version 1.2*. Gaithersburg, 2010.
- [134] A. V. Naumkin, A. Kraut-Vass, S. W. Gaarenstroom, and C. J. Powell. *NIST X-ray Photoelectron Spectroscopy Database*. 2012.
- [135] Olympus – Web Resource Center. URL <http://olympus.magnet.fsu.edu/index.html>.
- [136] Olympus Applications LEXT Optical Metrology. Brochure: The LEXT at work in cutting-edge research, 2010.
- [137] R. Sinton, A. Cuevas, and M. Stuckings. Quasi-steady-state photoconductance, a new method for solar cell material and device characterization. In *Conference Proceedings of the 25th IEEE Photovoltaic Specialists Conference*, pages 457–460, 1996.
- [138] Henning Nagel, Christopher Berge, and Armin G. Aberle. Generalized analysis of quasi-steady-state and quasi-transient measurements of carrier lifetimes in semiconductors. *Journal of Applied Physics*, 86(11):6218, December 1999.
- [139] K. Luke and L. J. Cheng. Analysis of the interaction of a laser pulse with a silicon wafer: determination of bulk lifetime and surface recombination velocity. *Journal of Applied Physics*., 61(6):2282, March 1987.

- [140] T. Otaredian. Separate contactless measurement of the bulk lifetime and the surface recombination velocity by the harmonic optical generation of the excess carriers. *Solid-State Electronics*, 36(2):153–162, February 1993.
- [141] J. Giesecke. *Quantitative Recombination and Transport Properties in Silicon from Dynamic Luminescence*. Springer International Publishing, Cham, Switzerland, 2014.
- [142] S.R. Wenham, M.A. Green, M.E. Watt, and R. Corkish. *Applied Photovoltaics*, volume 43. Earthscan - Science Publishers, 2nd edition, 2007.
- [143] F. M. Smits. Measurement of Sheet Resistivities with the Four-Point Probe. *Bell System Technical Journal*, 37(3):711–718, 1958.
- [144] P. Blood. Capacitance-voltage profiling and the characterisation of III-V semiconductors using electrolyte barriers. *Semiconductor Science and Technology*, 1:7–27, 1999.
- [145] R. Sinton and A. Cuevas. A quasi-steady-state open-circuit voltage method for solar cell characterization. In *Proc. 16th European Photovoltaic Solar Energy Conference*, pages 1–4, 2000.
- [146] K. Bothe, K. Ramspeck, D. Hinken, C. Schinke, J. Schmidt, S. Herlufsen, R. Brendel, J. Bauer, J. M. Wagner, N. Zakharov, and O. Breitenstein. Luminescence emission from forward- and reverse-biased multicrystalline silicon solar cells. *Journal of Applied Physics*, 106(10):104510, 2009.
- [147] M. Kasemann. *What photons tell us about solar cells - Infrared imaging techniques for crystalline silicon solar cell characterization and production control*. PhD thesis, Albert-Ludwigs-Universität Freiburg im Breisgau, 2010.
- [148] W. Kwapil. *Alternative materials for crystalline silicon solar cells Risks and implications*. PhD thesis, Universität Konstanz, 2010.
- [149] U. Eitner and L. C. Rendler. The Mechanical Theory Behind the Peel Test. *Energy Procedia*, 55:331–335, 2014.
- [150] C. Voyer. *Innovative Technologien Zur Emittererzeugung für Kristalline Silizium-Solarzellen Mittels Durchlaufdiffusion*. PhD thesis, Albert-Ludwigs-Universität Freiburg im Breisgau, 2009.
- [151] W. Hördt. *Lasermikrostrukturierung zur Herstellung von Nickel metallisierten Solarzellen*. Master’s thesis, Albert-Ludwigs-Universität Freiburg, 2013.
- [152] A. Kraft. *Plated Copper Front Side Metallization on Printed Seed-Layers for Silicon Solar Cells*. PhD thesis, Albert-Ludwigs-Universität Freiburg im Breisgau, 2015.

- [153] R. Brendel, A. Aberle, A. Cuevas, S. Glunz, G. Hahn, J. Poortmans, R. Sinton, A. Weeber, M. Rauer, A. Mondon, C. Schmiga, J. Bartsch, M. Glatthaar, and S. W. Glunz. Nickel-plated Front Contacts for Front and Rear Emitter Silicon Solar Cells. *Energy Procedia*, 38:449–458, 2013.
- [154] W. Hördt, S. Kluska, C. Geisler, S. Hopman, J. Bartsch, A. Mondon, and M. Glatthaar. Failure mechanisms for solar cells with laser doped selective emitter and plated Ni-Cu metal contacts. In *Proceedings of the 29th European Photovoltaic Solar Energy Conference, Amsterdam, Netherlands*, 2014.
- [155] F. K. Kneubühl and M. W. Sigrist. *Laser*. Springer, 2008.
- [156] Spectra-Physics. Millennia Prime - rugged high-power CW 532nm DPSS LASERS – Specification sheet, 2010.
- [157] Innolas Laser GmbH. Nanio series - Industrial DPSS Lasers - NANIO 532-20-V – Specification sheet, 2011.
- [158] A. Knorz, M. Peters, A. Grohe, C. Harmel, and R. Preu. Selective laser ablation of SiN<sub>x</sub> layers on textured surfaces for low temperature front side metallizations. *Progress in Photovoltaics: Research and Applications*, 17(2):127–136, 2009.
- [159] ImageJ Imaging Software. <http://imagej.nih.gov/ij/>, 2015.
- [160] R. Lopes Sauaia. *Development and analysis of silicon solar cells with laser-fired contacts and silicon nitride laser ablation*. PhD thesis, University of São Paulo, PUCRS – PGETEMA, Brasil, 2013.
- [161] Edax International and Alan Sandborg. Manual: Energy Dispersive X-Ray Spectrometry - EDS - Instrumentation & Signal Detection, 2000.
- [162] S. Hopman. *Anwendung des Laser Chemical Processing zur Herstellung von Silizium-Solarzellen*. PhD thesis, Albert-Ludwigs-Universität Freiburg im Breisgau, 2010.
- [163] C. Geisler, W. Hördt, S. Kluska, A. Mondon, S. Hopman, and M. Glatthaar. Overcoming electrical and mechanical challenges of continuous wave laser processing for Ni-Cu plated solar cells. *Solar Energy Materials and Solar Cells*, 133:48–55, 2015.
- [164] A. Cuevas and R. Sinton. Detail modelling of the effective minority carrier lifetime and the open-circuit voltage of silicon solar cells. In *Proceedings of the 22nd European Photovoltaic Solar Energy Conference*, pages 3–7, 2007.
- [165] D. Clugston and P. Basore. PC1D Version 5: 32-bit Solar Cell Modeling on Personal Computers. In *26th IEEE PVSC*, page 207, 1997.

- [166] D. E. Kane and R. M. Swanson. Measurement of the emitter saturation current by a contactless photoconductivity decay method. In *18th IEEE photovoltaic specialists conference*, pages 578–583, 1985.
- [167] H. Mäckel and K. Varner. On the determination of the emitter saturation current density from lifetime measurements of silicon devices. *Progress in Photovoltaics: Research and Applications*, 21(February):850–866, 2013.
- [168] P. P. Altermatt, J. Schmidt, G. Heiser, and A. G. Aberle. Assessment and parameterisation of Coulomb-enhanced Auger recombination coefficients in lowly injected crystalline silicon. *Journal of Applied Physics*, 82(10):4938, 1997.
- [169] J. S. Swirhun, R. Sinton, M. Keith Forsyth, and T. Mankad. Contactless measurement of minority carrier lifetime in silicon ingots and bricks. *Progress in Photovoltaics: Research and Applications*, 19(3):313–319, 2011.
- [170] J. Seiffe, L. Gautero, M. Hofmann, J. Rentsch, R. Preu, S. Weber, and R. Eichel. Surface passivation of crystalline silicon by plasma-enhanced chemical vapor deposition double layers of silicon-rich silicon oxynitride and silicon nitride. *Journal of Applied Physics*, 109(3):12, 2011.
- [171] K. R. McIntosh and S. C. Baker-Finch. OPAL 2.0: Rapid optical simulation of practical silicon solar cells. In *38th IEEE PVSC*, pages 1–4, 2012.
- [172] F. Secco d’ Aragona. Dislocation Etch for (100) Planes in Silicon. *Journal of The Electrochemical Society*, 119(7):948, 1972.
- [173] C. Reichel, F. Granek, J. Benick, O. Schultz-Wittmann, and S. W. Glunz. Comparison of emitter saturation current densities determined by IDLS in high and low injection regimes. *Progress in Photovoltaics: Research and Applications*, 20(1):21–30, January 2010.
- [174] J. Greulich, U. Jäger, S. Rein, and R. Preu. A review and comparison of one-and two-dimensional simulations of solar cells featuring selective emitters. *IEEE Journal of Photovoltaics*, 2(4):441–449, October 2012.
- [175] L. Xu, K. Weber, A. Fell, Z. Hameiri, S. Phang, X. Yang, and E. Franklin. The impact of SiO<sub>2</sub>/SiN<sub>x</sub> stack thickness on laser doping of silicon solar cell. *IEEE Journal of Photovoltaics*, 4(2):594–600, 2014.
- [176] S. M. Hu. Stress-related problems in Silicon Technology. *Journal of Applied Physics*, 70(6):R53–R80, 1991.
- [177] S. C. Baker-Finch and K. R. McIntosh. Reflection of normally incident light from silicon solar cells with pyramidal texture. *Progress in Photovoltaics: Research and Applications*, 19(4):406–416, 2011.

- [178] S. C. Singhal. Thermodynamic analysis of the high-temperature stability of silicon nitride and silicon carbide. *Ceramurgia International*, 2(3): 123–130, July 1976.
- [179] R. D. Pehlke and J. F. Elliott. High-Temperature Thermodynamics of the Silicon, Nitrogen, Silicon-Nitride System. *Transactions of the Metallurgical Society of AIME*, 215:781–785, 1959.
- [180] K. R. Williams and R. Müller. Etch rates for micromachining processing. *Journal of Microelectromechanical Systems*, 4(5):256–269, 1996.
- [181] K. R. Williams, K. Gupta, and M. Wasilik. Etch rates for micromachining processing - Part II. *Journal of Microelectromechanical Systems*, 12(4): 761–778, 2003.
- [182] J. Bartsch, M. Kamp, D. Hartleb, C. Wittich, A. Mondon, B. Steinhauser, F. Feldmann, A. Richter, J. Benick, M. Glatthaar, M. Hermle, and S. W. Glunz. 21.8% Efficient n-type Solar Cells with Industrially Feasible Plated Metallization. *Energy Procedia*, 55:400–409, 2014.
- [183] D. Shirley. High-Resolution X-ray Photoemission Spectrum of the Valance Bands of Gold. *Physical Review B*, 5(12):4709–4714, 1972.
- [184] A. Barranco, J. Mejias, J. P. Espinoos, A. Caballero, A. R. Gonzaaez-Elipe, and F. Yubero. Chemical stability of  $\text{Si}_n^+$  species in  $\text{SiO}_x$  ( $x < 2$ ) thin films. *Journal of Vacuum Science & Technology A: Vacuum, Surfaces, and Films*, 19(1):136–144, 2001.
- [185] M. Klasson, A. Berndtsson, J. Hedman, R. Nilsson, R. Nyholm, and C. Nordling. Electron escape depth in silicon. *Journal of Electron Spectroscopy and Related Phenomena*, 3:427–434, 1974.
- [186] A. J. Taylor, G. M. Lancaster, and W. J. Rabalais. Chemical reactions of  $\text{N}_2^+$  ion beams with group IV elements and their oxides. *Journal of Electron Spectroscopy and Related Phenomena*, 13:435–444, 1978.
- [187] C. D. Wagner and J. A. Taylor. Generation of XPS Auger lines by bremsstrahlung. *Journal of Electron Spectroscopy and Related Phenomena*, 20(1):83–93, January 1980.
- [188] R. V. Weeren, E. A. Leone, S. Curran, L. C. Klein, and S. C. Danforth. Synthesis and Characterization of Amorphous Si, N, O. *Journal of the American Ceramic Society*, 77(10):2699–2702, 1994.
- [189] R. Mroczynski, T. Bieniek, R. B. Beck, M. Ćwil, P. Konarski, P. Hoffmann, and D. Schmeißer. Comparison of composition of ultra-thin silicon oxynitride layers fabricated by PECVD and ultrashallow rf plasma ion implantation. *Journal of Telecommunications and Information Technology*, pages 20–24, 2007.

- [190] J. Viard, E. Beche, D. Perarnau, R. Berjoan, and J. Durand. XPS and FTIR study of silicon oxynitride thin films. *Journal of the European Ceramic Society*, 17:2025–2028, 1997.
- [191] H. D. Batha and E. D. Whitney. Kinetics and Mechanism of the Thermal Decomposition of Si<sub>3</sub>N<sub>4</sub>. *Journal of The American Ceramic Society*, 56(7):365–369, 1973.
- [192] Z. K. Huang, P. Greil, and G. Petzow. Formation of silicon oxynitride from Si<sub>3</sub>N<sub>4</sub> and SiO<sub>2</sub> in the presence of Al<sub>2</sub>O<sub>3</sub>. *Ceramics International*, 11(1):155, 1985.
- [193] J. T. Milek. *Silicon nitride for microelectronic applications, Part 2: Applications and devices*. Plenum Publishin Corporation, New York, 1972.
- [194] H. Du. Oxidation Studies of Crystalline CVD Silicon Nitride. *Journal of The Electrochemical Society*, 136(5):1527, 1989.
- [195] H. Du. Thermodynamics of the Si-N-O System and Kinetic Modeling of Oxidation of Si<sub>3</sub>N<sub>4</sub>. *Journal of The Electrochemical Society*, 136(11):3210, 1989.
- [196] L. U. Ogbuji and J. L. Smialek. Evidence from transmission electron microscopy for an oxynitride layer in oxidized Si<sub>3</sub>N<sub>4</sub>. *Journal of The Electrochemical Society*, 138(10):L51–L53, 1991.
- [197] L. T. Xiong, C. Mao-Sheng, and H. Zhi-Ling. Crystal structure and high hardness mechanism of orthorhombic Si<sub>2</sub>N<sub>2</sub>O. *Chinese Physics Letters*, 26(7):076201, 2009.
- [198] A. M. Alper. *Phase Diagrams in Advanced Ceramics*. Academic Press, 1995. ISBN 0-123-41834-8.
- [199] C. Brosset and I. Idrestedt. Crystal Structure of Silicon Oxynitride, Si<sub>2</sub>N<sub>2</sub>O. *Nature*, 201:1211–1211, 1964.
- [200] R. Weil and K. Parker. *Electroless plating, chapter 4: The properties of electroless nickel*, pages 111–137. American Electroplaters and Surface Finishers Society, 1990.
- [201] A. Karpour and S. R. Wenham. The importance of surface roughness in the adhesion of electroless-plated metal in inkjet printed grooves. In *Conference Proceedings of the IEEE Photovoltaic Specialists Conference*, pages 1410–1413. IEEE, 2010.
- [202] K. Maex and M. Rossum. Properties of metal silicides, Chapter 4: Electronic band structure of TM silicides. pages 155–163. The institution of electrical engineers, UK, 1995.

- [203] A. Büchler, S. Kluska, M. Kasemann, M. Breitwieser, W. Kwapil, A. Hähnel, H. Blumtritt, S. Hopman, and M. Glatthaar. Localization and characterization of annealing-induced shunts in Ni-plated monocrystalline silicon solar cells. *Physica Status Solidi - Rapid Research Letters*, 8(5):385–389, 2014.
- [204] P. Gundel, M. C. Schubert, W. Kwapil, J. Schön, M. Reiche, H. Savin, M. Yli-Koski, J. A. Sans, G. Martinez-Criado, W. Seifert, W. Warta, and E. R. Weber. Micro-photoluminescence spectroscopy on metal precipitates in silicon. *Physica Status Solidi - Rapid Research Letters*, 3(7-8):230–232, October 2009.
- [205] S. Mahadevan, S. M. Hardas, and G. Suryan. Electrical breakdown in semiconductors. *Physica Status Solidi (a)*, 8:335–374, 1971.
- [206] W. Kwapil, P. Gundel, M. C. Schubert, F. D. Heinz, W. Warta, E. R. Weber, A. Goetzberger, and G. Martinez-Criado. Observation of metal precipitates at prebreakdown sites in multicrystalline silicon solar cells. *Applied Physics Letters*, 95(23):232113, 2009.
- [207] J. Wendt, M. Träger, M. Mette, A. Pfennig, and B. Jaeckel. The Link Between Mechanical Stress Induced By Soldering And Micro Damages In Silicon Solar Cells. In *Conference Proceedings of the 24th EU Photovoltaic Specialists Conference*, pages 3420–3423, 2009.
- [208] A. Fell. A free and fast three-dimensional/two-dimensional solar cell simulator featuring conductive boundary and quasi-neutrality approximations. *IEEE Transactions on Electron Devices*, 60(2):733–738, 2013.
- [209] S.W. Glunz, J. Knobloch, C. Hebling, and W. Wettling. The range of high-efficiency silicon solar cells fabricated at fraunhofer ise. In *Conference Proceedings of the 26th IEEE Photovoltaic Specialists Conference*, pages 231–234. IEEE, 1997.
- [210] D. B. M. Klaassen. A unified mobility model for device simulation - II. Temperature dependence of carrier mobility and lifetime. *Solid-State Electronics*, 35(7):961–967, July 1992.
- [211] A. Knorz. *Entwicklung und charakterisierung strukturierender laserverfahren für die herstellung kristalliner silizium - solarzellen*. PhD thesis, Universität Konstanz, 2011.
- [212] A. Brand, A. Knorz, R. Zeidler, J. F. Nekarda, and R. Preu. Nanosecond laser annealing to decrease the damage of picosecond laser ablation of anti-reflection layers on textured silicon surfaces. In *Conference Record of the SPIE Conference, Solar Energy and Technology*, 2012.

# List of Publications

## Articles in Peer Reviewed Journals

C. Geisler, S. Kluska, S. Hopman, J. Giesecke, M. Glatthaar, “Passivation induced cavity defects in laser doped selective emitter Si solar cells – Formation model and recombination analysis”, *IEEE Journal of Photovoltaics*, published online: 11 March 2015, DOI:10.1109/JPHOTOV.2015.2407152.

C. Geisler, W. Hördt, S. Kluska, A. Mondon, S. Hopman, M. Glatthaar, “Overcoming electrical and mechanical challenges of continuous wave laser processing for Ni–Cu plated solar cells”, *Solar Energy Materials and Solar Cells*, vol. 133, pp. 48-55, 2015.

S. Kluska, C. Fleischmann, A. Büchler, W. Hördt, C. Geisler, S. Hopman and M. Glatthaar, “Micro characterization of laser structured solar cells with plated Ni–Ag contacts”, *Solar Energy Materials and Solar Cells*, vol. 120, pp. 323-331, 2014.

## Contributions to Conferences

C. Geisler, “Laser Doping from Liquid Films – Melting, Ablation, and Challenges for Ni–Cu Plated Contacts”, *Silicon Forest, Falkau, Germany, 2015*, oral presentation.

W. Hördt, S. Kluska, C. Geisler, S. Hopman, J. Bartsch, A. Mondon, M. Glatthaar, “Failure mechanisms for solar cells with laser doped selective emitter and plated Ni–Cu metal contacts”, *29th European PV Solar Energy Conference and Exhibition, Amsterdam, The Netherlands, 2014*, poster presentation and publication in conference proceedings.

C. Geisler, W. Hördt, S. Kluska, A. Mondon, S. Hopman and M. Glatthaar, “Continuous wave laser processing for electrical and mechanical stable solar cells with Ni-Cu metallization”, *4th International Conference on Silicon Photovoltaics, 's-Hertogenbosch, The Netherlands, 2014*, poster presentation and publication in conference proceedings.

The combination of localized laser patterning and metal plating allows to replace conventional silver screen printing with nickel-copper plating to form inexpensive front contacts for crystalline silicon solar cells. In this work, a focus is put on effects that could cause inhomogeneous metal deposition and low metal contact adhesion. A descriptive model of the silicon nitride ablation mechanism is derived from SEM imaging and a precise recombination analysis using QSSPC measurements. Surface sensitive XPS measurements are conducted to prove the existence of a parasitic surface layer, identified as  $\text{SiO}_x\text{N}_y$ . The dense  $\text{SiO}_x\text{N}_y$  layer is an effective diffusion barrier, hindering the formation of a nickel silicide interlayer. After removal of the  $\text{SiO}_x\text{N}_y$  layer, cells show severe degradation caused by metal-induced shunting. These shunts are imaged using reverse biased electroluminescence imaging. A shunting mechanism is proposed and experimentally verified. New laser process sequences are devised and proven to produce cells with adhering Ni-Cu contacts. Conclusively the developed processes are assessed based on their industrial feasibility as well as on their efficiency potential.

